NASA Contractor Report 4211

An Experimental Study of Near Wall Flow Parameters in the Blade End-Wall Corner Region

Rakesh K. Bhargava and Rishi S. Raj
City College of New York
New York, New York

Prepared for
Lewis Research Center
under Grant NAG3-122

National Aeronautics
and Space Administration

**Scientific and Technical
Information Division**

1989

TABLE OF CONTENTS

SUMMARY

The objective of the present study was to experimentally investigate the near wall flow parameters in the blade end-wall corner region. The blade end-wall corner region was simulated by mounting an airfoil section (NACA 65-015 base profile) symmetric blades on both sides of the flat plate with semi-circular leading edge. The initial 7 cm from the leading edge of the flat plate was roughened by gluing No. 4 floor sanding paper to artificially increase the boundary layer thickness on the flat plate. The initial flow conditions of the boundary layer upstream of the corner region are expected to dictate the behavior of flow inside the corner region. Therefore, an experimental investigation was extended to study the combined effect of initial roughness and increased level of free stream turbulence on the development of a two-dimensional turbulent boundary layer in the absence of the blade.

The measurement techniques employed in the present investigation included, the conventional pitot and pitot-static probes, wall taps, the Preston tube, piezoresistive type pressure transducer and the normal sensor hot-wire probe. The pitot and pitot-static probes were used to obtain mean velocity profile measurements within the boundary layer. The measurements of mean surface static pressure were obtained with the surface static tube and the conventional wall tap method. The wall shear stress vector measurements were made with a specially constructed Preston tube. The flush mounted piezoresistive type pressure transducers were employed to measure the wall pressure fluctuation field. The velocity fluctuation measurements, used in

obtaining the wall pressure-velocity correlation data, were made with the normal single sensor hot-wire probe.

The changes in the initial flow conditions significantly influenced the development of a two-dimensional turbulent boundary layer. The increase in free stream turbulence level, in the presence of initial roughness, had an opposite effect on the variation of different mean flow characteristics relative to the case when initial roughness was absent.

At different streamwise stations, in the blade end-wall corner region, the mean values of surface static pressure varied more on the end-wall surface than on the blade surface. The observed large changes in the values of mean surface static pressure on the end-wall surface in the corner region were mainly caused by the changes in the curvature of the streamlines. The magnitude of the wall shear stress in the blade end-wall corner region increased significantly in the close vicinity of the corner line. The maximum value of the wall shear stress and its location from the corner line, on both the surfaces forming the corner region, were observed to change along the corner. These observed changes in the maximum values of the wall shear stress and its location from the corner line could be associated with the stretching and attenuation of the horseshoe vortex. The wall shear stress vectors in the blade end-wall corner region were observed to be more skewed on the end-wall surface as compared to that on the blade surface. The differences in the wall shear stress directions obtained with the Preston tube and the flow visualization method were within the range in which the Preston tube was found to be insensitive to the yaw angle.

The values of wall pressure fluctuation intensity in the blade end -wall corner region were found to be influenced by the changes in the strength of the horseshoe vortex. The spectral content of the wall pressure fluctuation increased, at any streamwise station, as the blade surface was approached. The correlation of the wall pressure fluctuation with the velocity fluctuation indicated, in general, higher values of correlation coefficient in the inner region as compared to the outer region of the shear layer. Also, the values of wall pressure-velocity correlation coefficient in the blade end-wall corner region decreased and increased in the presence of favorable and adverse pressure gradients, respectively, in the streamwise direction.

Based on the measurements of various flow parameters, it became quite evident that in the upstream region of the blade leading edge the effect of the presence of the blade diminished in a distance of approximately 8 and 6 times the blade leading edge diameter in the streamwise and lateral directions, respectively.

ACKNOWLEDGEMENTS

The work reported was done under NASA grant NAG3-122 with D. R. Boldman as the technical monitor. The authors also wish to express their deep appreciation to many NASA scientists, who made useful suggestions from time to time to the completion of this work. In particular, the authors wish to recognize late Dr. William D. McNally who helped initiate this work.

NOMENCLATURE

A_1	constant in King's law
A_θ	empirical constant, Eqn. 2.21
A_τ	empirical constant, Eqn. 2.20
B	universal constant in logarithmic law of the wall
B_1	constant in King's law
c	blade chord length
C_f	local skin friction coefficient (= $2\ \tau_w/\rho U_e^2$)
C_p	surface static pressure coefficient (= $(P_s - P_a)/0.5\ \rho U_\infty^2$)
c_p	constant pressure specific heat
d	Preston tube outer diameter
d_1	diameter of the sensitive area of the piezoresistive type of pressure transducer
d_1^+	non-dimensional diameter of the piezoresistive type pressure transducer (= $d_1 u^*/\nu$)
D	diameter of the leading edge of the blade
$\tilde{E}_b$	instantaneous bridge voltage from the hot-wire probe
f	frequency in Hz
f_k	discrete frequency
f_s	sampling rate of digitization
G	Clauser's shape parameter (= $\int_0^\infty [(U - U_e)/u^*]^2\ d(z/\Delta)$)
H	shape factor (= δ^*/θ)
k	wave number, thermal conductivity of air
K	Von-Karman constant in logarithmic law of the wall

k_1	ratio of duct cross-sectional area to its wetted perimeter, Eqn. 2.22
k_2	empirical constant, Eqn. 2.29
l	characteristic length scale of heated element thin-film sensor, Eqn. 2.31 or of an obstacle, Eqn. 2.32
l_e	effective length of heated element thin-film sensor
L_e	free stream turbulence length scale
l_m	mixing length
n	exponent in King's law
N	number of digitized samples
Nu	Nusselt number
P_a	atmospheric pressure
P_p	Preston tube pressure
$P_p(\alpha)$	total pressure recorded by the Preston tube at yaw angle of α with the local flow direction
$P_p(\alpha_0)$	total pressure recorded by the Preston tube when aligned in the local flow direction
Pr	Prandtl number ($= \mu c_p/k$)
P_s	surface static pressure
$P_s(\alpha)$	static pressure recorded by the surface static tube at yaw angle of α with the local flow direction
$P_s(\alpha_0)$	static pressure recorded by the surface static tube when aligned in the local flow direction
P_t	total pressure
p_w	fluctuating wall pressure
p'_w	root-mean-square value of fluctuating wall pressure

$\overline{p_w u}$	time averaged mean value of correlation of fluctuating wall pressure with the streamwise fluctuating velocity component
q_∞	free stream dynamic pressure (= $0.5\rho U_\infty^2$)
$\mathcal{Q}$	heat convection rate from heated element thin-film sensor, Eqn. 2.31
R	radius of the sensitive area of the piezoresistive type pressure transducer
R_{pu}	wall pressure-velocity correlation coefficient (= $\overline{p_w u}/p'_w u'$)
Re_x	local Reynolds number based on streamwise distance (= $U_e x/\nu$)
Re_θ	local Reynolds number based on boundary layer momentum thickness (= $U_e\theta/\nu$)
St	Stanton number
t	time
T	time interval of the sample record (= N/f_S)
Tu_∞	free stream turbulence intensity (= u'_∞/U_e)
u	fluctuating velocity component in X-direction
u^*	friction velocity (= $[\tau_w/\rho]^{0.5}$)
u'_∞	root-mean-square value of free stream fluctuating velocity
U	local streamwise mean velocity within the boundary layer
U_c	convection velocity of pressure producing eddies
U_e	local free stream mean velocity
U_∞	undisturbed free stream mean velocity
v	fluctuating velocity component in Z-direction

V	voltage output of the variable reluctance type pressure transducer
W	Coles's wake function
x, y, z	distances in X-, Y- and Z- directions, respectively
$x_{p_w}(t)$	sample record of wall pressure fluctuation
X, Y, Z	cartesian coordinate frame of reference (Fig. 3.11)
x1	distance in X-direction with reference to the flat plate leading edge
$Xp_w(f,T)$	fourier transform of the wall pressure fluctuation at any frequency f
$Xp_w(k)$	fourier component of the wall pressure fluctuation at discrete frequency f_k
x*	parameter in Preston tube calibration equations (= $\log_{10} [\Delta P d^2/4\rho\nu^2]$)
y1	location of normalized maximum wall shear stress on end-wall surface in corner region
y*	parameter in Preston tube calibration equation (= $\log_{10} [\tau_w d^2/4\rho\nu^2]$)
z^+	non-dimensional distance is Z-direction (= zu^*/ν)
z1	location of normalized maximum wall shear stress on blade surface in corner region

GREEK SYMBOLS

α	local flow direction
α_0	flow angle when Preston tube is aligned with the local flow direction

α_1	empirical constant for free stream turbulence effect in velocity-defect law, Eqn. 2.6
Γ	cross-spectral density function
δ	boundary layer thickness corresponding to $U/U_e = 0.995$
δ^*	displacement thickness
Δ	Clauser's integral thickness, Eqn. 4.5
Δ_p	pressure gradient parameter (= $1/\rho$ dp/dx)
Δ_p^+	non-dimensional pressure gradient (= $\Delta_p \nu/u^{*3}$)
ΔP	pressure difference between the Preston tube and mean surface static pressure (= $P_p - P_s$)
ε	eddy viscosity
ε_u	normalized standard deviation for calculated velocity, Eqn. A.2
ζ	position vector, $\zeta(\xi,\eta)$, with reference to flush-mounted pressure transducer
η	distance in Y-direction with reference to pressure transducer location on end-wall surface
θ	momentum thickness
$\Delta\theta$	temperature difference between heated thin-film sensor and free stream, Eqn. 2.31
λ^+	non-dimensional longitudinal wave length
μ	coefficient of dynamic viscosity
ν	kinematic viscosity
ξ	distance in X-direction with reference to pressure transducer location
Π	Coles's wake strength parameter
ρ	air density

τ_w	wall shear stress
$\phi_{p_w}(f)$	frequency spectra of fluctuating wall pressure
ω	angular frequency
ω^+	non-dimensional angular frequency (= $\omega \nu/u^{*2}$)

SUBSCRIPTS

a	atmospheric value
eff	effective value
f	frictional value
m	modified value
max	maximum value
n	normal value
p	Preston
ref	reference
s	static
t	total
tr	transition
w	wall
∞	free stream condition
0	zero free stream turbulence condition

SUPERSCRIPTS

~	instantaneous value
_	time average mean value
'	root-mean-square value

CHAPTER I

INTRODUCTION

1.1 Statement of the Problem

The corner flows, generally turbulent and three-dimensional in nature, are encountered in many engineering applications. Flow along a streamwise corner in a non-circular duct, at the junction of wings and tail planes with the fuselage, in the root and tip regions of the turbomachinery stator and rotor blades, at the root of fins with the heat exchanger surface, and at the junction of a bridge pier in a river bed are a few examples of the typical corner flows. The flow at the junction of stabilizing fins and a submarine's hull is another practical problem of interest where the noise caused due to two body juncture is of great concern. As the turbulent wake produced by the juncture flow is intercepted by propeller blades a pulse of sound is generated. This noise can lead to early detection of the submarine by enemy's Sonar. In turbomachinery some of these types of flows are termed blade end-wall flows.

An understanding of the blade end-wall boundary layer in turbomachinery is particularly important because the total pressure loss associated with the end-wall flow is much larger than the blade profile loss. The available literature shows that the secondary flow losses form approximately half the total losses in axial turbines. In the blade end-wall corner region, mainly two types of secondary flows have been found to exist. These are called secondary flows of the "first kind" and the "second kind". The secondary flow of the "first kind", also termed "skew induced secondary flow", leads to the formation of a horseshoe

vortex which wraps around the blade. The secondary flow of the "second kind" is generated due to the lateral gradients of the Reynolds stresses in an anisotropic and inhomogeneous turbulent flow and is also called "stress induced secondary flow". The "skew induced secondary flow" can occur both in laminar and turbulent flows, whereas, the "stress induced secondary flow" occurs only in turbulent flows. Moreover, the "stress induced secondary flows" are expected to dominate in the near wall region. A schematic of the flow in a blade end-wall corner region is shown in Fig. 1.1. Numerous experimental studies have been reported to understand development of various types of secondary flows existing in axial flow turbomachines[1-24]. Based on the informative review, Sieverding[25] observed that the experimental research on the secondary flows has resulted in a fairly detailed description of the complex end-wall flow pattern in a turbine blade passage. However, it was remarked that the information concerning the turbulent structure of the end-wall flow and the mixing processes on both the blade suction side and downstream of the cascade are not available.

To examine the influence of the horseshoe vortex on the end-wall losses a simplified blade end-wall corner flow has been studied by many investigators[26-47]. The horseshoe vortex effect was investigated either by mounting a circular cylinder or a constant thickness body with a semi-elliptic leading edge on the flat plate. Also investigations have been made of a blade with an airfoil section (representing one component of a cascade) mounted on the flat plate as in the present study. With this arrangement streamwise curvature effects could also be considered. However, most of the previous investigators con-

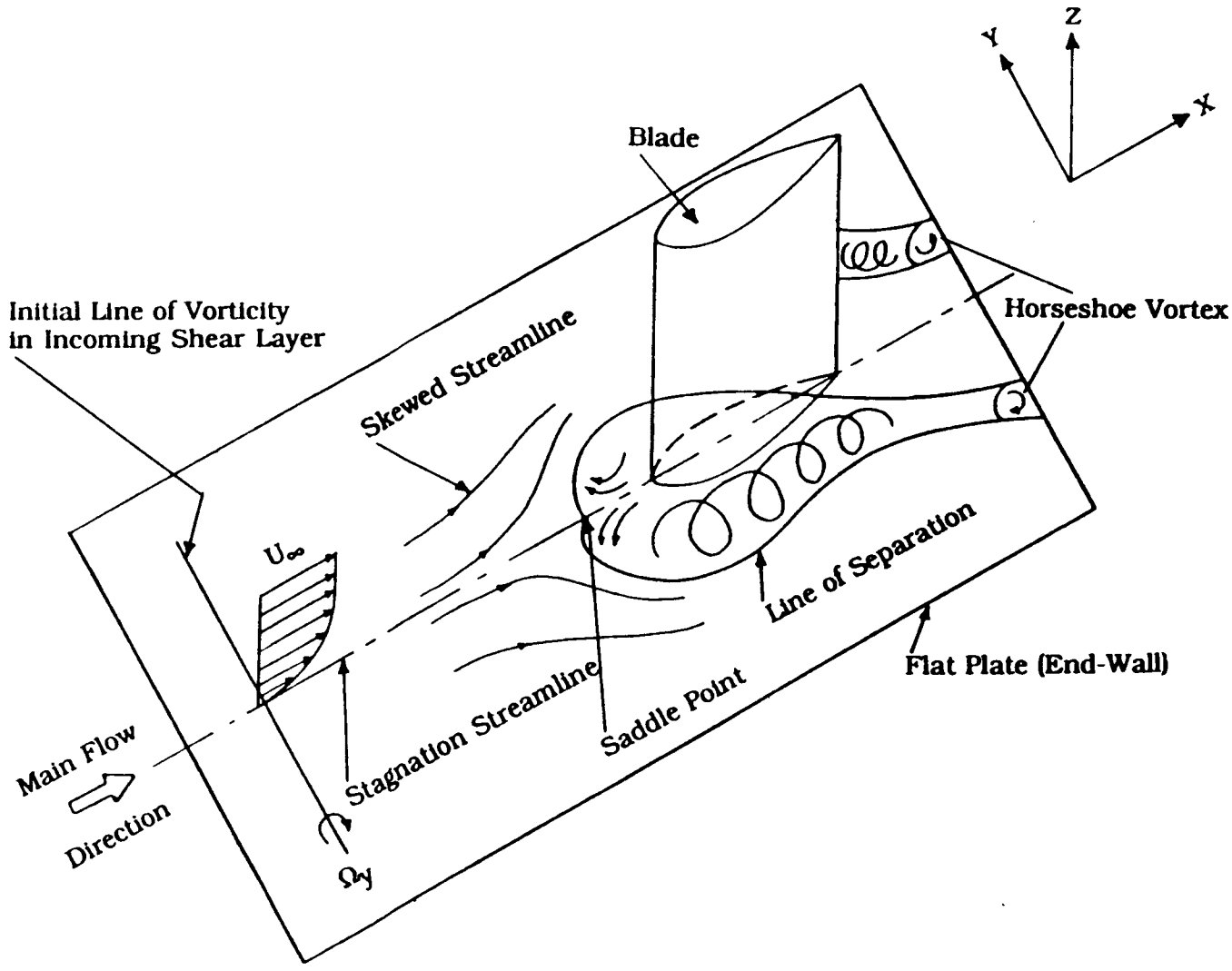

Fig. 1.1 Schematic of Flow in the Blade End-Wall Corner Region

centrated their efforts to understand the evolution of secondary flows and their interaction with the velocity field only. Very little emphasis was given to the understanding of the wall shear stress, fluctuating wall pressure field, and their interaction with the fluctuating velocity field in three-dimensional flows. The interpretation of these quantities requires the understanding of turbulence phenomena near the wall and corners.

An interesting fact on the understanding of the near wall turbulence structure was revealed by Townsend[48]. He hypothesized that the turbulent motion in the inner region of a turbulent boundary layer can be divided into an active and an inactive part. The active part is responsible for the shear stress (τ) and scales with the local flow parameters (τ and z), where z is the normal distance from the wall. The inactive or passive and effectively irrotational part is of large scale and is associated with the pressure fluctuations of the outer region. Bradshaw[49] supported Townsend's hypothesis and noted that the only noticeable effect of the inactive motion is an increased dissipation of the turbulent kinetic energy into heat in the viscous sublayer. This turbulent kinetic energy is supplied from the outer region to the region near the wall through the diffusion process. This implies that the outer and inner regions of a turbulent boundary layer are interdependent.

The interdependence of the inner and the outer region of the turbulent boundary layer was also reported by Thomas[50]. It was noted that the large scale structure influences the sweep and burst mechanisms (small scale motions) in the wall region. Thomas also concluded that the pressure field of the large scale structure did not

directly influence the generation of small scale events. The reason suggested was that the pressure field of the large eddy did not have sufficient intensity to change the velocity profile.

It can easily be seen by examining the equation for the pressure fluctuation[51] that the pressure fluctuation at a point is influenced by the entire flow field. Willmarth[52] suggested that the pressure at a given point will not be highly correlated with the velocity fluctuations at any one neighboring point. It is not difficult to observe from the fluctuating pressure equation that the fluctuating values of the wall shear stress and the surface pressure are indirectly correlated. Both play an important role in the understanding of the near wall turbulence structure. The wall shear stress is also used as the velocity scale in the inner region of a turbulent boundary layer. In a three-dimensional flow an accurate determination of the wall shear stress requires the knowledge of both its magnitude and direction. The wall shear stress vector variation in the presence of the two types of secondary flows, mentioned earlier, needs to be examined in detail.

For a two-dimensional turbulent flow the available literature (see for detailed review reference 52) shows the existence of a relation between the RMS value of the wall pressure fluctuation (p'_w) and the time averaged value of the wall shear stress (τ_w) in the form

$$p'_w = C\,\tau_w$$

where C is a constant of proportionality. The value of C is found to be weakly dependent on the Reynolds number and a strong function of the pressure transducer diameter (attenuation due to spatial resolution)[52]. The average value of constant C reported in the literature is 3 for flows with Mach number less than one[52]. However, very little

information is available about the fluctuating wall pressure field in the three-dimensional flows.

The correlation between the wall pressure fluctuation and the fluctuating velocity field is also important from the point of view of gaining insight about the near wall turbulence structure. The knowledge of these correlations can be used in identifying the regions of the shear layer which contribute to the wall pressure fluctuations. The available measurements[49, 53-55], in general, are for two-dimensional flows. In a two-dimensional turbulent boundary layer the mechanism leading to the production of intense pressure and velocity fluctuations due to stretching of the vorticity produced by the viscous stresses in the sublayer was suggested[55]. Bradshaw[49] reported that the correlations of wall pressure fluctuation with the velocity fluctuations are also influenced by the presence of the pressure gradient. The present measurements were intended to gather such data in the blade end-wall corner region.

There is another important effect which needs to be examined. This is the combined effect of initial roughness and increased level of free stream turbulence on the development of a turbulent boundary layer. In most of the turbulent boundary layer experimental work some transition promoting device is used to trigger the transition and also artificially increase the boundary layer thickness. The two most commonly used transition promoting devices are a thin wire and distributed roughness strip. It has been shown that a boundary layer developing downstream of such devices reaches a equilibrium state if compared at the same momentum thickness Reynolds number[56]. Also the streamwise distance required to achieve the equilibrium state

differ for different devices. However, very little information is available on whether similar results are achievable if the free stream turbulence level is increased, especially when the distributed roughness is used as the transition promoting device.

The above discussion clearly shows that detailed measurements of the wall pressure fluctuation intensity and the mean wall shear stress vector in the blade end-wall corner region are required. Also required is the information on wall pressure-velocity correlations in three-dimensional turbulent flows in general, and in a blade end-wall corner flow in particular. It is hoped, that this data will help in understanding the reasons leading to the interference losses, flow induced noise, and structural vibration problems in the field of turbomachines.

1.2 Objectives of the Present Investigation

Based on the discussion in section 1.1, this experimental study was undertaken to gain insight about the near wall turbulence structure in the blade end-wall corner region. The blade end-wall corner region was constructed by mounting a symmetric airfoil (NACA 65-015 base profile) on a flat plate at a distance of 620 mm from the plate leading edge. The specific objectives of the research undertaken were as follows :

(a) To study the effect of initial conditions (distributed roughness of certain streamwise extent placed downstream of the plate leading edge) and increased level of free stream turbulence on the development of a two-dimensional turbulent boundary layer

(b) To obtain detailed measurements of time averaged mean value of the surface pressure in an upstream region and in the blade end-wall corner region

(c) To obtain detailed measurements of the wall shear stress vector in an upstream region and in the blade end-wall corner region

(d) To measure the wall pressure fluctuation intensity and its power spectral density in the blade end-wall corner region

(e) To measure the correlation of wall pressure fluctuation with the streamwise fluctuating velocity component in the blade end-wall corner region

(f) To obtain measurements of steps (b) and (c) in the presence of a separation bubble in the blade end-wall corner region.

CHAPTER II

LITERATURE REVIEW

The available literature relevant to the present research work is reviewed in four sections. In the first section, the effect of free stream turbulence on the development of a two-dimensional turbulent boundary layer is reviewed. In section 2.2 the present state of knowledge about the understanding of secondary flow phenomenon and their associated end-wall losses in a blade end-wall corner region is discussed. Much emphasis is given to the experimental research work done in the last decade. Various available wall shear stress measurement techniques are briefly described in section 2.3. The literature on the wall shear stress measurements in three-dimensional turbulent shear flows and difficulties associated with these measurements are also included in section 2.3. In section 2.4, literature related to the wall pressure fluctuation is reviewed. The available literature on the correlation of wall pressure fluctuation with the fluctuating velocity field is also discussed in this section.

2.1 Combined Effect of Initial Roughness and Free Stream Turbulence on the Turbulent Boundary Layer Development

A number of techniques are available to trigger the transition and artificially increase the thickness of a turbulent boundary layer. Various devices to promote transition and artificially thicken the turbulent boundary layer such as the circular wire, normal plate or strip, slotted or toothed strip, distributed roughness, screen and air jet have been used[56,57]. A detailed investigation on the development of a turbulent boundary layer downstream of different types of transition

devices was reported by Klebanoff and Diehl[56]. Mean velocity profiles were found to become independent of flow distortions introduced by the transition device at a certain distance from the plate leading edge, the extent of which depended on the type of transition device used. The comparison of non-dimensional mean velocity profiles showed self-similarity for different transition promoting devices at approximately the same value of momentum thickness Reynolds number Re_θ. Among the different transition devices tested, the distributed roughness in the form of a sand paper strip was found to give good results.

The effects of free stream turbulence on the characteristics of a two-dimensional turbulent boundary layer have been studied by many investigators[58-73]. Kline, Lisin, and Waitman[58] investigated the effect of free stream turbulence on the development of a turbulent boundary layer with zero pressure gradient. The boundary layer was tripped using 0.009 in. diameter wire located 3/8 in. downstream of the plate leading edge. Transition was found to occur within first 3 in. of the plate leading edge. The free stream turbulence intensity ($Tu_\infty = u'_\infty/U_e$) without the presence of a turbulence generating grid was 0.5%, where u'_∞ and U_e are the RMS value of the streamwise fluctuating velocity and the local free stream velocity, respectively. The measurements were made at a free stream velocity of 100 ft/s, and Tu_∞ varied between the range $0.005 < Tu_\infty < 0.2$. It was concluded that the increase in free stream turbulence increased boundary layer thickness, created a fuller mean velocity profile, and increased the skin friction coefficient. Also, the law of the wall and the law of the wake were found to be influenced by the increased level of free stream turbulence intensity.

The influence of free stream turbulence and pressure gradient on the boundary layer transition was reported by Hall and Gibbings[59]. Various available methods for predicting transition including their advantages and limitations were reviewed. The mesh size of the grid producing free stream turbulence was found to influence the transition position. Free stream turbulence intensity and its length scale both were reported to influence the boundary layer transition position. An empirical relation

$$\ln (Re_{\theta tr} - Re_{\theta 1}) = - 103\ Tu_{\infty} + 6.88 \qquad (2.1)$$

was proposed to predict the transition Reynolds number. Equation 2.1 represents a best fit of the available data and the experiment[59], where $Re_{\theta 1}$ has a value of 190 and $Re_{\theta tr}$ is the momentum thickness Reynolds number corresponding to the transition position. This equation is valid only for the zero pressure gradient case. Free stream turbulence effects on turbulent boundary layers in the presence of an adverse pressure gradient were studied by Evans[61]. A distinct decrease in the wake component was observed with the increased level of free stream turbulence. This decrease in the wake component was attributed to the increased fullness of the outer profile because of increased mixing with the turbulent free stream. A modification to the Coles's profile was proposed. A reasonable collapse of the velocity-defect profiles on to a single curve was obtained by multiplying the defect velocity by a factor of $(1 + 5Tu_{\infty})$. Therefore, the velocity-defect law in functional form, taking into account the effect of free stream turbulence, could be written as

$$(1 + 5Tu_{\infty})(U_e - U)/u^* = f\,[z/\delta] \qquad (2.2)$$

where U_e is the local free stream velocity and δ is the boundary layer thickness, and u^* is the friction velocity.

The first detailed investigation of the effects of free stream turbulence on a turbulent boundary layer behavior was presented by Huffman, Zimmerman and Bennet[62]. Sandpaper of 3.5 grit size having a streamwise extent of 1 in. was used as a boundary layer trip to promote the transition. The structural properties of the turbulence were observed to be more strongly affected by the changes in the free stream turbulence level than the mean boundary layer properties. As the free stream turbulence level was increased, the boundary layer thickness (δ) and skin friction coefficient (C_f) increased, whereas, the shape factor (H) decreased. It was concluded that the inner layer shear stress producing mechanism is of universal nature and is largely unaffected by external conditions. It was also found that the eddy viscosity increased rapidly with increased level of free stream turbulence and its value at $Tu_\infty = 0.05$ was approximately an order of magnitude greater than the value at $Tu_\infty = 0.01$. It was also noted that the boundary layer became highly non-equilibrium in nature mainly because of the advection of the free stream turbulent energy and the non-equalization of production and dissipation.

Robertson and Holt[63] studied the effect of free stream turbulence on a turbulent boundary layer in the range of Re_θ from 400 to 2000. The free stream turbulence intensity was varied from 1% to 10%. The skin friction showed a linear variation with Tu_∞ up to its value of approximately 7% and became constant for $Tu_\infty > 7\%$. The maximum increase in C_f value was approximately 20% at $Tu_\infty \approx 7\%$. The value of δ/θ increased with an increase in Tu_∞. The maximum in-

crease was approximately 25% at $Tu_\infty \approx 7\%$. The value of shape factor decreased with an increase in free stream turbulence level. The values of different parameters (Viz., C_f, δ/θ, and H) at approximately zero free stream turbulence level, i.e., in the absence of grid generated turbulence were evaluated using well established empirical relations

$$C_{f0} = (4.4 + 3.8 \log_{10} Re_\theta)^{-2} \tag{2.3}$$

$$(\delta/\theta)_0 = 8.22 + 0.475 \log_{10} Re_\theta \tag{2.4}$$

$$H_0 = 1.09 + 0.40 [0.72 \log_{10} Re_\theta - 1.0]^{-1} \tag{2.5}$$

where the subscript '0' with the different parameters refers to their values at zero free stream turbulence.

Charnay, Comte-Bellot, and Mathieu[64] noted that both the intensity and the length scale of free stream turbulence influenced the characteristics of a turbulent boundary layer. Compared to a turbulent boundary layer evolving in an undisturbed flow (i.e., in the absence of the free stream turbulence), the influence of increasing the free stream turbulence was to increase the growth rate of the boundary layer and the wall shear stress. It was also found that the law of the wake did not follow the relation applicable to the undisturbed flow case. A modification to the velocity-defect law was proposed in which

$$(U_e - U)/(u^* - \alpha_1 u'_\infty) = f [z/\delta] \tag{2.6}$$

where the quantity $\alpha_1 u'_\infty$ takes into account the rearrangement due to the external turbulence. The measurement of turbulence quantities showed that the turbulent shear stress and turbulent kinetic energy production increased with an increase in the free stream turbulence level.

Green[65] analyzed the existing results of the previous studies and proposed some empirical relations. The influence of free stream turbulence intensity on the fractional change in C_f and H is given below.

At constant Re_θ

$$\Delta C_f/C_{f0} = 4.8\ Tu_\infty, \tag{2.7}$$

$$\Delta H/H_0 = -\ [2.4 - 0.25\ H]\ Tu_\infty, \tag{2.8}$$

and at constant H

$$\Delta Re_\theta/(Re_\theta)_0 = -\ [0.27/C_f - 0.97(2/C_f)^{0.5}]\ Tu_\infty \tag{2.9}$$

An analytical method to predict the effect of free stream turbulence on the turbulent boundary layer development was presented by McDonald and Kreskovsky[66]. By allowing the entrainment of free stream turbulence into the turbulent boundary layer and performing an overall turbulent energy balance, it was found that satisfactory quantitative predictions of the free stream turbulence effect on the turbulent boundary layer behavior could be made. Furthermore, a 30% increase in skin friction with a 5% increase in free stream turbulence was predicted. This result compared well with the experimental data.

The influence of wind-tunnel turbulence on the development of a turbulent boundary layer was investigated by Meier and Kreplin[67]. The results were obtained for a turbulence intensity in the range $0.06\% < Tu_\infty < 1\%$. Based on the experimental results, the following empirical relations for the change in skin friction were proposed:

$$\Delta C_f/C_{f0} = 190\ Tu_\infty^2 \qquad Tu_\infty < 1\% \tag{2.10}$$

$$\Delta C_f/C_{f0} = 3.8\ Tu_\infty - 0.019 \qquad Tu_\infty > 1\% \tag{2.11}$$

The influence of free stream turbulence in the range 0.3%-6% on a turbulent boundary layer development at high Reynolds number ($Re_\theta = 10^4$) was studied by Raghunathan and McAdam[68]. The influence of free stream turbulence on integral parameter δ/θ was found to be non-linear and an empirical relation was proposed:

$$(\delta/\theta)/(\delta/\theta)_0 = 1 + 500\ Tu_\infty^2 \tag{2.12}$$

which fitted the available and their experimental data well for $0 < Tu_\infty < 0.04$. It was also pointed out that the results of Robertson and Holt[63] showed a linear variation of $(\delta/\theta)/(\delta/\theta)_0$ with Tu_∞ which could be represented by

$$(\delta/\theta)/(\delta/\theta)_0 = 1 + 5\ Tu_\infty \tag{2.13}$$

However, this linear relationship appeared to be accurate only up to $Tu_\infty = 0.01$ beyond which it underestimates the effect of Tu_∞. The influence of Tu_∞ on change in shape factor was found to be well represented by an empirical relation

$$\Delta H/H_0 = -\ 2\ Tu_\infty \tag{2.14}$$

The influence of free stream turbulence on the wake strength parameter (Π) was found to be well represented by an empirical relation

$$\Delta\Pi/\Pi_0 = -\ 0.9\ (u'_\infty/u^*) \tag{2.15}$$

The change in skin friction coefficient due to an increased level of free stream turbulence was found to be well represented by an empirical relation in the range $0 < Tu_\infty < 0.04$

$$\Delta C_f/C_{f0} = 12.6\, Tu_\infty^{1.4} \qquad (2.16)$$

The measurements of Raghunathan and McAdam also showed that the streamwise turbulence intensity (u') within the boundary layer was more sensitive to free stream turbulence level especially in the outer region, whereas, the streamwise turbulence intensity did not change in the inner region. It was also observed that the wall pressure fluctuation intensity increased with the increase in free stream turbulence level. For example, the value of p'_w/q_∞ changed from 0.65% to 2.05% when the value of Tu_∞ increased from 0.0034 to 0.063, where p'_w and q_∞ are the RMS value of the wall pressure fluctuation and free stream dynamic head, respectively.

Some investigators[for example ref. 64, 65, 68] reported that both the free stream turbulence intensity and its length scale influenced the turbulent boundary layer characteristics. However, no systematic investigation on the effect of free stream turbulence length scale was attempted.

Recently, a detailed experimental study of the effect of typical free stream turbulence length scale ratio (i.e., the ratio of the free stream turbulence dissipation length scale, L_e, to the boundary layer thickness) on the turbulent boundary layer characteristics was reported by Hancock and Bradshaw[69]. In general, two turbulence length scales are commonly used in the literature. These length scales are the integral length scale and the dissipation length scale of the free stream turbulence. Hancock and Bradshaw preferred to use turbulence dissipation length scale which can be easily calculated once the decay characteristics of the free stream turbulence downstream of

a turbulence generating grid are known. The turbulent kinetic energy equation applied to free stream flow reduces to

$$U_\infty[d(u'^2_\infty)/dx] = - u'^3_\infty/L_e \qquad (2.17)$$

and the variation of grid generated free stream turbulence can be written as

$$[u'^2/U^2]_\infty^{-0.8} = C_1 (x/M - C_2) \qquad (2.18)$$

where M is the mesh size of the grid, x is the streamwise distance from the turbulence generating grid, and C_1 and C_2 are constants which can be determined experimentally for any grid. Using Eqns. 2.17 and 2.18 one can easily calculate the value of L_e. A wider range of turbulence length scale ratio, $0.7 < L_e/\delta < 5.0$, was covered in their study. It was found that the effect of free stream turbulence on a turbulent boundary layer increased with the increase in free stream turbulence intensity. On the other hand, the effect of free stream turbulence decreased with the increase in its length scale ratio. It was also reported that the skin friction and other boundary layer parameters have a nonlinear dependence on the free stream turbulence intensity. The change in skin friction at constant Re_θ with the change in free stream turbulence intensity could be made to fall on a single curve if the effect of length scale ratio was also included. The parameter for abscissa for plotting change in C_f selected was $Tu_\infty/(L_e/\delta + 2.0)$, where the denominator was selected by trial and error procedure.

More recently, Castro[70] studied the effect of both the free stream turbulence intensity and the length scale ratio on a low Reynolds number turbulent boundary layer. This investigation was made at a momentum thickness Reynolds number in the range 500 <

$Re_\theta < 2500$, $Tu_\infty < 0.07$, and $0.8 < L_e/\delta < 2.9$. Direct Reynolds number effects were observed to be significant and it was shown that such effects diminished as the free stream turbulence level was increased. A modification to the empirical correlation, suggested by Hancock and Bradshaw[69], relating the fractional change in skin friction coefficient at constant Re_θ, to a free stream turbulence parameter containing a dependence on both the turbulence intensity and the length scale was proposed. At low Reynolds number in the range $600 < Re_\theta < 2000$, the correlation between fractional change in skin friction and modified free stream turbulence parameter was written as

$$(\Delta C_f/C_{f0})[\ 1 + (10/F^2) \exp(-Re_\theta/400)] = f[F] \qquad (2.19)$$

where $F = 100\ Tu_\infty/(0.5\ L_e/\delta + 2.5)$, is a modified free stream turbulence parameter.

Effects of free stream turbulence and pressure gradient on mean velocity profiles and heat transfer were investigated by Junkhan and Serovy[71]. The measurements, obtained at low local Reynolds number ($4x10^4 < Re_x < 4x10^5$), indicated no influence on the heat transfer with the increase in free stream turbulence intensity. Simonich and Bradshaw[72], however, argued that if Reynold's analogy were to be exact, one would expect the percentage change in turbulent heat transfer because of increased free stream turbulence intensity to be the same as percentage change in skin friction. Based on the available measurements, the change in skin friction due to free stream turbulence, at constant Re_θ, was written as

$$C_f/C_{f0} = 1 + A_\tau\ Tu_\infty \qquad (2.20)$$

where $A_\tau = 3$ and depends strongly on the free stream turbulence length scale. For turbulent heat transfer a relation similar to Eqn. 2.20 was written as

$$St/St_0 = 1 + A_\theta \, Tu_\infty \qquad (2.21)$$

which gives the influence of turbulence intensity on heat transfer, where St is the Stanton number. The measurements showed the value of $A_\theta = 5$ suggesting that the Reynolds analogy factor increases slightly in the presence of free stream turbulence. Quantitatively, it was reported that the Stanton number increased by about 5% for each 1% increase in free stream turbulence intensity. Also the Stanton number, at a given free stream turbulence intensity, decreased as the free stream turbulence length scale increased.

A more detailed investigation of the effect of free stream turbulence on a turbulent boundary layer was recently reported by Blair[73]. This investigation showed increase of approximately 14 and 18 percent for skin friction and heat transfer, respectively, for a 6% increase in free stream turbulence intensity. This study covered Reynolds numbers, Re_θ, ranging from 1000 to 6000, whereas the free stream turbulence intensity was varied from 0.25% to 7%.

The influence of free stream turbulence on the turbulent boundary layer characteristics was recently reviewed by Pal[74] while studying the effects of free stream turbulence on the development of wakes produced by a thin plate and also the wake-boundary layer interaction phenomena.

Based on the discussion presented above, the quantitative effect of the free stream turbulence on various turbulent boundary layer parameters of importance is presented in Table 2.1.

From the available literature reviewed here it is quite evident that very little information about the influence of free stream turbulence on the development of a turbulent boundary layer developing downstream of initially distributed roughness is available.

2.2 Secondary Flow Effects in End-Wall Corner Flows

In this section recent advances made in the understanding of the development of secondary flows in the blade end-wall corner region are described. It is important to mention that no attempt is made here to present a detailed review on the corner flows. A detailed review of existing literature on the corner flows up to mid-seventies was presented by Shabaka[36]. Recently, a good description on corner flows with the systematic classifications of various types of corner flows of practical interest was given by Hazarika[47]. However, in this section experimental results on the nature of secondary flows and end-wall losses obtained by various researchers in the last ten years are briefly discussed.

Various empirical and semi-empirical correlations developed by the late fifties to predict secondary losses in cascades and axial-flow turbomachines were compiled and discussed by Lakshminarayana and Horlock[75]. In this review article, different types of secondary flows encountered in axial-flow turbomachines and cascade were described. Based on the available experimental results it was remarked that the end-wall losses resulted primarily from the separation of the boundary

TABLE 2.1. Free Stream Turbulence Influence on Mean Flow Boundary Layer Parameters

Parameter	Tu_∞ (%)	% Variation in Parameter	Remarks	Investigator (Year)
Boundary Layer Thickness (δ)	11.0	14.3		Kline et al. (1960)
	3.9	50.0		Huffman et al. (1972)
	7.0	45.0	Re_θ = 400-2000	Robertson & Holt (1972)
	1.94	16.7	Re_θ = 2113	Evans (1974)
	3.42	25.6	Re_θ = 1760	Evans (1974)
	1.0	10.0	$Re_\theta = 1.0 \times 10^4$	Raghunathan & McAdam (1983)
Displacement Thickness (δ^*)	11.0	4.0		Kline et al. (1960)
	3.9	- 9.8		Huffman et al. (1972)
	1.94	20.7	Re_θ = 2113	Evans (1974)
	3.42	5.2	Re_θ = 1760	Evans (1974)
Momentum Thickness (θ)	11.0	10.0		Kline et al.(1960)
	3.9	- 1.6		Huffman et al. (1972)
	1.94	25.0	Re_θ = 2113	Evans (1974)
	3.42	8.0	Re_θ = 1760	Evans (1974)
δ/θ	7.0	35.0		Robertson & Holt (1972)
	1.94	- 6.7	Re_θ = 2113	Evans (1974)
	3.42	16.0	Re_θ = 1760	Evans (1974)
	3.14	49.0	$Re_\theta = 1.0 \times 10^4$	Raghunathan & McAdam(1983)
$H = (\delta^*/\theta)$	11.0	- 5.5		Kline et al.(1960)
	3.9	- 8.5		Huffman et al. (1972)

TABLE 2.1 (Continued)

Parameter	Tu_∞ (%)	% Variation in Parameter	Remarks	Investigator (Year)
$H = (\delta^*/\theta)$	7.0	- 5.0	Re_θ = 400-2000	Robertson & Holt (1972)
	4.1	- 8.7	Reported by Pal (1981)	Tsuji & Iida (1972)
	1.94	- 3.5	Re_θ = 2113	Evans (1974)
	3.14	- 8.0	$Re_\theta = 1.0 \times 10^4$	Raghunathan & McAdam (1983)
Wake Strength Parameter (Π)	1.94	- 81.0	Re_θ = 2113	Evans (1974)
	3.14	- 55.0	$Re_\theta = 1.0 \times 10^4$	Raghunathan & McAdam (1983)
Skin Friction Coefficient (C_f)	3.9	16.9		Huffman et al. (1972)
	4.1	10.8	Reported by Pal (1981)	Tsuji & Iida (1972)
	1.94	5.3	Re_θ = 2113	Evans (1974)
	3.42	10.5	Re_θ = 1760	Evans (1974)
	3.14	9.9	$Re_\theta = 1.0 \times 10^4$	Raghunathan & McAdam (1983)
Re_θ	1.94	25.0		Evans (1974)
	3.42	4.0		Evans (1974)
	3.14	47.0		Raghunathan & McAdam (1983)
Mixing Length (l_m)	4.1	96.0	Reported by Pal (1981)	Tsuji & Iida (1972)
Eddy Viscosity (ϵ)	4.1	233.0	Reported by Pal (1981)	Tsuji & Iida (1972)

layer on the corner formed by the end-wall and the blade suction surface. An interesting explanation was presented for the observed higher losses in turbines and relatively smaller losses in compressors due to relative motion between the wall and the blade. It was noted, that the effect of a moving wall was to impart a rolling motion to the air in the vicinity of the blade leading edge. Moreover, the effect of moving wall was observed to be favorable in the case of compressor and adverse in the case of turbine. The above mentioned factors explained the differences in the influence of the relative motion between the wall and the blade in turbines and compressors.

Dunham[76] reviewed different analytical and experimental studies on secondary losses in a turbine cascade. Using the available results, an empirical relation was proposed which correlated the effect of blade loading and incoming boundary layer thickness on secondary flow losses. A list of various parameters which influence secondary flow losses were provided and their effects, based on the available data, were analyzed. Also different mechanisms of the secondary flow losses as envisaged by numerous investigators were discussed. He also noted that the secondary flow losses were approximately half of the total losses in a turbine. Based on this study he concluded that even though the flow pattern associated with secondary losses is understood the reasons for the magnitude of these losses are not well understood. Therefore, it was suggested that more detailed studies of the flow inside the blade passage would be required before accurate secondary loss prediction schemes could be developed.

The suggestion of Dunham did not go in vain as the number of detailed experimental studies to understand three-dimensional flows

in the blade passage came into existence in the literature in late seventies. Langston, Nice and Hooper[2] reported a detailed experimental study of the three-dimensional flow in a large scale turbine cascade with particular emphasis on the end-wall flows. Mean flow and surface pressure measurements on the blade and the end-wall, including flow visualization studies, were made. The effect of the change in incoming boundary layer thickness was also investigated. Three-dimensional flow separation was observed to be an important feature of the end-wall flows. The position of the saddle point of separation and its associated attachment and separation lines were found important in defining the flow field near the end-wall. The saddle point was observed to depend on the pressure field in the blade passage and not on the change in incoming boundary layer thickness. However, it was noted that in the case of symmetric flow (such as cylinder mounted on a flat plate) the location of the saddle point depended on the state of the incoming boundary layer (laminar or turbulent), the boundary layer Reynolds number, and the cylinder diameter[4]. The size of the passage vortex was found to increase in the downstream direction entraining fluid from the main stream as well as separated fluid from the end-wall and the blade suction surface boundary layers. The passage vortex was found to significantly alter the pressure field from that of a potential flow. It was concluded that any attempt to model analytically all or part of the flow field in the cascade passage must in some way take account of the three-dimensional separation process.

Using the results of extensive mean flow measurements and flow visualization studies made by Langston, Nice, and Hooper[2], a model (Fig. 2.1) for the secondary flows in a cascade passage was proposed by

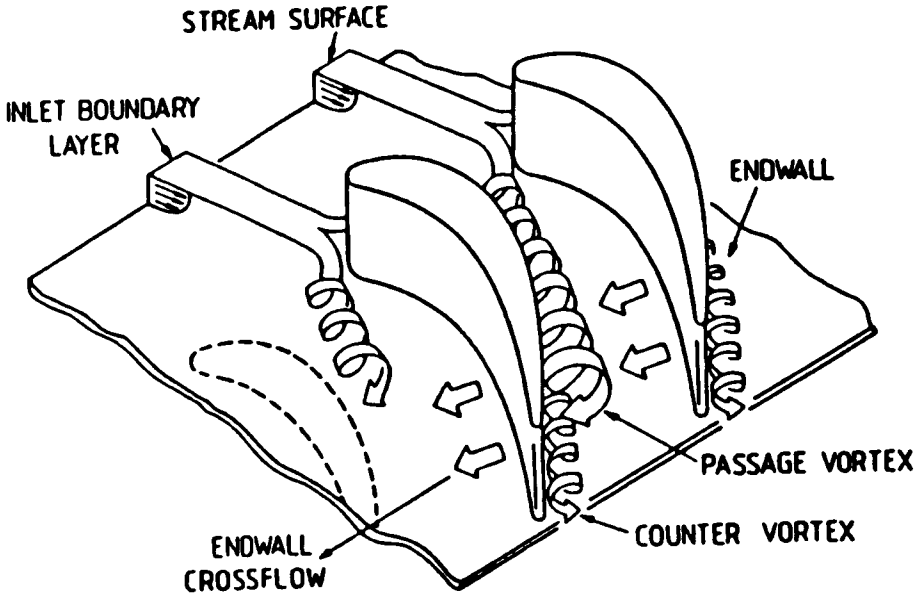

Fig. 2.1 End-Wall Flow Model in Cascade by Langston[5]

Langston[5]. General mechanisms leading to the generation of different secondary flows in the cascade as described by Langston and also later observed by many other investigators will now be discussed. Basically, there are two mechanisms which influence the generation of secondary flows in a turbomachinery passage. First of all, secondary flow is produced due to rotation or curvature which causes the flow with an initial distribution of normal vorticity to generate a streamwise component of vorticity. This phenomenon, it should be noted, also occurs in curved ducts. Secondly, as the end-wall boundary layer encounters the blade leading edge, a horseshoe shaped vortex is formed. A majority of the fluid from the incoming boundary layer gets trapped in this vortex which has two legs. These two legs are known as pressure- and suction-side legs. During this process the normal component of the vorticity associated with the incoming boundary layer is transformed into the streamwise component of the vorticity. This phenomenon is a dominating feature in simple blade end-wall flows (for example wing-body junction).

The interaction of the pressure-side leg of the horseshoe vortex with the crossflow from the end-wall boundary layer formed within the cascade and the entrained fluid from the mainstream flow in the cascade passage leads to the formation of a vortex which is generally known as a passage vortex. The suction-side leg of the horseshoe vortex remains in the suction-end-wall corner region and is known as a counter vortex. The counter vortex has been observed to have a sense of rotation opposite to the passage vortex and is much smaller in size than the passage vortex. These vortices explained above are shown in

Fig. 2.1. Langston also noted that the counter vortex may be dissipated by viscosity.

The loss mechanisms and the behavior of secondary flows downstream of a large scale stator and rotor by Hunter[6] and downstream of a stator by Binder and Romey[7] were investigated. Hunter found that the presence of spanwise pressure gradient in the annular geometry enhanced a migration of boundary layer fluid towards the hub end-wall via the blade trailing edge and on the suction surface in the laminar flow regions. It was also observed that the secondary flows in the rotor blade row, mainly at the high turning hub section, were considerably more complex than in the case of stators. The comparison of data obtained in a single stage turbine with the cascade data revealed that the behavior of the end-wall flow in the stators and cascade was almost similar. A major difference was the existence of appreciable radially directed flow in the case of stator. Binder and Romey noted that the mixing losses existed far downstream from the trailing edge. They also noted that some vortices existed even far downstream of the trailing edge which will affect the flow in the following rotor passages.

The secondary flow field at each downstream plane was found to be dominated by a passage vortex which decayed in its strength because of mixing occurring in the flow. It was also noted that the increase in total pressure loss was accompanied by a decrease in the secondary kinetic energy of the flow. Furthermore, they found that the spanwise component of secondary velocity contributed more than 75% to the total decrease in the secondary kinetic energy. Finally, it was

remarked that more than one-third of the total secondary losses were found to occur downstream of the blade trailing edge.

Sieverding and Van Den Bosche[8] studied secondary flows in a turbine cascade using a colored smoke flow visualization technique. In this technique a tungsten wire of 0.25 mm diameter was coated with Waxoline dye mixed with oil. The dye evaporated as the wire was heated and produced smoke filaments which could be obtained in different colors. The main conclusion, besides identifying various secondary vortices, was that the horseshoe vortex and the passage vortex did not exist independently of each other but were observed to be a part of the same vortex structure.

Moore and Ransmayr[10] experimentally investigated the effect of the blade leading edge shape on the overall losses in a large scale rectilinear turbine cascade. Two leading edge shapes (circular cylinder and a wedge) were studied. The influence of leading edge shape on different measured parameters viz., surface pressure on the blade and end-wall and the total pressure loss and the flow directions downstream of the cascade, was found insignificant. The loss distribution measured downstream of the cascade showed regions of high loss near the mid-span irrespective of the shape of the blade leading edge. In fact Moore and Ransmayr expected suppression of the formation of a horseshoe vortex with wedge shape leading edge. Sieverding[25] presented an interesting explanation on the leading edge effects observed by Moore and Ransmayr. He observed that, in the case of cascade, the stagnation streamline is curved and the incidence angle to the sharp nose will be different from zero. Therefore, the flow "sees" a sharp leading edge as a blunt leading edge. Hence the size of the horseshoe

vortex will greatly depend on the incidence angle of the incoming flow. Sieverding also observed that the shape and position of the passage vortex would not be much influenced by the reduction or elimination of the horseshoe vortex. Furthermore, the rotational speed of the particles near the vortex center might be affected by the strength of the pressure-side leg of the horseshoe vortex.

Sieverding[25] reviewed the existing results of secondary flow research and presented a detailed description of secondary flow structures and their effects on end-wall boundary layer characteristics and loss growth through a rectilinear turbine blade cascade. He noted that the vortex model in a turbine cascade proposed by Kline (reference No. 8 of Sieverding) and Langston[5] differed with regard to the interpretation of the suction-side leg of the horseshoe vortex. The main difference in these two vortex models was as follows: Langston suggested that the suction-side leg of the horseshoe vortex continued in the suction surface-end-wall corner, whereas Kline suggested that the suction-side leg of the horseshoe vortex gradually dissipated as it came in contact with the passage vortex. Also, Marchal and Sieverding[3] in their flow visualization study found that the suction-side leg of the horseshoe vortex was observed in the trailing edge plane on the mid-span side of the passage vortex rather than in the suction-side end-wall corner. Among the various loss contributions the corner losses in the suction surface-end-wall corner was found to be more significant than the end-wall losses in the pressure surface-end-wall corner. In conclusion, two important remarks were made: (i) a clear description of the merging process between pressure-side leg of the horseshoe vortex and the passage vortex and also of the interac-

tion between suction-side leg of horseshoe vortex and the passage vortex has yet not emerged, and (ii) the experimental research on secondary flows has resulted in a fairly detailed description of the complex end-wall flow pattern in turbine blade passage. However, more information concerning the turbulent structure of the end-wall flow and the mixing process on the both the blade suction-side and downstream of the cascade is desired.

At the same time the Sieverding review became available, an interesting flow visualization study on the spatial development of streamwise vortices in a turbine cascade was reported by Sonoda[12]. Based on many cross-sectional views normal to the flow, the evolution of the horseshoe vortex into streamwise vortices and the generation of a new type of streamwise vortex pair on the suction surface near the end-wall was described in detail. A brief description on this recent study on the secondary flow development in a turbine blade cascade is presented here. More detailed description can be obtained in Sonoda's original paper.

At x/C_a = 0.3 (section 1 in Fig. 2.2) the pressure-side and suction-side legs of the horseshoe vortex were observed to exist as a vortex pair, where C_a is the axial chord length of the blade. As this vortex moved downstream, at x/C_a = 0.85 (section 10 in Fig. 2.2) it rotated by 90^0 and then was observed to rotate by another 90^0 at the blade trailing edge. This rotating motion of the vortex pair was attributed to the increase in circulation of the pressure-side leg (Hp) of the horseshoe vortex due to the transverse pressure gradient as compared to the circulation of the suction-side leg (Hs) of the horseshoe vortex. Also as the vortex pair moved downstream it was observed to be divided into

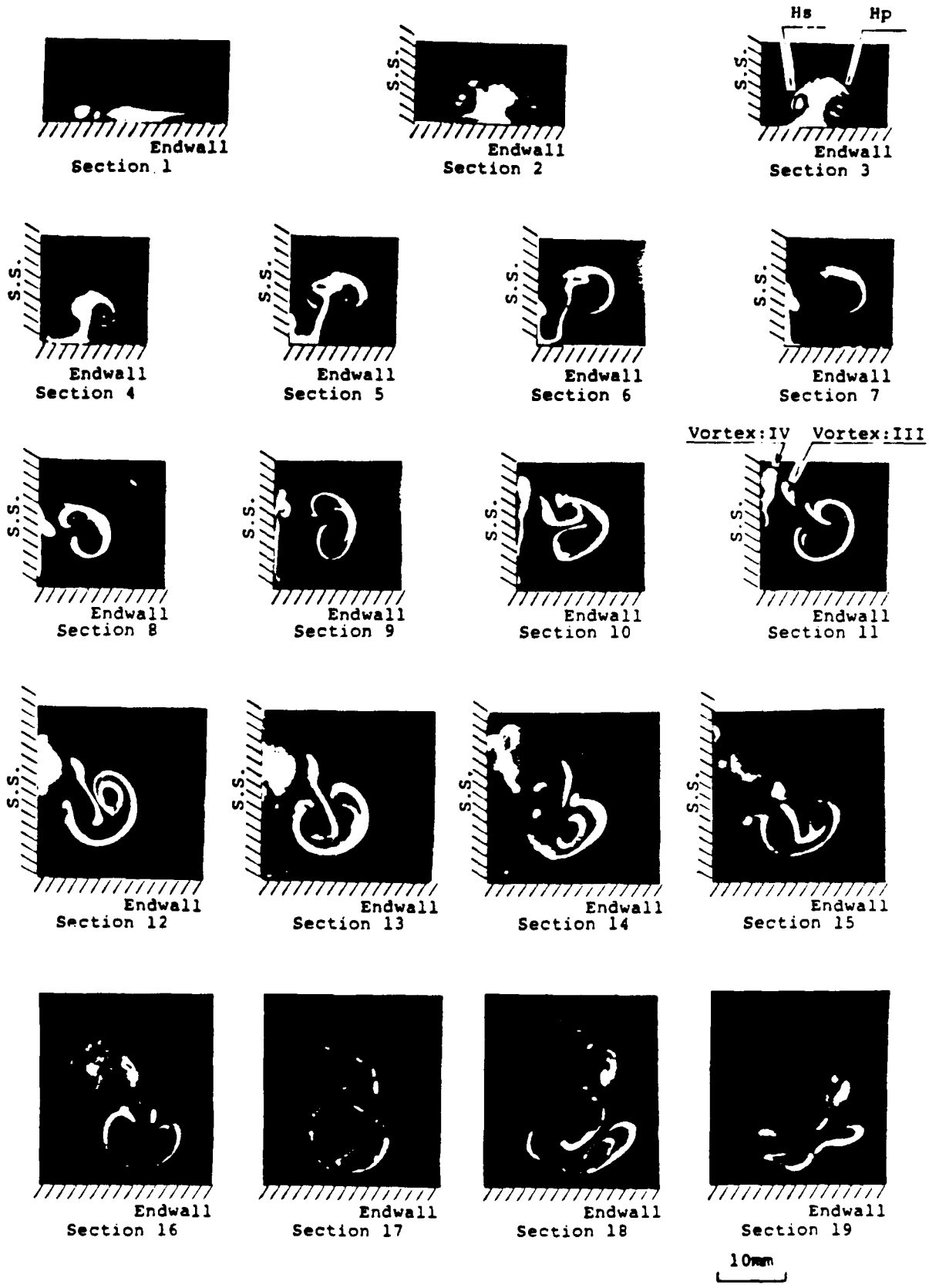

Fig. 2.2 Development of Streamwise Vortices in a Turbine Cascade Passage (Fig.10 of reference[12])

two parts at approximately x/C_a = 0.54 (section 5 in Fig. 2.2). One part corresponded to the "leg" of the vortex pair (Hs and Hp), whereas the other part evolved as another vortex pair (termed as III and IV). It was noted that the migration of the root of the "leg" of this new vortex pair on the suction surface corresponded to Langston's separation line on the suction surface. This study also concluded that the pressure-side and suction-side leg of the horseshoe vortex did not exist independently but as a pair of vortices. Furthermore, this vortex pair showed a mutual vortical induction motion which in the literature is known as a passage vortex.

Moustapha, Paron and Wade[13] reported experimental measurements on the secondary losses in a large scale annular cascade of highly loaded turbine rotor blades. The blades had a turning angle of 128.5^0 and aspect ratio of 0.88. Distribution of the losses and flow angles revealed the presence of two large vortices which occupied a major portion of the trailing edge plane. A large high loss core was observed in the center of the blade passage and it coincided with the region of maximum flow underturning.

More recently, Govardhan, Venkatrayulu, and Prithvi Raj[14] investigated the effect of the incoming boundary layer thickness on secondary losses in large deflection (120^0) annular turbine cascade. The incoming boundary layer thickness was systematically varied both on the hub- and the casing-walls. In general, the loss core near the hub-wall was found larger than that near the casing-wall. With the increase in inlet boundary layer thickness on the hub-wall, the magnitude of the hub loss core increased due to the increased feeding of the inlet boundary layer fluid into the loss core by the pressure-side leg of the

horseshoe vortex. However, with the increase in inlet boundary layer thickness on the casing-wall, the magnitude of the hub loss core was again increased, whereas the magnitude of the casing core loss remained more or less unchanged. In the latter case increased radial flow from the tip to the hub of the blade was found to be the cause of the differences observed. The measurement of pitchwise mass averaged flow angles showed that the flow overturned near the walls and underturned in the region of loss cores. The degree of underturning increased with the increase in inlet boundary layer thickness.

Production and development of secondary flows and associated losses in stator and rotor blade rectilinear cascade were measured by Yamamoto[16]. In the case of the stator, a significant contribution of the secondary flows on the loss production process was observed only near the blade suction surface downstream of the cascade throat. However, in the rotor blade case larger turning resulted in a much stronger contribution of the secondary flows on the loss development mechanism. It was also noted that the evolution of overall loss started quite early within the blade passage and also the rate of the loss growth was much larger in the rotor blade case compared to the stator blade case.

Very recently, the growth of losses, secondary kinetic energy, and the streamwise vorticity in a highly turning turbine rotor blade cascade was experimentally investigated by Gregory-Smith, Graves, and Walsh[18]. The effect of a change in inlet boundary layer thickness on various parameters was also considered. A new technique was developed to calculate streamwise vorticity component from the mean flow velocity data. The new method consisted of fitting a least square

bi-cubic spline surface to the data points and then the gradient of the surface was taken in the required direction at each data point coordinate. It was noted, that the negative vorticity associated with the passage vortex agreed with the predictions of classical secondary flow theory in the early part of the blade passage. However, towards the blade passage exit, distortion of the flow by the secondary velocities resulted in inaccurate predictions by analytical methods. The positions of the loss core, end-wall loss region, and vortex center were observed to be alike with the change in inlet boundary layer thickness. The main difference caused due to change in inlet boundary layer thickness was that the above mentioned features became broader and less intense with an increase in inlet boundary layer thickness. For example, the maximum values of positive and negative vorticity were found to be much lower in the thin boundary layer case compared to the thick boundary layer case. This observed change was attributed to the high values of vorticity in the thin boundary layer which are concentrated near the end-wall. Moreover, areas of positive vorticity were observed to be associated with the transfer of losses into the bulk flow.

The first measurements of turbulence characteristics related to the secondary flows in the blade passage of a turbine cascade were reported recently by Zunino, Ubaldi, and Satta[19]. The secondary flow pattern was observed to be dominated by the presence of a passage vortex which caused high losses near the suction side. The passage vortex was found to play a double role: it was found to transport low momentum flow towards the suction side and changed the mean velocity and turbulent stress distributions. The action of Reynolds stresses on the shear flow was then to extract energy from the mean

flow and produce losses within and downstream of the cascade. It was concluded, that the secondary loss generation in cascades is related to the production of turbulent kinetic energy in the vortex flow and its viscous dissipation.

Using the available studies in conjunction with the flow visualization studies by Sharma and Butler[17], an interesting interpretation of the mechanism of secondary flows and associated secondary losses in a turbine cascade evolved. Sharma and Butler agreed with the mechanism of the formation of the horseshoe vortex as described earlier. But, according to them, the streamwise component of the vorticity due to the horseshoe vortex is generated as soon as the fluid enters the cascade before most of the turning of the mainstream flow has been achieved. However, it was noted, that the existing secondary flow theories used for the prediction of secondary vorticity relies on the assumption that the inlet boundary layer entering the cascade experiences flow turning in the passage. Therefore, the assumption made in the theory is inconsistent with the revelations made by their flow visualization studies. Moreover, their flow visualization studies also revealed that the fluid particles closest to the wall in the cascade inlet boundary layer did not become part of the horseshoe vortex. These fluid particles, in fact, were observed to move towards the suction-side of the blade where they climbed the blade surface and exited the blade on the top of the passage vortex.

Moreover, the pressure-side leg of the vortex was observed to be immediately influenced by the blade to blade pressure gradient as it entered the passage and moved towards the suction-side, meeting the surface near the minimum pressure point. Since all the fluid particles

from the inlet boundary layer either became part of the horseshoe vortex or moved towards the suction side, a new boundary layer started at the end-wall downstream of the separation line defined by the horseshoe vortex system. As the pressure-side leg of the horseshoe vortex moved across the passage it entrained low momentum fluid particles from this newly formed passage end-wall boundary layer and it grew to become the passage vortex. This passage vortex was noted to be the most dominant feature of the flow. This entrainment of the passage end-wall boundary layer fluid significantly affected the development of the passage vortex and is a key mechanism in the generation of the secondary flows and end-wall losses. Since this mechanism is governed by viscosity, inviscid secondary flow theories are not expected to provide accurate magnitudes of the secondary vorticity or end-wall losses in a cascade.

Furthermore, in the close vicinity of the leading edge, the suction-side leg of the horseshoe vortex was observed to follow the contour of the airfoil surface. Also, the suction-side leg of the horseshoe vortex was observed to remain near the end-wall until the point where the passage vortex interacted with the suction-side of the blade. Near the minimum pressure point in the cascade passage, the suction-side leg of the horseshoe vortex was forced off the end-wall as it interacted with the passage vortex. As the flow proceeded downstream, the suction-side leg of the vortex moved around the outside edge of the passage vortex. This observation, it should be noted, is similar to that observed by Marchal and Sieverding[3]. The location of this suction-side leg of the horseshoe vortex in the cascade exit plane depended on the size and vorticity associated with it and the passage vortex.

Based on the flow visualization and the discussion presented above, a schematic of the flow in turbine cascade as proposed by Sharma and Butler is shown in Fig. 2.3. The height (Z_{TE}) of the separation line S_2 at the trailing edge of the blade approximates the diameter of the passage vortex. It was noted that the knowledge of the penetration height of this separation line (S_2) at the trailing edge on the suction surface can be used in estimating both the end-wall losses and the secondary flows. Based on the available data it was reported that penetration of the separation line towards the mid-height of the blade suction surface was found to give good estimates of the secondary flows. It was also found from the available literature that the region adjacent to the suction surface between the separation line and the end-wall was one of high loss and high external heat load associated with the passage vortex. The information of separation line and its penetration height, especially at the trailing edge, was used to develop an empirical relation to predict end-wall losses.

The earlier measurements showed that the net loss generated inside the passage was approximately same for both the thick and thin inlet boundary layers. Using the foregoing observation, the total loss was divided into two parts; namely, the inlet loss contained within the cascade inlet boundary layer and the passage loss. The passage loss was further divided into the profile loss and the end-wall secondary flow losses. An empirical equation was suggested to predict end-wall losses and was found to agree within ±10% compared with the available experimental data.

The measurement of mean flow and turbulence characteristics inside the hub and annulus wall boundary layer in the trailing edge and

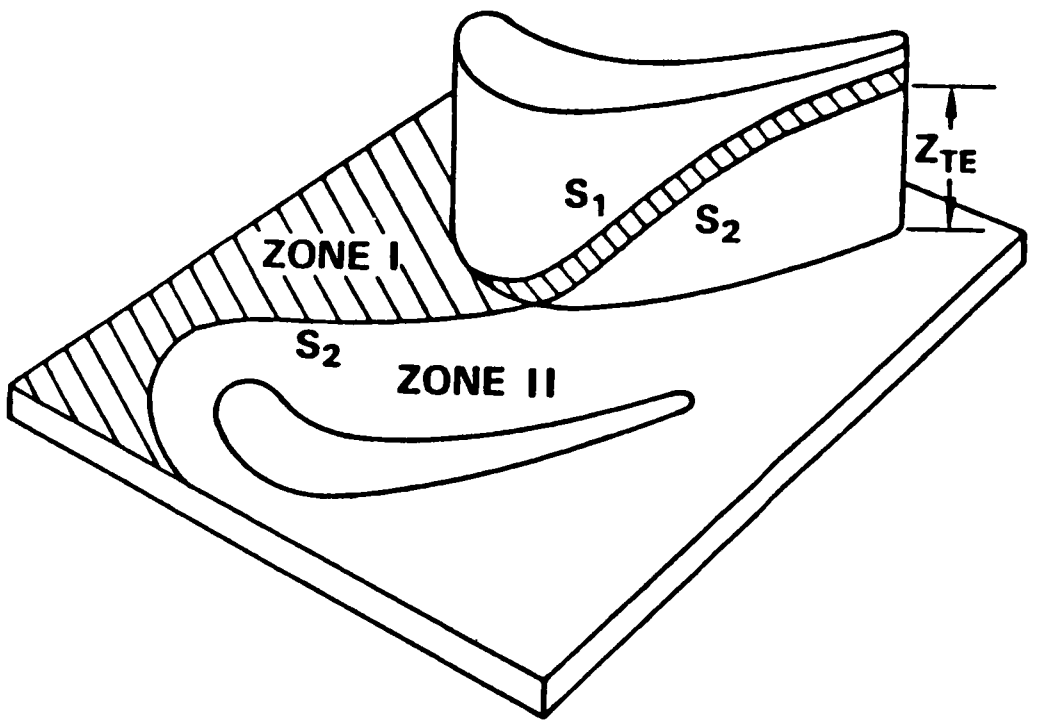

Fig. 2.3 End-Wall Flow Model in Cascade Showing Separation Line Penetration Height as Proposed by Sharma and Butler[17]

near-wake regions of a moderately loaded compressor rotor blade was reported by Lakshminarayana and Ravindranath[20]. Interaction of the wake with the annulus-wall boundary layer, secondary flow, tip leakage flow, and the trailing vortex system resulted in slower decay and larger width of the wake. The end-wall boundary layers and the secondary flows were found to have a significant influence on both the decay characteristics and the profile of the wake.

A detailed investigation of three-dimensional flow in a low speed axial compressor stage with an aspect ratio of two was reported by Cyrus[22]. The flow in a compressor stage was found to be considerably affected by a large area of low total pressure fluid arising near one end-wall of the rotor and stator rows. The origin of large high loss regions in each blade row, rotor and stator, was found by means of a diffusion factor.

The experimental investigation of the blade and the end-wall boundary layers in a subsonic compressor stator was reported by Gallus and Hoenen[23]. An increase of the separated region of the hub boundary layers and reverse flow at the blade suction side were observed with the decrease in flow coefficient.

In an axial compressor excessive diffusion was found to cause substantial regions of separated flow near the junctions of the blade suction surface and the end-wall[24]. This leads to deterioration in compressor performance. Dong, Gallimore, and Hodson[24] observed that on the hub of the rotor, where the diffusion factor was 0.56, significant secondary flows existed. However, no suction surface-end-wall separation was found. But at both the ends of the stator, suction surface-end-wall corner separation was found to exist. Also, the sepa-

ration was more prevalent on the hub. Surface flow visualization studies revealed the existence of large radial movements of the surface flow within and outside these regions. It was reported that the introduction of clearance between the stator blade and the hub resulted in a significant reduction in the extent of the suction surface-hub separation with an attendant decrease in loss.

It is quite evident from the discussion presented so far that the passage vortex is a dominating feature in cascades and axial turbomachines. Also it is the existence of the horseshoe vortex which leads to the formation of a passage vortex. Therefore, it would be of interest to first understand the effect of the horseshoe vortex alone on secondary flow generation in the end-wall corners. It appears that the above mentioned fact led many researchers, in recent years, to study the structure of the horseshoe vortex itself. It is often easy to study simple fluid flows to explain and predict the behavior of more complex flows.

Many investigators (for example, references 29, 30, 32) studied the cylinder end-wall flows to examine the horseshoe vortex structure. Belik[29] reported that the saddle point location depended on the state of the incoming boundary layer (laminar or turbulent), the boundary layer Reynolds number and the cylinder diameter. Han, Ma, and Rapp[30] found heat transfer in the vicinity of the leading edge near the end-wall plane higher for a thick inlet boundary layer than for a thin boundary layer.

Ishii and Honami[33] generated the horseshoe vortex effect by impinging a confined jet on the plane wall placed normal to the jet flow main direction. It was reported, that four vortices existed in the detached region which were generated by different processes. The

detached region could be divided into two parts (region I and II). Region I included the horseshoe vortex and the corner vortex, whereas region II contained the detachment point and the separation and counter vortex. A new model of the flow field associated with the detached region was suggested.

More recently, Eckerle, and Langston[32] investigated the horseshoe vortex formation around a large diameter ($D/\delta = 10$) circular cylinder centered between the sidewalls of a wind tunnel. The main aim of their study was to obtain measurements in the vortex region, especially in the region of vortex formation (i.e., between the saddle point and the leading edge of the cylinder). Only one end-wall saddle point and a single horseshoe vortex were observed. However, Moore and Forlini[31] reported a multi-vortex system implying the existence of multiple saddle points. Eckerle and Langston also noted that the horseshoe vortex was fully formed between 5^0 and 25^0 planes and not on the streamwise plane of symmetry (i.e., on the stagnation streamline). Furthermore, the horseshoe vortex was observed to be confined to a region less than one boundary layer thickness from the end-wall. Also the scale of the separation process at the saddle point was found to be much smaller than the scale of incoming boundary layer thickness. It was also observed that the vortex core moved radially outward and slightly away from the end-wall as the vortex moved around the cylinder. It was concluded that a key implication of these measurements was that the saddle point region did not exhibit swirl.

In other studies the end-wall corner region was generated either by mounting a constant thickness body with semi-elliptic leading edge[36-41] or an airfoil section body[42-47] on a flat plate. Shabaka

[36] made extensive mean and turbulent flow measurements in a simplified wing-body junction. The wing had an elliptic nose with constant thickness in the downstream direction. It was found that the attenuation of the skew-induced secondary flow by the Reynolds stresses was very slow. Also, the skew-induced secondary flow dominated over the stress-induced secondary flow even at a distance from the wing leading edge equal to 50 times the boundary layer thickness at the wing leading edge location. The turbulence structure was observed to be far from equilibrium. A logarithmic region was found to exist in the mean velocity profiles in the first 10% to 20% of the shear layer thickness, except very close to the corner (~20% of the shear layer). It was also reported that the eddy viscosity attained a negative value in the corner region. The detailed measurements of the surface pressure and wall shear stress on both the surfaces in the corner region were also obtained. The wall shear stress measurements were made with the Preston tube; however, no information about the direction of the wall shear stress was obtained.

Oguz[37] and Kubendran[38] reported mean flow and turbulence measurements in a simplified wing-body junction formed by a constant thickness body having an elliptical (1.5:1) leading edge mounted normal to a flat plate. Kubendran also investigated the influence of the leading edge shape on various parameters. The strength of the secondary flow vortex in the corner region was found to increase as the leading edge of the wing was made more blunt.

The effect of the wing nose shape on the flow in a wing-body junction was also studied by Mehta[39]. The effects of three types of wing nose shapes (elliptic, super-elliptic and wedge-elliptic section)

on the size, position, and strength of the horseshoe vortex were examined. The size and strength of the horseshoe vortex was found to increase with nose bluntness. This study revealed that the circulation in the horseshoe vortex decreased by approximately 40% as the nose shape changed from super-elliptic to a wedge-elliptic. Hawthorne[26] also demonstrated the effect of wing leading edge shape on the flow in the end-wall corner. He performed a simple experiment where the scouring of sand about a strut on the floor of water channel was taken as the strength of the vortex. Two leading edge shapes (bicuspid and elliptic) were examined. He found that the sand about the strut with the bicuspid leading edge was less influenced than that about an elliptic leading edge.

Chu, Rios-Chiquete, Sarohia, and Bernstein[40] developed a new probe, based on the same principle as the five-hole conrad tube yaw meter, to measure the mean velocity vector. This probe was used to measure the magnitude and direction of the mean velocity in a wing-body junction. The wing-body junction was formed by mounting a wing of constant thickness and semi-cylindrical leading edge on a flat plate. The measurements were obtained at two axial stations; namely, upstream of the wing leading edge and in the separation region. Yaw angles greater than 90^0 were observed very close to the wall indicating flow reversal ahead of the wing.

The strut-wall intersection losses were investigated by Barber [43]. The strut-wall junction was formed by mounting a symmetric airfoil section (65 series) normal to a flat plate. The losses were obtained by examining the wake region of the strut-wall junction. The effect of the strut thickness and incoming boundary layer thickness on the

strut-wall junction was also studied. It was found that the end-wall intersection losses were significantly lower for a thicker incoming boundary layer as compared to a thinner incoming boundary layer. It was also observed that the flow distortions extended up to one chord downstream of the intersection.

The spatial extent of the horseshoe vortex legs from the wing-plate junction at an incidence to the main flow was studied by Rood [44]. It was observed that the larger of the two vortex legs produced by the wing at incidence dominated the flow downstream of the junction. He also noted that the amount of skew in the downstream region of the junction depended on the wing geometry and the incoming boundary layer thickness. It was concluded that the two-point velocity correlation measurements provided better evaluation of the spatial extents of the horseshoe vortex legs on either side of the wing than the mean velocity measurements alone.

Kubendran and Harvey[45] showed the reduction in juncture drag with the use of leading-edge fillets. However, they noted a need for optimizing the fillet size to achieve overall improvement in the flow field.

The turbulent flow measurements in wing-body junction using laser velocimetry were reported by Scheiman and Kubendran[46]. The wing-body junction was formed by mounting a wing, having curved surface (circular arc) on one side and a flat surface on the other side, normal to the flat plate. This construction of the wing was used to study the corner flow with and without the streamwise pressure gradient. The effect of sharp leading edge and corner fillets on the junction flow field were also examined. In the case of juncture flow with a

sharp leading edge, no evidence of the presence of a horseshoe vortex was observed. It was noted, that the use of juncture fillets improved the flow characteristics near the wing trailing edge by removing regions of low momentum fluid. Recently, detailed measurements of mean and turbulent quantities using an inclined single sensor hot-wire probe in the blade end-wall corner region were obtained by Hazarika [47]. The blade end-wall corner region was constructed by mounting a blade (NACA 65-015 airfoil section) normal to a flat plate. Flow visualization using an ink-dot matrix method and oil film technique was also carried out. Based on total pressure, static pressure, mean velocity components, and the results of flow visualization, a horseshoe vortex and the corner eddy were identified upstream of the blade maximum thickness location[77]. Due to the action of inhomogeneous and anisotropic turbulence in the downstream direction the existence of a pair of contra rotating vortices were also reported. It was noted that the streamwise vorticity had a small influence on the static pressure field, whereas its effect was more pronounced on the total pressure, mean velocity, and the Bernoulli's surfaces.

More recently, Bhargava, Raj, and Boldman[78] reported detailed measurements of the mean surface pressure and the wall shear stress vector on both the surfaces in the blade end-wall corner region. The measurements were obtained on the same model used by Hazarika[47]. In the corner region, the magnitude of the wall shear stress was found to increase significantly compared to the value far upstream of the blade leading edge. The surface static pressure was observed to be significantly influenced on the end-wall, whereas very small changes were observed on the blade surface.

2.3 Wall Shear Stress

An important parameter in the analysis of near wall mean and turbulent flow properties is the wall shear stress. Besides providing the information about the friction drag force, it is also a useful parameter commonly used in the near wall similarity models. In the past, several techniques have been developed for the measurement of wall shear stress. Brown and Joubert[79] described various wall shear stress measurement methods while studying the effect of secondary forces on the floating element balance. A detailed review on the existing wall shear stress measurement techniques with their limitations and advantages among each other was presented by Winter[80]. More recently, Hanratty and Campbell[81], while reviewing various wall shear stress measurement techniques, have discussed in detail the mass transfer analogy method. In pursuit of measuring the wall shear stress with accuracy and without disturbing the flow a nonintrusive laser interferometry technique has also been reported in the literature[82-84]. Based on the available literature and following the work of Winter[80] a classification of various existing wall shear stress measurement techniques is shown in Fig. 2.4. A brief description of the different wall shear stress measurement methods is presented here. However, a very elaborate discussion on the Preston tube method, which was used in the present study, is included in this section.

2.3.1 Momentum Balance Technique

The momentum balance technique can be used for both developing and fully-developed flows. In a fully-developed flow through a

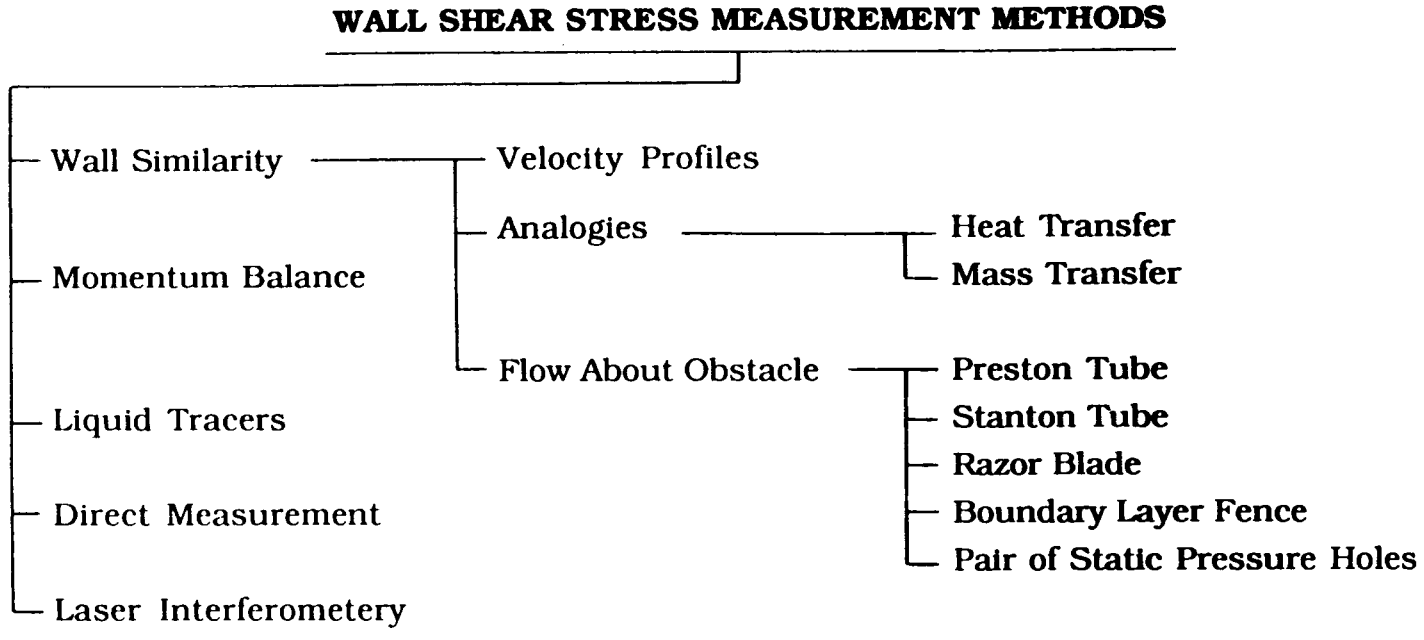

Fig. 2.4 Classification of Wall Shear Stress Measurement Techniques

duct a momentum balance provides an expression for the calculation of wall shear stress;

$$\tau_w = k_1 \, (dp/dx)_f \qquad (2.22)$$

where τ_w is the average value of the wall shear stress around the perimeter of the duct, k_1 is the ratio of duct cross-sectional area to the wetted perimeter, and $(dp/dx)_f$ represents frictional pressure drop. Ferriss[85] found that the superposition of additional pressure gradient due to contraction or diffusion in a duct passage caused large errors in the calculated value of the wall shear stress (reported in ref. 79). Secondly, whereas no circumferential variation in τ_w was observed for the fully-developed region, significant circumferential changes were noticed in the developing region[86]. It is evident from the available literature[87-88] that this technique has been widely used for calibrating various wall shear stress measuring devices such as the Preston tube, heated element probe, etc. In a developing two-dimensional flow such as the boundary layer under variable external pressure, a momentum integral equation (reference 89) may be used for evaluating the value of wall shear stress. This equation can be expressed as

$$U_\infty^2 \, d\theta/dx + (2\theta + \delta^*) \, U_\infty \, dU_\infty/dx = \tau_w/\rho \qquad (2.23)$$

which, in dimensionless form, can be written as

$$d\theta/dx + (2 + H) \, \theta/U_\infty \, (dU_\infty/dx) = C_f/2 \qquad (2.24)$$

The value of free stream velocity gradient in the streamwise direction is related to the streamwise external pressure gradient as

$$- U_\infty \, dU_\infty/dx = 1/\rho(dp/dx) \qquad (2.25)$$

and can be accurately evaluated. It is to be noted that the momentum integral Eqn. 2.23 or 2.24 is valid only for two-dimensional flows, and a suitable momentum integral equation is required in a three-dimensional flow. To evaluate the wall shear stress using Eqn. 2.24 it is necessary to calculate the derivative of momentum thickness. This can be done by measuring boundary layer mean velocity profile at a number of streamwise stations. However, a careful velocity profile measurement does not necessarily give rise to an accurate evaluation of the wall shear stress, mainly because the momentum thickness changes slowly with the streamwise distance x.

2.3.2 Direct Force Measurement Technique

In this technique a floating element experiences a force caused by the shear which causes the element to deflect. This deflection is directly measured and, through calibration, provides the magnitude of the wall shear stress. This method of measurement does not employ any assumptions regarding the similarity in the flow near the wall and is, therefore, suitable in any flow situation. Kempf[90] was probably the first to use direct force measurement technique for the study of a flat plate boundary layer in water. Smith and Walker[91] used this method for an incompressible two-dimensional boundary layer with zero pressure gradient in air. Most of the earlier studies were limited to the zero pressure gradient case where the secondary effects due to pressure gradient, misalignment of the floating element, etc., were neglected. Brown and Joubert[79] studied the effect of secondary forces caused by the pressure gradient. The maximum secondary force was found to be approximately 15% of the wall shear force. The direct

force measurement technique has been shown to be useful in three-dimensional flows where both the magnitude and direction of the wall shear stress are important. Tennant, Pierce, and McAllister[92] developed an omnidirectional floating element balance to measure the wall shear stress in three-dimensional flows. The basic difference between this device and all of the other two-dimensional floating element devices was its ability to simultaneously measure the magnitude and direction of the wall shear stress. McAllister, Pierce, and Tennant[93] pointed out that, because indirect devices are calibrated only in two-dimensional flows there is some doubt regarding their obtaining results in three-dimensional flows. The measurements obtained by McAllister, Pierce, and Tennant also showed that their technique was suitable for flows with varying wall shear stress. In addition, the results indicated good agreement for the wall shear stress direction and the limiting streamlines direction obtained by an oil film technique[93]. The direct force measurement technique, however, is deficient in the following respects: (i) the size of the sensing element must be large to experience sufficient force for deflection. For this reason, the measured wall shear stress is the average value over the sensing element area and, therefore, the floating element is difficult to use in flow situations where the wall shear stress varies rapidly from point to point in a small region (for example, corner region). The diameter of the sensing element in the work of McAllister, Pierce, and Tennant was 2.86 cm, whereas Brown and Joubert[79] used a smaller size (1.9 cm) sensing element. (ii) Traversing of the device is difficult because of device's stability requirements. Therefore, the test model must move while the device stays stationary and this is very cumbersome when

the model is large. (iii) The gap around the sensing element and misalignment of the sensing element are another problems associated with such a device which introduce error in the wall shear stress measurement. Recently Acharya, Bornstein, Escudier, and Vokurka[94] studied the effect of varying gap size and sensing element thickness. From this investigation it was concluded that the main source of uncertainty in determining the wall shear stress was the buoyancy force resulting from the non-uniformity of pressure within the gap surrounding the sensing element. Tennant, Pierce, and McAllister[92] reported good agreement between the wall shear stress measurements obtained with the floating element balance and the Preston tube in two-dimensional turbulent flows. A detailed study on the comparison of the wall shear stress measurements, in three-dimensional turbulent flows, with different techniques was reported by Pierce and Krommenhoek[95]. Different techniques compared were the Preston tube, the heated element, and the floating element balance. The Preston tube results were found to be within 5% of the values obtained with the floating element balance.

2.3.3 Wall Similarity Technique

The techniques developed for measuring the wall shear stress using the velocity profile similarity near a wall are also termed as indirect methods in the literature. Various devices (e.g., the Preston tube, heated element, etc.,) for the measurement of wall shear stress have been developed in the past using the principle of near wall flow similarity. This principle is based on the observation that in a two-dimensional turbulent flow near a wall, the motion of the fluid is influenced

by the wall variables only. These wall variables are the wall shear stress (τ_w), kinematic viscosity (ν), density of the fluid (ρ), and the distance from the wall (z). From the dimensional analysis it can be shown that [79],

$$U/u^* = f\,[zu^*/\nu] \tag{2.26}$$

where U is the local mean velocity at a distance z from the wall and $u^* = (\tau_w/\rho)^{0.5}$ is called the frictional velocity. Prandtl termed this near wall behavior the "Law of the Wall". It is quite evident from Eqn. 2.26 that if such a functional relationship is known, then local wall shear stress can be calculated from the measurement of the other variables (for example, mean streamwise velocity, U). Studies have been made to establish the range of validity for the law of the wall. These studies indicated that in a two-dimensional boundary layer with adverse pressure gradient the following equations may be applicable[79]

Region (1), the viscous sublayer, $U/u^* = zu^*/\nu$ (2.27)

Region (2), the logarithmic region, $U/u^* = 1/K\ \ln(zu^*/\nu) + B$ (2.28)

Region (3), Half-power region, $U/u^* = k_2(\Delta_p z/u^{*2})^{0.5}$

$$+f_1[\Delta_p \nu/u^{*3}] \tag{2.29}$$

where K, k_2 and B are universal constants and $\Delta_p = 1/\rho(dp/dx)$.

The above division of a turbulent boundary layer is based on the criterion that the deviation in velocity profile from the law of the wall is caused due to the adverse pressure gradient. It is obvious that the law of the wall is valid up to the edge of Region (2), and in Region (3) non-wall effects simulated through variable Δ_p dominate. The range of Re-

gion (2) was described by $30\nu/u^* < z < 1.41\ u^{*2}/\Delta p$ and $\Delta p\nu/u^{*3} < 0.05$[79]. The methods and devices based on the above discussed principle and used in measuring the wall shear stress are briefly discussed below.

2.3.3.1 Velocity Profile Method

Clauser[96] proposed a method in which the mean velocity profile measurement is used to evaluate the magnitude of the wall shear stress. This method uses the logarithmic law (Eqn. 2.28) and can be rewritten as,

$$U/U_\infty = (1/K)(C_f/2)^{0.5} \ln(zU_\infty/\nu) + (C_f/2)^{0.5}[(1/K)\ln(C_f/2)^{0.5}+B] \quad (2.30)$$

In this method, a chart (called Clauser's chart) is constructed by plotting U/U_∞ against $\log_{10}(zU_\infty/\nu)$ for different values of C_f using Eqn. 2.30. Then, the measured mean velocity profile is plotted on this chart and compared with the constant C_f curves. The plotted points closest to a constant C_f line gives an estimate of C_f. A modification to Clauser's method was proposed by Bradshaw[97]. This method avoids plotting the velocity profile on U/U_∞, $\log_{10}(zU_\infty/\nu)$ axes. Instead, in this simplified method of Bradshaw, one suitable reference point (the value of zu^*/ν) is chosen on the inner law curve and plotted on the axes U/U_∞, z (which are the usual coordinates on which mean velocity profile is normally plotted) for different values of U_∞/u^*. The resulting curve on the U/U_∞, z axes has a well defined intersection with the measured velocity profile in the region of $U/U_\infty \sim 0.6$ for the more usual value of U_∞/u^*. The value of U/U_∞ corresponding to the point of intersection

and U/u^* selected at the reference point then gives the value of C_f using,

$$C_f = 2(u^*/U_\infty)^2 = 2[(U/U_\infty)/(U/u^*)_{ref}]^2$$

It was suggested that with little practice only two or three reference points need to be plotted, in the manner described above, to find the intersection and C_f value.

2.3.3.2 Heat Transfer Similarity Method

In this method wall shear stress is calculated from the measurement of heat transfer from a heated element provided the thickness of the thermal boundary layer over the heated element remains within the range of the distance of validity of the law of the wall. In this case, the heat transfer correlates only to the wall variables. Based on dimensional analysis it can be shown that [79],

$$Q/lk\Delta\theta = Nu = f[\,\mu c_p/k,\ lu^*/\nu] \qquad (2.31)$$

where Q is the rate of heat convected from the heated element, k, μ and c_p are fluid properties, l is the characteristic length of the heated element and $\Delta\theta$ is the temperature difference between the heated element and the free stream. The temperature difference ($\Delta\theta$) is assumed to be small so that the natural convection is absent. For a given fluid, the Prandtl number Pr ($= \mu c_p/k$) is constant and, therefore, the measurement of Q and $\Delta\theta$ is required to calculate the wall shear stress (τ_w) provided the functional relation, Eqn. 2.31 is known. Fage and Falkner[98] appear to be the first to use the heat transfer technique in a laminar boundary layer flow. Ludwieg[99], Liepmann and Skinner[100] and Bellhouse and Schultz[101] have used heated ele-

ment technique in turbulent flows. It was shown in the previously mentioned literature that the heat loss from the sensing element is proportional to the cube root of the wall shear stress[100]. The thin-film probe developed by Bellhouse and Schultz[101] was also useful in calculating the wall shear stress fluctuations. The condition to calculate the fluctuating value of the wall shear stress is that the thermal boundary layer should not only lie within the law of the wall but should remain entirely within the viscous sublayer. A similar restriction applies if the same calibration is to be used for both the laminar and the turbulent flows. The range of application of the heated element probe is expressed by the inequality[50]

$$Pr/C_f > Nu >> 1$$

The above mentioned inequality, expressed in terms of Reynolds number based on effective sensor length, can be rewritten as[50]

$$6.6/(Pr)^{0.5} < u^* l_e/\nu < 64\ Pr$$

If the working medium is air, the above mentioned inequality reduces to

$$7.8 < u^* l_e/\nu < 46$$

where l_e is the effective sensor length. In the above relation, the lower limit is the result of the boundary layer approximation. The upper limit is due to the fact that the thermal boundary layer of the film lies within the viscous sublayer of the turbulent boundary layer so that the linear velocity profile could be accurately assumed.

McCroskey and Durbin[102] have used a dual sensor probe to calculate both the magnitude and direction of the wall shear stress.

This is essential in the measurement in a three-dimensional turbulent flow. The dual sensor flush mounted probe was used in a three-dimensional turbulent flow by Higuchi and Peake[103]. It was observed that due to the small size of the sensor there will be a minimum thermal penetration into the skewed near wall flow and thus such a device can accurately predict the wall shear stress direction. The main advantage of such a method is that the miniature probes can be built and flush mounted and the point measurement of the wall shear stress vector can be accurately made without disturbing the flow field.

Gessner and Jones[104] reported the directional characteristics of the local wall shear stress in a fully developed turbulent flow through non-circular ducts. The measurements were obtained in square and rectangular channels. For both the channels the skewness of the local wall shear stress vector was found to increase in the close vicinity of the corner. The reason suggested was the presence of large secondary flows in the corner region. The results also showed that skewness of the local wall shear stress vector was greater along the longer wall than along the shorter wall of the rectangular channel at points equidistant from the corner. This result was in agreement with the measured secondary flow profiles. These secondary flow profiles suggested that most of the flow away from the corner was directed outward along the longer wall.

2.3.3.3 Similar Flows About Obstacles

The method of wall shear stress measurement in this case is based on the principle that the velocity field about any small obstacle immersed entirely in the law of the wall region will be influenced by

the wall variables. It is important to note that the obstruction must be small enough to have a negligible effect upon the growth of the boundary layer in which it is placed. Therefore, any pressure difference (for example, in the case of the Preston tube, this is the pressure difference between the Preston tube pressure and the local wall pressure) ΔP depends on the wall variables which can be written in a functional form as,

$$\Delta P = f [\tau_w, \rho, \nu, l] \tag{2.32}$$

where l is the characteristic length parameter of the obstacle (e.g., diameter of the Preston tube). Using dimensional analysis, Eqn. 2.32 becomes[105]

$$\Delta P l^2/\rho\nu^2 = f_1[\tau_w l^2/\rho\nu^2] \tag{2.33}$$

The form of the functional relationship can be obtained by calibrating the device in a known flow condition such as fully developed flow in a pipe. Several devices have been developed based on the above discussed principle. Commonly used devices are the boundary layer fence, the Stanton tube, the razor blade technique and the Preston tube. The Preston tube, which is widely used, was proposed by Preston[105] and is discussed in detail here. The Preston tube has the advantage that geometrically similar tubes can be produced and thus a single calibration can be used for different diameter probes. Patel[87] produced widely used calibrations of the Preston tube covering a wide range of flow conditions and tube sizes. Patel also noted that the original calibration suggested by Preston[105] was in error. Many other investigators have proposed calibration equations for the Preston tube which are tabulated in Table 2.2. The calibration equations in Table 2.2

TABLE 2.2 Preston Tube Calibration Equations

Investigator (Year)	Calibration Formulas	Range of Validity of Independent Variable	Reference
Preston (1954)	$y^* = 0.1505 + 0.5\ x^*$ $y^* = -\ 1.396 + 0.875\ x^*$	$2 \le x^* < 4.10$ $4.10 \le x^* \le 6.50$	105
Smith and Walker (1958)	$y^\bullet = -\ 1.366 + 0.877\ x^\bullet$	$5.0 \le x^\bullet \le 7.50$	91
N.P.L. staff (1958)	$y^\bullet = -\ 1.353 + 0.875\ x^\bullet$	$5.25 \le x^\bullet \le 7.20$	107
Head and Rechenberg (1962)	$y^\bullet = -\ 1.467 + 0.889\ x^*$	$5.14 \le x^\bullet \le 6.94$	86
Ferris (1965)	$y^* = -\ 1.422 + 0.881\ x^*$	$4.79 \le x^* \le 6.38$	85
Patel (1965)	$y^\bullet = 0.037 + 0.5\ x^*$ $y^* = 0.8287 - 0.1381\ x^* + 0.1437\ x^{*2} - 0.006\ x^{*3}$ $x^* = y^* + 2 \log_{10} (1.95\ y^* + 4.10)$	$x^\bullet < 2.90$ $2.90 \le x^* < 5.60$ $5.60 \le x^* < 7.60$	87
Bradshaw and Unsworth (1973)	$\Delta P/\tau_w = 96 + 60 \log_{10}(d^+/50) + 23.7\ [\log_{10}(d^+/50)]^2$	$50 < d^+ < 1000$	108
Bertelrud (1976)	$\Delta P/\tau_w = 87.77 \log_{10} d^+ - 51.93$ $\Delta P/\tau_w = 38.85\ x^* - 88.53$	$50 < d^+ < 1000$ $4.80 < x^* < 7.72$	110

Definition of Variables:

$x^* = \log_{10} (\Delta P d^2/4\rho\nu^2)$, $d^+ = du^*/\nu$, $\Delta P = P_p - P_s$, P_s - Surface Static Pressure

$y^\bullet = \log_{10} (\tau_w d^2/4\rho\nu^2)$, $u^* = (\tau_w/\rho)^{0.5}$, P_p - Preston Tube Pressure, d - Preston Tube Dia.

TABLE 2.3 Conditions Under which the Calibration Equations Presented in Table 2.2 were Obtained

Investigators	Flow Type	Standard used for Calibration	Pressure gradient dp/dx	Tube Size (mm)
Preston	Pipe	Pipe Pressure Drop	>0, <0	0.740 to 3.084
Smith and Walker	Flat Plate	Floating Element Device	0	0.762 to 3.091
Staff of N.P.L.	Flat Plate	Wake Traverse and Stanton Tube	0	1.194 to 3.175
Head and Rechenberg	Pipe	Sublayer Fence	0, >0, <0	0.597 to 9.520
Ferris	Channel	Sublayer Fence	0, >0	0.914 to 2.870
Patel	Pipe	Pipe Pressure Drop	0, <0, >0	0.597 to 12.649
Bradshaw and Unsworth	Not Available	Floating Element Balance	0	Not Available
Bertelrud	Pipe	Pipe Pressure Drop	0	0.6 to 19

were obtained under different flow conditions and different standards. These conditions are described in Table 2.3. The information in Tables 2.2 and 2.3 was also presented by McAllister[106]. The calibration equations (see table 2.2) provided by Patel were obtained for a two-dimensional flow with pressure gradient. Patel also suggested the limiting values of pressure gradient, both favorable and adverse, within which his calibration equations might be valid. His proposed limits were based on the value of non-dimensional pressure gradient parameter defined as

$$\Delta p^+ = \Delta p \nu / u^{*3}$$

The limits on pressure gradients are:

(a) for adverse pressure gradients

with maximum error 3%; $0 < \Delta p^+ < 0.01$, $du^*/\nu < 200$

with maximum error 6%; $0 < \Delta p^+ < 0.015$, $du^*/\nu < 250$

(b) for favorable Pressure gradients

with maximum error 3%; $0 > \Delta p^+ > -0.005$, $du^*/\nu < 200$

with maximum error 6%; $0 > \Delta p^+ > -0.007$, $du^*/\nu < 200$

Patel also pointed out that these limits are a rough guide only.

Brown and Joubert[79] observed that the Preston tube gave satisfactory results for much higher pressure gradient values than those suggested by Patel. The pressure gradient limit given by Brown and Joubert is $\Delta p^+ = 0.023$, whereas Patel[87] suggested a limit of $\Delta p^+ < 0.015$ with 6 percent accuracy. Brown and Joubert also noted that the

Preston tube can be used with higher values of Δp^+ and without loss of accuracy provided du^*/ν (Reynolds number based on the Preston tube outer diameter) is reduced (in their work du^*/ν ranged from 30 to 50). The main drawback associated with the calibration equations of Patel is that they do not match at the end of each region. Also the third equation is of transcendental nature and requires an iterative method to solve it. To overcome this problem Head and Ram[109] presented tabulated results for the calibration equations of Patel in terms of two new variables which in functional form are related as

$$\Delta P/\tau_w = F\,[\Delta P d^2/\rho\nu^2]$$

This expression was also plotted on the U_p/U_∞, $\log_{10}(dU_\infty/\nu)$ axes using C_f as the parameter (very much similar to the Clauser's chart) where $U_p/U_\infty = (\Delta P/0.5\rho U_\infty^2)^{0.5}$.

Bertelrud[110] suggested a single calibration equation (see Table 2.2) for the Preston tube in terms of two variables $\Delta P/\tau_w$ and du^*/ν. It was noted that the variables used in Patel's equations are the logarithms of the non-dimensional pressure and skin friction and, therefore, are less suitable for evaluating the measurement accuracy. It was shown that suggested new parameters gave better accuracy compared to the usual variables x^* and y^*.

It is important to note that all the techniques developed and mentioned under the category of flow about the obstacles (see Fig. 2.4) require the knowledge of local surface static pressure to calculate the magnitude of the wall shear stress. Conventionally, the surface pressure is measured by providing a tap on the surface. At many locations of interest the provision of surface static tap may be impracticable, for

example, near the trailing edge of a thin airfoil model. Moreover, a large number of surface taps on a surface in a three-dimensional flow, where the wall shear stress changes from point to point, need to be provided (for example, blade end-wall corner region). As a result, new designs of the Preston tube have been proposed either to eliminate the need of the measurement of surface static pressure or measure the surface pressure with a modified Preston tube[111,112]. A modified Preston tube proposed by Gupta[111] consisted of two different diameter tubes attached together which rest on the surface side-by-side. The tube with smaller diameter was chamfered side way at 45^0 to increase the measured pressure difference. In another design two chamfered tubes of smaller diameters were placed symmetrically about the main tube. This second design, it was suggested, could be useful in three-dimensional flows. The modified designs of the Preston tube proposed by Gupta are shown in Fig. 2.5. The design shown in Fig. 2.5(c) was suggested for three-dimensional flows in which pressure difference between the outer tubes is first used to align the probe in the local flow direction and then the pressure difference between central and outer tubes gives the value of the wall shear stress. The pressure difference measured for devices (a) and (b) (see Figs. 2.5(a) and 2.5(b)) was found to be a constant fraction of the Preston tube pressure. These values are also given in Fig. 2.5. It is important to mention that this new device was calibrated against the Preston tube and, therefore, depends on the calibration of the Preston tube for calculating the value of wall shear stress. Moreover, no results were presented for device (c). It is also felt that it would be interesting to calibrate these devices against direct force measuring device.

$\Delta P_m/\Delta P_n = 0.714$

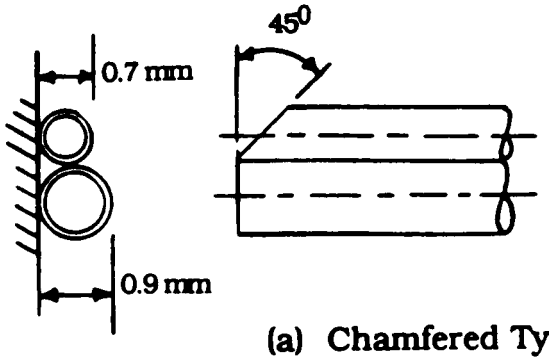

(a) Chamfered Type

$\Delta P_m/\Delta P_n = 0.798$

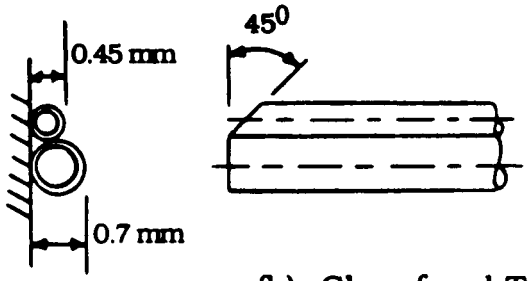

(b) Chamfered Type

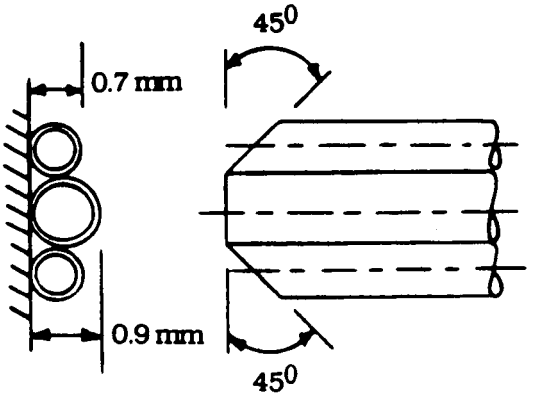

(c) Conrad Type

Fig. 2.5 Modified Designs of Preston Tube by Gupta[111]

Bertelrud[112] in an effort to avoid the use of wall taps to measure the surface pressure suggested a new design for the Preston tube. This probe consisted of a 1 mm outer diameter tube with a closed front end which was fixed to the wall inside a 3 mm outer diameter tube. A 0.5 mm hole was drilled at a distance of 5d (where d is the diameter of the outer tube) from the tip of the probe. Since the static pressure measured with this probe was not at the probe tip, a correction to the pressure difference obtained with this probe was suggested. It was also noted that the difference in measured static pressure and true pressure was a function of L/d where L is the distance from the probe tip to the location of static tap.

The available literature also shows that the Preston tube can be used in three-dimensional flows provided it is aligned in the flow direction[113,114]. Mojola and Young[115] and Shabaka[36] have made use of the Preston tube in three-dimensional flows (corner flows). They have not mentioned about the alignment of the tube in the flow direction. Prahlad[114] observed that consistent values of the local wall shear stresses were obtained provided the Preston tube was aligned in the local flow direction. Moreover, it was noted that an accurate alignment of the tube to the streamline direction was very cumbersome and, therefore, the Preston tube should also be calibrated for its yaw characteristics. The yaw calibration of three types of Preston tubes was presented by Prahlad. These three designs were the normal Preston tube, a single tube chamfered at 45^{0}, and two tubes chamfered at an equal angle of 45^{0} (termed the Conrad probe). For each design different size tubes were investigated. The yaw characteristics of the Preston tube were found to be represented by an equation

$$(P_p(\alpha) - P_s)^* = C_\alpha\ (P_p(\alpha_0) - P_s)^{*n_\alpha}$$

where $(P_p(\alpha_0) - P_s)^* = (P_p(\alpha_0) - P_s)\ d^2/4\rho v^2$, $P_p(\alpha_0)$ is the pressure obtained from the Preston tube when aligned in the flow direction, and P_s is the surface static pressure. $(P_p(\alpha) - P_s)^*$ is defined similarly, $P_p(\alpha)$ being the pressure recorded by the Preston tube when oriented at an angle α to the local flow direction. C_α and n_α are constants and can be calculated for a given Preston tube by calibration. The main advantage of the chamfered tube was reported to be its greater sensitivity to yaw angle near $\alpha = 0$ as compared to a normal Preston tube. It was also suggested that for accurate determination of the wall shear stress vector with the Preston tube both the pressure gradient components in the wall shear direction and normal to it should be small. The method suggested by Prahlad[114], although simple in principle, requires an iterative method for evaluating the wall shear stress magnitude and direction.

Bragg[116] reported measurements of the local wall shear stress for a turbulent flow in the corner region formed by two flat plates. The wall shear stress had an inflexion point in the close vicinity of the corner. At any streamwise location, the maximum wall shear stress value in the vicinity of the corner was comparatively smaller than the values measured far away from the corner. Similar trends in the variation of the wall shear stress were observed for zero as well as adverse pressure gradient cases. Bragg also derived a momentum integral equation for the corner flows and noted that some of the terms in the equation were difficult to measure within the acceptable accuracy. Shabaka[36] measured wall shear stress using the Preston tube in the corner region of the simplified wing body junction. His measurements showed

that, in the corner region, the value of wall shear stress on the body surface (wind tunnel wall) near the wing leading edge was substantially higher than the measured wall shear stress far upstream of the wing leading edge. At any axial station in the corner region C_f increased from its asymptotic value (C_f value far away from the corner line at any axial station) to a maximum value as the corner was approached. This trend was different than the one observed in the work of Bragg. In the work of Bragg, as discussed earlier, the wall shear stress decreased from the asymptotic value as the corner was approached. The probable reason for this difference in Bragg's and Shabaka's results is due to the fact that a horseshoe vortex existed in Shabaka's case. Shabaka also noted that the maximum value of C_f, at different axial stations, decreased on both the surfaces of the test model in the downstream direction along the corner. The location of the maximum value of C_f on both the surfaces moved away from the corner line in the downstream direction. The direction characteristic of the local wall shear stress was not considered either in Bragg's or Shabaka's work. These characteristics generally would be influenced by the secondary flows of the "first kind" and the "second kind".

In the case of rotating three-dimensional turbulent boundary layer flow, the use of the Preston tube was reported by Anand[117]. Patel's calibration equations were used to evaluate the magnitude of the wall shear stress. The Preston tube was aligned in the direction of the limiting streamline angles obtained from the flow visualization. The value of the wall shear stress was also calculated using Clauser's method and good comparison was reported.

2.4 Wall Pressure Fluctuations and Wall Pressure-Velocity Correlations

An extensive review on the wall pressure fluctuation measurements was presented by Willmarth[52]. The available literature also indicates that only a few attempts[49, 53-55] have been made to measure the correlation of wall pressure fluctuation with the velocity fluctuations in a turbulent boundary layer. Moreover, most of these earlier studies were limited to two-dimensional turbulent flows. However, a considerable amount of information was obtained on the structure of a turbulent boundary layer through these measurements.

The first measurement of the wall pressure fluctuation under a turbulent boundary layer was reported by Willmarth[118]. The measured ratio of the RMS value of wall pressure fluctuation (p'_w) to the free stream dynamic head (q_∞) was 0.0035 and was constant over a wide range of Mach and Reynolds numbers.

Later extensive studies on the wall pressure fluctuation measurements were reported by Willmarth and Wooldridge[119] and Bull [120]. Willmarth and Wooldridge[119] reported measurements of the wall pressure fluctuation on the surface under a thick two-dimensional turbulent boundary layer. The ratio of the root-mean-square wall pressure to the wall shear stress was measured to be 2.19. It was reported that the power spectra of the wall pressure scaled with the free stream velocity and the boundary layer displacement thickness. From the measurements of space-time correlations of the wall pressure fluctuation information was obtained about the convection and decay characteristics of the pressure producing eddies. The convection

speed varied from 0.56 to 0.83 times the free stream velocity. The lower convection speeds were obtained when pressure fluctuations at high frequencies were correlated. On the other hand, higher convection speeds were measured when the low frequency pressure fluctuations were correlated. It was concluded from these observations that the large and small scale pressure producing eddies decay after travelling a distance proportional to their scale.

Bull[120] investigated the wall pressure fluctuations in a two-dimensional turbulent boundary layer with zero pressure gradient. Space time correlation measurements were made in both the broad and narrow frequency bands. The objective was to gain information about the small scale components of the wall pressure fluctuation, which could not be obtained earlier, because the size of the pressure transducer in relation to boundary layer thickness in previous studies was large. In this study d_1/δ^* varied from 0.15 to 0.51 (where d_1 is the diameter of the pressure transducer and δ^* is the boundary layer displacement thickness). In the work of Willmarth and Wooldridge[119] the transducers used had a value of $d_1/\delta^* = 0.33$. Bull's[120] measurements showed that the ratio, p'_w/τ_w increased from 2.11 to 2.80 as the value of Re_θ varied from 6400 to 33,800. Bull also noted that the observed trend for p'_w/τ_w in his study was in contrast to the results obtained in fully developed flow through pipe as reported by Corcos [121] and Bakewell et al.[122]. The Corcos[121] and Bakewell, et al. [122] studies, however, showed a decreasing trend for p'_w/τ_w with increasing Reynolds number. The wall pressure fluctuation field was divided into two families of wave-numbers[120]. The high wave-number family was associated with the turbulent motion in a constant

stress layer. The other family was a low wave-number family associated with the large-scale eddy motion in a turbulent boundary layer. The broad band convection velocity results indicated that for small separation distances there was a strong contribution from the constant stress layer and also possibly from the transition region. As the separation distance increased to a few displacement thicknesses the broad band convection velocity was found to increase to its asymptotic value of 0.825 U_∞ which is a characteristic of large scale structure. This observation suggested that the contribution to the wall pressure correlation from the fine scale motion in the near wall region decreased because of the rapid dissipation and dispersion of pressure sources due to the presence of high shear.

The spatial resolution of a pressure field associated with a local turbulent flow is limited by the finite size of the pressure transducer sensing element[123]. Consequently, a lack of resolution in space leads to an apparent inability to resolve in time. Corcos[123] presented an analytical method using spectral theory to evaluate the response function of the transducer. In this approach it was necessary to know in advance cross-spectral density function $\Gamma(\omega,\zeta)$, where ω is the frequency and ζ is the position vector. Based on experimental evidence, he represented Γ as

if $\zeta = (\xi,\eta)$

$$\Gamma[\omega,\xi,0] = \phi[\omega]\, A[\omega\xi/U_c] \exp(-i\omega\xi/U_c)$$

$$\Gamma[\omega,0,\eta] = \phi[\omega]\, B[\omega\eta/U_c]$$

Using the above expressions, a relation for the attenuation (ratio of measured to actual frequency-spectral density) at a given frequency caused by the finite size of the transducer was obtained. The theory developed for the attenuation of the mean square value of the wall pressure fluctuation was applied to the measurements of Willmarth and Wooldridge[119], and it was shown that the transducer used in the study of Willmarth and Wooldridge could not resolve a large fraction of the total pressure signal.

The correction to the power spectra measured by a finite size transducer was also suggested by Willmarth and Roos[124]. A similarity model similar to that suggested by Corcos[123] was used to evaluate the correction to the measured parameters. It was suggested that the similarity model for the cross-spectral density function was not valid for spatial separations less than $0.7\delta^*$ and dimensionless frequencies greater than 3.0. The RMS value of the wall pressure fluctuation was found to be considerably attenuated due to the finite size of the pressure transducer. For a vanishingly small size of the pressure transducer, p'_w/τ_w was calculated to be 2.66. For $R/\delta^* = 0.221$ the RMS value of the wall pressure fluctuation measured was 2.20 (R is the radius of the pressure transducer).

The influence of transverse curvature under a turbulent boundary layer on the wall pressure fluctuation and the structure of turbulence was studied by Willmarth and Yang[125]. Measurements of the longitudinal space-time correlation of the wall pressure fluctuation showed that the streamwise convection speed was similar to that in the plane boundary layer. The explanation for the unchanged convection velocity was that the pressure producing eddies in the boundary layer with

transverse curvature might be smaller. This implied that the eddies were near to the wall where the mean velocity was lower. Two reasons were suggested for the reduction in size of the turbulent eddies due to transverse curvature. The first reason was the increase in fullness of the velocity profile. The second reason was that the transverse scale decreased more for larger eddies than for smaller eddies because of transverse curvature. It was also concluded that the effect of transverse curvature was negligible on the RMS value of the wall pressure fluctuation.

The effect of roughness on the wall pressure fluctuation was investigated by Blake[126]. The measurements were made on the walls with different roughnesses using a pinhole microphone having a better high frequency resolution. The space-time decay rate was noted to be higher. The lower convection velocities were measured over the rough walls. The reason for the lower convection velocities was due to the retardation of the mean boundary layer motion by the surface roughness. It was also reported that, at moderately high frequencies where the pressure sources were nearer ($z < 0.18$) and the convection velocity did not reach its asymptotic value, the spectra for all the walls behaved as ω^{-1}. This also required that the pressure spectrum level and wave-numbers would be determined by the wall shear stress and the source position, respectively. The value of p'_w/τ_w was noted to be influenced by the type of roughness. The RMS value of the wall pressure fluctuation for densely packed small scale and densely packed large scale roughness elements was smaller than for sparsely packed small scale roughness elements or smooth walls. On the other hand, for sparsely packed small scale roughness elements the RMS value of the

wall pressure fluctuation was larger than for the smooth walls. It was also noted that the roughness separation influenced the large scale turbulence structure, whereas the roughness height influenced the medium and very small scale turbulence structure.

Schewe[127] studied the structure of turbulence and showed that the value of $d_1u^*/\nu = 19$ (dimensionless diameter of the transducer) was sufficient to resolve the essential structure of the turbulent wall pressure fluctuations. The power spectra measured with the smallest transducer showed the power law as $\sim \omega^{-7/3}$. This law is similar to the one predicted for locally isotropic turbulence. The pressure structures with high amplitude and the shape of short pulses were recognized using signal averaging in the time domain. These structures were found to have a characteristic frequency (ω^+) and longitudinal wave length (λ^+) of 0.52 and 145, respectively. The convection velocity associated with such structures had a mean value of 0.53 U_∞. The RMS value of the wall pressure fluctuation (non-dimensionalized by the free stream dynamic head) increased considerably from 0.5% to 1% as the d_1^+ reduced to the smallest transducer used. Also the difference in the RMS value measured with the smallest transducer and the value corresponding to $d_1^+ = 0$ was only 4%. Based on this result it was concluded that the smallest transducer used in his study could resolve the pressure structure essential to turbulence.

The wall pressure fluctuation measurements downstream of two rigid ribbons mounted in tandem and immersed in a turbulent boundary layer were reported by Beeler[128]. These ribbons are known as large eddy breakup devices (LEBUs). The intensity of wall pressure measured at a location (where the C_f value decreased by approximately

25%) downstream of the LEBUs showed a decrease of about 12.5% compared to the case when LEBUs were absent. This decrease in the wall pressure intensity also implies a reduction in noise generated due to the wall pressure fluctuations associated with a turbulent boundary layer.

The wall pressure field for flow separation and re-attachment processes in a turbulent boundary layer was experimentally investigated by Farabee and Casarella[129]. Two types of flow were investigated: flow over a forward-facing step and flow over a backward-facing step. The experimental results showed that the separation-re-attachment process produced large amplitude, low frequency wall pressure fluctuations. The wall pressure fluctuations were found to be largest at re-attachment where the highly turbulent free-shear flow impinges on the surface. In particular, RMS values of the wall pressure fluctuation at re-attachment for the forward-facing step were 10 times larger than the pressures measured for an equilibrium flow. However, for the backward-facing step, with the same step height as in case of forward-facing step, RMS values of the wall pressure fluctuation were only 5 times larger than the pressure measured for an equilibrium flow. This large increase in RMS values of the wall pressure fluctuation was attributed to the increase in the low frequency content of the pressure spectrum.

Recently, measurements of RMS values of the wall pressure fluctuation and its frequency spectra in a wing-body junction were reported by Hasan, Casarella and Rood[130]. The wing-body junction was formed by mounting a wing, of semi-elliptic nose with constant thickness mid-body and a NACA 0020 tail profile, normal to the wind-tun-

nel side wall. In upstream region, between the saddle point and the wing leading edge and on the stagnation streamline, a significant increase in the wall pressure intensity (five times its far upstream value) was obtained. This observed increase was partially attributed to the impingement of the re-circulating flow within the corner region. The demarcation line of the horseshoe vortex around the wing was observed to coincide with the peak values of the intensity of wall pressure fluctuation at different streamwise locations in the corner region. Also, at any streamwise location in the corner region on the body surface, the frequency spectra of the wall pressure fluctuation showed an increase in spectral content towards the wing surface in the low frequency range (80-200 Hz).

The effect of pressure gradient on the wall pressure fluctuation was also studied[49,131]. Schloemer[131] noted that, in comparison to zero pressure gradient case, the ratio of RMS value of the wall pressure fluctuation to the free stream dynamic head was more for adverse pressure gradient and less for favorable pressure gradient. On the other hand, the normalized RMS value of the wall pressure fluctuation (non-dimensionalized by the wall shear stress) was also larger for the adverse pressure gradient compared to the zero pressure gradient case. The increased value of p'_w/τ_w was higher compared to the increase observed for the ratio p'_w/q_∞. The spectral density was found to be influenced by the pressure gradient especially at low frequencies. At low frequencies the spectral density increased for both adverse and favorable pressure gradients compared to the zero pressure gradient case. At high frequencies the spectral density was approximately the same for the adverse and zero pressure gradient cases.

Bradshaw[49] noted that the low wave number pressure fluctuations are generated outside the inner layer. He suggested that this pressure fluctuation field consisted of all the spectral density at low wave number and contributed to the inactive motion in the inner region. Bradshaw also suggested that the active inner layer motion produced a high frequency contribution to the spectra which varied as τ_w^2/k up to wave numbers of the order of the inverse of the sublayer thickness. The influence of the different flow conditions and the effect of the size of the pressure transducer on the wall pressure fluctuation is presented in Table 2.4.

The correlation of fluctuating wall pressure and the streamwise component of velocity fluctuation was first reported by Serafini[53]. The advantage of such measurement is to evaluate the contribution to the wall pressure fluctuation from different regions of the turbulent flow field. Two regions were identified where the streamwise component of the velocity fluctuation contributed to the wall pressure fluctuation. These two regions were the inner region near the wall and the outer region. It was reported that the contribution to the pressure fluctuation at the wall from the outer region was less than one-half of that from the inner region.

The measurements of the wall pressure-velocity correlations were also reported by other investigators[49,54,55]. The measurements of correlations of the wall pressure fluctuation with all the three components of velocity fluctuation were obtained and a qualitative model for the structure of turbulence near the wall was proposed [54,55]. It was proposed that the stretching of the vorticity produced by the viscous stresses in the sublayer leads to the fluctuation of wall

TABLE 2.4 Influence of Different Flow Conditions and Pressure Transducer Size on the Root-Mean-Square Value of Wall Pressure Fluctuation

S. No.	Re_θ	d_1/δ^*	d_1^+	p'_w/τ_w	p'_w/q_∞ x 10^3	Remarks	Investigator (Year)
1(a)	29000	0.33	532	2.15	4.7	Smooth Flat Plate	Willmarth & Wooldridge(1962)
1(b)	38000	0.33	383	2.19	4.66	Smooth Flat Plate	
1(c)	-	-	555	3.09	7.0	Rough Flat Plate U_∞ = 205 ft/s	
1(d)	-	-	436	2.63	6.6	Rough Flat Plate U_∞ = 153 ft/s	
2(a)	6400	-	-	2.11	5.75		Bull(1967)
2(b)	33800	-	-	2.80	5.40		
3	38000	0.122	-	2.66	5.64	Smooth Flat Plate - Data Corrected for Finite Size of Transducer	Willmarth & Roos (1965)
4	26200	0.144	-	2.56	5.99	Axially Symmetric Boundary Layer	Willmarth & Yang (1970)
5(a)	17000	0.111	83	3.6	7.84	Smooth Flat Plat	Blake(1970)
5(b)	29800	0.054	130	3.8	20.15	Rough Surface(Equivalent Sand Roughness Height, Ks = 0.106 in.)	
5(c)	28800	0.052	143	3.2	20.43	Ks = 0.192 in.	
5(d)	28000	0.060	127	2.4	14.61	Ks = 0.074 in.	
6(a)	1400	0.217	19	2.53	10.0	Smooth Surface	Schewe(1983)
6(b)	1400	3.913	333	1.26	5.0	Smooth Surface	

pressure and velocity. It was also observed that the maximum magnitude of the correlation coefficient (R_{pu}) was 0.3.

Very recently, Kobashi and Ichijo[132] investigated the structure of coherent motions in a two-dimensional turbulent boundary layer. The measurements of the wall pressure fluctuation field and its correlation with streamwise and normal velocity components were obtained. From these measurements two types of coherent motions were identified. The first type included the large scale motions which prevailed through and outside the boundary layer. These large scale motions were observed to be initiated by the instability of the mean flow and rotate in the direction of the mean flow shear. The second type of coherent motion was the small scale motion (also known as burst) which was found to be limited to a narrow region near the wall. The small scale motions were like vortices, which rotated against the mean flow shear. A vortex ring model of coherent structure was proposed and it was concluded that the burst was bounded by two pairs of counter rotating vortices which were inclined forward. The ejection and sweep which characterized the burst phenomena are the flows which are induced by the paired vortices in front and back of the burst.

The influence of the pressure gradient on the wall pressure-velocity correlation was reported by Bradshaw[49]. The correlation coefficient R_{pu} was higher very close to the wall and lower away from the wall compared to the zero pressure gradient case. For a small distance z, correlation data was also presented in a narrow frequency band. At the lowest frequencies, the value of the correlation coefficient was 0.6. In the medium frequency range the value of the correlation coefficient

(R_{pu}) varied very little and was ~ 0.2 to 0.25. It was suggested that the variation from 0.2 to 0.25 corresponded to the wall pressure fluctuation generated in the inner layer. It was also noted that the v-component fluctuation in the inner region was less affected by the wall pressure fluctuations than the u-component.

The discussion presented in sections 2.1-2.4 suggests that a detailed experimental investigation of the influence of free stream turbulence on the development of a turbulent boundary layer downstream of distributed roughness, which is placed in the close vicinity of the leading edge of the flat plate, is needed. There is also a need to obtain a detailed measurement of the wall shear stress vector field in the blade end-wall corner region. The detailed knowledge of the wall pressure field and its correlation with the fluctuating velocity field is also desired to understand the near wall turbulence structure in three-dimensional flows.

CHAPTER III

EQUIPMENT, INSTRUMENTATION, EXPERIMENTAL METHOD AND DATA PROCESSING

The details of the equipment, instrumentation, methods of measurement, and the data processing techniques are described in this chapter. The present experimental study includes measurements of the mean velocity, wall shear stress, surface pressure, wall pressure fluctuation, and its correlation with the fluctuating velocity upstream and in the blade end-wall corner region.

3.1 Equipment and Instrumentation

3.1.1 Wind Tunnel

A low subsonic open circuit wind tunnel, designed and constructed at the Turbomachinery Laboratory of the City College of the City University of New York, was used for the experiments. A centrifugal blower fitted with variable inlet guide vanes was driven by a 25 H.P., 1770 rpm A.C. motor to generate the flow in the wind tunnel. Air velocity in the 46 cm x 46 cm test-section could be varied from about 5 m/s to 35 m/s by adjusting the inlet guide vane setting. The non-uniformity in the free stream mean velocity in the test-section was within ± 0.5% at the maximum flow rate. The free stream turbulence intensity in the test-section was found to vary from 0.6% at a velocity of 6 m/s to 0.1% at a velocity of 20 m/s and higher. An inlet filter was used to separate dust from air passing through the wind tunnel.

3.1.2 Test-Model

The blade end-wall corner test-model was constructed by mounting a blade with a symmetrical airfoil section on a flat plate. Two flat plates were designed to obtain the required measurements. The first flat plate (hereafter, will be referred to plate 'A') was constructed from two, 91 cm x 46 cm x 0.64 cm, 2024 T4 bare aluminum plates as shown in Fig. 3.1. Four 82.6 cm x 1.3 cm x 0.64 cm aluminum ribs were placed lengthwise between the plates and screwed together to produce flat surfaces. The holes were filled with epoxy and sanded to form smooth surfaces. The leading edge of the flat plate was made from a 1.9 cm diameter aluminum bar, whereas the trailing edge was constructed from a 2.5 cm x 1.9 cm bar. Six static pressure holes were provided on each side of the assembly with three holes in each row length-wise and two rows on each plate. Twelve polyethylene tubes connected to the wall static holes passed through the space between the plates and emerged from the side near the trailing edge of the flat plate assembly. These surface static taps were mainly provided so that the test-model could be aligned perfectly at zero incidence to the main flow. Flat plate 'A' was employed for the measurements of the mean velocity profiles, the wall shear stress, and the surface static pressure with the surface static tube.

The second flat plate (hereafter, called plate 'B') was constructed from a single 2024 T4 bare aluminum plate as shown in Fig. 3.2(a). The leading edge of the flat plate was made circular in shape by using a standard 3/4 in. cutter. At four axial locations provisions were made to fix interchangeable circular disks shown in Figs. 3.2(b) and 3.2(c)). Two instrumentation and four dummy disks were constructed. In one

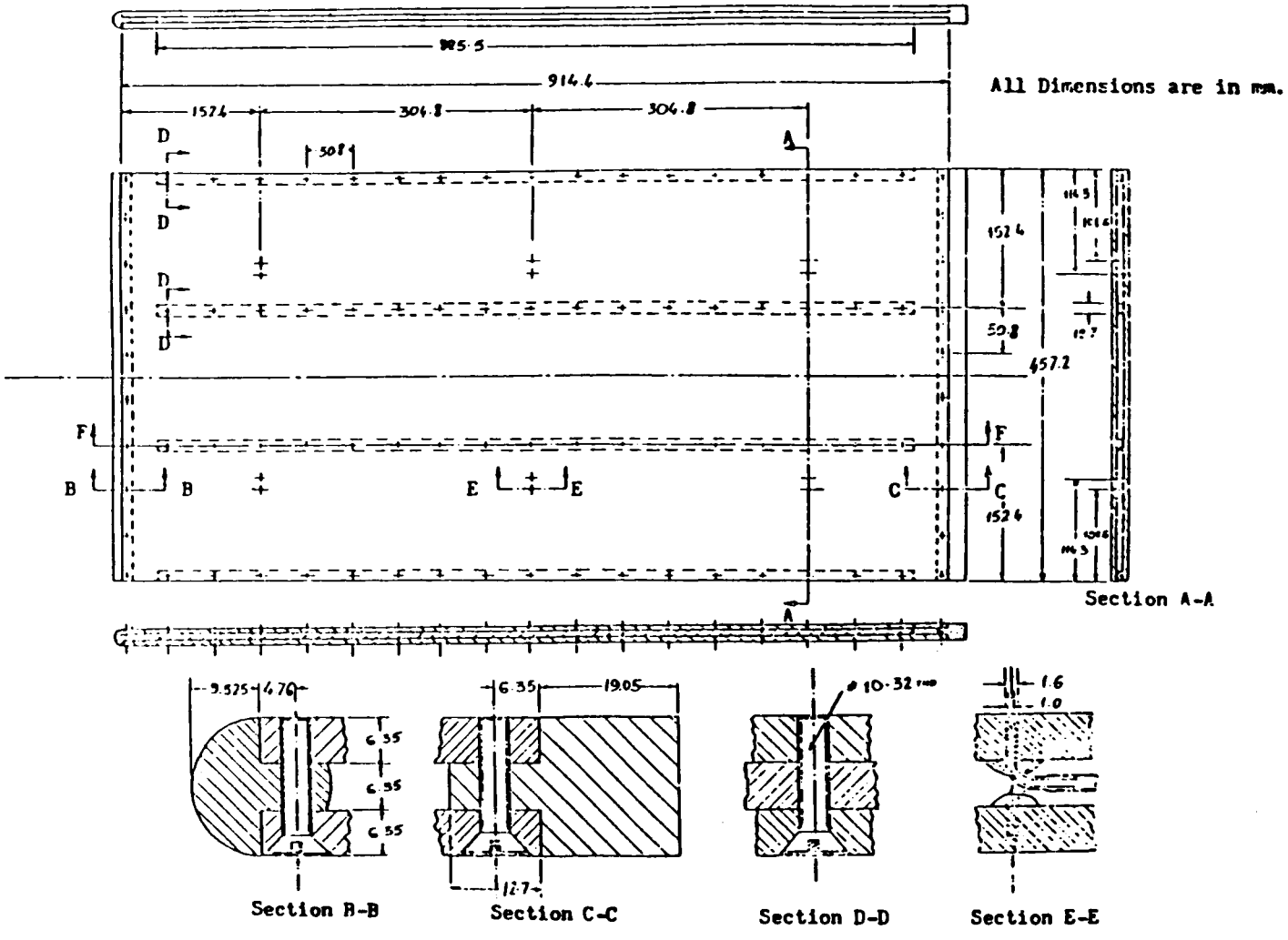

Fig. 3.1 Flat Plate Assembly- Plate 'A'

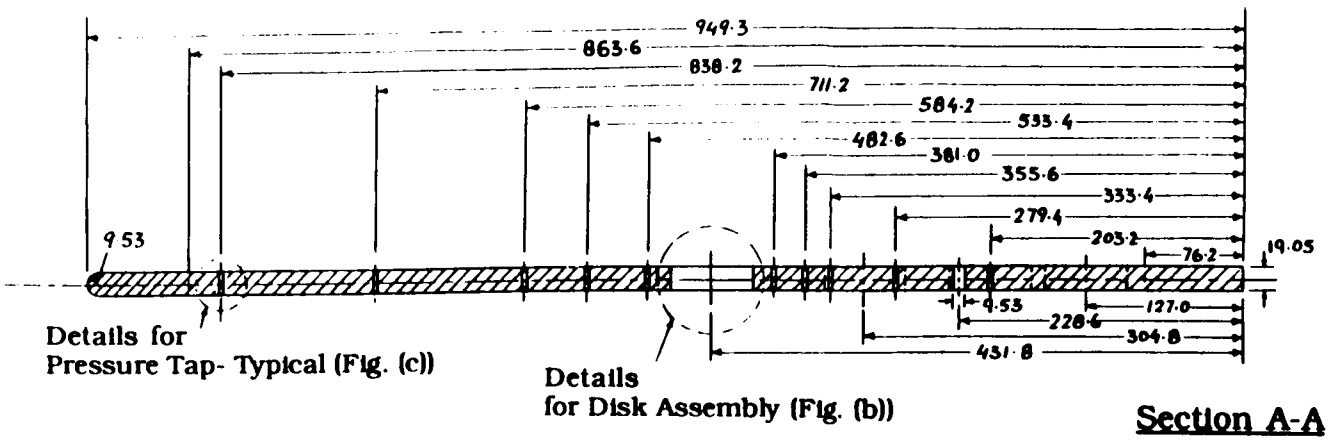

Section A-A

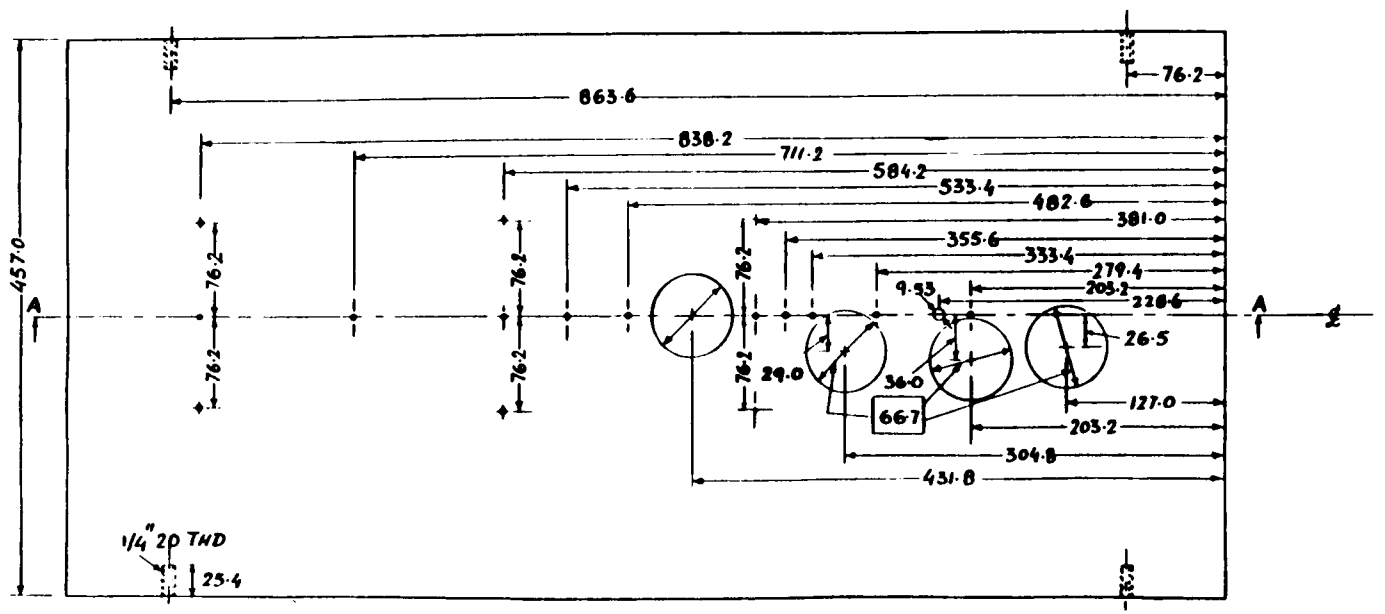

(a) Flat Plate Details

All Dimensions are in mm

Fig. 3.2 Flat Plate Assembly- Plate 'B'

C-2

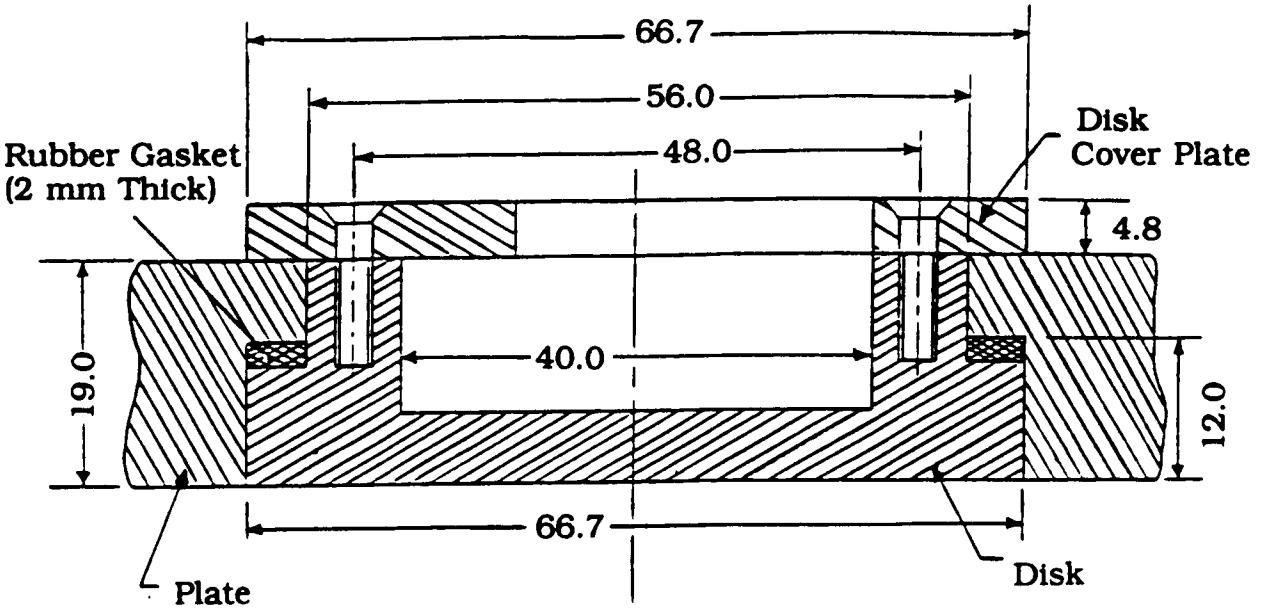

(b) Plate and Disk Assembly

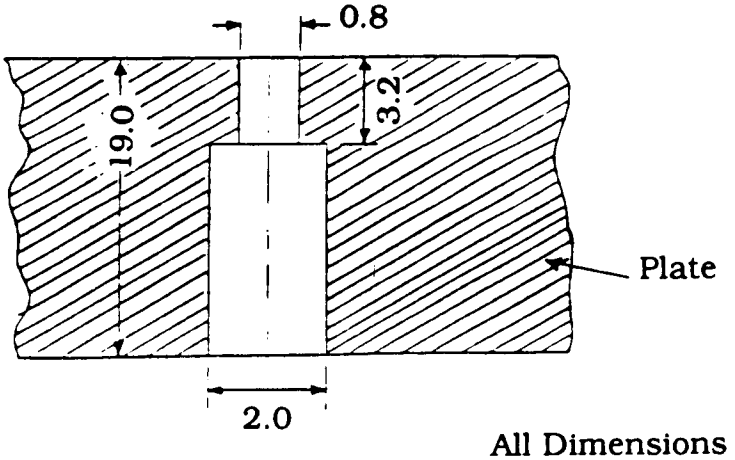

All Dimensions are in mm

(c) Schematic of Pressure Tap- Typical

Fig. 3.2 (Contd.) Flat Plate Assembly- Plate 'B'

of the instrumentation disks (hereafter, called Disk No. 1) five Kulite pressure transducers were installed (Fig. 3.3). The transducers were soft mounted using silicon rubber (RTV Dow Corning 3145). In the second instrumentation disk (hereafter, called Disk No. 2) nine surface pressure taps of 0.8 mm (1/32 in.) diameter were provided along its diameter (Fig. 3.4). The main dimensions of the flat plate 'B' were the same as those of the flat plate 'A' described earlier. A large number of surface static taps were also provided on the flat plate 'B' to obtain surface pressure distributions (Fig. 3.2(a)).

Based on the compromise of obtaining a thick boundary layer on the blade and its stall characteristics, a NACA 65-015 base profile was chosen for the blade. The chord length of the blade was 25.4 cm. The leading and the trailing edges of the blade had diameters of 1.27 and 0.25 cm, respectively (Fig. 3.5). The blade was made in two sections each with 21.9 cm span and a 0.95 cm hole in the spanwise direction at the position of maximum thickness on the chord line. A threaded rod passing through the hole in the flat plate and the blades held the entire assembly together. The distance between the leading edge of the flat plate and the blade was 62 cm. The initial seven cm from the leading edge of the flat plate was made rough by gluing a No. 4 sand paper to trigger the transition and artificially increase the boundary layer thickness on the flat plate (Fig. 3.6). The test-model assembly was bolted to the test section with the help of two threaded rods. The top and bottom test-section walls parallel to the flat plate were removed 10 cm ahead of the blade leading edge to facilitate probe traverses.

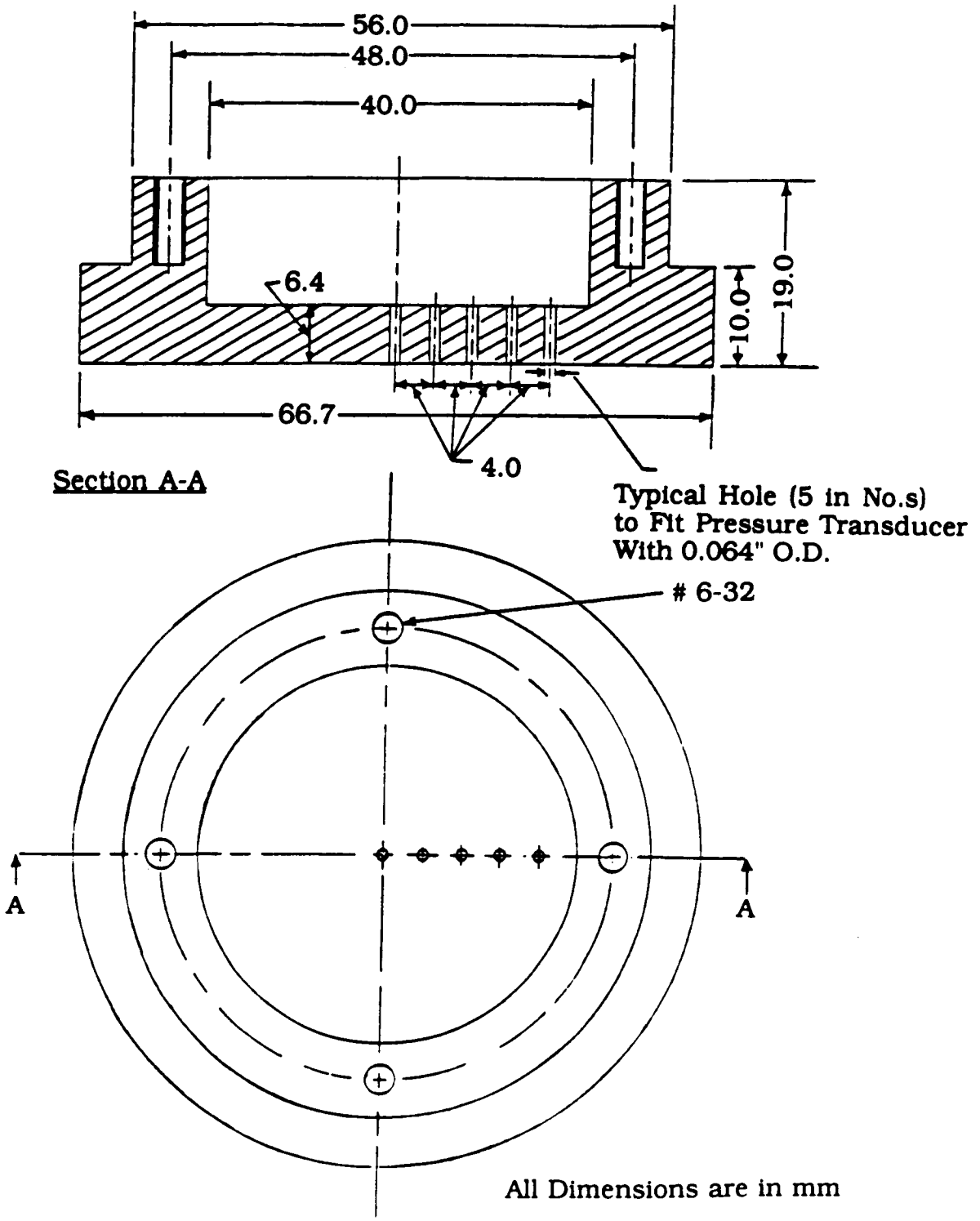

Fig. 3.3 Instrumentation Disk for Pressure Transducers- Disk No. 1

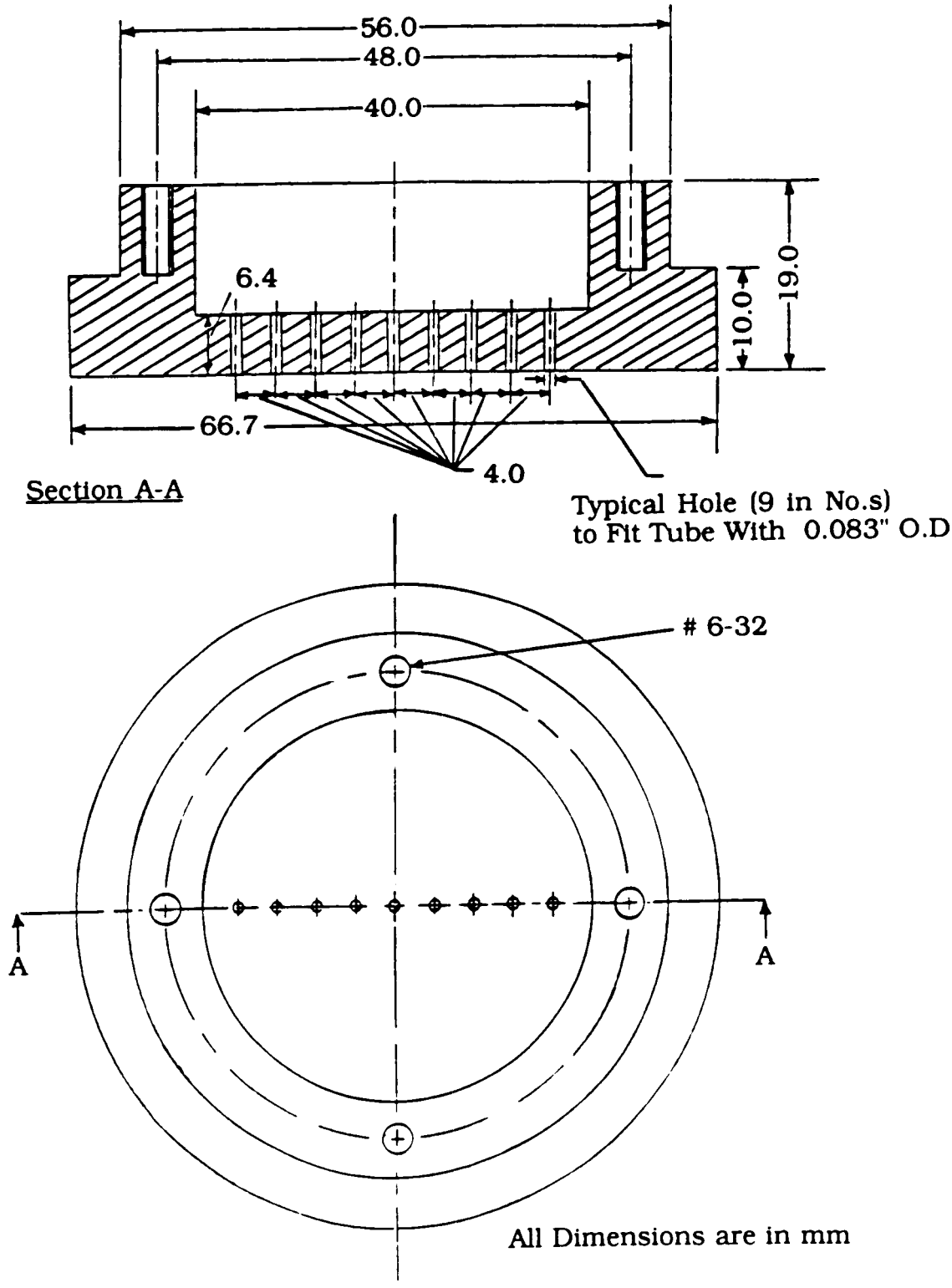

Fig. 3.4 Instrumentation Disk for Surface Pressure Taps- Disk No. 2

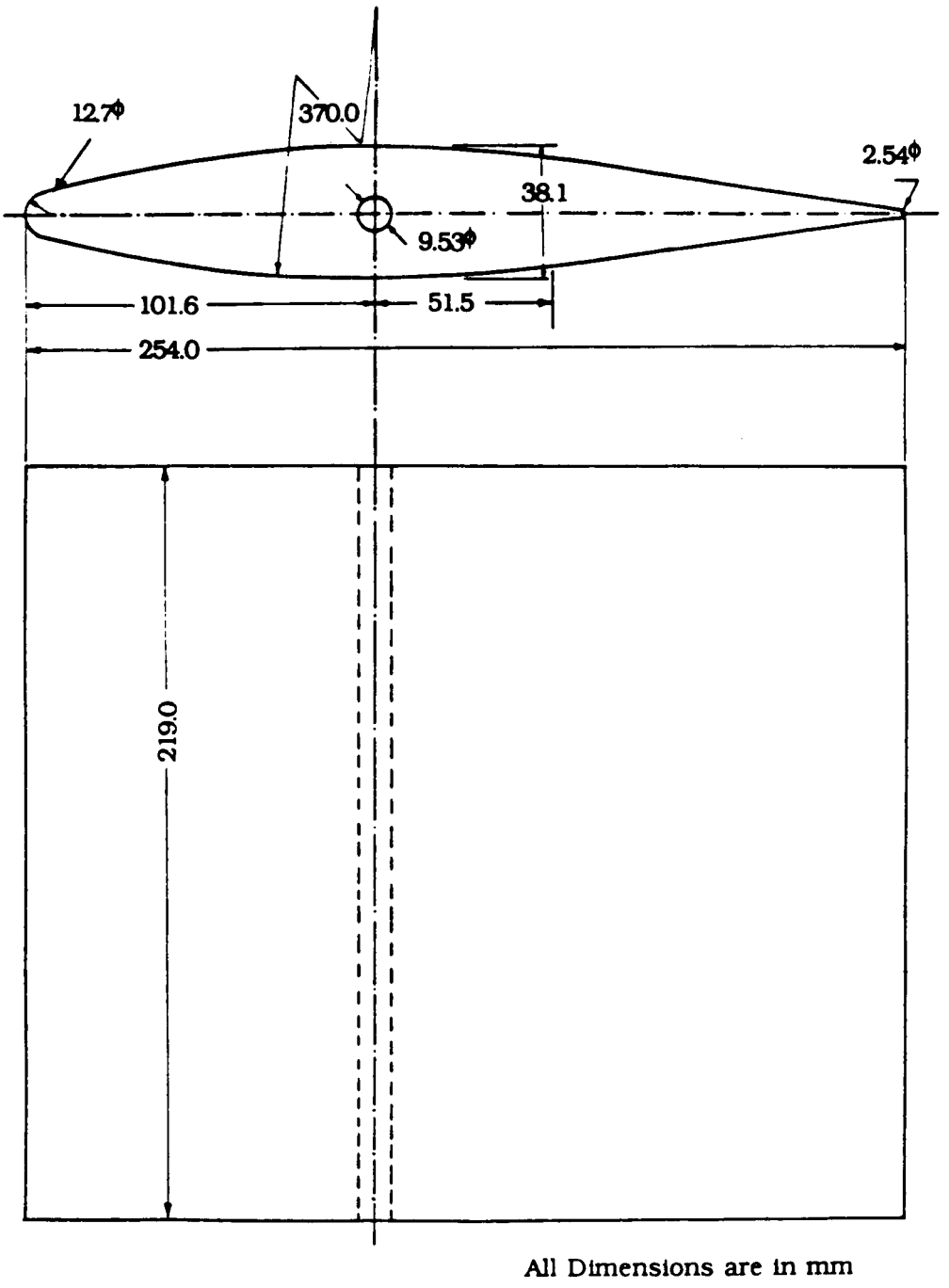

Fig. 3.5 Airfoil for Test-Model

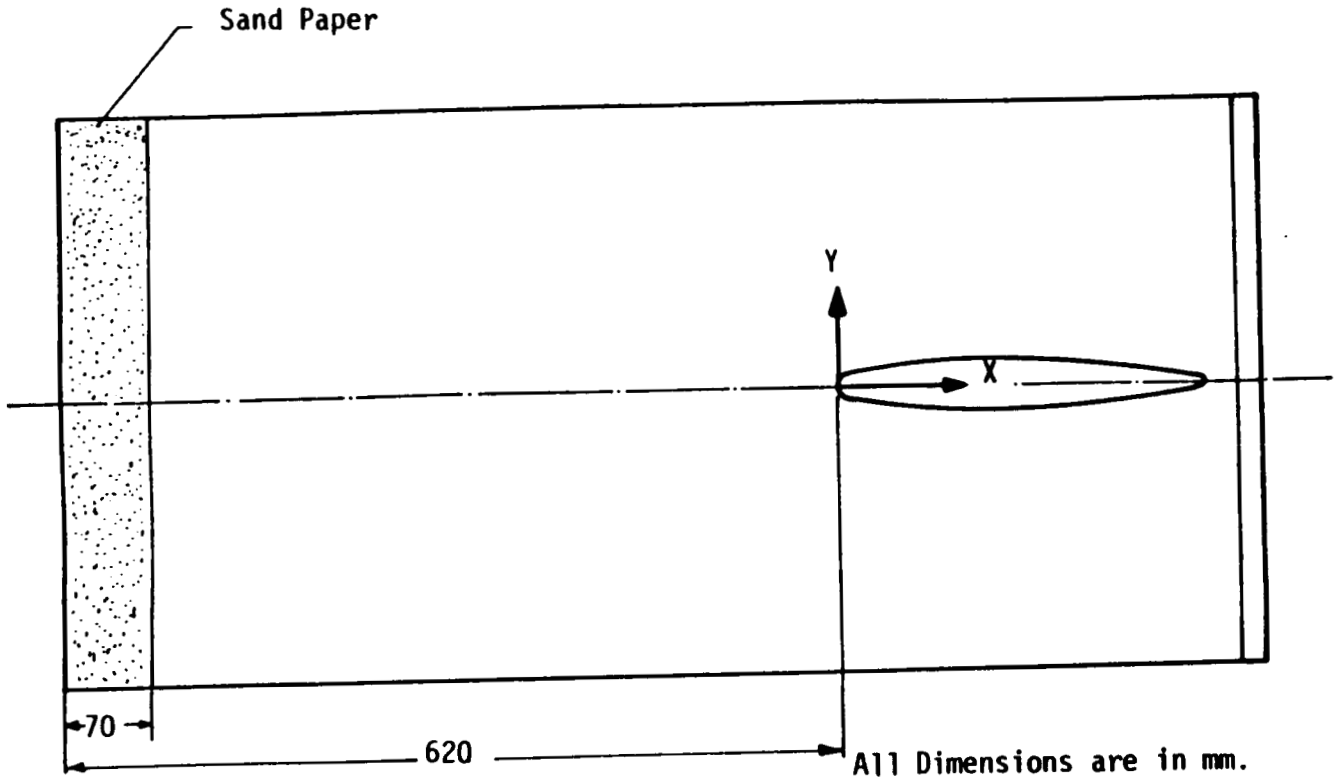

Fig. 3.6 Schematic of Location of Blade and Sand Paper on Flat Plate Assembly

3.1.3 Traverse Mechanism and Rotary Device

3.1.3.1 Traverse Mechanism:

The traverse mechanism was constructed with two compound slides held perpendicular to each other with an angle plate (Fig. 3.7). The assembly was bolted to a table anchored to the floor. A device to rotate the probe about its own axis was bolted to the connecting bar. The connecting bar was clamped to the compound slide with its axis perpendicular to the axis of the test-section.

The least count of the compound slides were 0.0254 mm. The total traverse distance parallel to the axis of the test-section was 33 cm, perpendicular to the axis. In the horizontal and vertical directions, the traverse distance was 20 cm. The traverse distance of the probe in all the three directions could be extended by 5 cm by changing the clamping position of the connecting bar on the vertical surface of the compound slide. Subsequent extension in traverse distance was possible by changing the position of the angle plate on the horizontal compound slide.

3.1.3.2 Rotary Device

The rotary device was machined from brass stock in two principal components. The base, which was bolted to the supporting rods, carried a rotating part in the shape of a frustum of a cone with a hole through its axis and a chuck to hold the guide tube. Three adjustable spring loaded steel balls provided sufficient pressure between the base and the rotating part to hold them together snugly without impeding rotary motion. Two supporting rods bolted to the base held a guide block which had a hole aligned with the axis of the guide tube holder chuck. The protractor mounted on the rotating part and the vernier

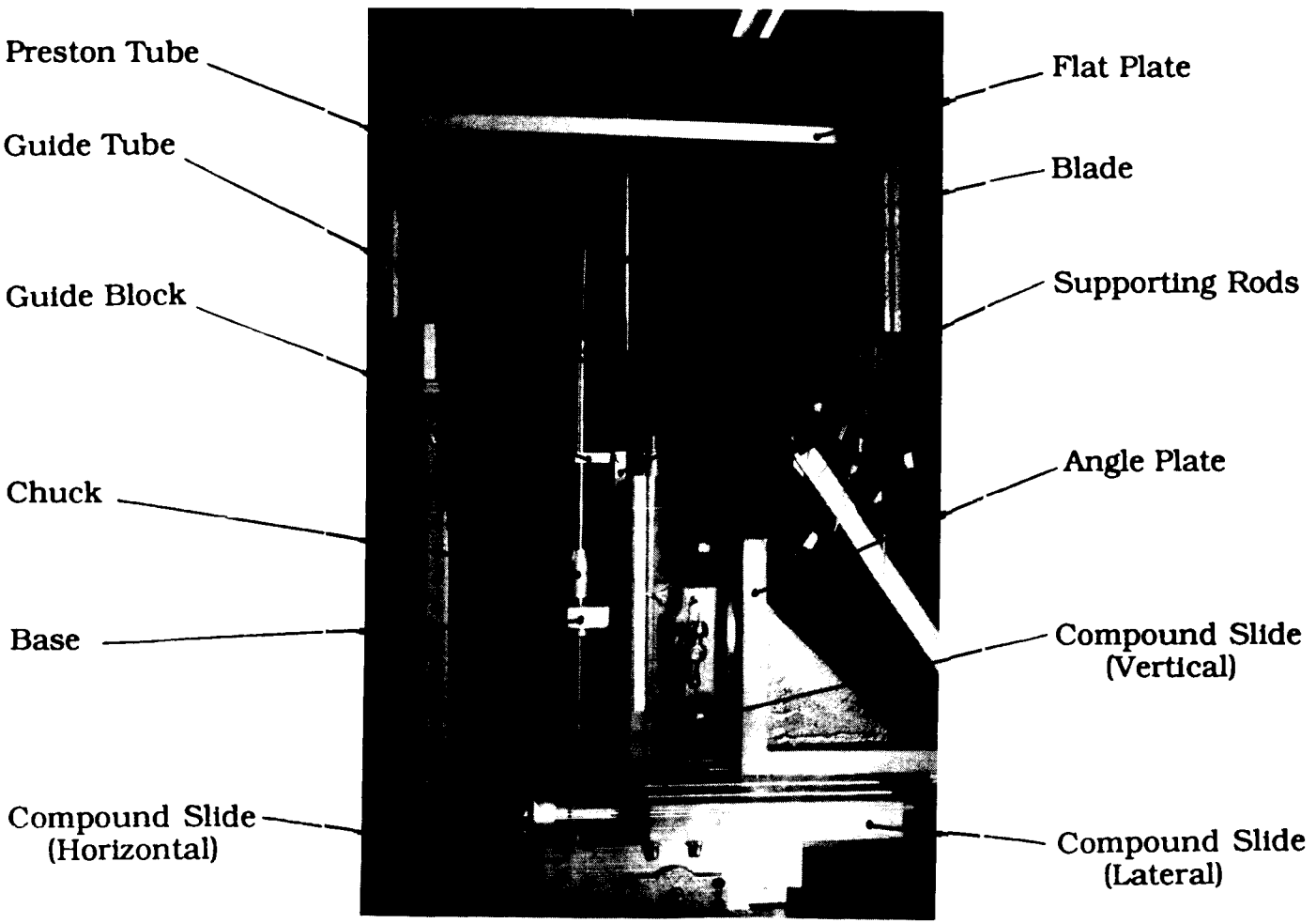

Fig. 3.7 Photograph of Traverse Mechanism and Rotary Device for the Wall Shear Stress Measurements With the Preston Tube

mounted on the base allowed the change in angle to be measured to the least count of 0.2 degrees. The Preston tube and guide tube assembly were held by the guide tube holder chuck. The rotary device was mounted on the traverse mechanism such that the axis of rotation made an angle of 90^0 with the axis of the test-section (Fig. 3.7).

3.1.4 Grids

A combination of two grids was used to create free stream turbulence level of 1.5% at 107 cm downstream of the grids (location of the blade leading edge) to avoid a separation bubble and increase the boundary layer thickness over the surfaces of the blade. The grids selected for this purpose were 1 mesh 2 mm diameter galvanized iron wire mesh followed by a 4 mesh 0.6 mm diameter galvanized iron wire mesh (Fig. 3.8). The wires of the grids were inclined 45^0 to each other. The grids were placed 45 cm ahead of the leading edge of the flat plate. The non-uniformity in the free stream mean velocity in the test section was less than 0.5% at a velocity of 27 m/s.

3.1.5 Probes and Instrumentation

The mean wall shear stress measurements were obtained with a specially constructed Preston tube. A Preston tube of 0.81 mm (0.032 in.) outer diameter with an inner-to-outer-diameter ratio of 0.61 was used to measure the wall shear stress. The Preston tube was bent as shown in Fig. 3.9 so that the tip of the probe could be concentrically rotated about its axis of rotation. This was essential to align the probe tip in the flow direction at the measurement location. The stem of the

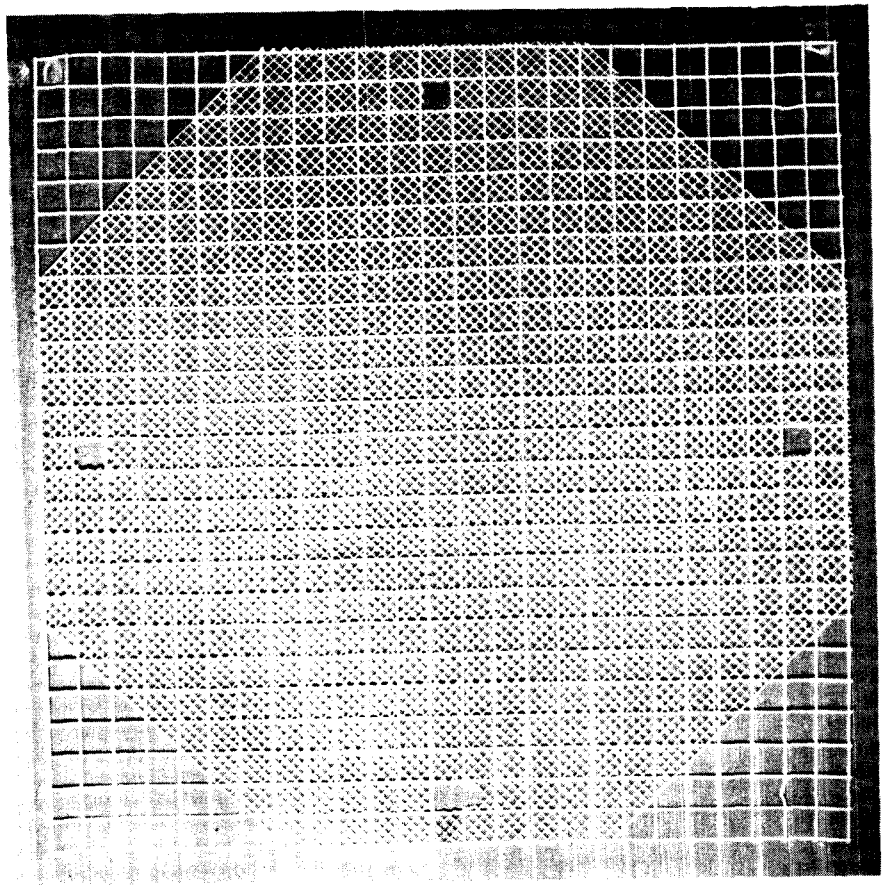

Fig. 3.8 Photograph of Turbulence Generating Grids

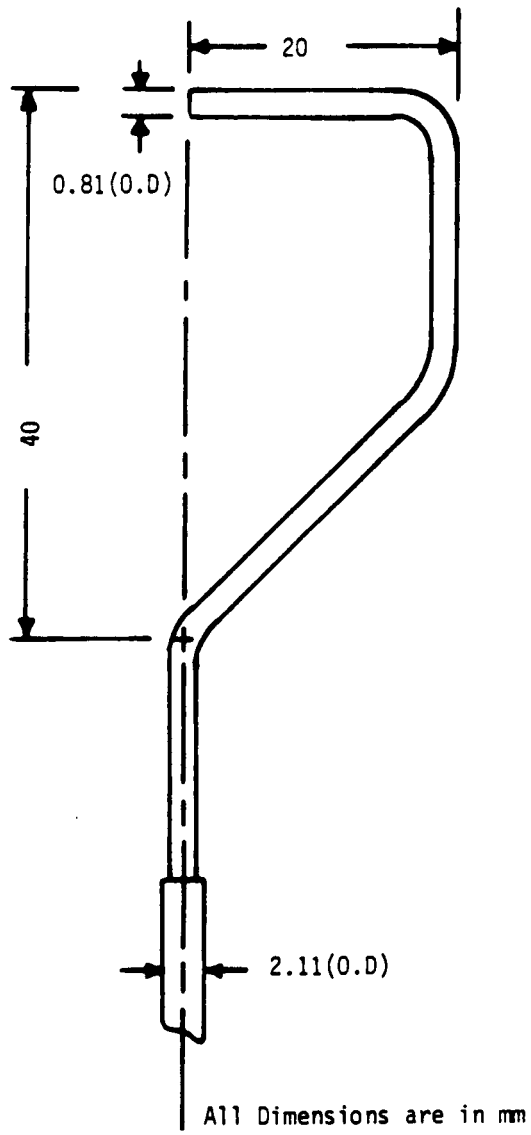

Fig. 3.9 Sketch of the Preston Tube Used in the Measurements of Wall Shear Stress

probe was soldered to increasing diameter tubes such that the probe could be mounted in the available fixtures.

The mean surface static pressure was measured by two methods. In the first method, the wall static pressure was measured using the United Sensor Corporation Pitot-static probe of 1.59 mm (1/16 in.) diameter, resting on the surface. In the second method, a large number of wall taps (also called a wall piezometer) provided on the surface of flat plate 'B' of the test-model and Disk No. 2 were used to measure the surface static pressure.

A Kiel probe also made by the United Sensor Corporation was used to measure the reference total pressure which was maintained constant during the experiment. This was essential to maintain the free stream velocity almost the same at different times of data collection.

A total head probe of 0.81 mm (0.032 in.) outer diameter along with the pitot-static probe, described earlier, were used to obtain the mean velocity profile data.

The different pressure measuring probes, discussed above, were connected to pre-calibrated variable reluctance type differential pressure transducers (Model DP 15) with a range of ± 0.5 PSID and CD 15 carrier demodulator. The output was read on a digital voltmeter.

The wall pressure fluctuation measurements were obtained with an integrated sensor pressure transducer (Model XCS-062-5G) manufactured by Kulite Semiconductor. This transducer is a piezoresistive type consisting of an integrated silicon sensor (also called a diaphragm). A four arm wheatstone bridge is diffused in the surface of the silicon sensor using a photolithographic process. The transducer con-

sisted of a reference tube for gage pressure measurement. The pressure transducer was also provided with the temperature compensation module. The pressure transducers were the smallest available in size and had a diameter of the pressure sensitive area of 0.71 mm (0.028 in.). Some of the important specifications of a typical piezoresistive type pressure transducer supplied by the manufacturer are given in Table 3.1. In Table 3.2 the characteristics of the five transducers used in the investigation are provided.

A single normal sensor hot wire probe was used to obtain the streamwise fluctuating velocity component. The sensor was made from platinum coated tungsten wire with diameter and length of 4μm and 1 mm, respectively.

3.1.6 Calibration Equipment

A Thermo System Inc. calibrator model 1125 was used to calibrate the variable reluctance type pressure transducers against a micromanometer with 0.0254 mm of water pressure resolution. A representative calibration curve for two differential pressure transducers is shown in Fig. 3.10.

3.2 Methods of Measurement

During the course of the flow visualization study which was conducted by Hazarika[47] on the same test-model, a separation bubble was observed on the blade surface in the blade-end-wall corner region.

As a result, the entire experimental investigation was performed in two parts. In the first part, termed Case A, different flow variables of interest were measured without the presence of separation bubble.

TABLE 3.1 Typical Specifications of a Piezoresistive Transducer (Model No. XCS- 062- 5G) as Supplied by Kulite Semiconductor Products Ltd.

Parameter	Specification
Bridge Type	Fully active four arm Wheatstone bridge diffused into silicon diaphragm
Rated Pressure	5 psig
Full Scale Output (nominal)	225 mv
Excitation voltage	15 V DC
Input Impedance (min.)	1200 Ω
Output Impedance (nom)	2500 Ω
Combined Nonlinearity and Hysteresis	0.5% BFSL
Repeatability	0.1% FS
Natural Frequency	150 KHz
Zero Balance	3% FS
Compensated Temperature Range	80 F - 180 F
Maximum Change of Sensitivity with Temperature	+ 2% / 100 F
Acceleration Sensitivity % FS/g	
Perpendicular	0.005
Transverse	0.0005
Resolution	Infinite

TABLE 3.2 Specifications of the Pressure Transducers (Model XCS- 062- 5G) Used in the Investigation

Parameters	Specification				
	TR# 1	TR# 2	TR# 3	TR#4	TR# 5
Manufacturer Sr. No.	1546- 3- 7	1546- 3- 8	1546- 3- 10	3014- 5- 138	3014- 5- 147
Rated Pressure (psig)	5	5	5	5	5
Excitation Voltage Tested(DC Volt)	15	15	15	15	15
Input Impedance(Ω)	1500	1531	1751	1489	1444
Output Impedance(Ω)	1853	1861	1928	2062	2076
Sensitivity (mV/psi)	30.22	35.98	29.65	33.89	33.37
Zero Pressure Output (% FS)	< ± 5	< ± 5	< ± 5	< ± 5	< ± 5
Thermal Effect on Zero (% FS/100^0 F)	< ± 2	< ± 2	< ± 2	< ± 2	< ± 2
Thermal Effect on Sensitivity (%/100^0 F)	< ± 2	< ± 2	< ± 2	< ± 2	< ± 2

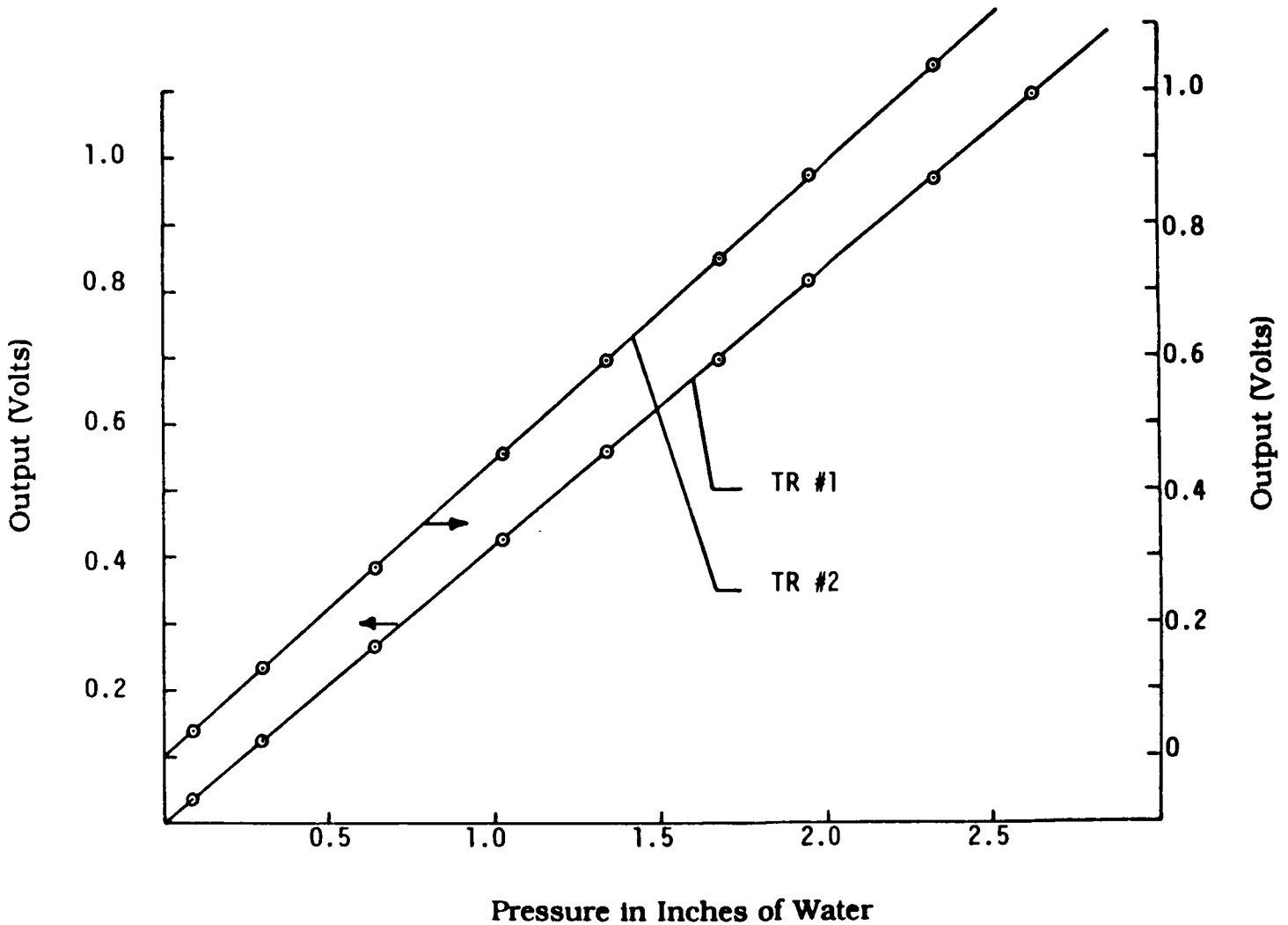

Fig. 3.10 A Typical Calibration of Variable Reluctance Type Differential Pressure Transducers

The flow variables measured included mean value of the surface static pressure and wall shear stress, mean velocity profiles, the fluctuating wall static pressure, and the streamwise fluctuating velocity component. In the second part, termed Case B, measurements were obtained in the presence of separation bubble. The flow parameters of interest in case B were mainly the surface static pressure and the wall shear stress. In this section, the methods of measuring the flow parameters discussed above along with their data processing procedures are described.

3.2.1 Reference Flow Condition

The reference total pressure was measured at the streamwise station which was located at 50.8 mm upstream of the blade leading edge and at 76 mm above the end-wall (flat plate) to determine the reference free stream velocity, U_∞ (Fig. 3.11). At this location (i.e., x = - 50.8 mm, y = 0 mm, and z = 76 mm) the static pressure was found to be equal to the atmospheric pressure. The reference total pressure was maintained nearly constant for the entire experiment. The free stream velocity obtained from the measured reference total pressure was 27.3 ± 0.3 m/s during the entire experiment. The distances of different streamwise stations with reference to the airfoil leading edge and the plate leading edge are shown in Table 3.3. Also included in Table 3.3 are corresponding values of x/c (c is the blade chord length).

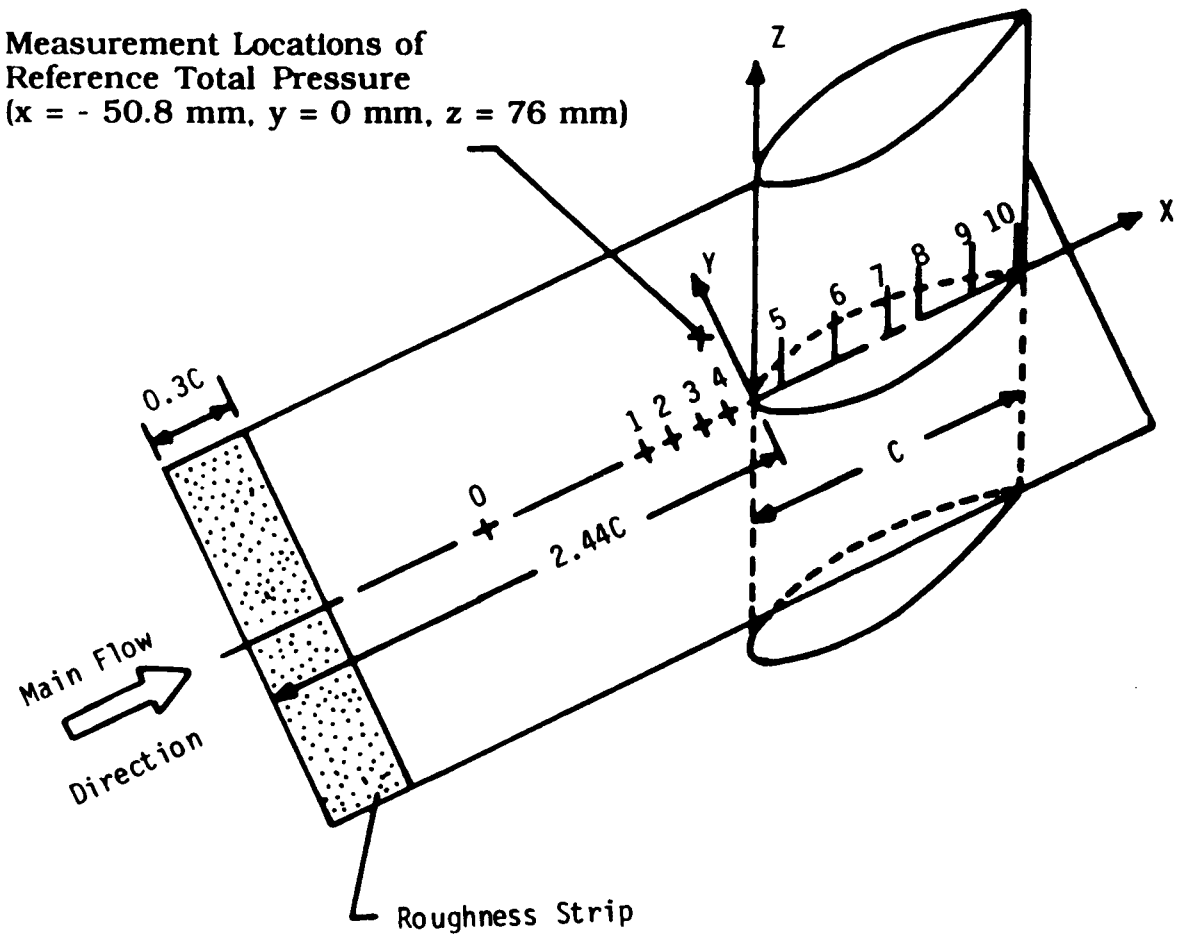

Fig. 3.11 Flow Geometry, Location of Reference Total Pressure, and Streamwise Stations

TABLE 3.3 Location of Streamwise Stations

Station No.	Streamwise Distance x1 (mm)	Streamwise Distance x (mm)	x/c (c = 254 mm)
0	366.0	- 254.0	- 1.0
1	518.4	- 101.6	- 0.4
2	543.8	- 76.2	- 0.3
3	569.2	- 50.8	- 0.2
4	594.6	- 25.4	- 0.1
5	645.4	25.4	0.1
6	696.2	76.2	0.3
7	747.0	127.0	0.5
8	772.4	152.4	0.6
9	823.2	203.2	0.8
10	871.0	251.0	0.99

NOTE :

(i) x1 is the streamwise distance with reference to the plate leading edge.

(ii) x is the streamwise distance with reference to the blade leading edge.

3.2.2 Mean Velocity Profile Measurement

3.2.2.1 Two-Dimensional Flow

A detailed experimental investigation was undertaken to study the influence of free stream turbulence on the development of a turbulent boundary layer developing downstream of the distributed roughness strip. In order to investigate the above mentioned effect, the following four cases were studied: (i) the development of a turbulent boundary layer with natural transition and no free stream turbulence (Case 1), (ii) the influence of free stream turbulence on the development of a turbulent boundary layer with natural transition (Case 2), (iii) the development of a turbulent boundary layer downstream of an initially distributed roughness (Case 3), and (iv) the combined effect of initial roughness and the increased level of free stream turbulence (Case 4).

For each case mean velocity profiles were measured at seven streamwise locations on the flat plate centerline. The two dimensionality of the flow was checked by measuring the variation of the surface static pressure and the wall shear stress, at the last measurement location, over a distance of approximately 75 mm from the plate centerline in the spanwise direction. From the measurements of the above mentioned two parameters, at the last measurement location, it was found that the variation in surface static pressure was very negligible (about 0.12 mm of water column). However, the value of wall shear stress changed within ± 2%.

The boundary layer thickness, δ, was obtained, from the mean velocity profile data, corresponding to $U/U_e = 0.995$, where U is the streamwise mean velocity within the boundary layer and U_e is the local

free stream velocity. The value of δ was also calculated following Coles's work[133]. Using the combined law of the wall and wake to represent velocity profile completely, as proposed by Coles, a relation of δ in terms of displacement thickness (δ^*) and the wake strength parameter (Π) can be written as,

$$\delta/\delta^* = K\,(U_e/u^*)/(1 + \Pi) \tag{3.1}$$

where K is the Von-Karman constant and u^* is the friction velocity. Once the value of δ^*, u^* and Π are known, the value of δ can be calculated from Eqn. 3.1. It is noted, that in Eqn. 3.1 the value of wake strength parameter, Π, and u^* are needed. Following Coles's[133] work the value of Π was calculated using the relation,

$$2\Pi - \ln(1 + \Pi) = K(U_e/u^*) - \ln(\delta^* U_e/\nu) - KB - \ln(K) \tag{3.2}$$

whereas, the value of u^* was calculated from the measured wall shear stress. The values of the constants K and B used in Eqn. 3.2 were 0.41 and 5.0, respectively. These values were suggested by Coles[134] in 1968 Stanford conference and are generally considered standard in turbulent boundary layer work.

The mean velocity profile data within the boundary layer, obtained using a pitot probe, was corrected for the pitot displacement effect as suggested by MacMillan[135].

The boundary layer integral parameters, viz., displacement thickness (δ^*), momentum thickness (θ), Clauser's shape parameter (G), and Clauser's universal integral thickness (Δ) were calculated using the standard definitions. The contribution to integrals for calcu-

lating various boundary layer integral parameters in the range $0 < zu^*/\nu < 50$ was evaluated following the work of Coles[134].

The various boundary layer parameters calculated were compared with the available empirical relations and also with the results of other investigators.

3.2.2.2 Three-Dimensional Flow

The measurements of mean velocity profile, using the pitot tube in combination with the pitot-static tube, were obtained in the flow field upstream of the blade leading edge. Five streamlines were selected upstream of the blade leading edge covering a distance of 0.4 and 0.3 of blade chord length in the streamwise and lateral directions, respectively. The measurement locations for the mean velocity profile data on five streamlines are shown in Fig. 3.12. In Fig. 3.12 the symbol 'S' corresponds to the streamline, whereas numeric subscripts correspond to the measurement location. The first numeric subscript corresponds to the streamline number, whereas the second subscript corresponds to the number of the streamwise station. Traces of the above mentioned streamlines were obtained from the flow visualization studies conducted by Hazarika[47].

The coordinates of the measurement locations on five streamlines are tabulated in Table 3.4. The data of the limiting streamline directions, obtained from the flow visualization[47], at each location of measurement is also included in the Table 3.4. The static and total pressure probes were aligned with the flow direction at an angle at each measurement location as given in Table 3.4. For the flow angles $< 4^0$, the probes were aligned parallel to the test model (flat plate) cen-

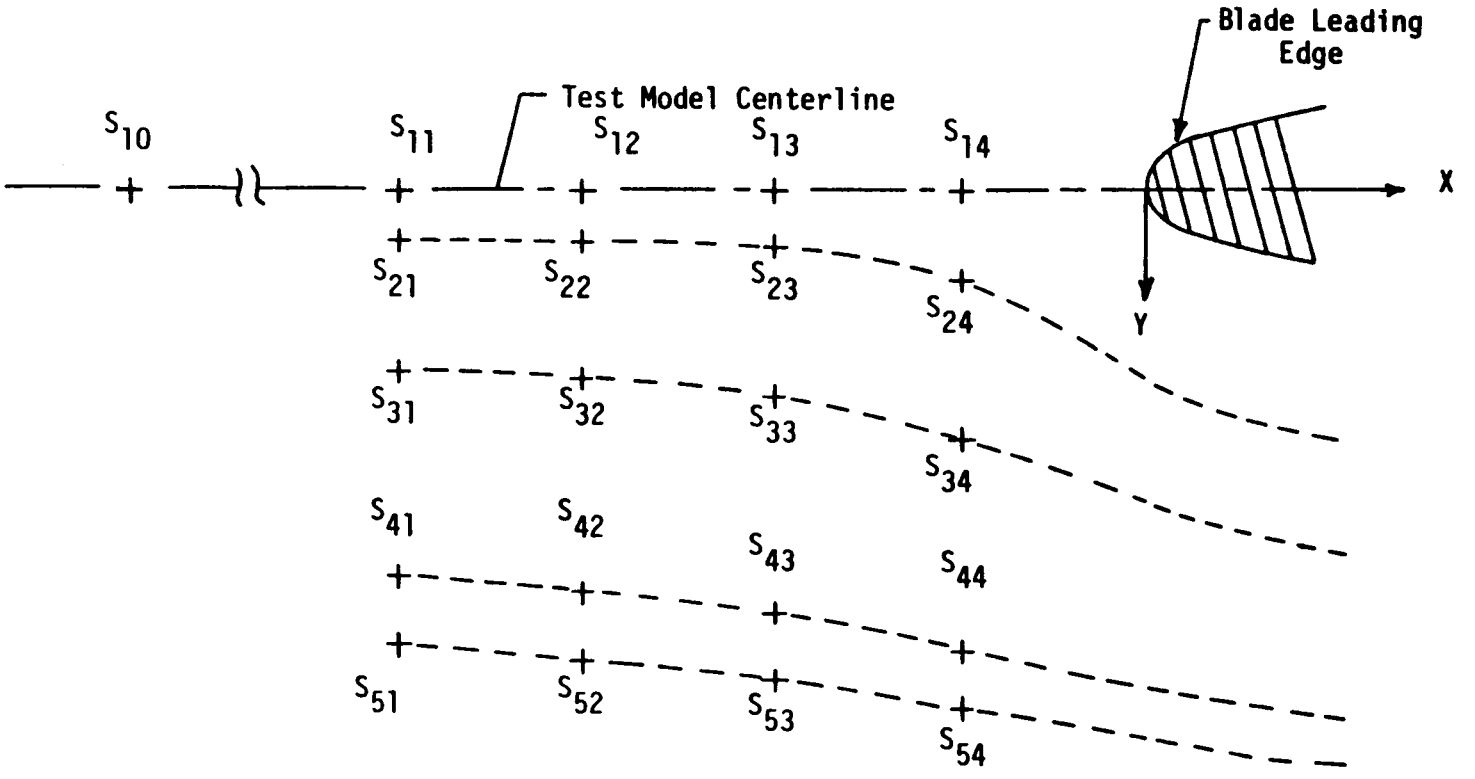

Fig. 3.12 Locations of Mean Velocity Profile Measurement Upstream of the Blade Leading Edge (For Coordinates of Measurement Locations, See Table 3.4)

TABLE 3.4 Coordinates of Measurement Locations for Mean Velocity Profile Data Upstream of Blade Leading Edge

S_{AB}		B = 0	B = 1	B = 2	B = 3	B = 4
	x (mm)	- 254.0	- 101.60	- 76.20	- 50.80	- 25.40
A = 1	y (mm)	0.0	0.0	0.0	0.0	0.0
	α (degree)	0.0	0.0	0.0	0.0	0.0
A = 2	y (mm)	-	7.0	7.0	7.5	12.0
	α (degree)	-	0.83	1.0	4.25	20.58
A = 3	y (mm)	-	24.0	25.0	27.0	33.0
	α (degree)	-	1.25	4.75	8.58	15.92
A = 4	y (mm)	-	51.0	53.0	56.0	61.0
	α (degree)	-	5.42	5.42	8.50	11.0
A = 5	y (mm)	-	60.0	63.0	65.0	69.0
	α (degree)	-	15.92	3.16	6.33	8.75

Note: S_{AB} represents the streamline in which letter "A" corresponds to the streamline number (A = 1, 2, ... , 5) and "B" corresponds to streamwise station number (B = 0, 1, ... , 4)

terline because the pitot-static and the total head probes are known to be insensitive to flow angles less than 5^0 (based on calibration curves supplied by United Sensor Corporation).

The velocity can be calculated from the total and static pressure measurements and is given by the relation

$$U = \{2C_1(V_t - V_s)/\rho\}^{0.5}$$

where V_t and V_s are transducer outputs in volts of total and static pressures, respectively, and C_1 is the calibration constant of the pressure transducer.

3.2.3 Wall Shear Stress and Wall Static Pressure Measurements

3.2.3.1 Two-Dimensional Flow

Two-dimensional wall shear stress data were collected on the flat plate 'A' with the blade removed. The traverses of the Preston tube and the static pressure probe were made at seven streamwise stations, station 1, and stations 5 to 10. The traverses in the Y-direction covered a distance of nearly 76 mm from the test-model centerline. The grid showing the locations of the two-dimensional wall shear stress measurements is shown in Fig. 3.13. The Preston tube was aligned parallel to the test-model centerline because in this case flow streamlines were parallel to the test-model centerline. The value of wall shear stress was also calculated using the mean velocity profile data with the help of Clauser's chart (see discussion on the method in section 2.3.3.1). The measured values of the wall shear stress were compared with the well established empirical relations available in the literature.

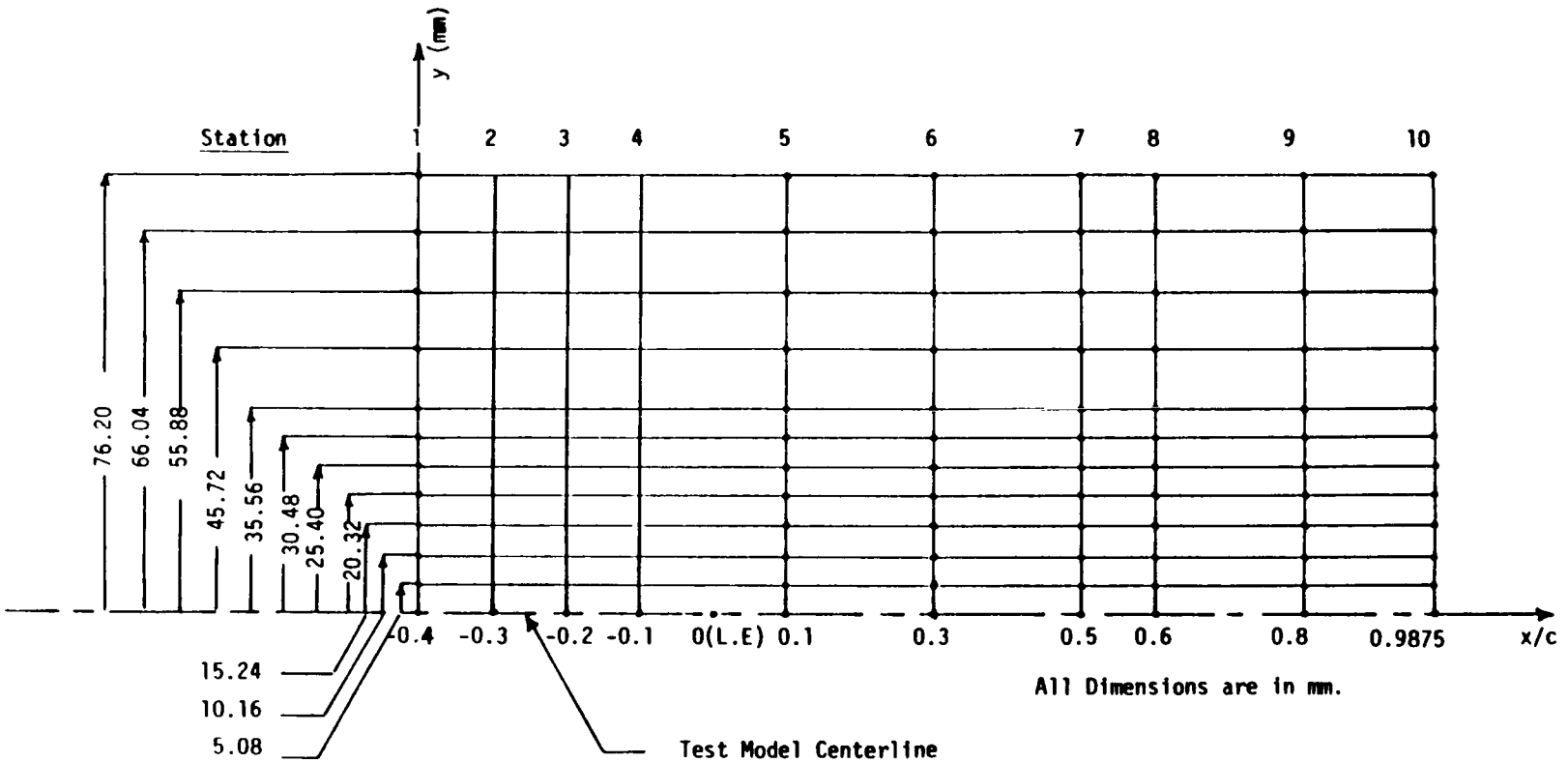

Fig. 3.13 Locations of Measurement on the Flat Plate Surface for Case A (Two-Dimensional Flow)

The yaw sensitivity of the Preston tube was examined in two- and three-dimensional flows. The yaw angle range covered was ± 30 degrees. A detailed analysis was done to evaluate the error due to misalignment of the Preston tube with the local flow direction.

The surface static pressure was measured with the static tube resting on the surface. The use of this technique (called surface tube method), to measure surface static pressure, was demonstrated by Sproston and Goksel[136] in a two-dimensional flow. They found that for a favorable pressure gradient the wall static pressure measured with the surface tube differed within 2% of the free stream dynamic head compared to the conventional method.

It is well known that a static tube placed in the flow stream, away from the solid boundary, is insensitive to the yaw angle of ± 5^0. However, beyond yaw angle of 5^0 the error in measured static pressure increases rapidly. The yaw characteristics of the surface tube in a two-dimensional flow without the presence of pressure gradient was examined by Sproston and Goksel. The comparison between the static pressure measured with the surface tube and the wall tap showed small differences (< 0.5% of the free stream dynamic head) within the range of yaw angles (up to 10 degrees) investigated. Also the difference in the two pressures was found to increase in the presence of pressure gradient. A detailed experimental investigation of the yaw characteristics of the surface tube in two and three-dimensional turbulent flows was performed in the present study. The surface static pressure measurements, on the flat plate centerline using plate 'B', were also obtained with the conventional method (i.e., with the wall

taps). The measurement locations of the surface taps in the flat plate centerline are shown in Fig. 3.2(a).

3.2.3.2 Three-Dimensional Flow

The wall shear stress and the surface static pressure measurements were obtained upstream of the airfoil leading edge of the test-model at four streamwise stations viz., stations 1 to 4. The measurement points ahead of the airfoil leading edge are shown in Fig. 3.14 (also see Fig.3.12). It should be mentioned here, that all the measurements on the flat plate surface of the test model were made on the right half of the test model (looking in the downstream direction). On the flat plate the Preston tube was first aligned parallel to the test-model centerline with its axis of rotation parallel to Z-axis and then the probe was rotated for the maximum value of the pressure. Corresponding to this setting of the Preston tube, the reading of the pressure and the angular position of the Preston tube were recorded. This procedure was followed at each measuring grid point. Proper care was taken to make sure that the Preston tube tip rested on the flat plate at each measuring point. This was essential because the pressure measured by the Preston tube at the wall is needed to evaluate the wall shear stress. The Preston tube tip contact with the flat plate surface was checked with an electrical circuit (Fig. 3.15) in addition to the visual inspection. In the electrical circuit method the contact of the Preston tube tip was ensured once the non-zero voltage was recorded on the digital voltmeter.

In the blade end-wall corner region, the Preston tube and the surface static pressure probe traverses were made at six streamwise

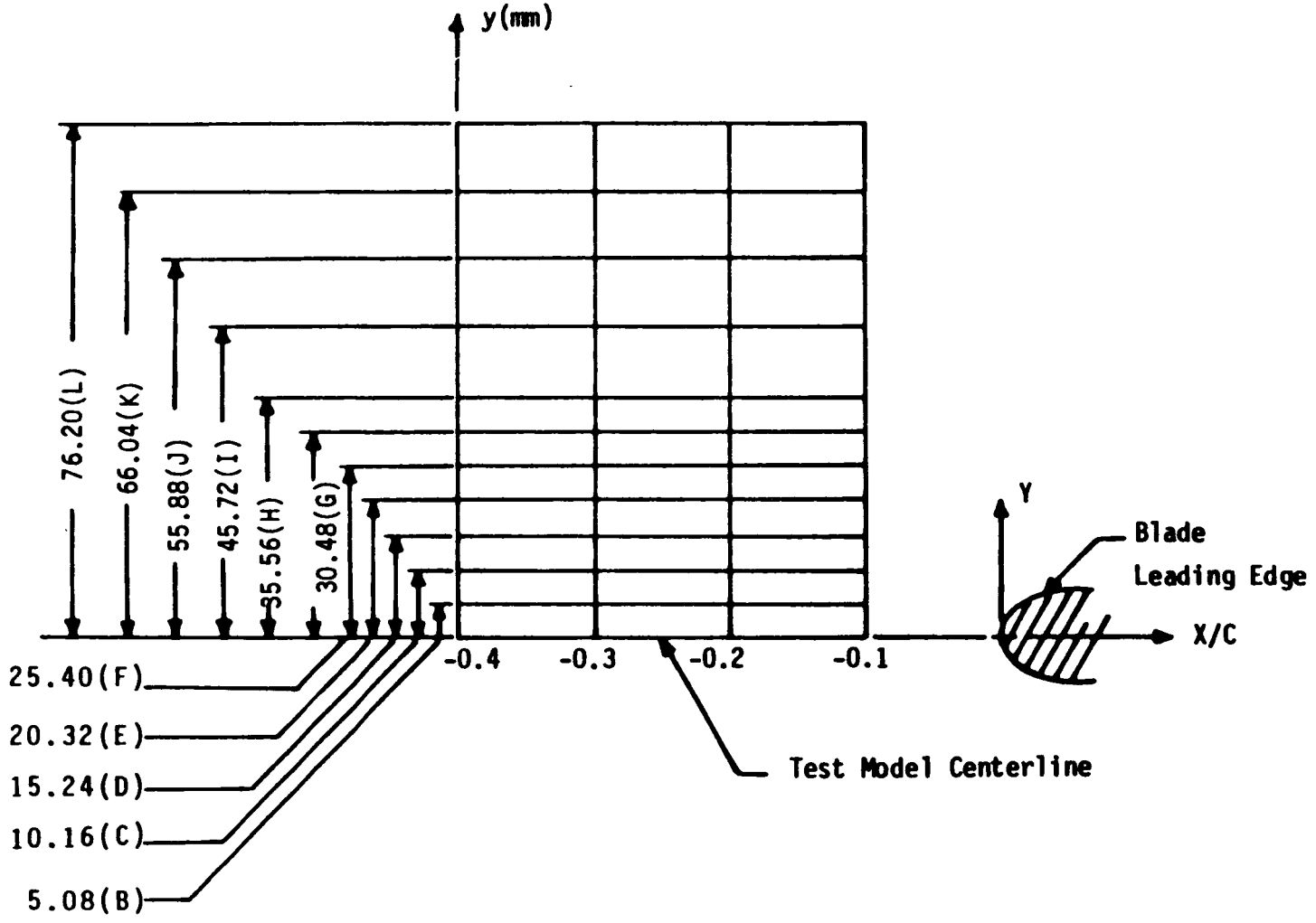

Fig. 3.14 Locations of Measurement Upstream of the Blade Leading Edge

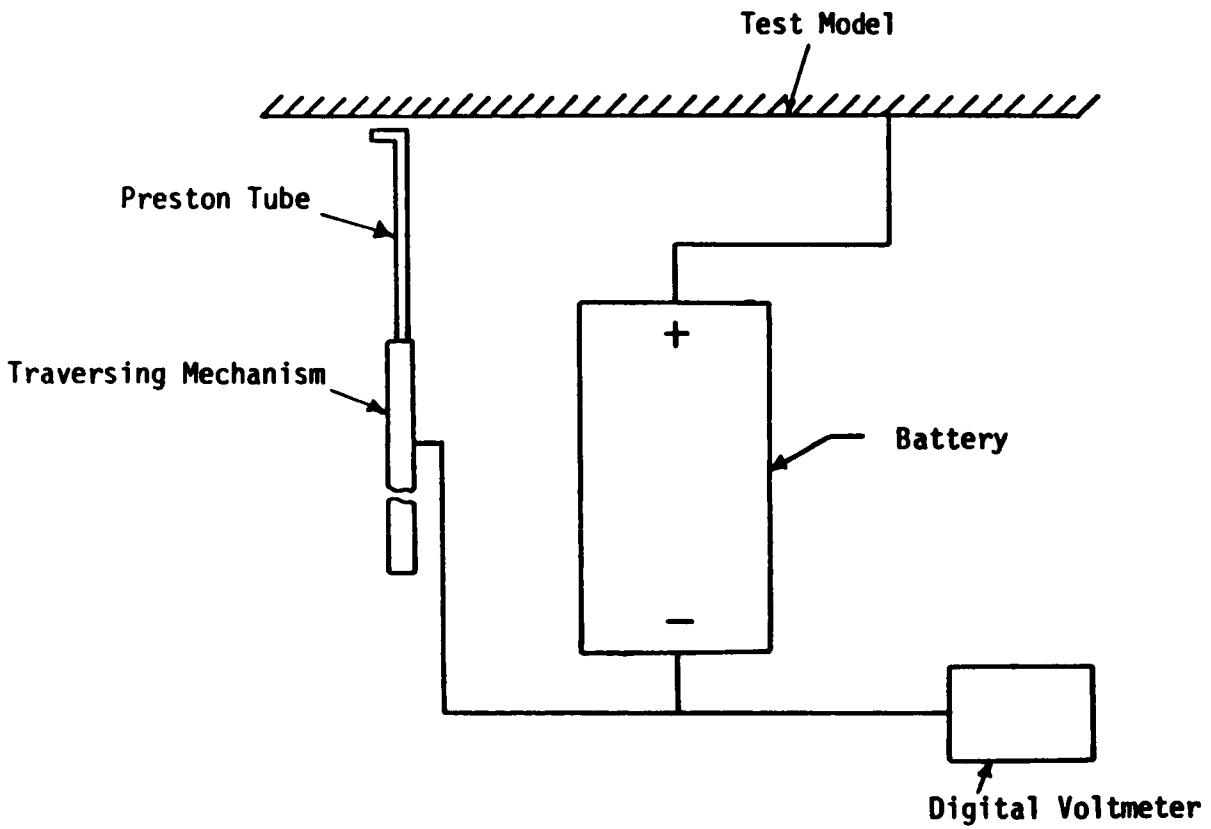

Fig. 3.15 Sketch Showing Line Diagram of Electrical Circuit to Check the Preston Tube Tip Contact With the Surface

stations, stations 5 to 10. The traverses in Y- and Z-directions ranged up to 76 mm from the test-model centerline. For the three-dimensional case the locations of measurement on the flat plate are shown in Fig. 3.16. In order to obtain adequate spatial resolution a large number of measuring points were selected near the corner line in the three-dimensional case as compared to the two-dimensional case. Figs. 3.17(a) and 3.17(b) show the measurement locations on the blade surface. Also, for the three-dimensional case proper precautions were taken to make sure that the Preston tube tip rested on the flat plate and the airfoil surface at each measuring location. On the airfoil surface additional precautions were necessary because of the surface curvature.

The Preston tube alignment procedure for the flat plate has already been described. On the airfoil surface the Preston tube tip was first made parallel to the flat plate (axis of rotation parallel to Y-axis) and then it was made tangential to the airfoil surface at the point of measurement making sure the tip touched the airfoil surface. The Preston tube was then rotated for the maximum pressure and, for this setting of the Preston tube, data was recorded for the pressure and its angular position.

In the blade end-wall corner region, detailed measurements of the wall static pressure were also obtained with the conventional technique. The interchangeable instrument Disk No. 2 at three streamwise stations, stations 5, 7 and 9, was used to acquire the surface static pressure data. The disk was also rotated at each streamwise station so that the information about the surface static pressure over large surface area could be obtained.

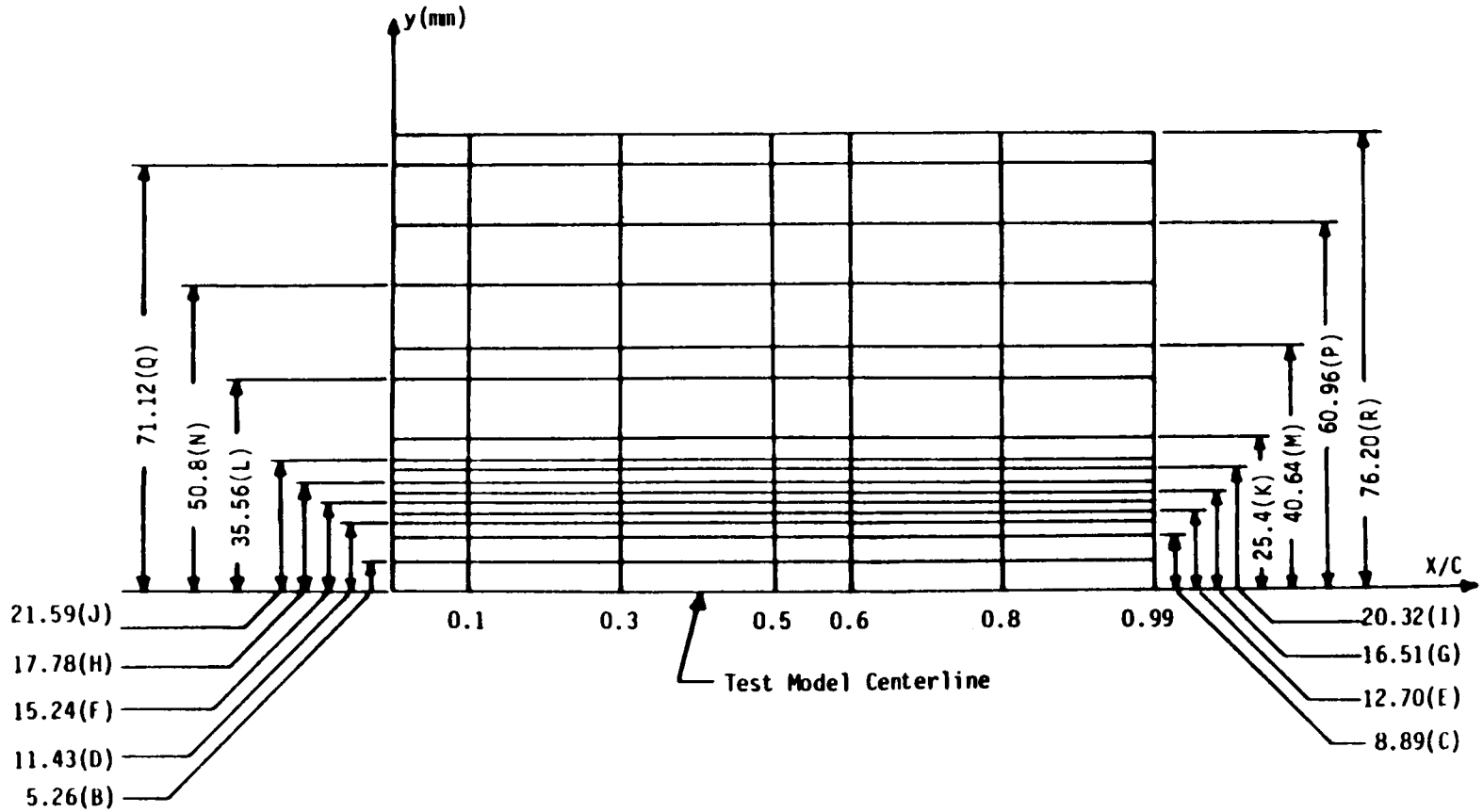

Fig. 3.16 Locations of Measurement on the Flat Plate Surface of the Test-Model in Corner Region

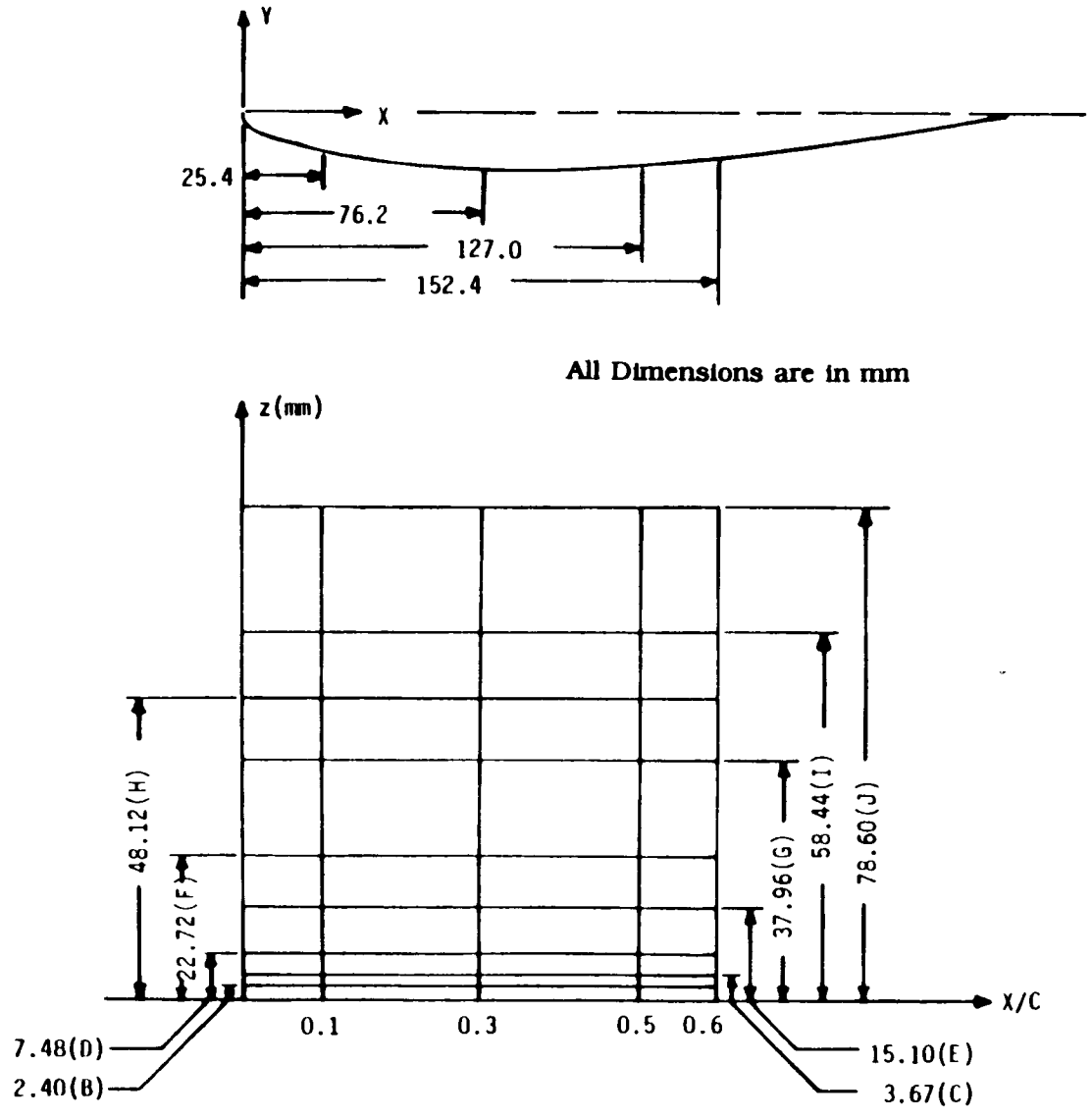

Fig. 3.17(a) Locations of Measurement on the Blade Surface of the Test-Model in Corner Region

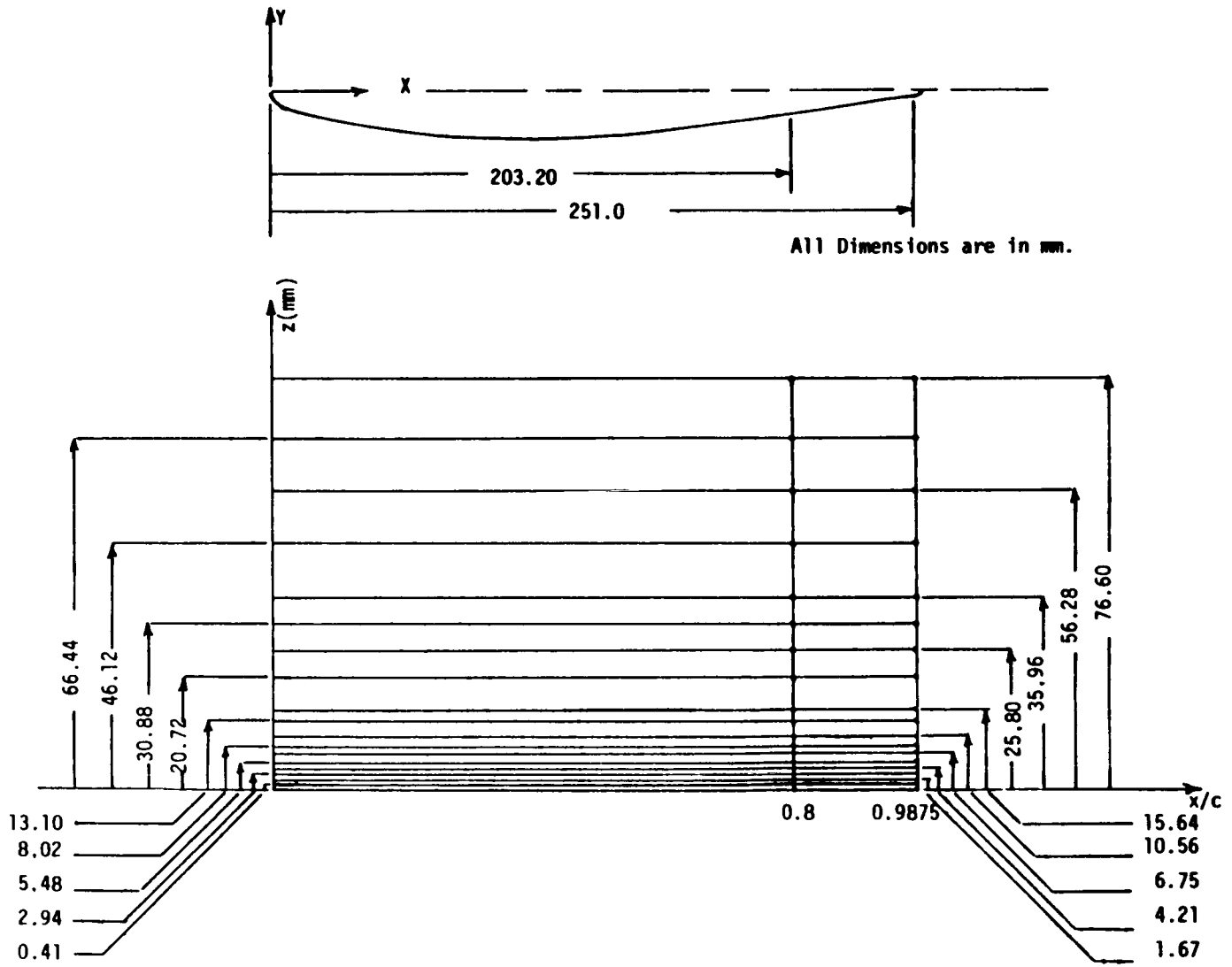

Fig. 3.17(b) Locations of Measurement on the Blade Surface of the Test-Model in Corner Region

In the second case (Case B without the turbulence generating grids) wall shear stress data were collected on both the surfaces of the test-model in the blade end-wall corner region. The Preston tube and the pitot-static probe traverses were made at four axial stations, station 5 and stations 7 to 9. The measurement locations on both surfaces in this case are the same as in Case A (see Figs. 3.16 and 3.17).

3.2.4 Calibration Equations of the Preston Tube and the Calculation Procedure

The magnitude of the wall shear stress was calculated using Patel's[87] two-dimensional calibration equations. These equations were discussed in Chapter II. Patel used various sizes of Preston tubes ranging from an outer diameter of 0.60 mm to 12.65 mm. In the present study the outer diameter of the Preston tube was 0.81 mm and was within the range of Preston tubes used by Patel. The Preston tube and the static pressure probe data were converted into units of the wall shear stress using proper conversion factors. First the value of the parameter x^* was calculated which is defined as,

$$x^* = \log_{10} (\Delta P d^2/4\rho v^2)$$

A suitable calibration equation was selected based on the magnitude of the parameter x^*, and the value of y^* was then calculated. Once the value of y^* was known, the value of τ_w could be calculated from the relation,

$$y^* = \log_{10} (\tau_w d^2/4\rho v^2)$$

The value of the free stream velocity (U_∞) was calculated from the recorded reference total pressure using the relation,

$$U_\infty = [2(P_t - P_a)_{ref}/\rho)^{0.5}$$

During the period of experimentation the atmospheric pressure and the temperature were recorded a number of times and their average values were used to calculate fluid properties (ρ and ν).

3.3 Wall Pressure Fluctuation and Wall Pressure-Velocity Correlation Measurements

3.3.1 Wall Pressure Fluctuation Intensity

The root-mean-square(RMS) value or the intensity of the wall pressure fluctuation was measured at four streamwise stations, stations 1, 5, 7 and 9, using the flush-mounted piezoresistive type pressure transducers. At streamwise station 1, x/D = - 8, the wall pressure fluctuation intensity was obtained only on the stagnation streamline. At the other three streamwise stations, stations 5,7 and 9, the wall pressure fluctuation intensity was measured at selected locations (Fig. 3.18) on the flat plate surface of the test-model in the blade end-wall corner region. The output of the pressure transducer was directly fed to a Masscomp computer. The analog output was digitized at a 20 KHz sampling rate and 100,000 samples were taken. The excitation voltage to the pressure transducers was supplied with the differential DC amplifier signal conditioning system (Model No. 7600A) supplied by Dynamics Division of Waugh Controls. The excitation voltage was front panel controlled on the signal conditioning system. In the present work the excitation voltage was set at 15 V DC. The signal conditioning system had a built-in 11 position filter switch. This switch had a capability of selecting a - 3 dB cutoff point from 1 Hz to a wideband position that made the - 3 dB frequency well above the highest desig-

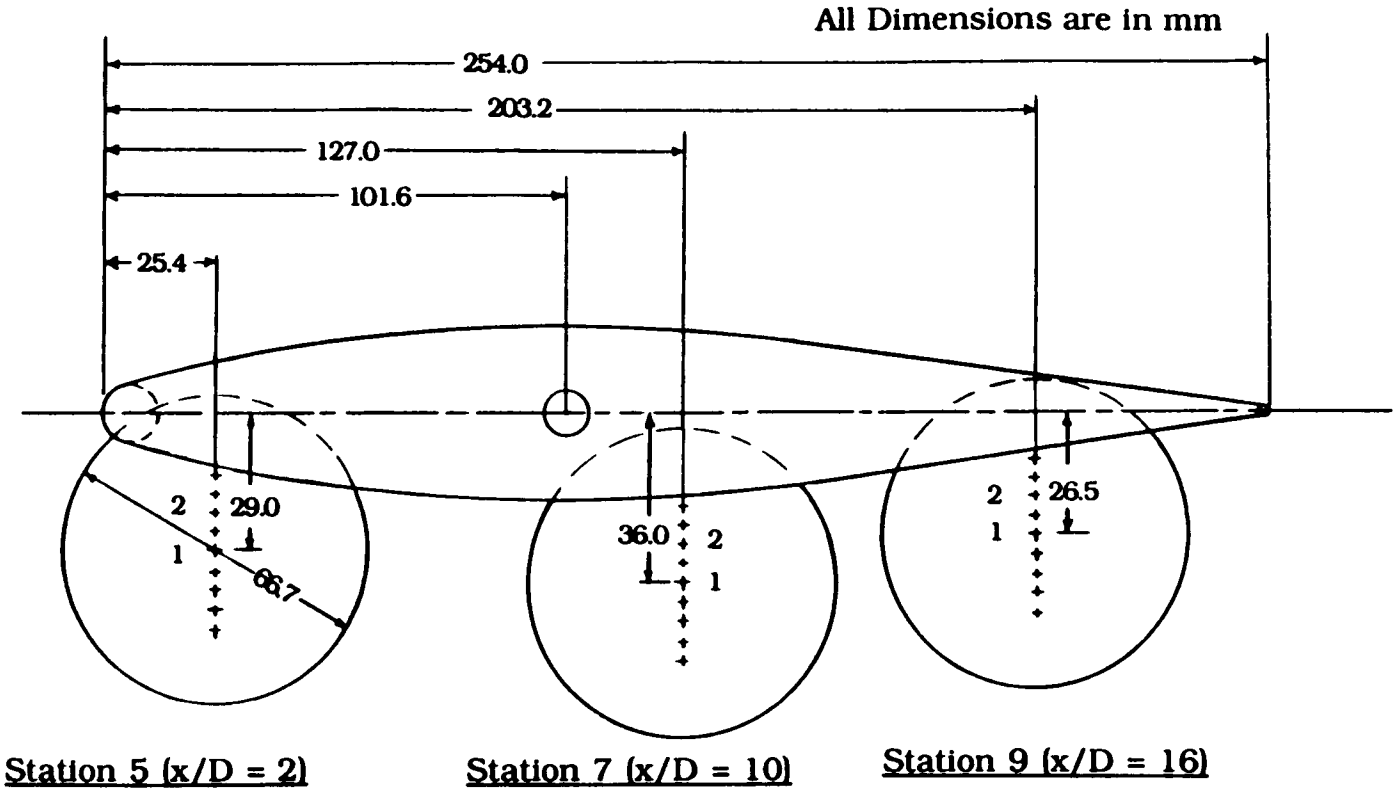

Note: (1) At each streamwise station pressure transducers are separated by 4 mm center to center.

(2) Pressure-velocity correlation measurements are obtained at locations marked ① and ② at different streamwise stations.

Fig. 3.18 Locations of Piezoresistive Type Pressure Transducers on the Flat Plate Surface in Corner Region

nated cutoff frequency. In the present study, the higher value of cutoff frequency used was 30 KHz. Table 3.5 presents specifications of the signal conditioning system as provided by the manufacturer. The amplified data of the wall pressure fluctuation obtained from the signal conditioning system was directly fed to the A/D (analog to digital) unit of the Masscomp mini-computer. The A/D unit having 16 channels which, in combination with an S/H (sample and hold) unit, had a capability of simultaneously sampling all the channels. The maximum throughput rate of the A/D with an S/H unit was 1 MHz.

3.3.2 Power Spectra of the Fluctuating Wall Pressure

The power spectral density function of the fluctuating wall pressure was obtained at different locations described earlier (see section 3.3.1) using a Fast Fourier Transform (FFT) technique. This technique is commonly used because computational time and cost can be significantly reduced compared to the direct Fourier series method. The power spectral density function, $\phi_{p_w}(f)$ at any frequency is related to the Fourier transform, $Xp_w(f,T)$ by the relation[137],

$$\phi_{p_w}(f) = (2/T) \mid Xp_w(f,T) \mid^2 \tag{3.3}$$

where $T = N/f_s$ is the finite time interval of the sample record $x_{p_w}(t)$ and N and f_s represent the number of samples and sampling rate, respectively. The Fourier transform of the sample record, $x_{p_w}(t)$ is given by,

$$Xp_w(f,T) = (1/f_s) \sum_{n=0}^{N-1} x_{p_w}(n) \exp[- i2\pi fn/f_s] \tag{3.4}$$

TABLE 3.5 Performance Characteristics and Specifications of Differential DC Amplifier Signal Conditioning System as Supplied by Manufacturer (Waugh Controls Corporation)

Parameter	Characteristics
A. Input	
1. Input Impedance	25 MΩ shunted by 500 pF
2. Source Impedance	Specifications met with up to a source impedance of 1 KΩ (10 KΩ operation permitted)
3. Overscale Input	± 30 V DC, or peak AC without damage
4. Input Bias Current	< 2 nA at 25^0C < 0.5 nA / ^{0}C
B. Tape Output	
1. Output Capability	± 10 V at 5 mA, limited to ± 15 V at 25 mA. short-circuit protected
2. Capacitive Loading	up to 0.1 μF, no instability
3. Output Impedance	1.0 Ω in series with 20 μH
4. Output Level	Adjustable from 0 V to ± 10 V
5. Output Zero Control	
(a) Adjustment Range	± 40 mv
(b) Resolution	± 0.5 mv
6. Zero Indicator	LED indicates the tape output zero status (a) Red if positive (b) Green if negative (c) off if within 1 mv of zero

TABLE 3.5 (Continued)

C. AC

(All AC Specifications are independent of gain steps or Variable gain setting)

1. Frequency Response	± 1% (DC to 10 KHz) ± 1 dB (10 KHz to 50 KHz) - 3 dB (above 100 KHz)
2. Setting Time	< 25 μs to 0.1% of final value
3. Overload Recovery Time	< 50 μs to 5% of full scale for any overload up to 10 times full scale input not exceeding ± 20 V DC or peak AC
4. Slewing Rate	3.7 V/μs, 20 V p-p output to 60 KHz

5. Noise

RTI	Bandwidth
5.0 μV rms	0.1 Hz to 100 KHz
3.0 μV rms	0.1 Hz to 50 KHz
2.0 μV rms	0.1 Hz to 10 KHz
4.0 μV p-p	0.1 Hz to 100 KHZ
1.0 μV p-p	0.1 Hz to 10 KHz
+ 200 μV rms	RTO

D. DC

1. Zero Drift (Constant Temperature)	± 2 μV RTI, ± 200 μV RTO ± 200 μV/vV(output offset)/8 hours after 1/2 hr. warmup
2. Temperature Coefficient of Drift	± 0.5 μV/^{0}C RTI, ± 100 μV/^{0}C RTO ± 100 μV/V/^{0}C of output offset
3. Linearity	± 0.005% of full scale at DC
4. Gain Accuracy	± 0.1% in calibrate position of the CAL switch

TABLE 3.5 (Continued)

5. Gain Stability	± 0.005% / 200 hours. ± 0.005% / ^{0}C
6. Zero Range	± 100 µV RTI of zero adjustment RTO set by output controls

E. Common-Mode

1. Rejection Ratio

	Source Impedance	
Gain	0 ohm	350 Ohm
1000	126 dB	120 dB
100	106 dB	100 dB
10	86 dB	80 dB
1	66 dB	66 dB

2. Operating Level	± 50 V DC from DC to 60 Hz. Decrease at a rate of 6 dB/Octave above 1 KHz. Limited to 1 V p-p up to 100 MHz
3. Overscale	± 75 V DC or peak AC without damage
4 Input Impedance	2000 MΩ shunted by 1.5 pF

The Fourier components at discrete frequencies, f_k are computed and related to $Xp_w(f,T)$ as follows,

$$Xp_w(k) = Xp_w(f_k,T)\ f_s = \sum_{n=0}^{N-1} x_{p_w}(n)\ \exp[-\ i2\pi kn/N] \qquad k = 0,1, \ldots ,N-1 \qquad (3.5)$$

where $f_k = kf_s/N$. The values of Fourier components are calculated at different frequencies, f_k using Eqn. 3.5 in FFT technique. Further details related to the FFT technique are given in reference[137]. In the present work, a standard FFT subroutine was used to calculate the values of $Xp_w(k)$[138]. Once the values of the Fourier components were known, the power spectral density functions at discrete frequencies were calculated using Eqn. 3.3

3.3.3 Wall Pressure-Velocity Correlations

The measurement of wall pressure-velocity correlations required information about the fluctuating velocity. The fluctuating velocity was measured with the single normal sensor hot wire probe. The correlation of the fluctuating wall pressure with the fluctuating velocity was measured at one streamwise station, station 1, upstream of the blade leading edge and three streamwise stations, stations 5,7 and 9, in the blade end-wall corner region. At each streamwise station in the corner region two locations were selected in the Y-direction where the pressure transducers were flush-mounted (Fig. 3.18). Corresponding to each Y-location the hot wire probe was traversed in the Z-direction covering a distance of approximately 30 mm. The wall pressure and velocity fluctuation data were simultaneously sampled at a 20 KHz

sampling rate. The number of samples recorded were 80,000 because of the space limitations of the floppy disk.

3.3.4 Data Processing for Wall Pressure Fluctuation Intensity, Power Spectral Density Function, and Wall Pressure-Velocity Correlation

The wall pressure and velocity fluctuation data were obtained in digitized form. The digitized data were first converted into units of volts using the conversion factor of the A/D unit. The A/D unit used had a 12 bit resolution. Therefore, for the voltage range selected, which was ± 5 volts, the conversion factor became 10/4096 volts/ digits. Once the digitized output was converted into volts further processing depended on the variable of interest. The various parameters of interest which were calculated are briefly described in this section.

3.3.4.1 Wall pressure Fluctuation Intensity

The digitized wall pressure output was converted into pressure units using an appropriate calibration constant (see Table 3.2) for the pressure transducer. The wall pressure fluctuation intensity was calculated from the relation,

$$(p'_w)^2 = \left(\sum_{1}^{N} (\tilde{p}_w)^2 \right)/N - (\bar{p}_w)^2 \qquad (3.6)$$

where $\bar{p}_w = \left(\sum_{1}^{N} \tilde{p}_w \right)/N$ and $\tilde{p}_w$ represent the mean and instantaneous values of the wall pressure, respectively. In Eqn. 3.6, N represents the total number of samples. The value of p'_w then gives the required wall pressure fluctuation intensity. The wall pressure fluctuation intensity was also calculated from the power spectrum. If $\phi_{p_w}(f)$ represents power spectral density function of wall pressure, then the total area

under the plot of power spectral density function versus frequency represents square of the wall pressure fluctuation intensity. Mathematically,

$$(p'_w)^2 = \int_o^\infty \phi_{p_w}(f)\, df \qquad (3.7)$$

The calculation of p'_w using Eqn. 3.7 gave a check on its value obtained from Eqn. 3.6.

3.3.4.2 Power Spectra of Wall Pressure Fluctuation

A general procedure to obtain the power spectral density function was described in section 3.3.2. The digitized wall pressure data were first converted into pressure units. The standard FFT subroutine was then used to obtain discrete Fourier components. Once the Fourier components were known, then the power spectral density function at discrete frequencies was calculated using Eqn. 3.3.

3.3.4.3 Wall Pressure-Velocity Correlation

The digitized wall pressure data were converted into pressure units as described earlier. The digitized output in volts from the hot wire was converted into the instantaneous velocity using King's law,

$$\tilde{E}_b^2 = A_1 + B_1 \tilde{U}^n \qquad (3.8)$$

where $\tilde{E}_b$ and $\tilde{U}$ are the instantaneous voltage output of hot wire and velocity, respectively. In Eqn. 3.8, A_1, B_1 and n are constants which were obtained by calibration of the hot wire. The calibration procedure for the hot wire is given in appendix A. The mean component of velocity was calculated using the relation,

$$U = \left(\sum_1^N \tilde{U} \right)/N \qquad (3.9)$$

Once the mean value of wall pressure and velocity were known, the wall pressure-velocity correlation was calculated from the relation,

$$\overline{p_w u} = \left(\sum_{1}^{N} \tilde{p}_w \tilde{U} \right)/N - \overline{p}_w U \qquad (3.10)$$

The correlation coefficient was calculated using the relation,

$$R_{pu} = \overline{p_w u}/p'_w u' \qquad (3.11)$$

where u' is the RMS value of the velocity fluctuation which was calculated like p'_w described earlier. Computer programs were written to calculate the various parameters described above and are presented in appendix B.

CHAPTER IV

RESULTS AND DISCUSSION ON COMBINED EFFECTS OF INITIAL ROUGHNESS AND FREE STREAM TURBULENCE ON THE TURBULENT BOUNDARY LAYER DEVELOPMENT

The mean velocity profiles, the surface static pressure and the wall shear stress measurements were obtained for four cases described in chapter III (section 3.2) at seven streamwise stations on a flat plate. The data obtained for these four cases was then used to analyze the influence of free stream turbulence on a turbulent boundary layer developing downstream of the distributed roughness strip in the vicinity of the plate leading edge. The results of the above mentioned investigation are presented and discussed here.

4.1 Boundary Layer Development in the Absence of a Transition Promoting Device and Free Stream Turbulence (Case 1)

A turbulent boundary layer developing with a natural transition and low level of free stream turbulence (usually present in wind-tunnels) is considered ideal and is well documented in the literature. Therefore, this case was investigated first so that the other cases could be compared against this ideal case. For such an ideal case, similarity in mean velocity profiles at different streamwise locations is attained if the velocity defect non-dimensionalized by the local friction velocity, $(U_e-U)/u^*$, is plotted against z/δ[56,139], where U_e and u^* are local free stream velocity and friction velocity, respectively, and δ is the local boundary layer thickness. The mean velocity profiles at four streamwise locations (viz., at x1 = 366.0 mm, 518.4 mm, 620.0 mm,

and 823.2 mm) on $(U_e-U)/u^*$ and z/δ axes are shown in Fig. 4.1(a). Four streamwise locations are chosen mainly to minimize overlapping of the data points. The velocity profiles are clearly observed to be self-similar except at x = 366 mm. This deviation from self-similarity can possibly be because the boundary layer has not yet attained its fully-developed state. The mean velocity profiles in the inner law variables, at seven streamwise locations, are shown in Fig. 4.1(b). The values of friction velocity (u^*) used in Fig. 4.1, described above, were calculated from the local wall shear stress measured with the Preston tube. The solid lines in Fig. 4.1(b) represent the logarithmic law of the wall written as

$$u^+ \equiv U/u^* = 1/K \ln z^+ + B \qquad (4.1)$$

where $z^+ = zu^*/\nu$, and K and B are constants with the values as described earlier (section 3.2). The law of the wall, in general, is observed to exist in a region $z^+ < 250$ and results agree with Eqn. 4.1 with a small change in the value of B. A larger shift from the solid line at x1 = 366 mm, compared to that at the other measurement locations, again suggests some deviation from its fully-developed state as was observed in Fig. 4.1(a).

The skin friction coefficient (C_f) measured with the Preston tube and its comparison with the C_f values calculated from Clauser's[96] technique, using the mean velocity profile data in the inner region, is shown in Fig. 4.2. The skin friction coefficient values were also calculated by using empirical relations proposed by other investigators.

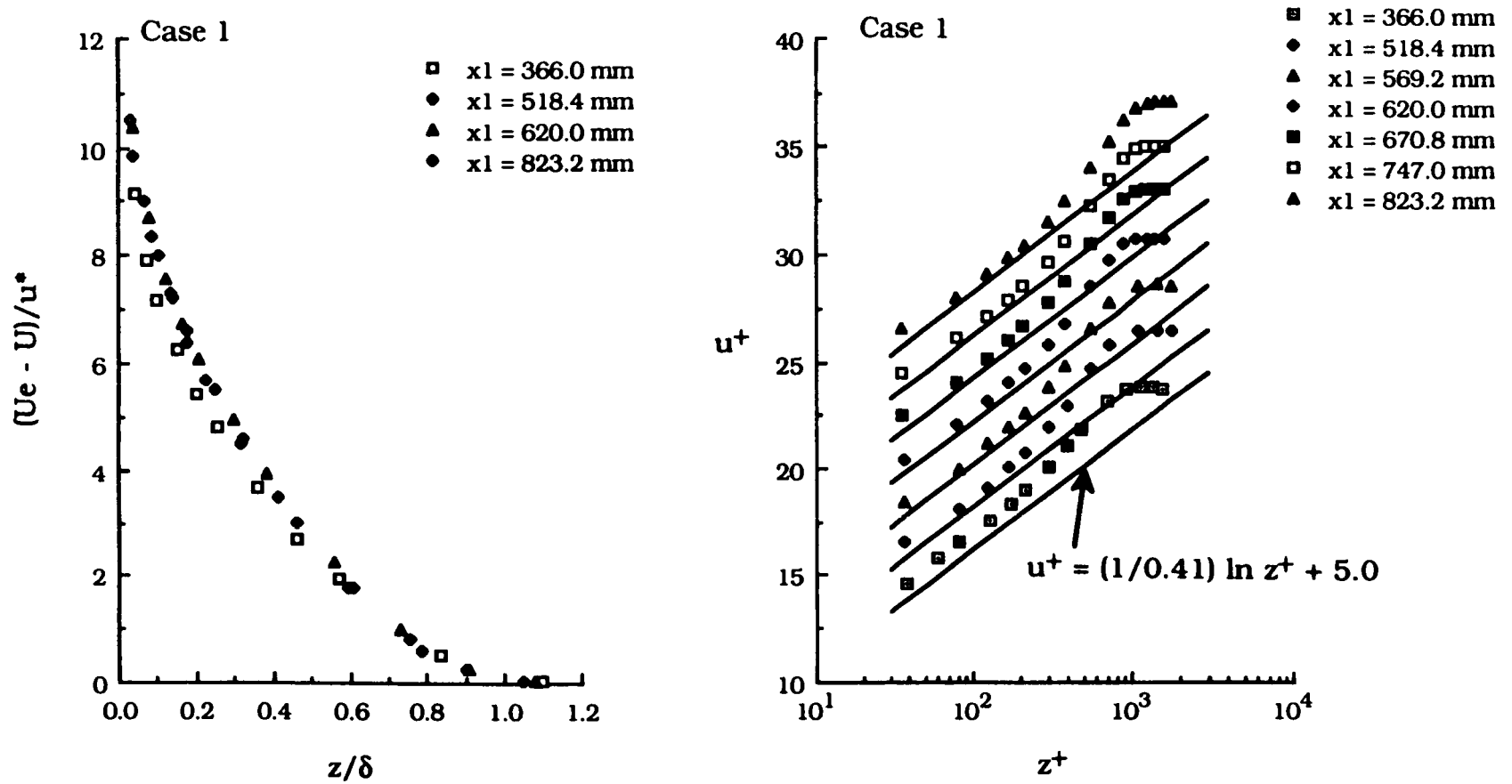

(a) Velocity-Defect Plot

(b) Logarithmic-Law Plot

(Note: Ordinate Scale Refers to Lowest Profile. Also Ordinate Scale Shifted by 2 Units for Second Profile Onwards)

Fig. 4.1 Development of Mean Velocity Profiles for Case 1

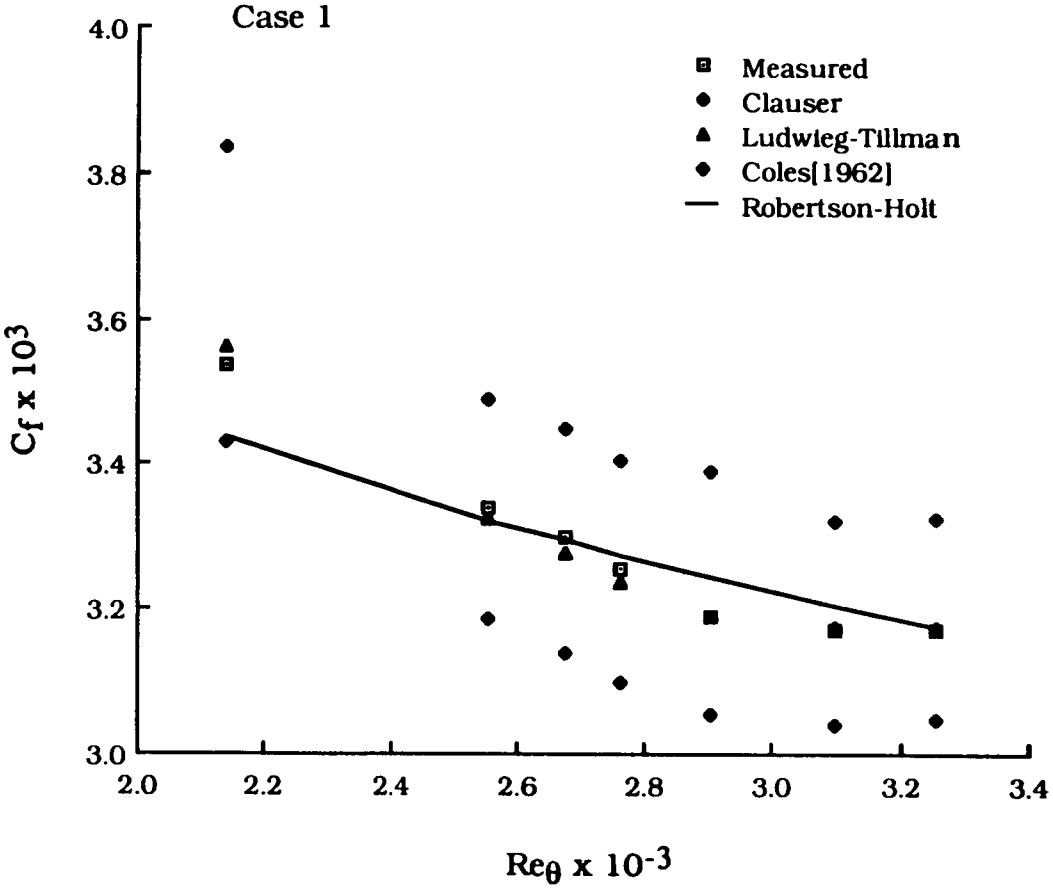

Fig. 4.2 Variation of C_f With Re_θ for Case 1

These empirical relations are

Ludwieg-Tillman[140]: $C_f = 0.246\ Re_\theta^{-0.268}\ 10^{-0.678H}$ (4.2)

Coles[141]: $C_f = 0.3\ \exp(-1.33H)/(\log_{10} Re_\theta)^{1.74} + 0.31H$ (4.3)

Robertson and Holt[63]: $C_f = (4.4 + 3.8 \log_{10} Re_\theta)^{-2}$ (4.4)

The values of C_f calculated from Eqns. 4.2-4.4 are also shown in Fig. 4.2. The measured C_f values compare well (maximum difference < 1.5%) with the values obtained from Eqn. 4.2 and Eqn. 4.4. The values of C_f calculated using Eqn. 4.3 are consistently smaller (≈ 4%). The C_f values obtained with Clauser's method are consistently larger (≈ 5%).

The variation of the boundary layer integral parameters δ, δ^*/δ and δ/θ with streamwise distance is shown in Fig. 4.3. The values of δ calculated from Eqn.3.1 are found to be in good agreement with the values obtained from the velocity profiles corresponding to U/U_e = 0.995. Clauser[139] noted, that the usual boundary layer thickness (δ) was not a well defined thickness. Therefore, the boundary layer thickness should be defined such that it could be determined mainly from the parameters of the universal plot. He further noted, that the integral expression defined as

$$\Delta = \delta \int_0^\infty (U_e - U)/u^*\ d(z/\delta) \quad (4.5)$$

showed the required property. The integral parameter Δ is known as Clauser's integral thickness. For a zero pressure gradient turbulent boundary layer, the value of Δ/δ was reported to be 3.6[139]. In the present study the average calculated value of Δ/δ is 3.8. In Fig. 4.3

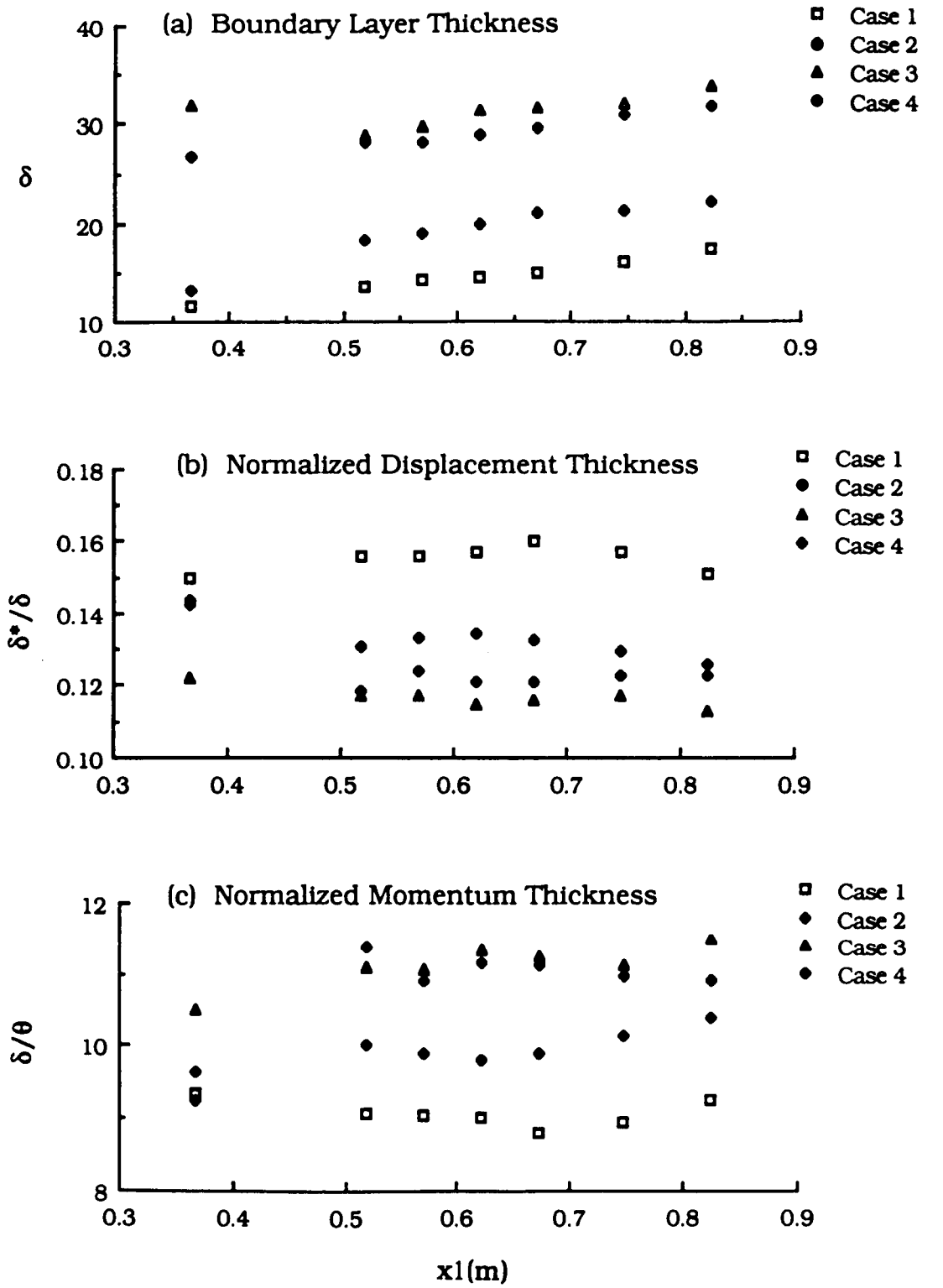

Fig. 4.3 Variation of Boundary Layer Parameters as a Function of Streamwise Distance

other cases are also shown for comparison and will be discussed later. The boundary layer data for four cases investigated is presented in Table 4.1.

Fig. 4.4 shows the variation of Clauser's shape parameter (G), shape factor ($H = \delta^*/\theta$), and Coles's wake profile parameter (Π). The Clauser's shape parameter is defined as

$$G = \int_0^\infty [(U - U_e)/u^*]^2 \, d(z/\Delta) = (1 - 1/H) \, (2/C_f)^{0.5} \qquad (4.6)$$

The average value of G = 7.15 (see Fig. 4.4(a)) is obtained in the present investigation. Clauser[139] reported a value of G = 6.8 for a constant pressure turbulent boundary layer. In Fig. 4.4 other cases investigated are also shown for the comparison and will be discussed later.

The variation of the boundary layer integral parameters for the four cases, with Reynolds number based on momentum thickness, is shown in Fig. 4.5. In Fig. 4.5(c) values of δ/θ obtained from an empirical relation reported by Robertson and Holt[63], written as

$$\delta/\theta = 8.22 + 0.475 \log_{10} Re_\theta \qquad (4.7)$$

are also included. The values of δ/θ obtained in the present study were consistently smaller (by maximum of 10%) than the values predicted from Eqn. 4.7. The variation with Re_θ of Clauser's shape parameter (G), shape factor (H), and Coles's wake profile parameter (Π) for the four cases is shown in Fig. 4.6. The value of H was also calculated from an empirical relation reported by Robertson and Holt[63]

$$H = 1.09 + 0.40/(0.72 \log_{10} Re_\theta - 1.0) \qquad (4.8)$$

TABLE 4.1 Details of Mean Flow Parameters for Four Cases

Case 1 : Natural Transition, No Grids

x1 (mm)	δ (mm)	θ (mm)	$C_f \times 10^3$	H
366.0	11.6	1.243	3.536	1.396
518.4	13.6	1.502	3.339	1.410
569.2	14.2	1.569	3.301	1.412
620.0	14.6	1.621	3.254	1.414
670.8	15.0	1.703	3.191	1.414
747.0	16.2	1.811	3.173	1.407
823.2	17.5	1.893	3.173	1.398

Case 2 : Natural Transition With Grids

x1 (mm)	Tu_∞	δ (mm)	θ (mm)	$C_f \times 10^3$	H
366.0	0.0172	13.2	1.368	3.626	1.383
518.4	0.0155	18.4	1.621	3.473	1.348
569.2	0.0153	19.0	1.745	3.443	1.349
620.0	0.0149	19.9	1.788	3.436	1.349
670.8	0.0144	21.0	1.888	3.362	1.345
747.0	0.0139	21.3	1.947	3.340	1.343
823.2	0.0136	22.2	2.038	3.323	1.340

TABLE 4.1 (Continued)

Case 3 : Initial Roughness, No Grids

x1 (mm)	δ (mm)	θ (mm)	$C_f \times 10^3$	H
366.0	31.8	3.026	3.369	1.285
518.4	29.0	2.616	3.347	1.299
569.2	29.8	2.693	3.323	1.301
620.0	31.4	2.773	3.298	1.300
670.8	31.7	2.824	3.271	1.300
747.0	32.2	2.895	3.221	1.303
823.2	33.8	2.944	3.269	1.303

Case 4 : Initial Roughness and Grids

x1 (mm)	Tu_∞	δ (mm)	θ (mm)	$C_f \times 10^3$	H
366.0	0.0172	26.7	2.887	3.347	1.316
518.4	0.0155	28.2	2.817	3.207	1.313
569.2	0.0153	28.4	2.869	3.183	1.315
620.0	0.0149	28.9	2.951	3.184	1.315
670.8	0.0144	29.5	2.984	3.169	1.314
747.0	0.0139	30.9	3.049	3.140	1.314
823.2	0.0136	32.0	3.077	3.196	1.311

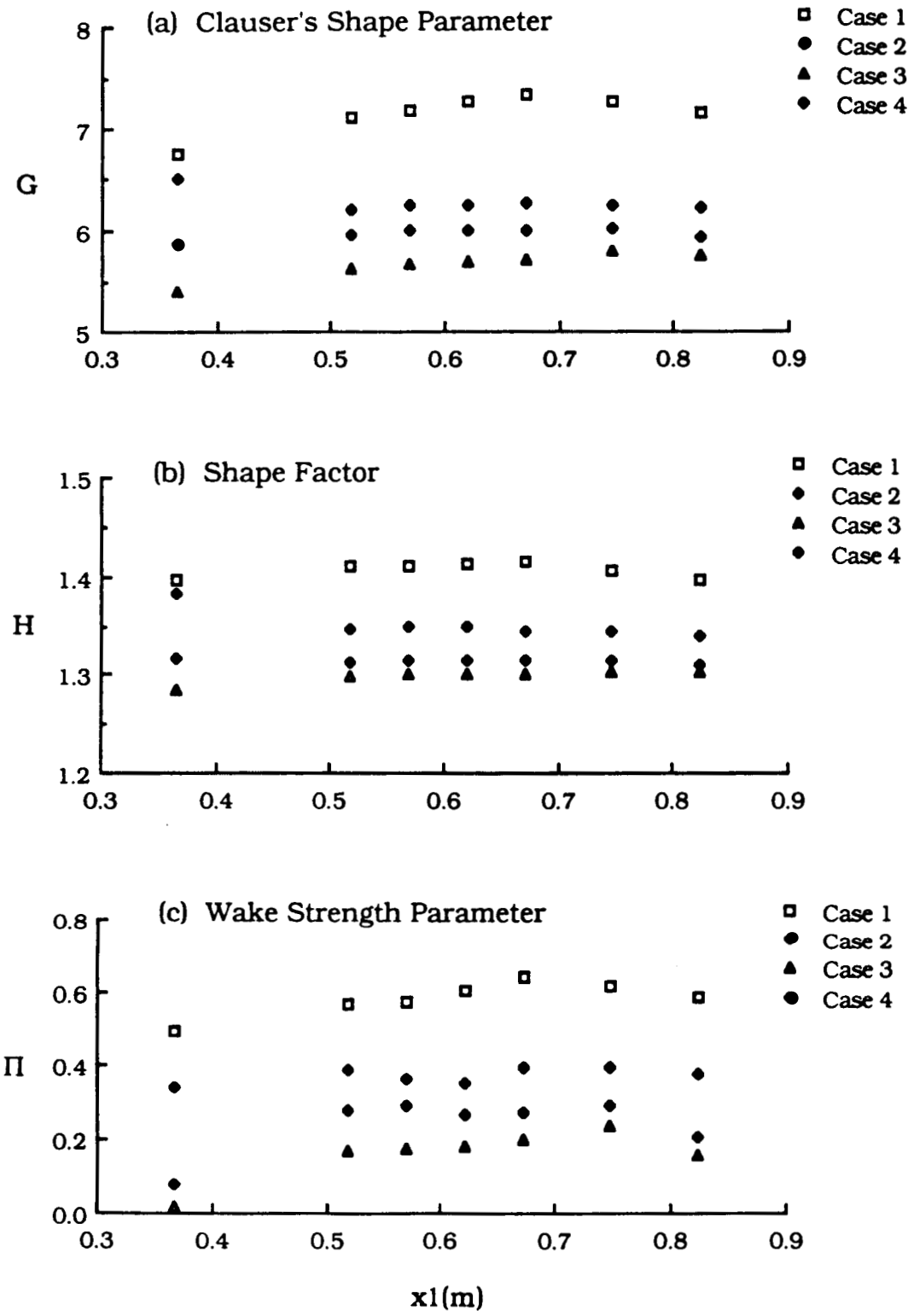

Fig. 4.4 Variation of Boundary Layer Parameters as a Function of Streamwise Distance

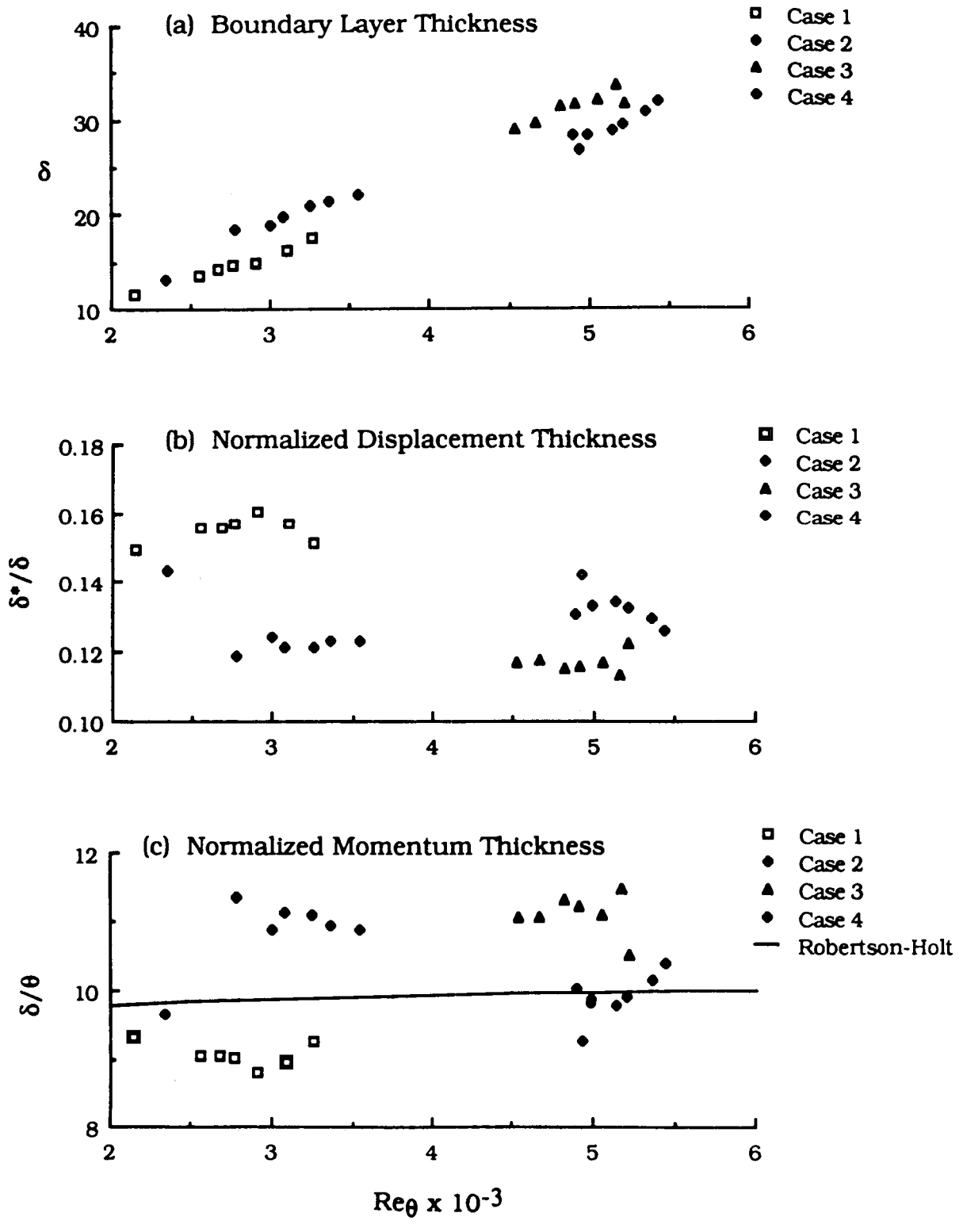

Fig. 4.5 Variation of Boundary Layer Parameters With Re_θ

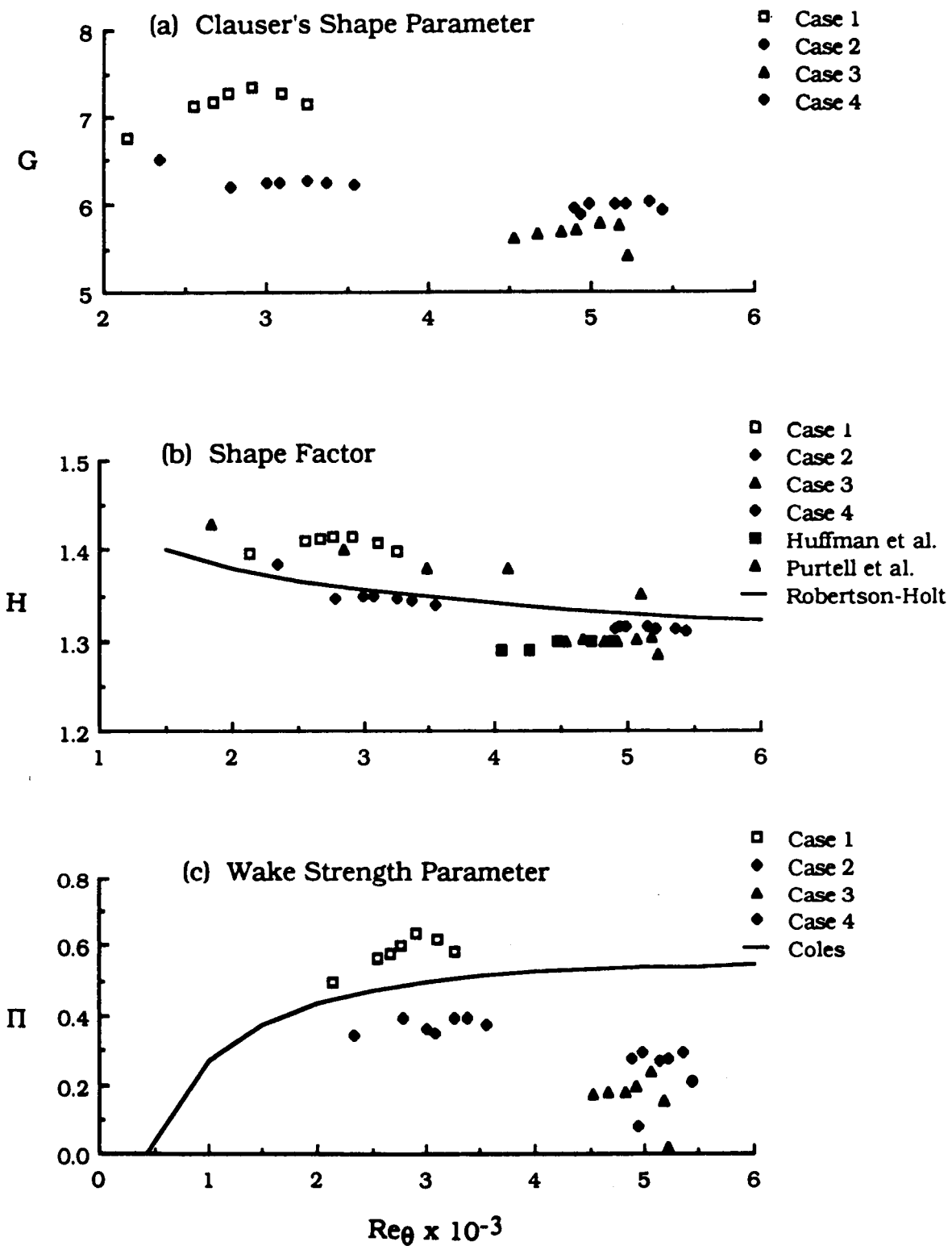

Fig. 4.6 Variation of Boundary Layer Parameters With Re_θ

The values of H obtained from Eqn. 4.8 are shown as a solid line in Fig. 4.6(b). In general, Eqn. 4.8 predicts lower values (≈ 3%) compared to the values obtained in the present investigation. In Fig. 4.6(c) the solid line corresponds to Coles's empirical relation

$$\Pi = 0.55[1 - \exp(- 0.243\xi^{0.5} - 0.298\xi)] \qquad (4.9)$$

where $\xi = Re_\theta/425 - 1.0$

The values of Π obtained in the present study are generally higher compared to those predicted from Eqn. 4.9.

4.2 Turbulent Boundary Layer Development With Natural Transition and the Turbulence Generating Grids (Case 2)

Fig. 4.7(a) shows mean velocity profiles at different streamwise stations, in the presence of increased free stream turbulence, on $(U_e - U)/u^*$ and z/δ, axes. The velocity profiles are observed to be self-similar except at x1 = 366 mm. In this case also, as in case 1, the boundary layer appears to have not reached its fully-developed state at x1 = 366 mm. The mean velocity profiles, in inner law variables at different streamwise locations, are shown in Fig. 4.7(b). The region in which law of the wall exists has not changed with the increased free stream turbulence level compared to case 1.

The comparison of mean velocity profiles non-dimensionalized by local free stream velocity (U_e), for four cases at four streamwise locations, is shown in Fig. 4.8. The other cases (viz., cases 3 and 4) are also shown in Fig. 4.8 for comparison purposes and will be discussed later (see sections 4.3 & 4.4). The mean velocity profiles are observed to be fuller compared to case 1 at each streamwise location.

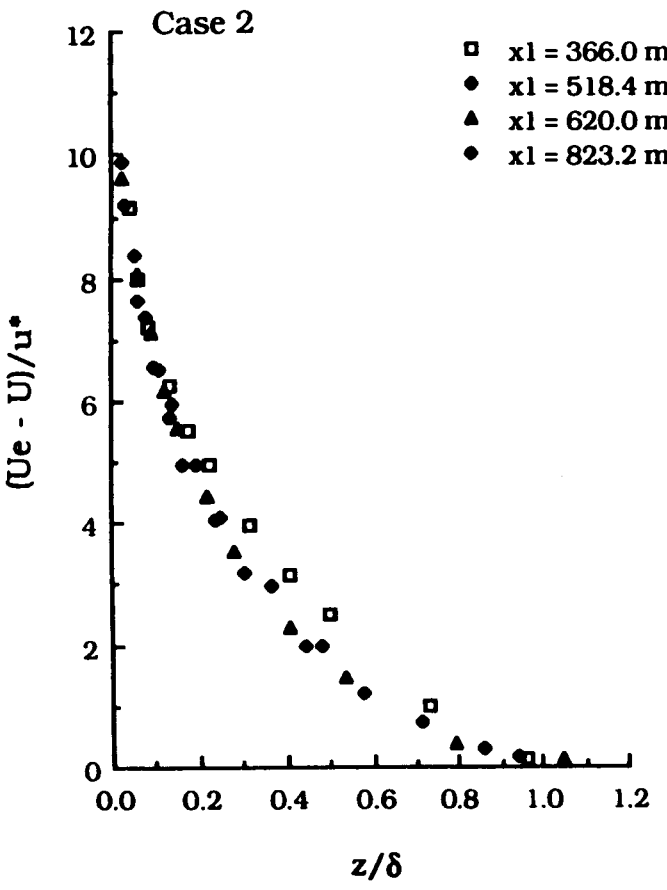

(a) Velocity-Defect Plot

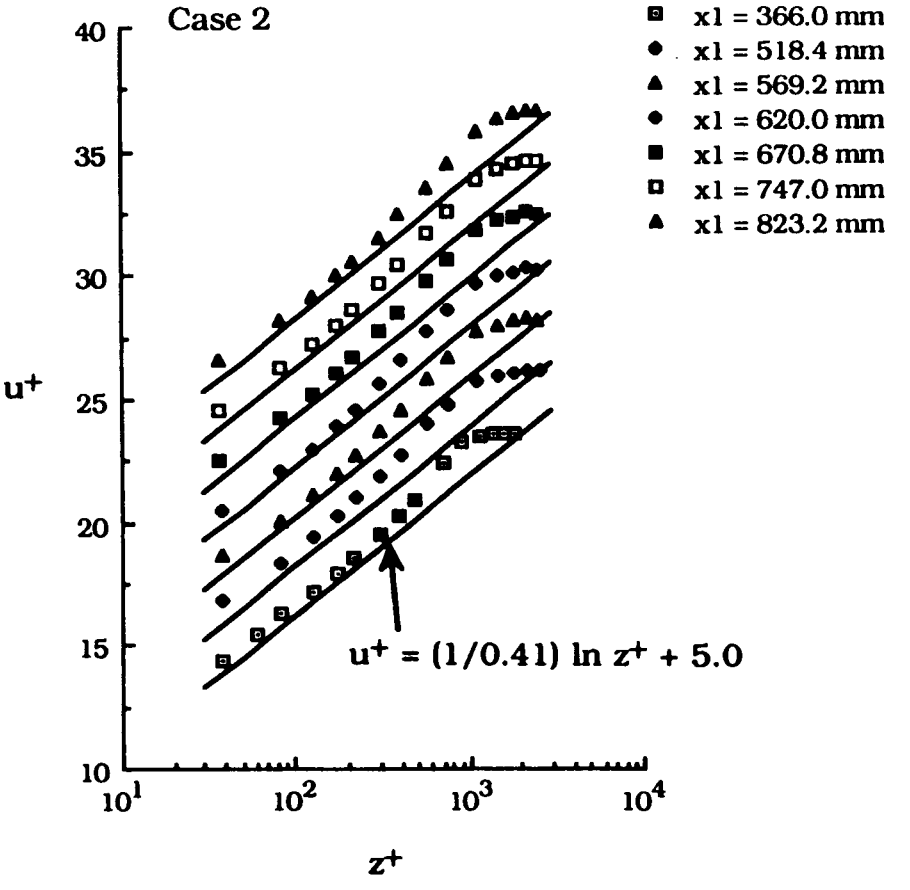

(b) Logarithmic-Law Plot

(Note: Ordinate Scale Refers to Lowest Profile. Also Ordinate Scale Shifted by 2 Units for Second Profile Onwards)

Fig. 4.7 Development of Mean Velocity Profiles for Case 2

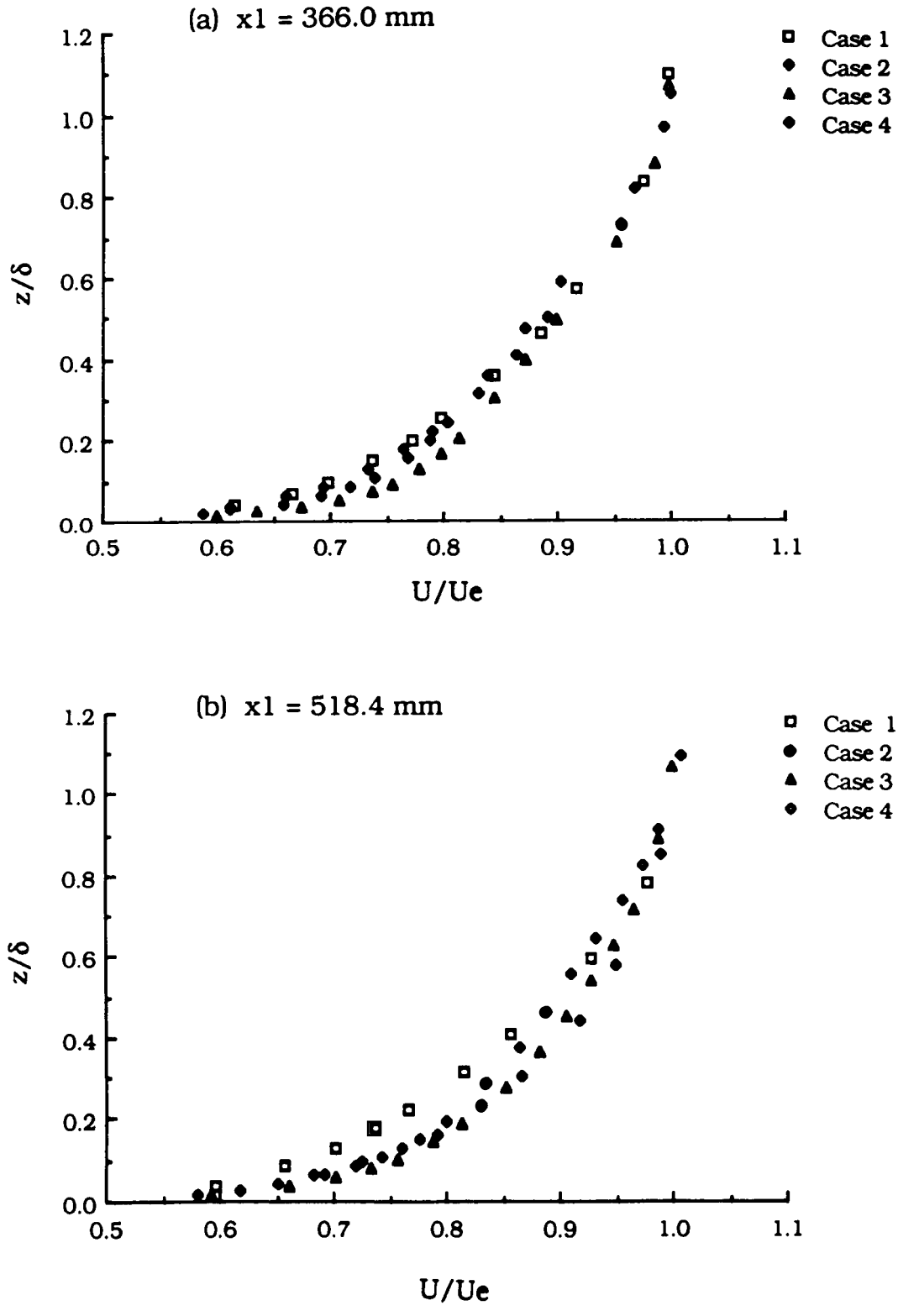

Fig. 4.8 Comparison of Non-Dimensional Mean Velocity Profiles

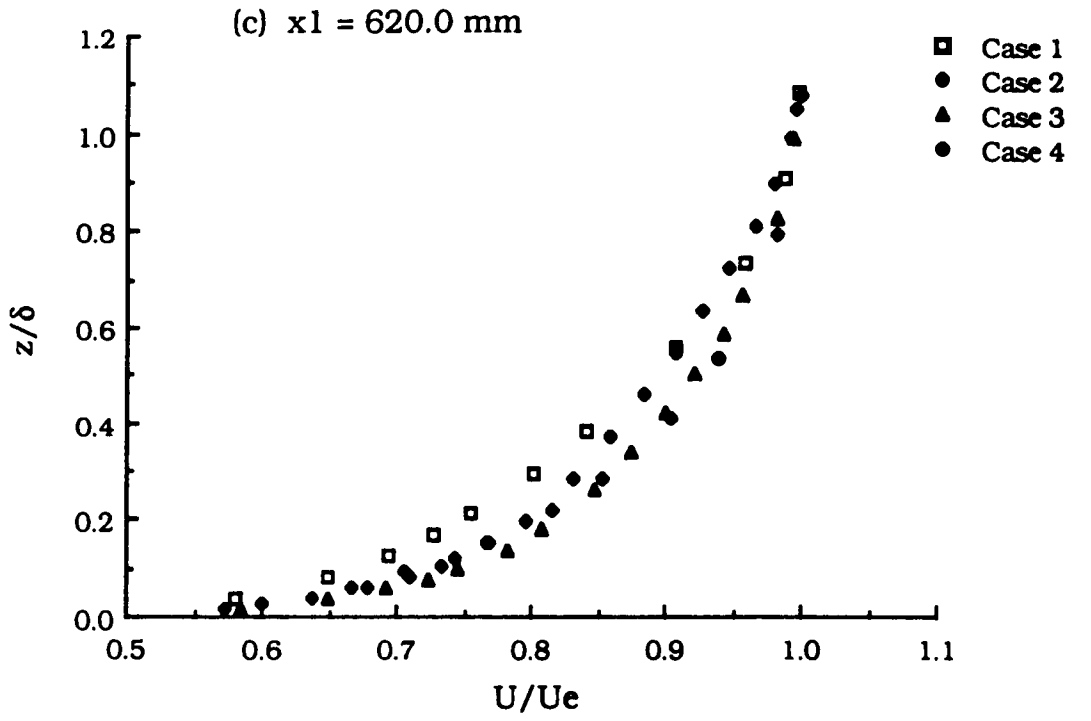

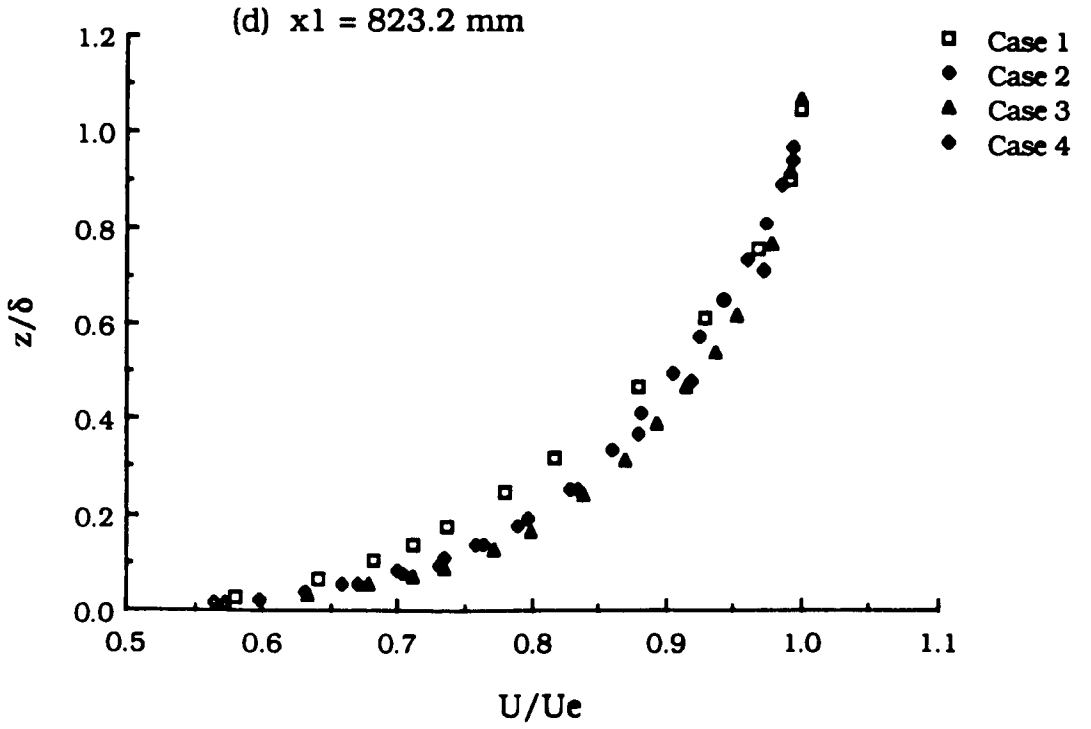

Fig. 4.8 (Contd.) Comparison of Non-Dimensional Mean Velocity Profiles

The fullness of velocity profile implies larger velocity gradient at the wall and, therefore, increased wall shear stress. This trend of increased wall shear stress due to the fullness of velocity profiles is in good agreement with the measured values of wall shear stress (see Fig. 4.12).

The comparison of velocity-defect profiles for four cases at four streamwise stations is shown in Fig. 4.9. Cases 3 and 4 will be discussed in sections 4.3 and 4.4, respectively. The influence of increased free stream turbulence is to decrease the velocity-defect. Similar observations i.e., fullness of velocity profiles and decrease in velocity-defect because of the increase in free stream turbulence, were reported earlier by Evans[60].

Fig. 4.10 shows the comparison of velocity profiles, for four cases at four streamwise locations, in inner law variables. In case 2, the wake component is observed to decrease as compared to case 1 which is in agreement with the calculated value of the wake profile parameter, Π (see Fig. 4.4(c)). Earlier studies by other investigators for example, Evans[60] and Raghunathan & McAdam[68] have reported similar influences of increased level of free stream turbulence. The decrease in wake component and velocity-defect can be attributed to the increased mixing in the outer region due to the increased level of the free stream turbulence.

The comparison of C_f values at various streamwise locations by different methods is shown in Fig.4.11. The Ludwieg-Tillman relation (Eqn. 4.2) predicts closer values (within 3%), whereas the differences with Clauser's method are within 4% to 6%. The comparison of C_f values at the same streamwise locations, measured with the Preston tube

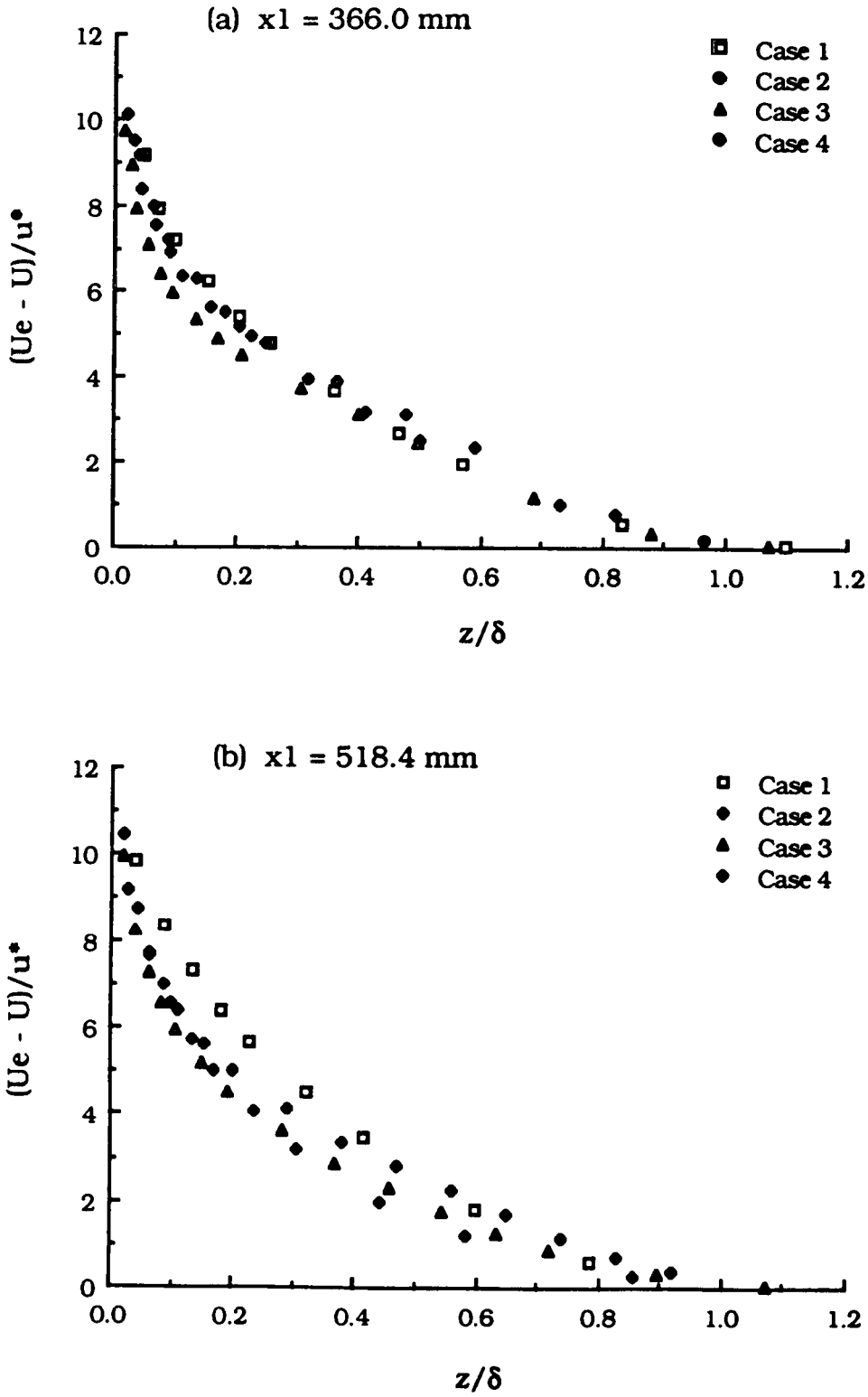

Fig. 4.9 Comparison of Mean Velocity Profiles on Velocity-Defect Plot

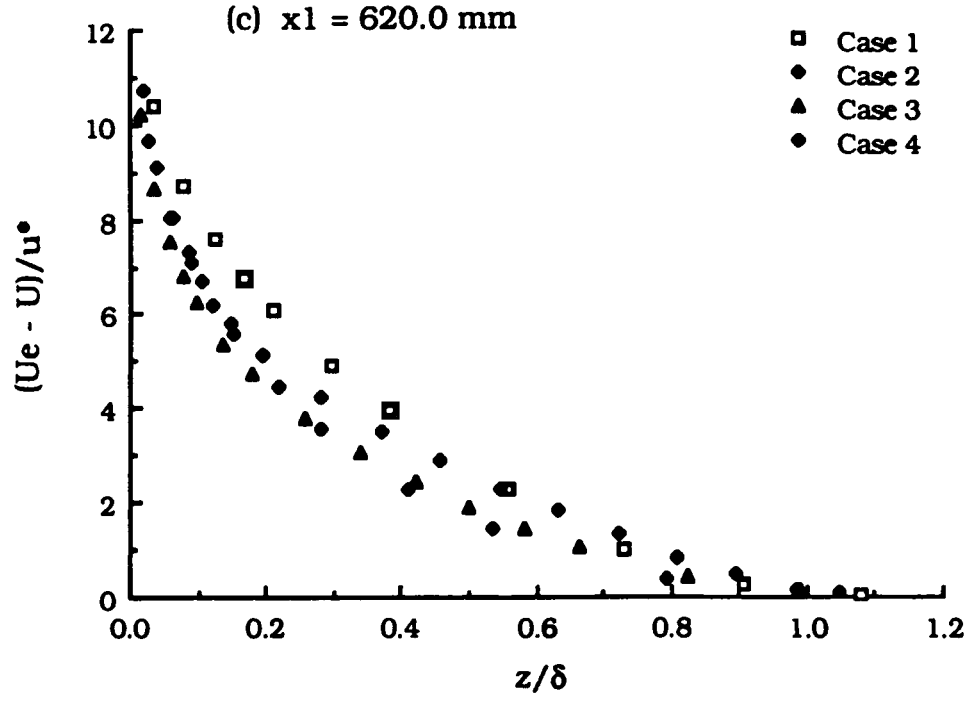

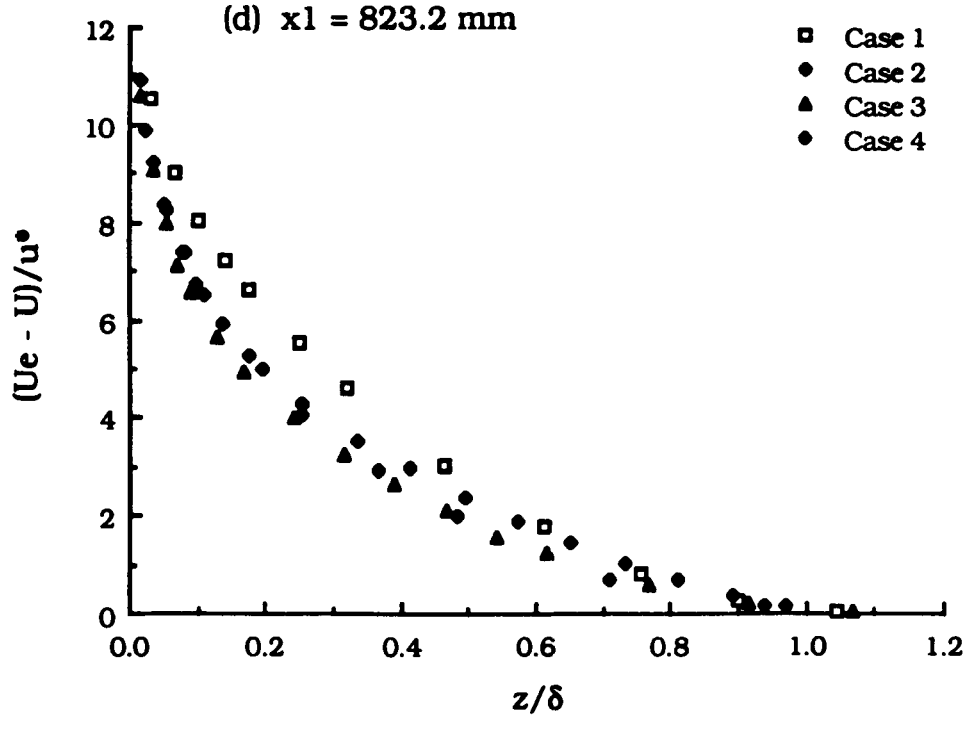

Fig. 4.9 (Contd.) Comparison of Mean Velocity Profiles on Velocity-Defect Plot

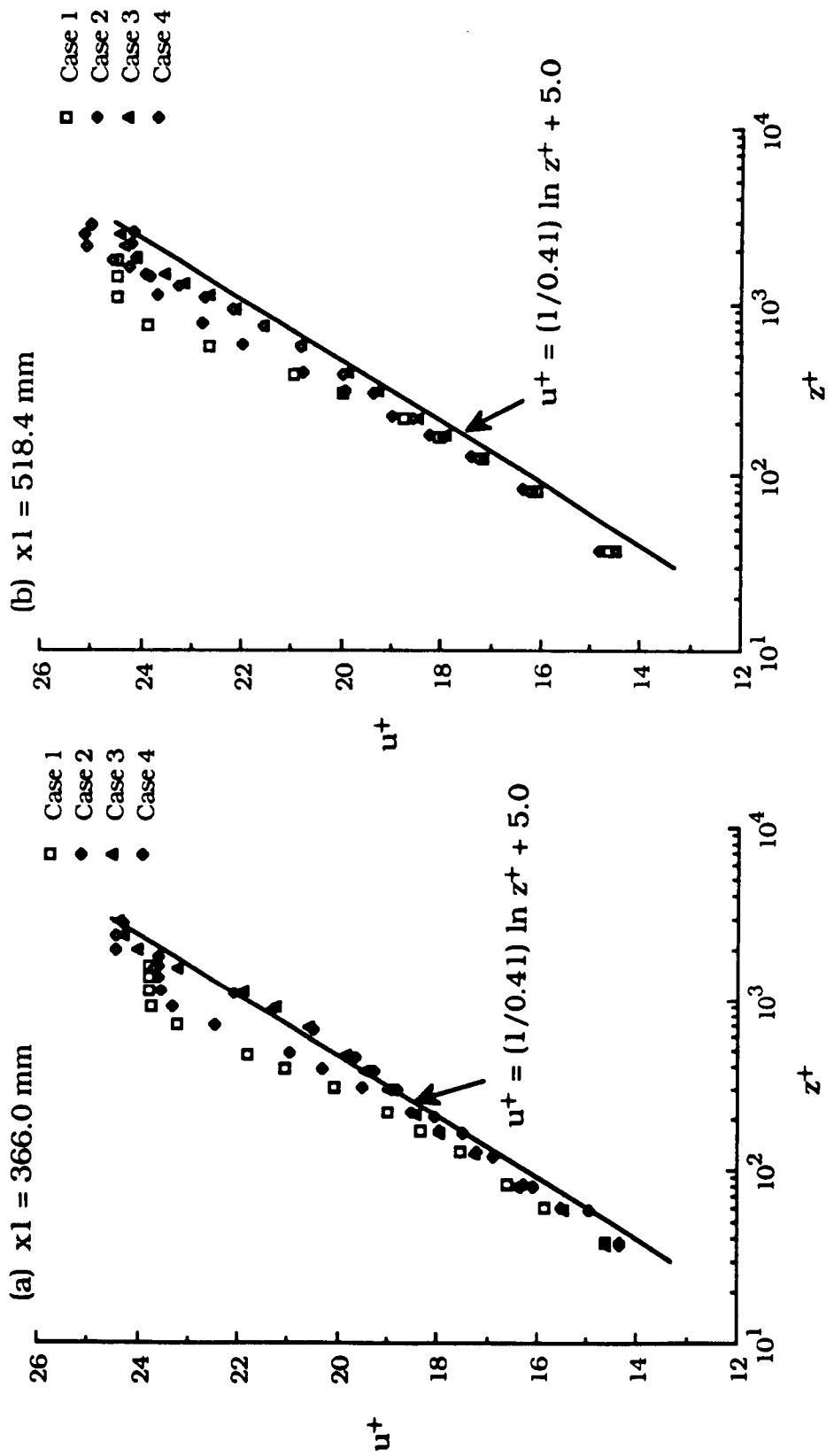

Fig. 4.10 Comparison of Mean Velocity Profiles on Logarithmic-Law Plot

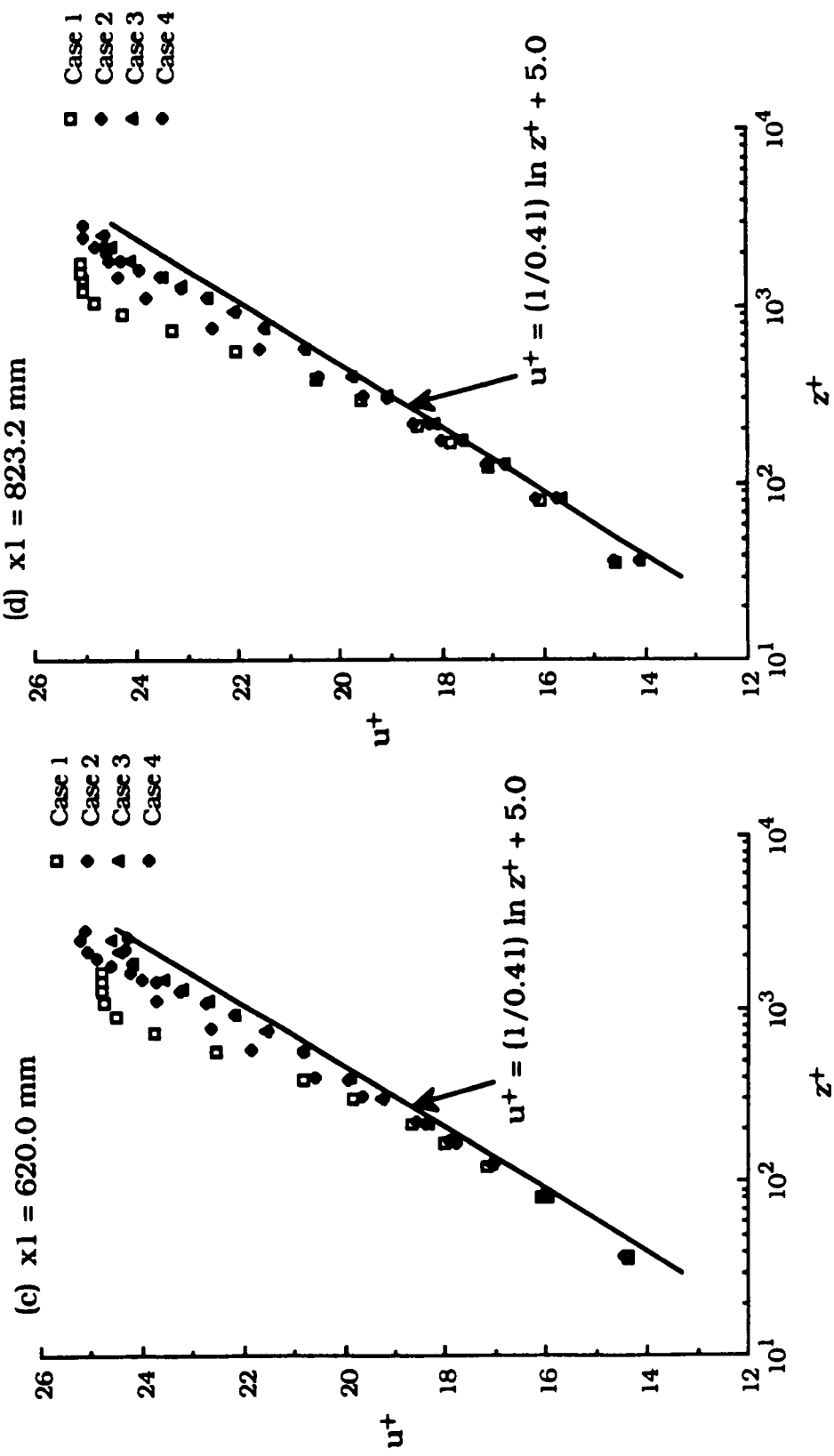

Fig. 4.10 (Contd.) Comparison of Mean Velocity Profiles on Logarithmic-Law Plot

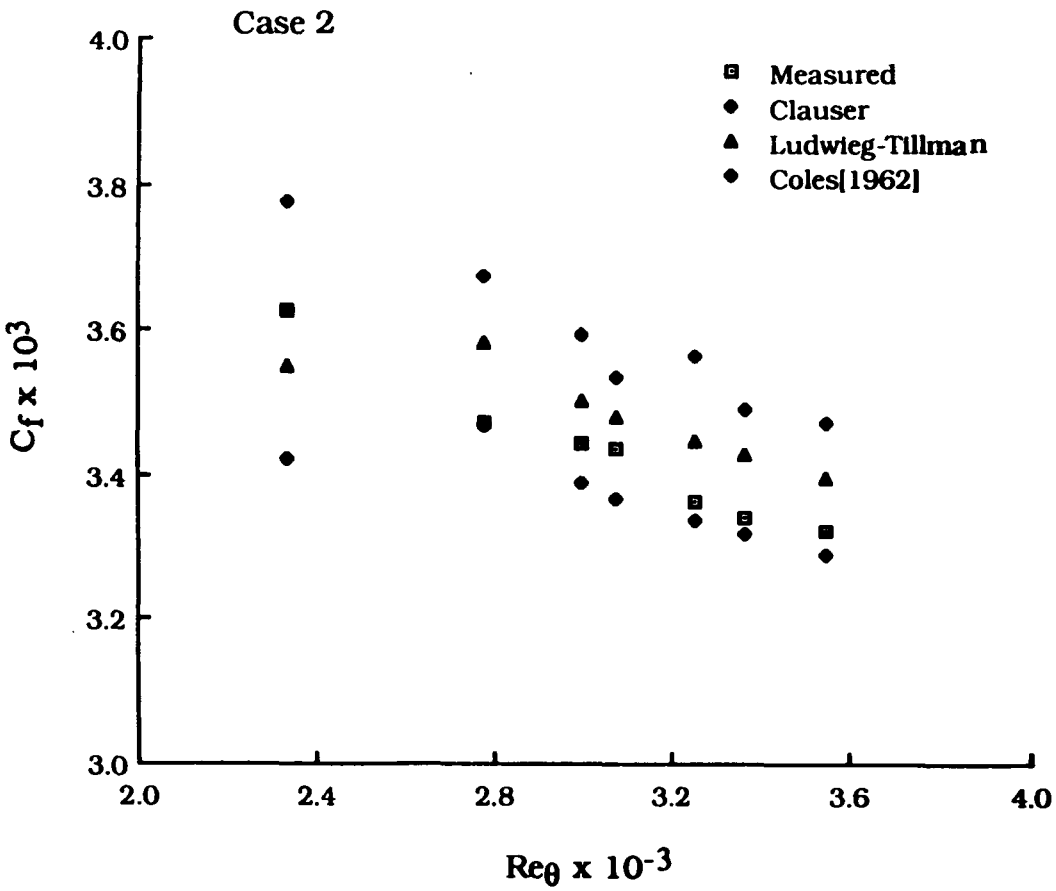

Fig. 4.11 Variation of C_f With Re_θ for Case 2

for four cases, is shown in Fig.4.12(a). The comparison of C_f with Re_θ for the four cases is shown in Fig. 4.12(b). The increase in the value of C_f because of the increased free stream turbulence level as compared to case 1 is ≈ 5%. Bradshaw[142] proposed an empirical relation (reported by Raghunathan & McAdam[68]) to evaluate increase in C_f value due to the increase in free stream turbulence as

$$\Delta C_f/C_{f0} = 3.2\, Tu_\infty \qquad (4.10)$$

where C_{f0} is the value corresponding to the zero turbulence level case. C_f values obtained in the present study are found to be in good agreement with the values predicted by Eqn. 4.10. The recent studies of Raghunathan & McAdam[68] and Hancock & Bradshaw[69] have shown a non-linear effect on C_f at low levels of free stream turbulence. For a free stream turbulence in the range $0 < Tu_\infty < 0.04$, Raghunathan & McAdam[68] proposed an empirical relation (Eqn. 2.16) for evaluating change in C_f.

The C_f values predicted by Eqn. (2.16) are smaller than the measured values. No significant changes in $\Delta C_f/C_{f0}$ at different streamwise locations are observed implying an independence of the change in C_f on Re_θ with the increase in free stream turbulence level. Similar observations were reported by other investigators[68,69].

At the same streamwise location, the increase in δ for case 2 compared to case 1 in the present study is approximately 35% (see Fig. 4.3(a)). The increase in δ observed at the same streamwise location can be due to the shift in the origin of the boundary layer. It is well established in the literature that the increase in free stream turbulence level leads to early transition and an upstream shift of the ori-

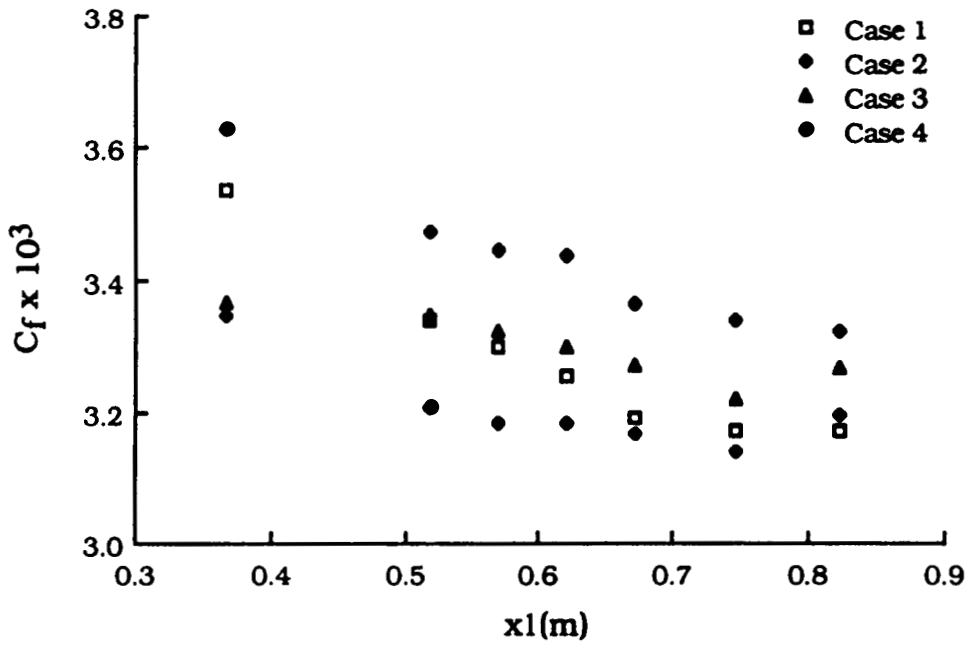

(a) Variation of C_f as a Function of Streamwise Distance

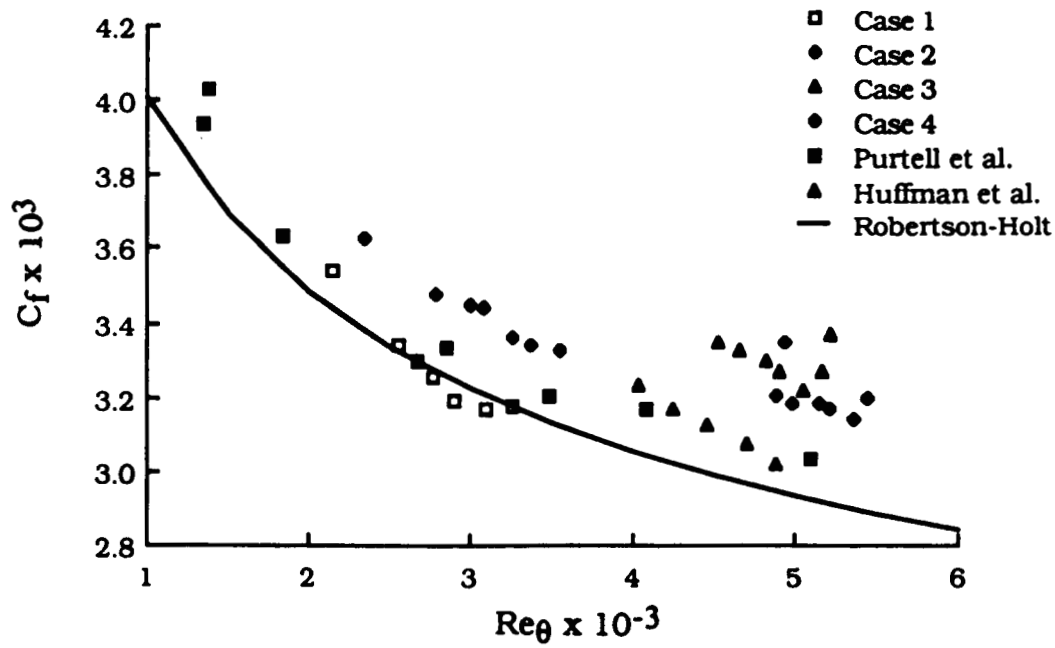

(b) Variation of C_f With Re_θ

Fig. 4.12 Variation and Comparison of Skin Friction Coefficient

gin of the turbulent boundary layer. Therefore, it would be more appropriate to compare the variation of δ with Re_θ in the two cases. It is observed that at the same value of Re_θ the value of δ is higher in case 2 compared to its value in case 1 (Fig. 4.5(a)). At the same streamwise distance, the non-dimensional value of the displacement thickness (δ^*/δ) is observed to decrease with the introduction of free stream turbulence (Fig. 4.3(b)). The decrease in δ^*/δ on the average is $\approx$ 22%. The main reason for this decrease in δ^*/δ is because δ increases much more than δ^* as the turbulence level is increased. The value of δ/θ increased in case 2 compared to case 1 (Fig. 4.3(c)). The average increase in δ/θ is found to be $\approx$ 22%. The comparison of results obtained in the present investigation with the values of δ/θ obtained from empirical relation, Eqn. 2.12, proposed by Raghunathan and McAdam[68] suggests that Eqn. 2.12 underestimates the changes in δ/θ because of the increase in the free stream turbulence level.

The value of G is observed to decrease due to the presence of free stream turbulence, the average decrease being $\approx$ 13% (Fig. 4.4(a)). The results obtained in the present study compare well with the values obtained from an empirical relation reported by Raghunathan and McAdam[68]

$$\Delta G/G_0 = -1/3\ (u'_\infty/u^*) \qquad (4.11)$$

where G_0 corresponds to the zero free stream turbulence case. The average value of G $\approx$ 6.2 (less than the value of 7.15 of case 1) again suggests that the mean velocity profiles are far from the self-similar state of case 1.

The values of H decreased compared to case 1. The decrease in the value of H is ≈ 5%. The value of H was also calculated from an empirical relation (Eqn. 2.14) proposed by Raghunathan and McAdam. The values obtained in the present measurements are little higher compared to those predicted by Eqn. (2.14).

Fig. 4.4(c) shows the effect of increased free stream turbulence on Π at the same streamwise locations. The decrease in the value of Π compared to case 1 is in agreement with the decrease in wake component observed in Fig. 4.10. The value of Π was also calculated using empirical relation (Eqn. 2.15) proposed by Raghunathan and McAdam. Present measurements suggest that Eqn. 2.15 underestimates the effect of Tu_∞ on changes in Π.

To summarize, the effect of increased free stream turbulence on various mean flow parameters, it can be stated that the trends in the variation of different mean flow boundary layer parameters is similar to those reported by other investigators (see Table 2.1).

4.3. Influence of Initial Roughness on the Turbulent Boundary Layer Development Without the Turbulence Generating Grids (Case 3)

In this section the results of a boundary layer developing downstream an initially distributed roughness strip and its comparison with case 1 are discussed.

Fig. 4.13(a) shows velocity profiles at four streamwise locations on a velocity-defect plot. The self-similarity of velocity profiles is quite evident except at the first station (located ≈ 300 mm from the end of roughness strip). The velocity profiles in inner wall variables are shown in Fig. 4.13(b) for seven streamwise locations. The law of the

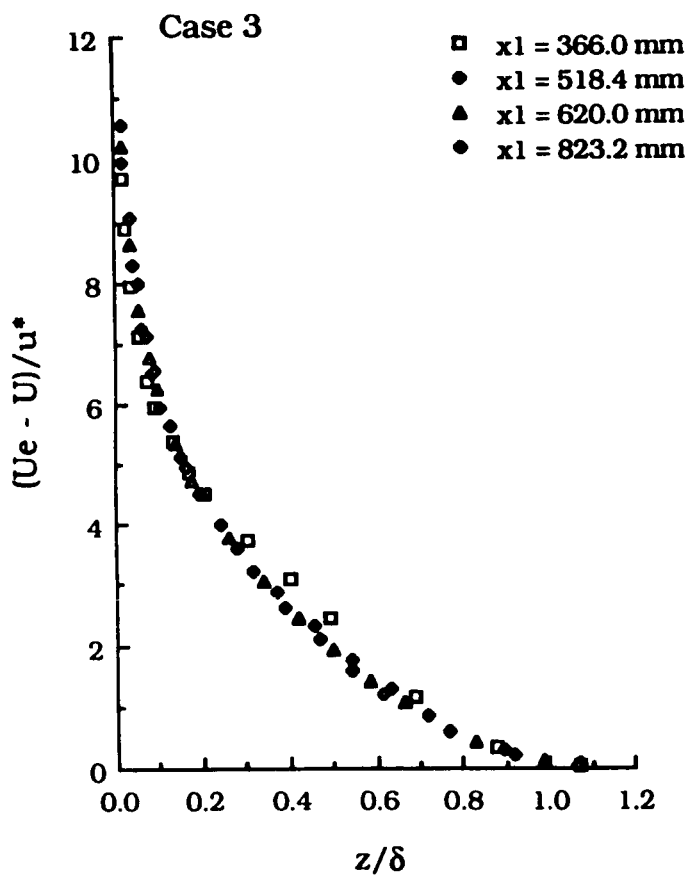

(a) Velocity-Defect Plot

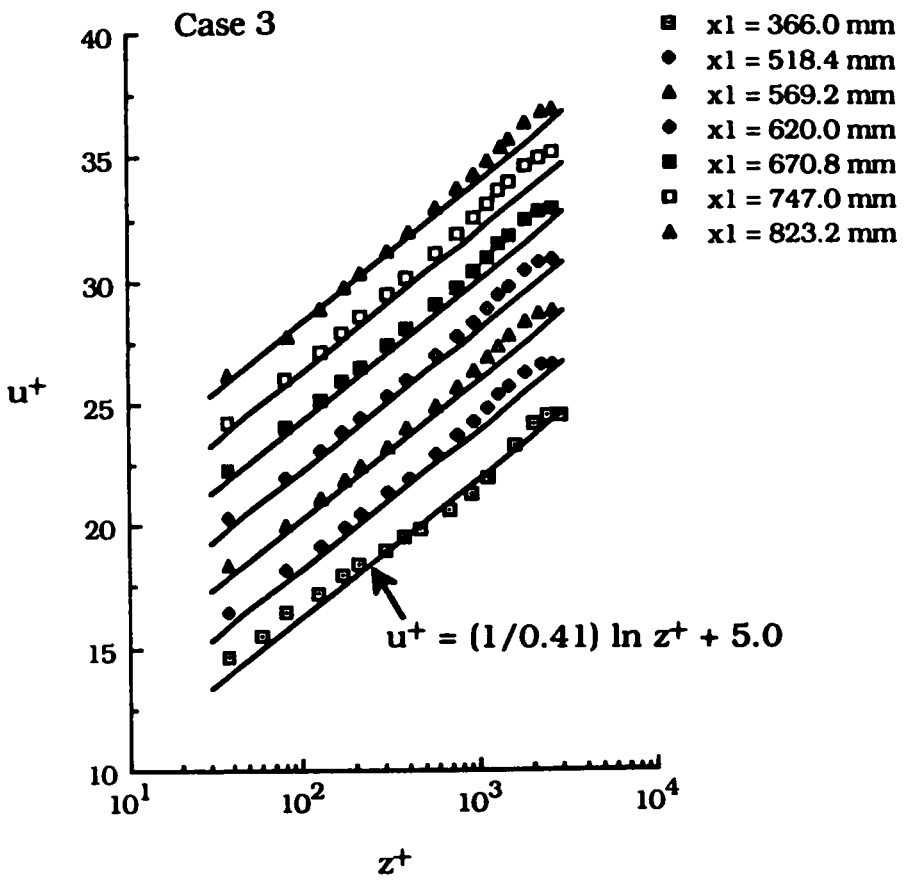

(b) Logarithmic-Law Plot

(Note: Ordinate Scale Refers to Lowest Profile. Also Ordinate Scale Shifted by 2 Units for Second Profile Onwards)

Fig. 4.13 Development of Mean Velocity Profiles for Case 3

wall region is observed to extend over a larger distance ($z^+ < 600$) compared to case 1. The velocity profiles in the presence of initial roughness are fuller compared to the velocity profiles in case 1 (see Fig. 4.8). The fullness of the velocity profile implies a higher wall shear stress which is in good agreement with the measured C_f values except at x1 = 366 mm (see Fig. 4.12(a)). At the first station the measured C_f value is smaller compared to the C_f value in case 1 and, therefore, is in contradiction with the observed fuller profile. A comparison of C_f values for case 1 and case 3 shows lower C_f values close to the roughness strip. Further downstream C_f values are slightly higher compared to case 1 (see Fig. 4.12(a)). It is observed that a distance of $\approx 40\ \delta_0$ (δ_0 is the boundary layer thickness at x1 = 366 mm for case 1) from the roughness strip is needed for C_f values to reach the values obtained in case1. A comparison of C_f values by different techniques is shown in Fig. 4.14. The C_f values calculated from Ludwieg-Tillman relation differ by < 2% from the measured values. Smaller differences ($\approx$ 3%) in C_f values, obtained by Clauser's technique and measured values, are observed compared to those observed in case 1.

The variation of C_f with Re_θ for case 1 and case 3 is shown in Fig. 4.12(b). Although, similar values of Re_θ could not be achieved in the two cases, but it was quite clear that at the same Re_θ, the values of C_f in case 3 are larger than for the case 1. The data obtained by Purtell, Klebanoff and Buckley[143] and Huffman, Zimmerman and Bennet[62] are also included in Fig. 4.12(b). These two data sets were selected as their study also used a roughness strip to artificially thicken the boundary layer. The values of C_f in the present investiga-

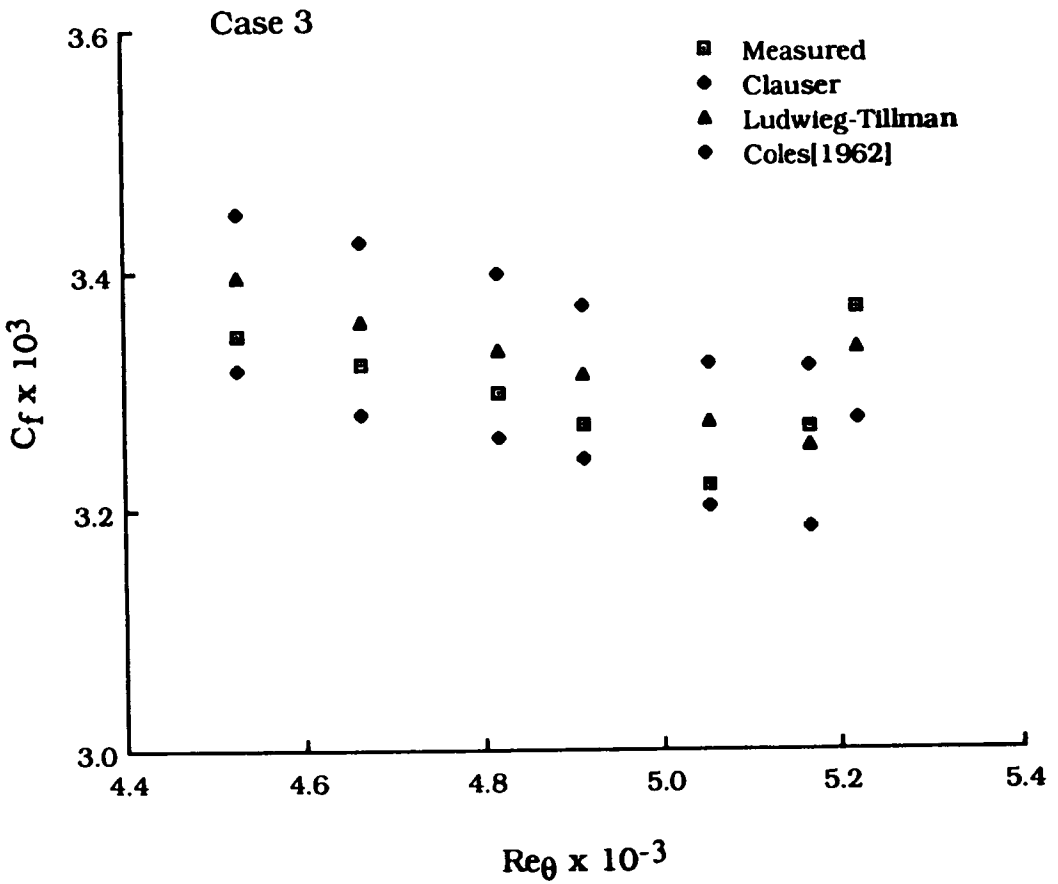

Fig. 4.14 Variation of C_f With Re_θ for Case 3

tion are higher compared to these two data sets at similar values of Re_θ.

A comparison of the velocity profiles for cases 1 and 3, on the velocity-defect plot shows a decrease in the velocity-defect up to the last measurement location (see Fig. 4.9). Although, the self-similarity is observed at different streamwise locations (see Fig. 4.13(a)), the mean flow has not reached the self-similarity distribution of case 1 up to the last measurement location which is located at a distance of $\approx 65\ \delta_0$ from the end of roughness strip. A comparison of the velocity profiles in the presence of initial roughness with case 1 on a log-law plot (see Fig. 4.10) shows a decrease in the wake component implying a lower wake profile parameter, Π, which agrees with the calculated value of Π (see Fig. 4.4(c)).

The boundary layer thickness for case 3 increases considerably ($\approx$ 100%) compared to the value for case 1 (see Fig. 4.3(a)). A higher value of δ is observed at the first station. A similar trend in the variation of δ was obtained from Coles' method (Eqn. 3.1).

The value of δ^*/δ for case 3 is lower ($\approx$ 25%) than the value in case 1 (Fig. 4.3(b)). This is mainly because δ for case 3 is much higher than the value of δ in case 1. Moreover, the decrease in δ^*/δ is observed to be independent of Re_θ. On the contrary, δ/θ is observed to increase ($\approx$ 23%) compared to the value of case 1 (see Fig. 4.3(c)). The increase in δ/θ is also observed to be independent of Re_θ.

A considerable decrease ($\approx$ 20%) in the value of G for case 3 compared to the value for case 1 is observed (Fig. 4.4(a)). The average value of G is $\approx$ 5.7, which is different from the case 1 value ($\approx$ 7.15), also suggests that the flow has not reached the self-similar state of

case 1. The values of H for case 3 decrease (≈ 8%) in the presence of initial roughness compared to case 1 values (Fig. 4.4(b)).

4.4 Combined Influence of Initial Roughness and Free Stream Turbulence (Case 4)

The self-similarity of mean velocity profiles, on a velocity-defect plot, at different streamwise locations is clearly observed in Fig. 4.15(a). At the first streamwise station in this case also, as in previously discussed cases, some deviation from similarity law is observed. The presence of initial roughness in combination with free stream turbulence seems to have a little influence on the law of the wall (Fig. 4.15(b)).

In comparison to case 1, the mean velocity profiles are observed to be fuller at all streamwise locations implying larger wall shear stress (Fig. 4.8). On the contrary, the measured C_f values show lower values compared to case 1 except at the last measurement location (see Fig. 4.12(a)). A comparison of C_f values for two cases, i.e., case 4 with case 1, suggests the need for a larger distance downstream of roughness strip ≈ 65 δ_0, compared to case 3, to reach a smooth plate value of wall shear stress. The above mentioned discrepancy of fuller velocity profiles but decreased C_f values can be resolved if the comparison of case 4 is made with case 3. In comparison to case 3, mean velocity profiles for case 4 are observed to be less full implying a lower wall shear stress which is in agreement with the measured C_f values (see Figs.4.8 and Fig. 4.12(a)).

A comparison with case 1 of mean velocity profiles on velocity-deflect plot shows a decrease in velocity-defect and the decrease is

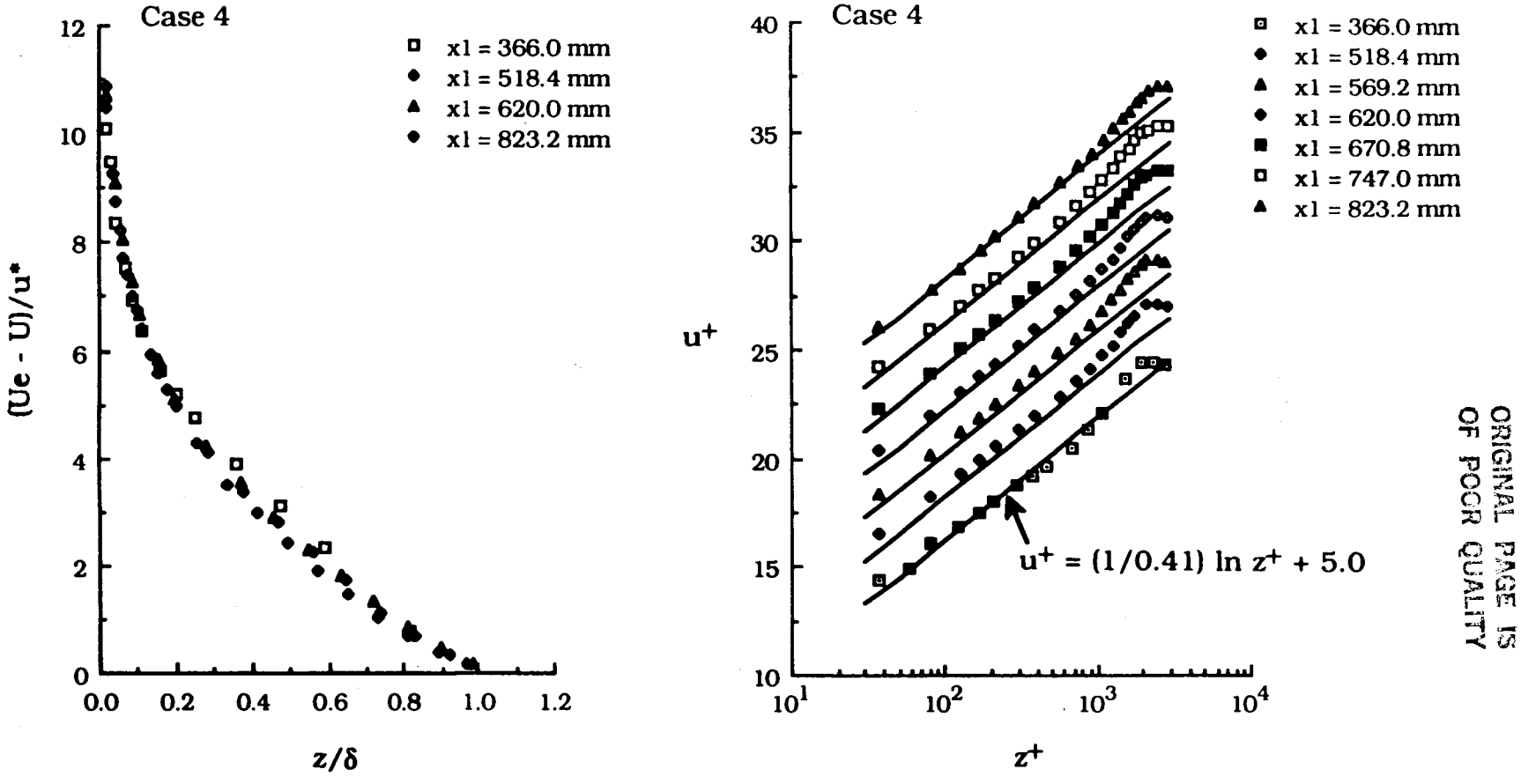

(a) Velocity-Defect Plot

(b) Logarithmic-Law Plot

(Note: Ordinate Scale Refers to Lowest Profile. Also Ordinate Scale Shifted by 2 Units for Second Profile Onwards)

Fig. 4.15 Development of Mean Velocity Profiles for Case 4

observed to be smaller compared to case 3 (Fig. 4.9). The observed change in the velocity-defect law (Fig. 4.9) in combination with the existence of self similarity (Fig. 4.15) implies that also in this case (case 4) the mean flow is far from achieving the self-similar state of case 1.

At the same streamwise station, in comparison to case 1, the wake component is observed to be smaller and agrees with the calculated value of Π (see Fig. 4.10 and Fig. 4.4(c)). However, this decrease in wake component is smaller compared to the decrease observed in case 3. This observation is also confirmed by the variation of Π (Fig. 4.4(c)). Based on the above mentioned discussion on mean velocity profiles it appears that the influence of increased free stream turbulence level on a turbulent boundary layer with and without the presence of initial roughness have opposite effects. This observation will find more support once the changes in boundary layer integral parameters are discussed.

The value of δ for case 4, even though, increased compared to case 1 but a decrease in δ is observed compared to the value for case 3 (Fig. 4.3(a)). In comparison to case 1, δ^*/δ values for case 4 are smaller by $\approx$ 16% (Fig. 4.3(b)). This may be attributed to the increase in the value of δ compared to the value for case 1. However, an increase ($\approx$ 10-16%) in δ^*/δ values are noticed compared to the values for case 3. The observed increase in the values of δ^*/δ is because of the decrease in the values of δ and the increase in the values of δ^* compared to the values for case 3. The values of δ/θ increased compared to the values for case 1, with the increase being smaller than that observed for case

3 (Fig. 4.3(c)). A decrease of ≈ 9% in δ/θ values was observed compared to the values of case 3.

A comparison of the boundary layer thickness, shape factor and skin friction coefficient for the four cases at the last streamwise station, x1 = 823.2 mm, is presented in Table 4.2. It is clearly observed that in the presence of initial roughness, the increase in free stream turbulence level has an opposing effect on the above mentioned parameters compared to the case without the initial roughness.

The average value of G calculated was ≈ 6.0 and is far from the value obtained for case 1(Fig. 4.4(a)). Moreover, the value of G is larger (by ≈ 5%) compared to its value of case 3. The shape factor, H, variation shows a decrease of ≈ 7% compared to the values for case 1(Fig. 4.4(b)). However, a smaller increase in the values of H was obtained compared to the values in case 3. A comparison of measured C_f values for case 4 with other techniques is shown in Fig. 4.16. The differences observed are larger with Clauser's method than with the Ludwieg-Tillman law.

A comparison of the influence of free stream turbulence on different boundary layer parameters, with and without an initial roughness is presented in Table 4.3. This comparison clearly shows that in the presence of initial roughness, the influence of free stream turbulence on a turbulent boundary layer has an opposite effect compared to the case without the initial roughness. The numerical values given in Table 4.3 are the average values taken over all the streamwise stations investigated. One of the plausible reasons can be the nature in which local wall shear stress changes. This is because in a turbulent boundary layer various boundary layer parameters are dependent on C_f.

TABLE 4.2 Comparison of Some Mean Flow Parameters for Four Cases at x1 = 823.2 mm

Parameter	Case1	Case 2	Case 3	Case 4
δ(mm)	17.5	22.2	33.8	32.0
H	1.398	1.340	1.303	1.311
$C_f \times 10^3$	3.173	3.323	3.269	3.077

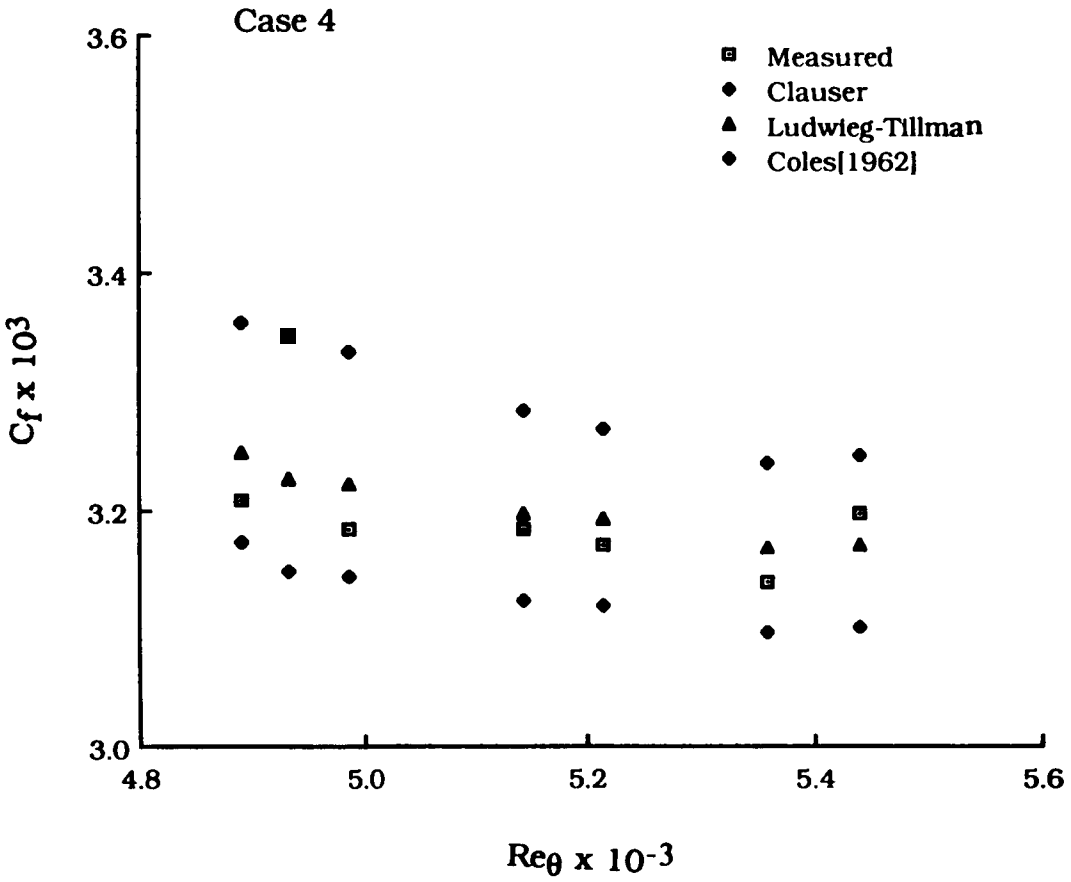

Fig. 4.16 Variation of C_f With Re_θ for Case 4

TABLE 4.3 Influence of Free Stream Turbulence on Mean Flow Boundary Layer Parameters With and Without the Initial Roughness

	Without Initial Roughness		With Initial Roughness	
Parameter	Qualitative	% variation in parameter	Qualitative	% variation in parameter
Mean velocity profile fullness	More full		Less full	
Defect velocity	Decreases		Increases	
Wake component	Decreases		Increases	
δ	Increases	35.0	Decreases	- (3.0 - 8.0)
δ^*/δ	Decreases	- 22.0	Increases	10.0 - 16.0
δ/θ	Increases	22.0	Decreases	- 9.0
G	Decreases	-13.0	Increases	3.0 - 6.0
H	Decreases	- 5.0	Increases	< 2.0
C_f	Increases	5.0	Decreases	- (2.0 - 4.0)
Π	Decreases	- (30.0 - 40.0)	Increases	20.0 - 70.0

CHAPTER V

RESULTS AND DISCUSSION ON THE SURFACE STATIC PRESSURE, THE WALL SHEAR STRESS, AND THE MEAN VELOCITY PROFILES IN A BLADE END-WALL CORNER REGION

Experimental results on the surface static pressure and the local wall shear stress vector in an upstream region and in the blade end-wall corner region are presented and discussed in this chapter. The measurements of mean velocity profiles obtained only in an upstream region of the blade leading edge are also described here. Yaw sensitivities of the static tube resting on the surface and the Preston tube were experimentally investigated in two- and three-dimensional flows. Measurement of various flow parameters, as mentioned above, were also made on the flat plate centerline without the presence of the blade (i.e., two-dimensional flow). The results of measurements for two -dimensional flow are also discussed in this chapter. As described in Chapter III, two flow conditions were investigated: the first case (Case A) is without the presence of separation bubble, and in the second case (Case B) a separation bubble existed in the blade end-wall corner region. Therefore, the results of two cases, Case A and Case B, are presented in section A and section B, respectively.

SECTION A

5.1 Two-Dimensional Flow (Case A)

There were two main reasons, as mentioned earlier in Chapter III, to obtain measurements of various flow parameters of interest in a

two-dimensional flow. The first reason was to check the proper working of the different probes used in the investigation. This was achieved by comparing the results obtained in the present investigation for a two-dimensional flow case with similar results available in the literature. Secondly, these results are also used to compare stress values obtained in the blade end-wall corner region.

5.1.1 Surface Static Pressure and Mean Velocity Profiles

The surface static pressure coefficient, C_p, variation on the flat plate centerline in the streamwise direction is shown in Fig. 5.1. In the streamwise direction, a small decrease (approximately 1.5% of the free stream dynamic pressure) in C_p value is observed implying an existence of favorable pressure gradient. The existence of favorable pressure gradient in streamwise direction is also evident from the free stream mean velocity measured at different streamwise stations (Fig. 5.2). This observed decrease in the surface static pressure or increase in the free stream mean velocity in the streamwise direction can be attributed to the boundary layer growth on the sidewalls of the wind tunnel test-section. In Fig. 5.1, the surface static pressure measured using the conventional (wall tap) technique is also included. The C_p values obtained with the two techniques agree within one percent of the free stream dynamic pressure.

It needs to be mentioned here, that the flow conditions for the case under discussion were similar to Case 4 discussed in detail in Chapter IV. The detailed description on the mean velocity profiles are presented in section 4.4.

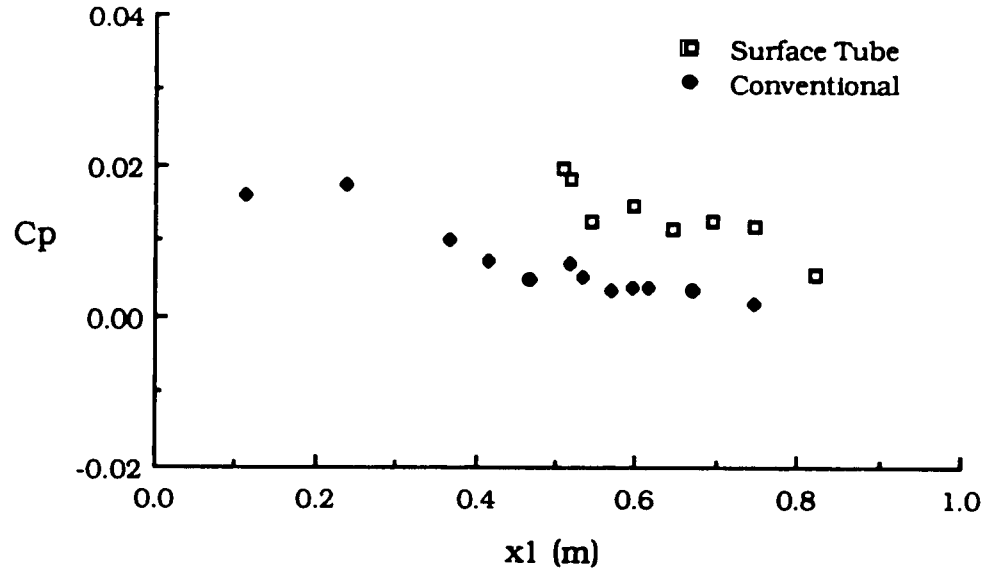

Fig. 5.1 Surface Static Pressure Variation Along Flat Plate Centerline (Two-Dimensional Flow)

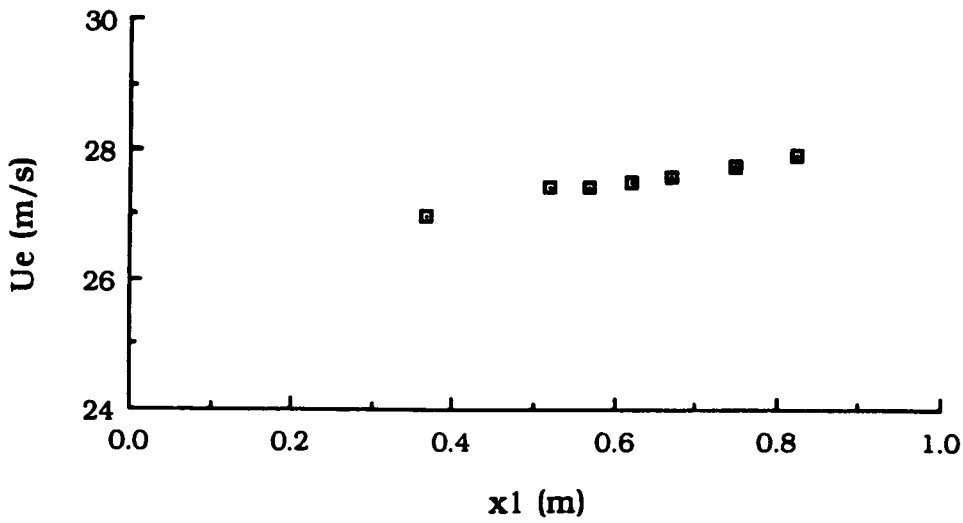

Fig. 5.2 Local Free Stream Velocity Variation Along Flat Plate Centerline (Two-Dimensional Flow)

5.1.2 Wall Shear Stress

The wall shear stress measured with the Preston tube at different streamwise stations on the flat plate centerline (two-dimensional case) is presented in Table 5.1. The values of the wall shear stress at different streamwise stations were also obtained from the measured mean velocity profiles using Clauser's[96] method and the empirical relation proposed by Ludwieg and Tillman[140]. The wall shear stress values obtained with the Preston tube, at different streamwise stations, are observed to agree within 1.5% as compared to Ludwieg-Tillman relation. However, C_f values obtained by Clauser's technique are, in general, found to be higher (within 5%) compared to the values obtained with the Preston tube. These larger differences, as compared to the latter technique, are probably due to changes in the values of constants used in the logarithmic law of the wall.

5.2 Three-Dimensional Flow (Case A)

The results of the yaw sensitivities of the static tube resting on the surface and the Preston tube are discussed in detail in appendix C. However, briefly the main observations are presented here. The results of the surface static pressure and the wall shear stress measurements upstream and in the blade end-wall corner region are presented in this section.

5.2.1 Yaw Sensitivities of the Surface Static Tube and the Preston Tube

The yaw characteristics of the surface static tube showed that the smaller value (approximately 20%) of the surface static pressure would be obtained if the static tube was not aligned in the local flow

TABLE 5.1 Comparison of C_f Values by Different Methods (Two-Dimensional Flow- Case A)

xl (mm)	Re_θ	$C_f \times 10^3$		
		Preston Tube	Clauser	Ludwieg-Tillman
366.0	4933	3.3473	3.3473	3.2260
518.4	4892	3.2071	3.3571	3.2492
569.2	4987	3.1827	3.3327	3.2215
620.0	5143	3.1836	3.2836	3.1980
670.8	5213	3.1694	3.2694	3.1915
747.0	5358	3.1398	3.2398	3.1677
823.2	5439	3.1961	3.2461	3.1707

direction (see Fig. C2 of appendix C). Also the surface static tube was found to be insensitive to the yaw angle within $\pm 5^0$. The experimental results on the yaw characteristics of the Preston tube showed that it was insensitive to the yaw angle of $\pm 5^0$. It was also observed that if the Preston tube was not aligned in the local flow direction, it would have recorded approximately 15% less total pressure (see Fig. C3 of appendix C). For the wall shear stress measurement, this observed error in the Preston tube output due to misalignment would lead to approximately 10% error in the calculated value of the wall shear stress.

5.2.2 Surface Static Pressure in Upstream Region of the Blade Leading Edge

The surface static pressure coefficient variation in the Y-direction upstream of the blade leading edge at four streamwise stations is shown in Fig. 5.3. All linear distances are non-dimensionalized by the blade leading edge diameter. The available literature, as presented in Chapter II, clearly shows that the blade leading edge shape significantly influences the flow characteristics in an upstream region and in the blade end-wall corner region. The characteristic length scale, therefore, can be the maximum thickness of the blade leading edge. In the present study, because the blade leading edge shape is circular, the diameter of the blade leading edge is considered a suitable choice for non-dimensionalizing various linear distances. In an upstream region of the blade leading edge, the surface static pressure coefficient, C_p, decreases in the Y-direction and the rate of decrease is observed to be maximum at $x/D = -2.0$ in the vicinity of the blade leading edge. At a distance of $y/D = 6$, the value of C_p is found to approach approxi-

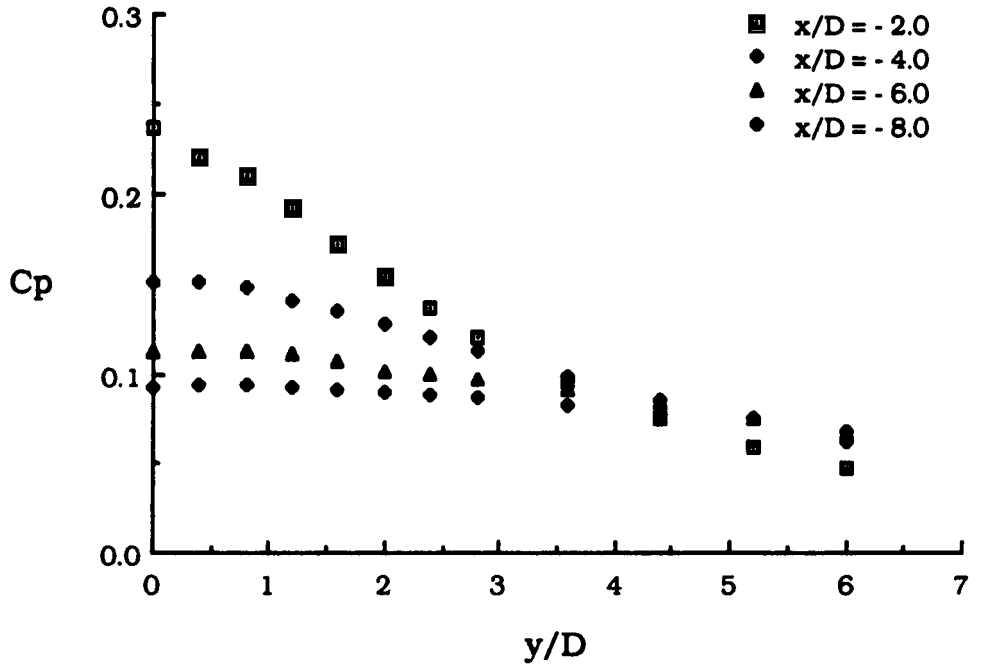

Fig. 5.3 Surface Static Pressure Distribution Upstream of the Blade Leading Edge

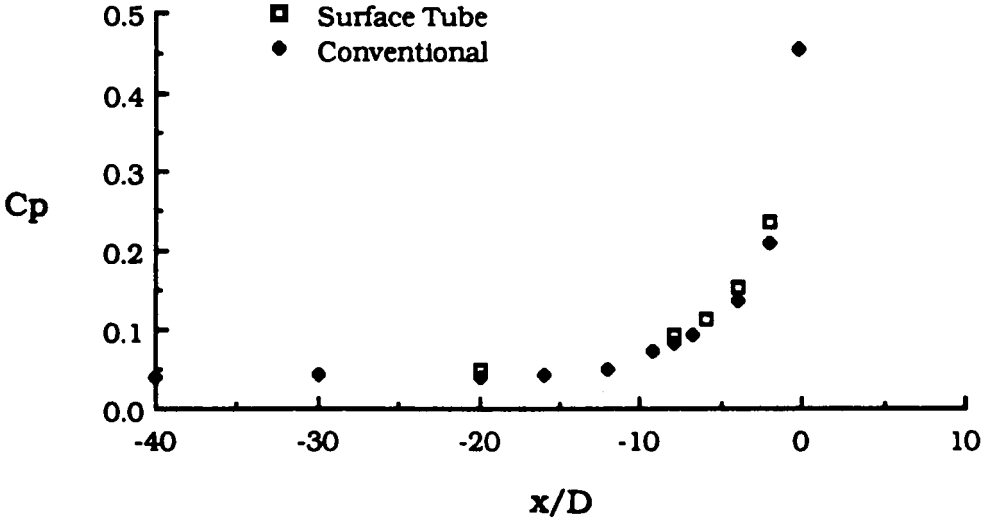

Fig. 5.4 Surface Static Pressure Variation on Stagnation Streamline- A Comparison Between Surface Static Tube and Conventional Techniques

mately (within 2% of the free stream dynamic pressure) to its value far upstream, i.e., at x/D = - 20, of the blade leading edge.

The variation of C_p on the stagnation streamline, in an upstream region of the blade leading edge, is shown in Fig. 5.4. The measured value of C_p obtained with conventional wall taps is also included in Fig. 5.4. The maximum difference in measured C_p values by two techniques is found to be less than 2% of the free stream dynamic pressure.

5.2.3 Wall Shear Stress in Upstream Region of the Blade Leading Edge

The variation of the local wall shear stress, normalized by the far upstream value (at x/D = - 20, y/D = 0), at four streamwise stations upstream of the blade leading edge is shown in Fig. 5.5. This presentation of the local wall shear stress rather than the skin friction coefficient, is chosen for two main reasons. Firstly, the local free stream velocity is expected to change at different streamwise stations. Moreover, in the blade end-wall corner region, it is difficult to define the local free stream velocity because of the interacting nature of the shear layers. Secondly, this presentation clearly shows how the local wall shear stress, in the blade end-wall corner region, varies relative to the far upstream value at x/D = - 20. It is important to mention here, that the local wall shear stress at x/D = - 20 is approximately equal (within 3%) to the two-dimensional value at the same streamwise location. The normalized local wall shear stress decreases as the blade leading edge is approached. A maximum decrease in wall shear stress of ≈ 40%, from the value far upstream of the blade leading edge, occurs on the stagnation streamline where the adverse pressure gra-

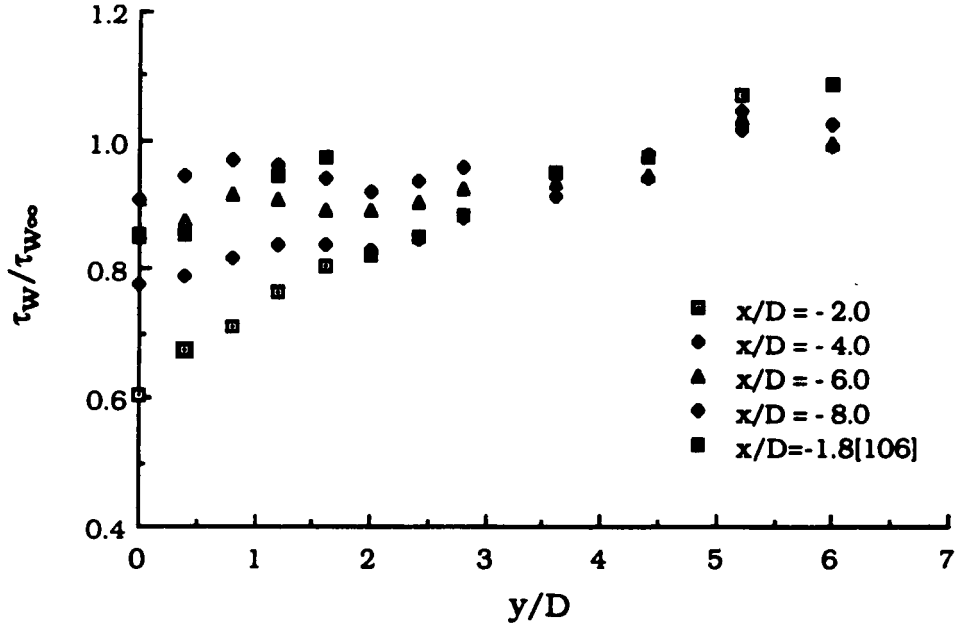

Fig. 5.5 Wall Shear Stress Variation Upstream of the Blade Leading Edge

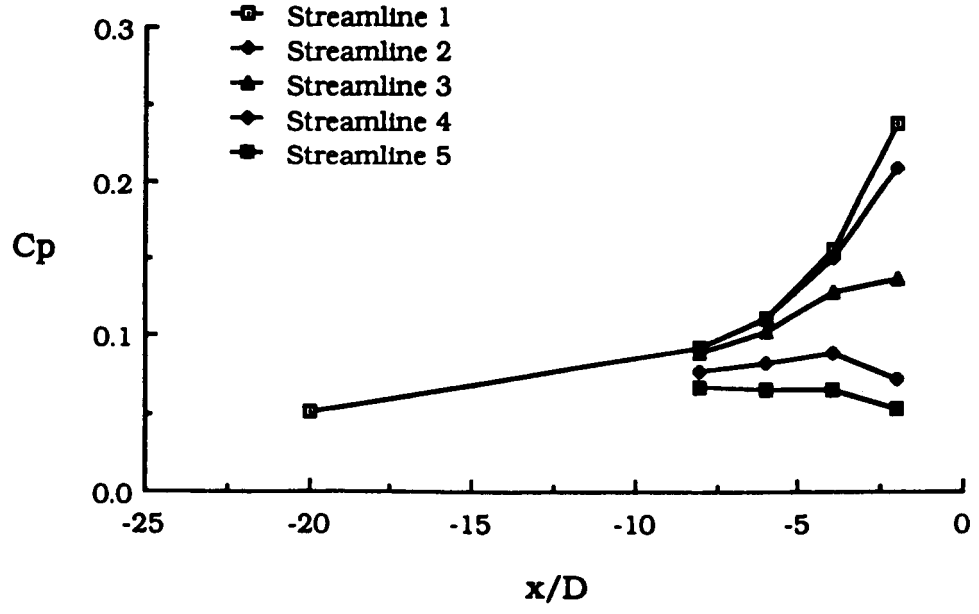

Fig. 5.6 Variation of Surface Static Pressure Along Different Streamlines

dient is also found to be maximum (see Fig. 5.3). The wall shear stress values, at different streamwise stations, reach the two-dimensional value within a distance of ≈ 6D in the Y-direction. The wall shear stress values obtained with the floating element balance by McAllister[106] in an upstream region of his test-model at approximately the same x/D distance are also presented in Fig. 5.5. The test-model used in McAllister's study consisted of a cylindrical body mounted on a flat plate. The body had a large circular leading edge (12.7 cm diameter) and was tapered in streamwise direction. It should be mentioned that the blade leading edge diameter of the present study is 1/10 that of the McAllister's study. It is quite evident that the trend in the variation of the local wall shear stress in Y-direction obtained in McAllister's measurements is similar to that obtained in the present study. However, the magnitude of the normalized wall shear stress, at different y/D distances, is relatively higher in McAllister's study than in the present study. The possible reason for these observed differences of the order of 25% in the two cases can be because of the pressure gradient effects.

5.2.4 Mean Velocity Profiles Upstream of the Blade End-Wall Corner Region

The mean velocity profiles were measured on the flat plate surface upstream of the blade leading edge on five streamlines (see Fig. 3.12 for the measurement locations). The traces of these five streamlines were obtained from flow visualization using an oil dot matrix method. The local wall shear stress and the surface static pressure

were also measured at different measurement locations. The results of the above mentioned measurements are discussed in this section.

The variation of surface static pressure coefficient along five streamlines is shown in Fig. 5.6. It is clearly observed that the maximum adverse pressure gradient in the streamwise direction exists on the stagnation streamline (streamline no.1) where the value of C_p changed from 0.05 to 0.24. Moreover, away from the stagnation streamline i.e., as the distance y increases, the adverse pressure gradient in the streamwise direction decreases. In fact, the value of C_p on streamline no. 5, does not change significantly except between streamwise stations 3 and 4, where the value of C_p changed by 1% of the free stream dynamic pressure.

Fig. 5.7(a) shows the comparison of non-dimensional mean velocity profiles at x/D = - 20 for two- and three-dimensional flow cases. The mean velocity profiles on the logarithmic inner law of the wall plot for two- and three-dimensional flows at x/D = - 20 is shown in Fig. 5.7(b). The solid line in Fig. 5.7(b) represents

$$u^+ \equiv U/u^* = (1/K) \ln z^+ + B \qquad (5.1)$$

where the values of the universal constants, K and B, used are the same as described in Chapter IV. The value of u^* used in Fig. 5.7(b) was calculated from the local wall shear stress measured with the Preston tube. The mean velocity profiles are observed to be self-similar in the outer-layer variables (Ue and δ^*). However, on the logarithmic law plot, deviation from the solid line for the three-dimensional flow case is observed.

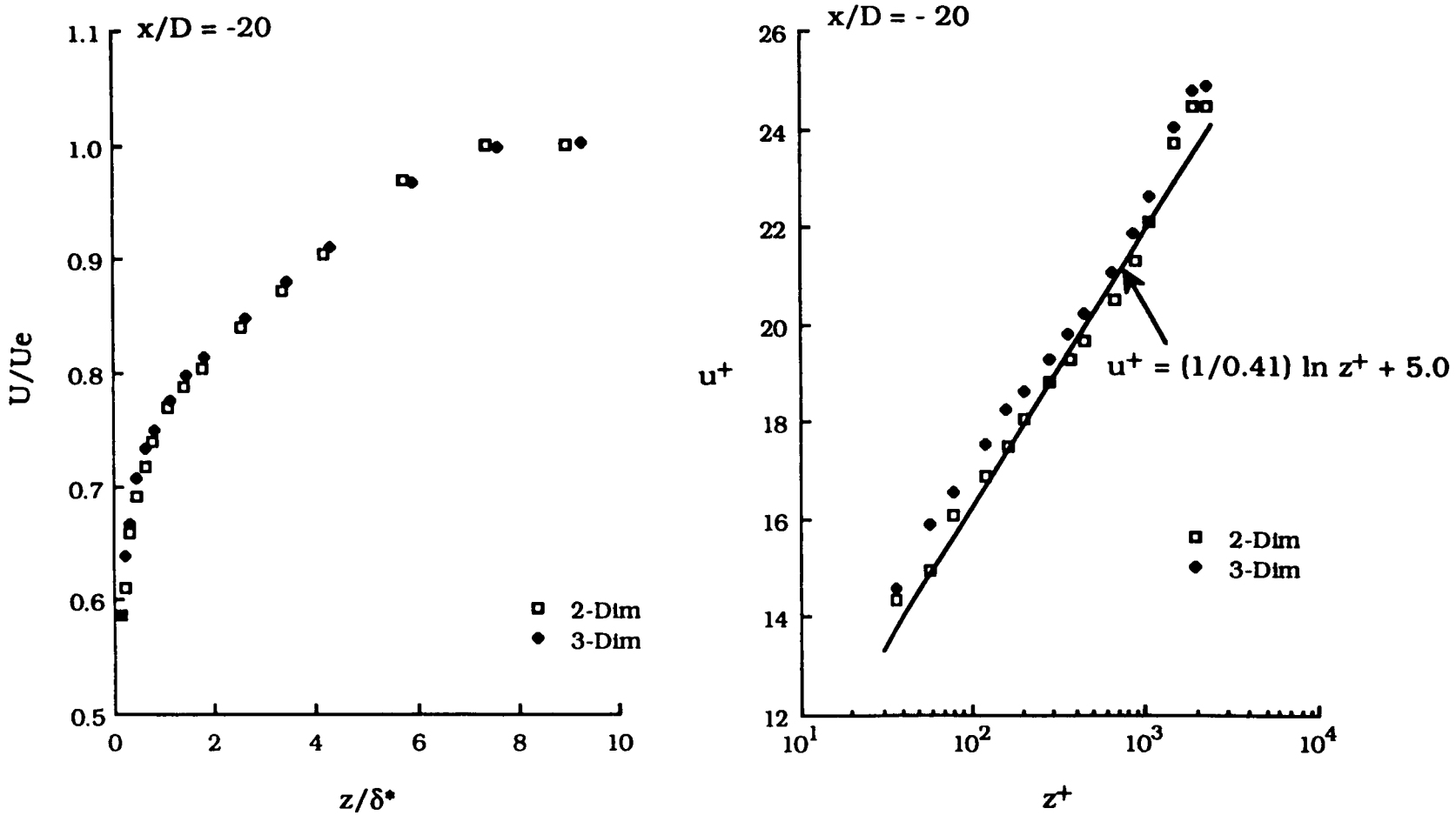

(a) In Outer-Layer Variables

(b) In Inner-Layer Variables

Fig. 5.7 Variation of Mean Velocity Profiles at Streamwise Location of x/D = - 20

Figs. 5.8 - 5.12 show mean velocity profiles in the outer-layer and inner-layer variables on 5 streamlines. Along each streamline, at different streamwise stations, the mean velocity profiles show self-similarity (Figs. 5.8(a) - 5.12(a)). However, the inner region of the boundary layer on various streamlines is influenced differently. If the mean velocity profile is represented as a combination of the law of wall and the law of the wake, as proposed by Coles[133], and is written as

$$u^+ \equiv U/u^* = (1/K) \ln z^+ + B + (\Pi/K)\, W[z/\delta] \qquad (5.2)$$

where K and B are universal constants with the values given in Chapter IV. Π is the wake strength parameter, and $W[z/\delta]$ is the wake function with the condition that at $z = \delta$, $W[z/\delta] = 2$. Along streamline no.1, the values of constants K and B change. Also, the value of wake strength parameter increases as the blade leading edge is approached. This trend of an increase in the value of Π in the streamwise direction is observed up to streamline no. 3. However, on streamlines no. 4 and 5, the variation of Π in streamwise direction changes. In fact on streamline no. 5, the value of Π decreases as the blade leading edge is approached. Hsing and Teng[35] during their investigation of the upstream region of a wing-body junction also reported a variation in the values of K, B, and Π. They noted that the observed variation in the values of K, B, and Π could be attributed to the changes in adverse pressure gradient and three-dimensional curvature of the streamlines.

The variation of constants K and B and the wake strength parameter is shown in Fig. 5.13. The value of constant 1/K increases in the streamwise direction up to streamline no. 3. However, on streamlines no. 4 and 5, the value of 1/K decreases.

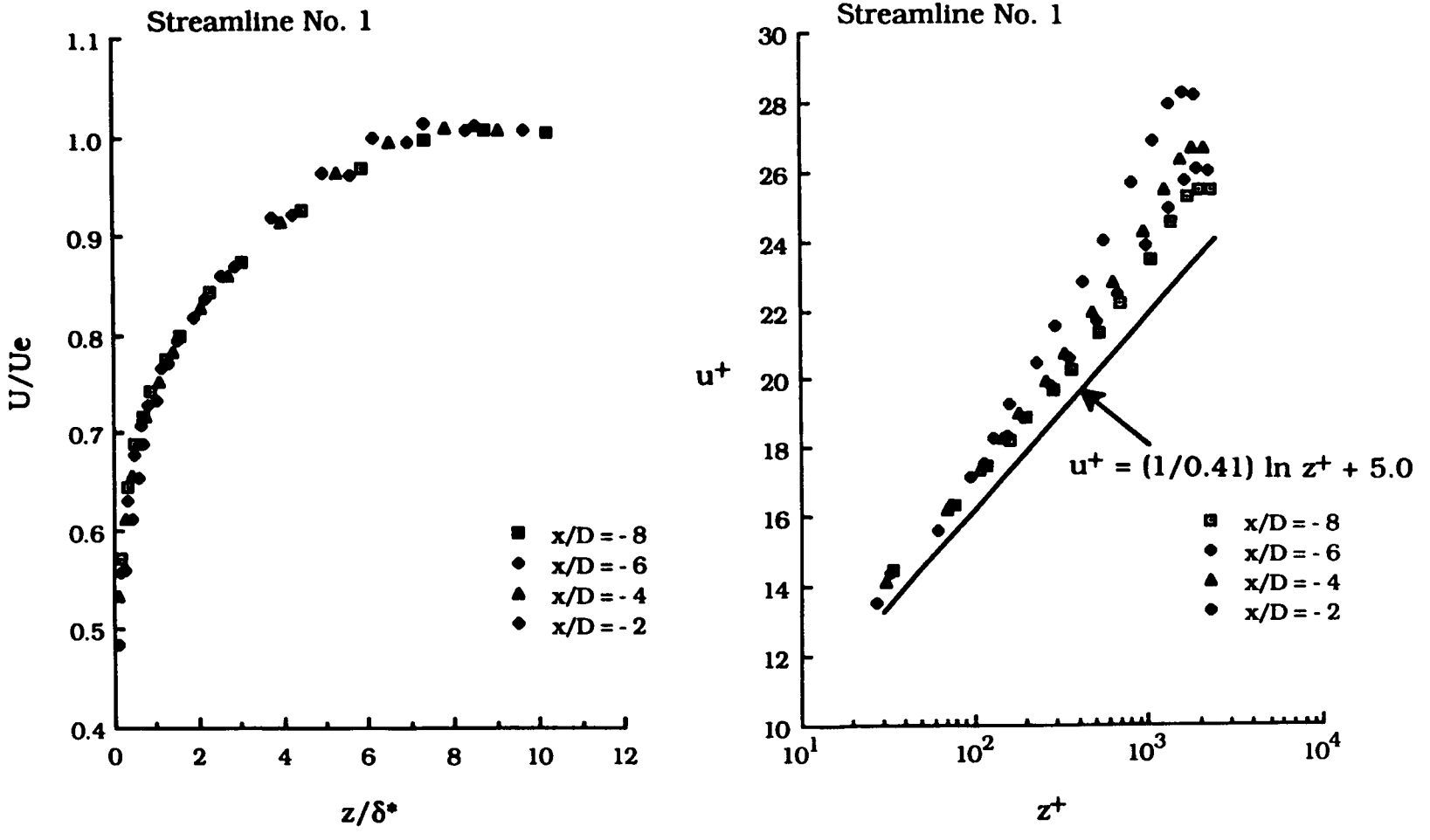

(a) In Outer-Layer Variables

(b) In Inner-Layer Variables

Fig. 5.8 Variation of Mean Velocity Profiles Along Streamline No. 1

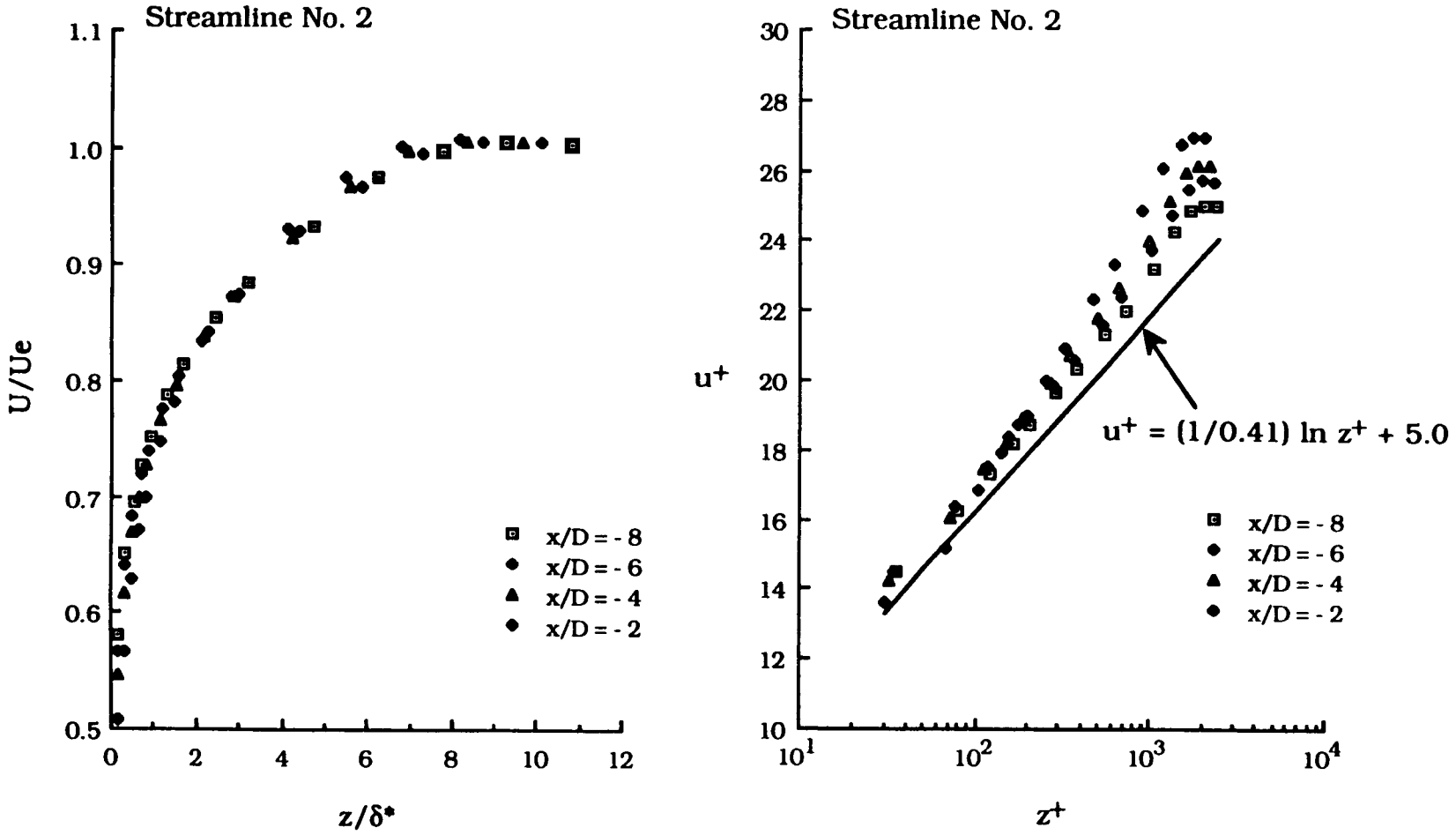

(a) In Outer-Layer Variables

(b) In Inner-Layer Variables

Fig. 5.9 Variation of Mean Velocity Profiles Along Streamline No. 2

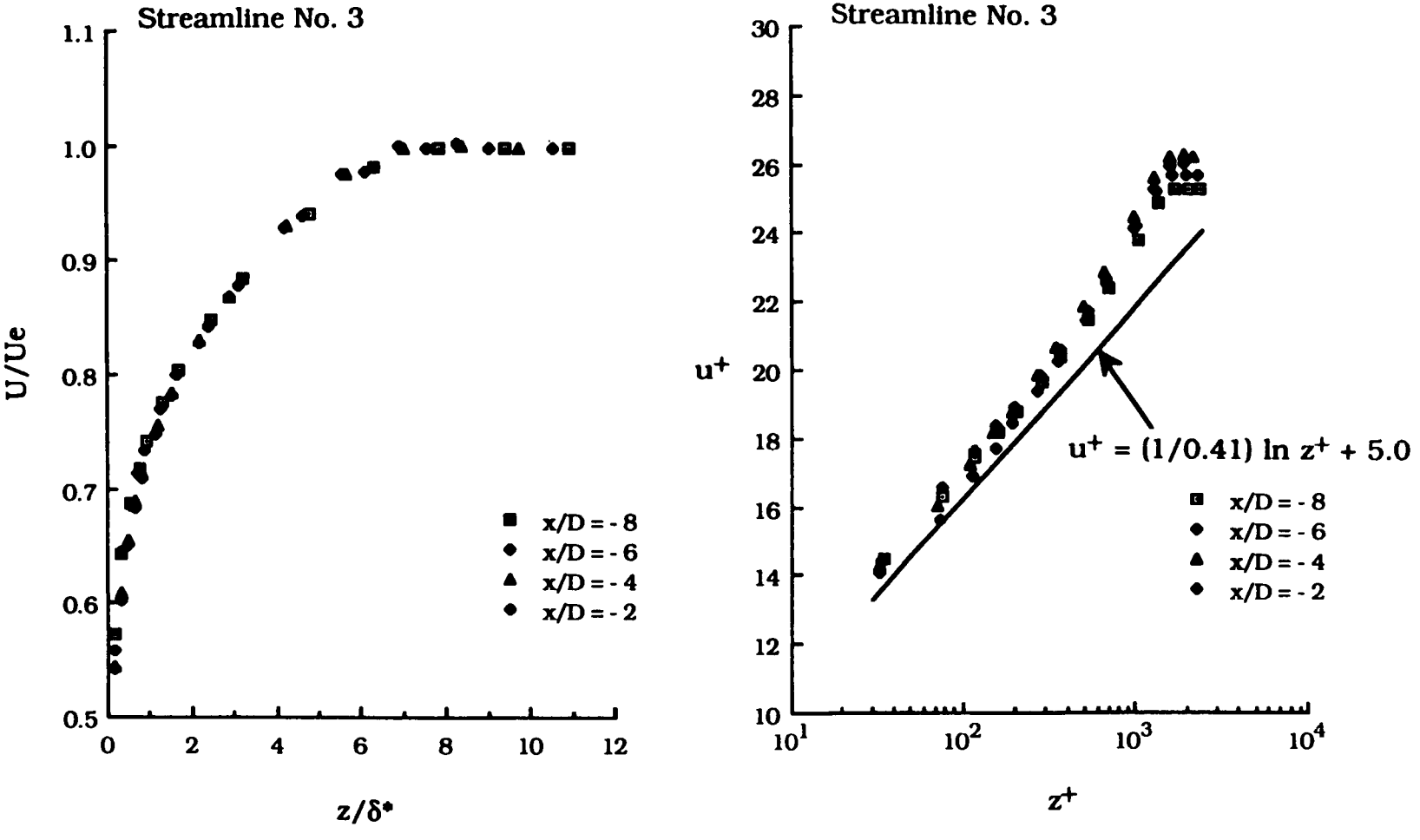

(a) In Outer-Layer Variables

(b) In Inner-Layer Variables

Fig. 5.10 Variation of Mean Velocity Profiles Along Streamline No. 3

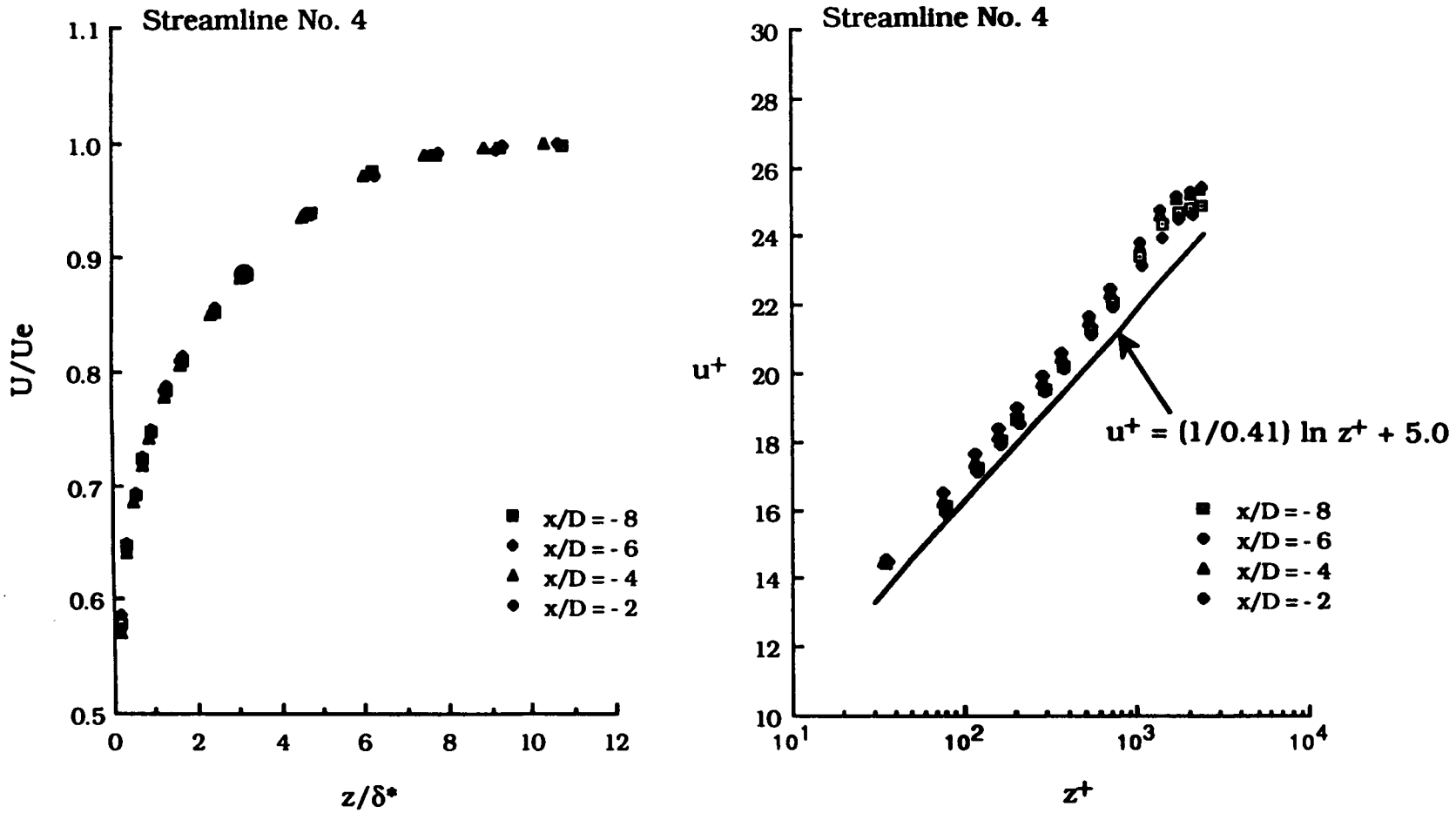

(a) In Outer-Layer Variables

(b) In Inner-Layer Variables

Fig. 5.11 Variation of Mean Velocity Profiles Along Streamline No. 4

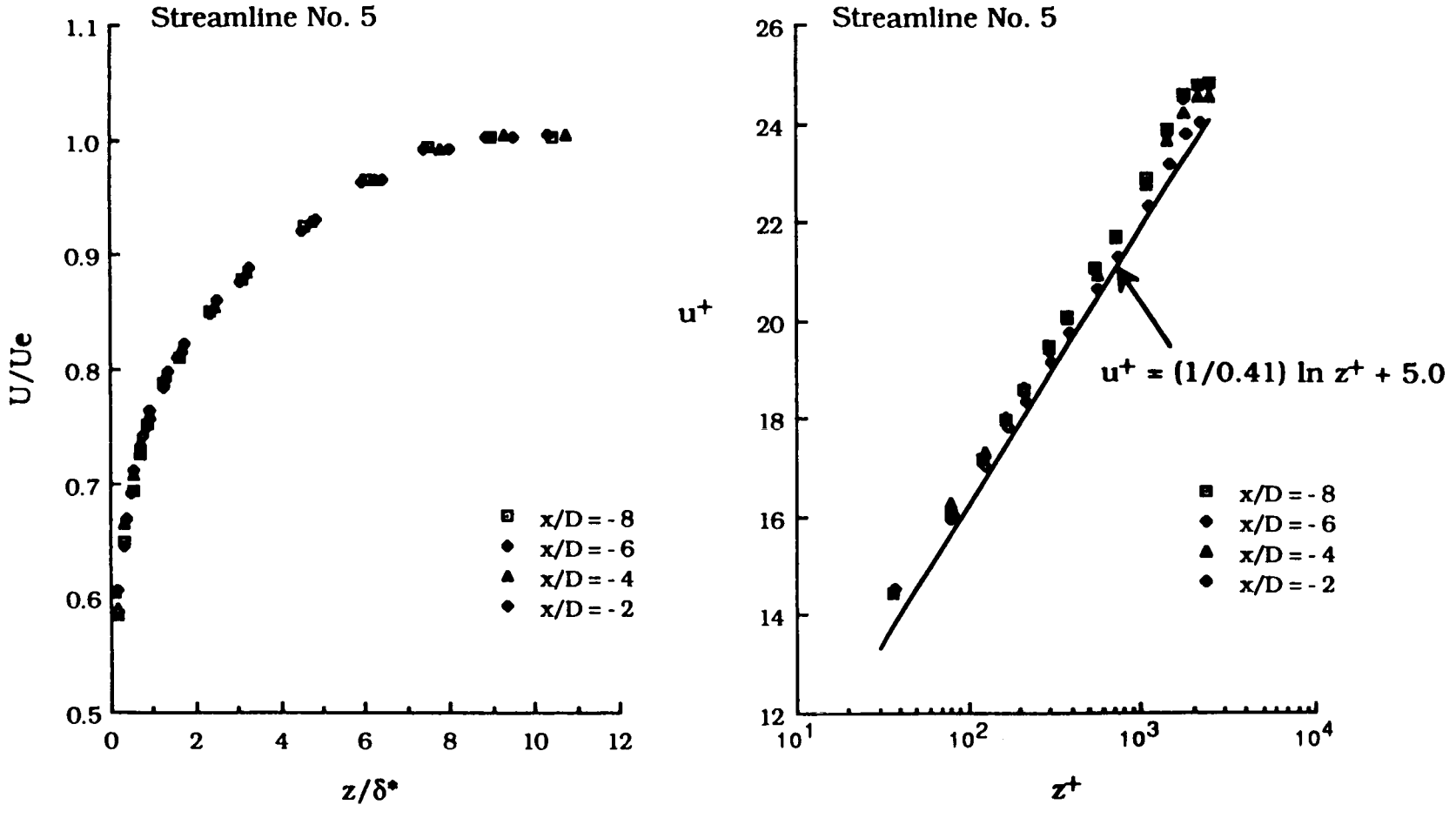

(a) In Outer-Layer Variables

(b) In Inner-Layer Variables

Fig. 5.12 Variation of Mean Velocity Profiles Along Streamline No. 5

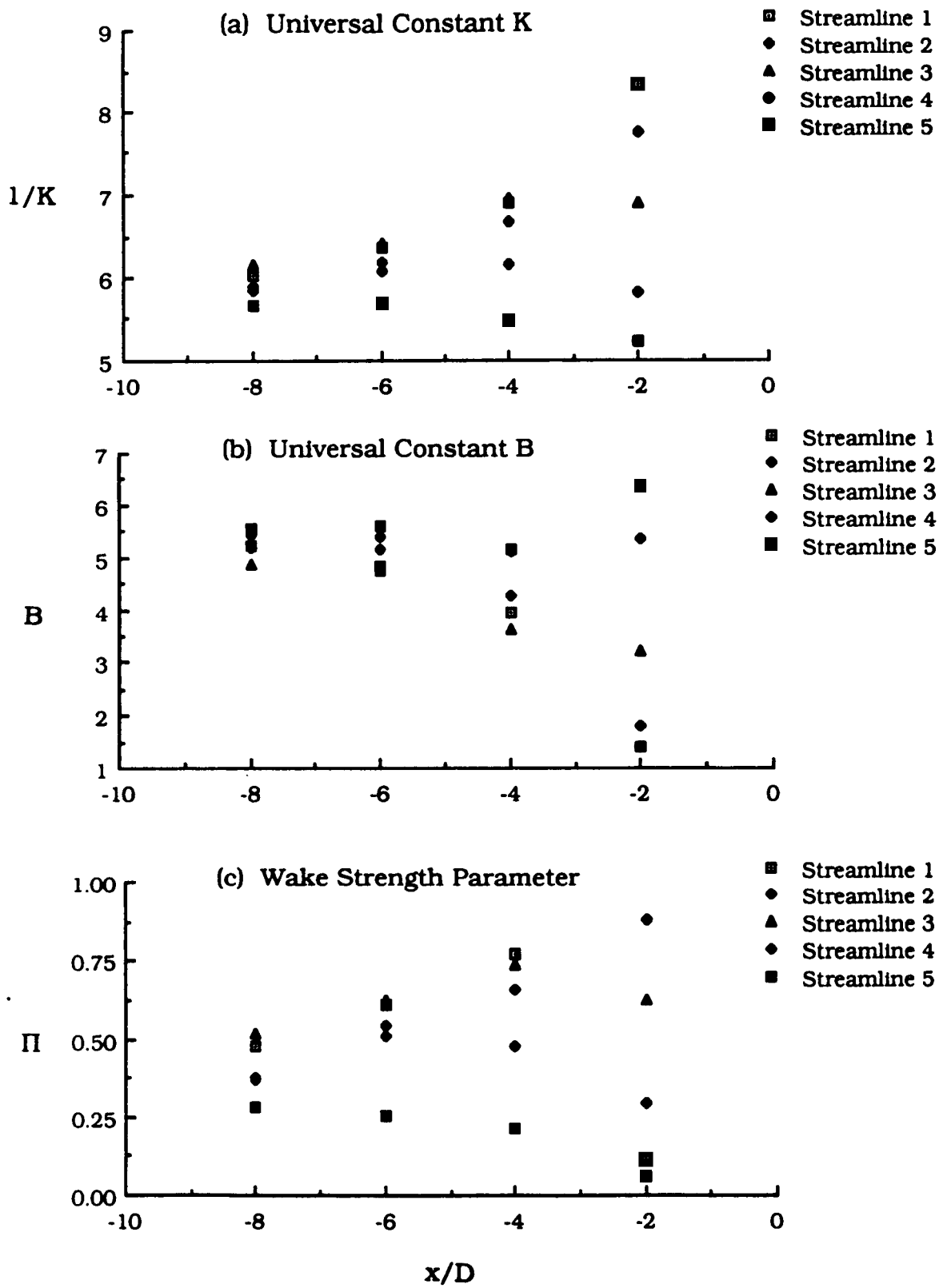

Fig. 5.13 Variation of 1/K, B, and Π in Combined Law of the Wall and the Wake in Upstream Region of the Blade Leading Edge

The trend in the variation of B is just opposite that for 1/K. On the first three streamlines, the value of B decreases as the blade leading edge is approached. However, on streamlines no. 4 and 5 the value of B increases in the streamwise direction.

The variation of the wake strength parameter, Π, along different streamlines is shown in Fig. 5.13(c). The variation in the value of Π in the streamwise direction is found to be consistent with the observations made in the logarithmic law plot (see Figs. 5.8(b) - 5.12(b)).

Fig. 5.14 shows the variation of non-dimensional boundary layer integral parameters (δ^*/δ, δ/θ, H) along different streamlines. The value of δ^*/δ increases as the blade leading edge is approached on all the streamlines, except on the streamline no. 5 (Fig. 5.14(a)). On streamline no. 5 the value of δ^*/δ decreases in the streamwise direction.

The value of δ/θ decreases as the blade leading edge is approached on all the streamlines, except on streamline no. 5 (Fig. 5.14(b)). On streamline no. 5 the value of δ/θ increases slightly.

The value of shape factor, H, increases in the streamwise direction along different streamlines except the last two streamlines (Fig. 5.14(c)).

The variation of Clauser's shape parameter, G, and the skin friction coefficient, C_f, is shown in Fig. 5.15. The value of G increases in the streamwise direction along all the streamlines except the last streamline (Fig. 5.15(a)). Along streamline no. 5, the value of G decreases in the streamwise direction.

Since there exists an adverse pressure gradient in the streamwise direction and a favorable pressure gradient in the Y-direction, it

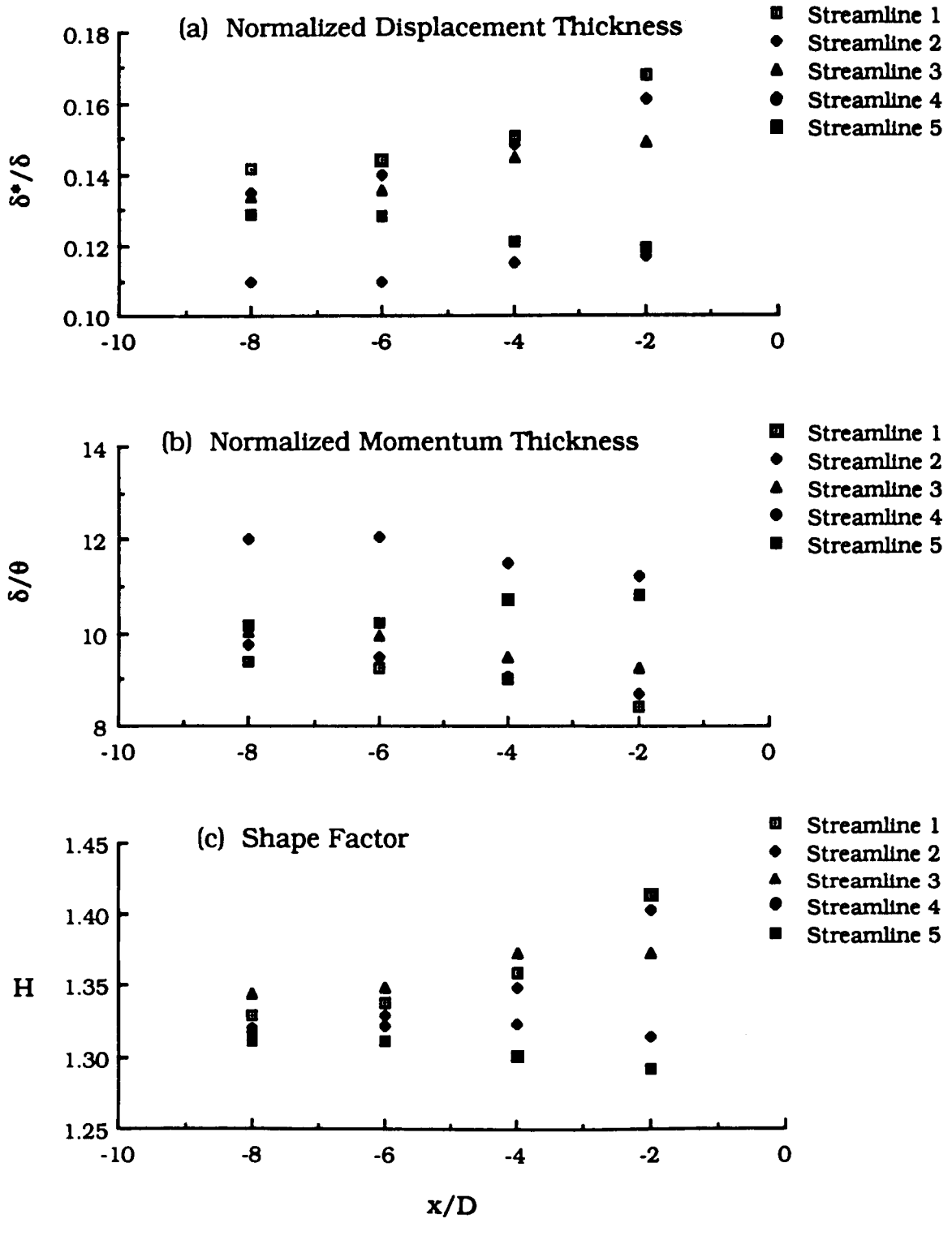

Fig. 5.14 Variation of Boundary Layer Integral Parameters Upstream of the Blade Leading Edge

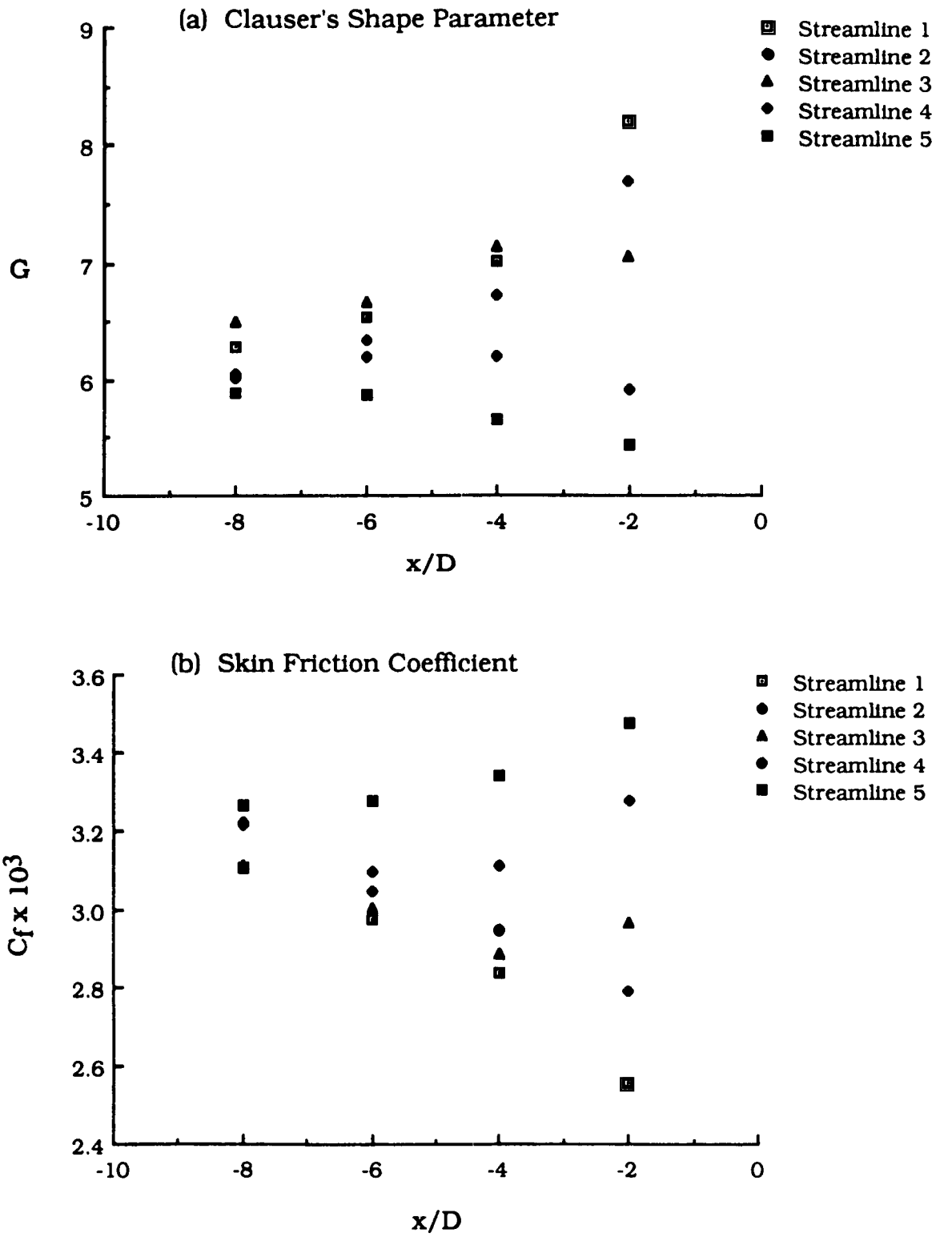

Fig. 5.15 Variation of Clauser's Shape Parameter and Skin Friction Coefficient in Upstream Region of the Blade Leading Edge

is of interest to analyze the development of mean velocity profiles at different streamwise stations.

Figs. 5.16 - 5.19 show the variation in the mean velocity profiles in the Y-direction. These profiles are presented in terms of the inner- and outer-layer variables at four different streamwise stations. At streamwise station 4 (x/D = - 2) the non-dimensional mean velocity profiles, in outer-layer variables, show lack of self-similarity in the Y-direction (Fig. 5.16(a)). This is possibly due to the presence of a high degree of skewness and strong favorable pressure gradient. Moreover, on the logarithmic law plot, a change in the values of K, B, and Π are evident. The wake component of the boundary layer decreases as the distance y/D increases. This is also evident from the calculation of the wake strength parameter, Π, (Fig. 5.13(c)).

At x/D = - 4 (streamwise station 3) self-similarity in the mean velocity profiles, in outer-layer variables, at different y/D distances is observed (Fig. 5.17(a)). Also, at this streamwise station the wake component of the boundary layer decreases as y/D increases (Fig. 5.17(b)).

At x/D = - 6 and - 8, a similar trend, as at streamwise stations 3 and 4, in the variation of the wake component is evident(Figs. 5.18(b) and 5.19(b)). Furthermore, it is observed that the strength of the wake component at the last two streamwise stations, stations 1 and 2, is relatively smaller than that observed at stations 3 and 4.

It is also interesting to note that various non-dimensional boundary layer integral parameters change in the Y-direction in an opposite manner to that observed for the streamwise direction (Fig. 5.14). For example, the value of δ^*/δ decreases in the Y-direction, whereas it increases in the X-direction (Fig. 5.14(a)). It is quite evident from the

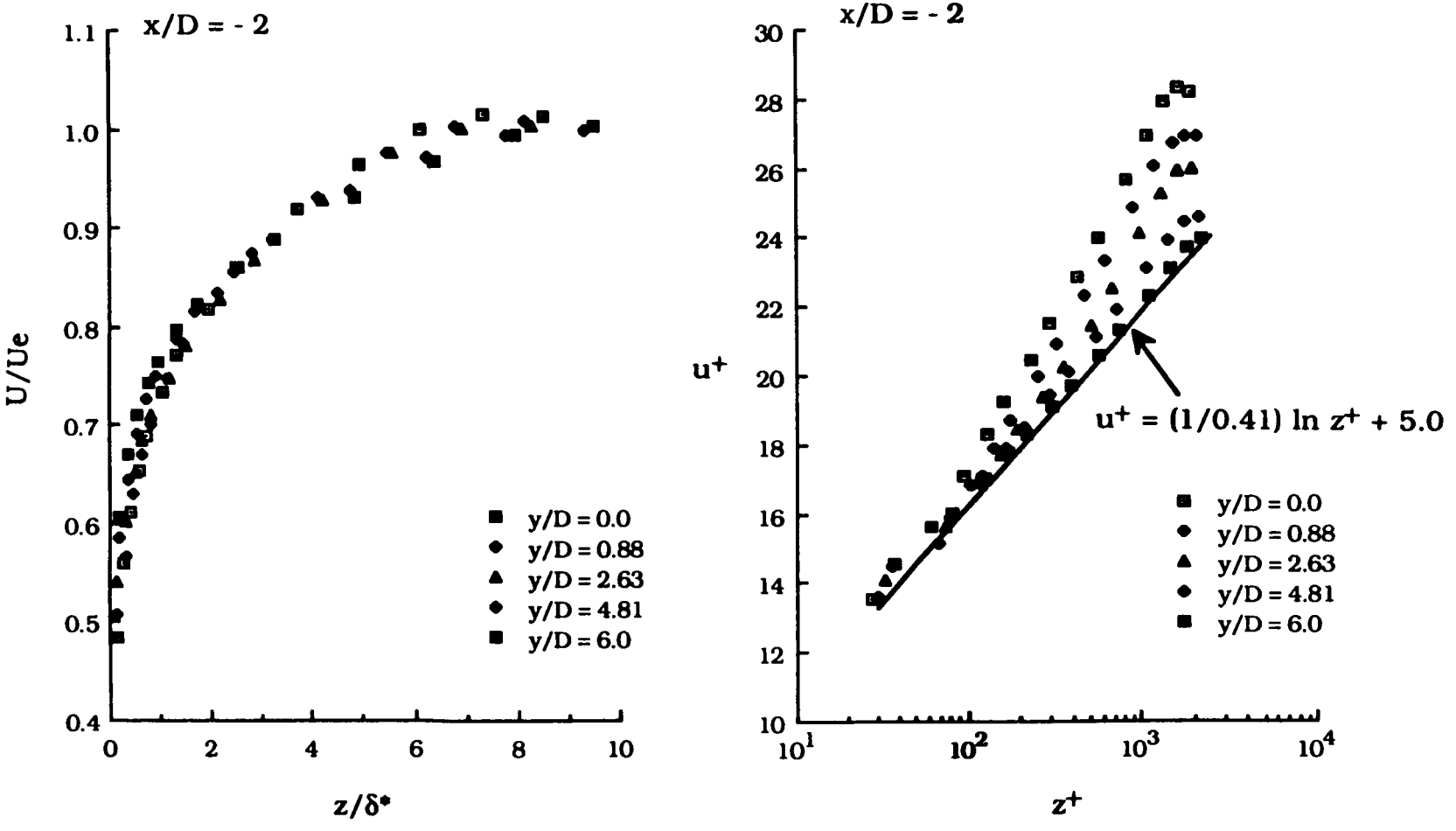

(a) In Outer-Layer Variables

(b) In Inner-Layer Variables

Fig. 5.16 Variation of Mean Velocity Profiles in Y-Direction at x/D = - 2

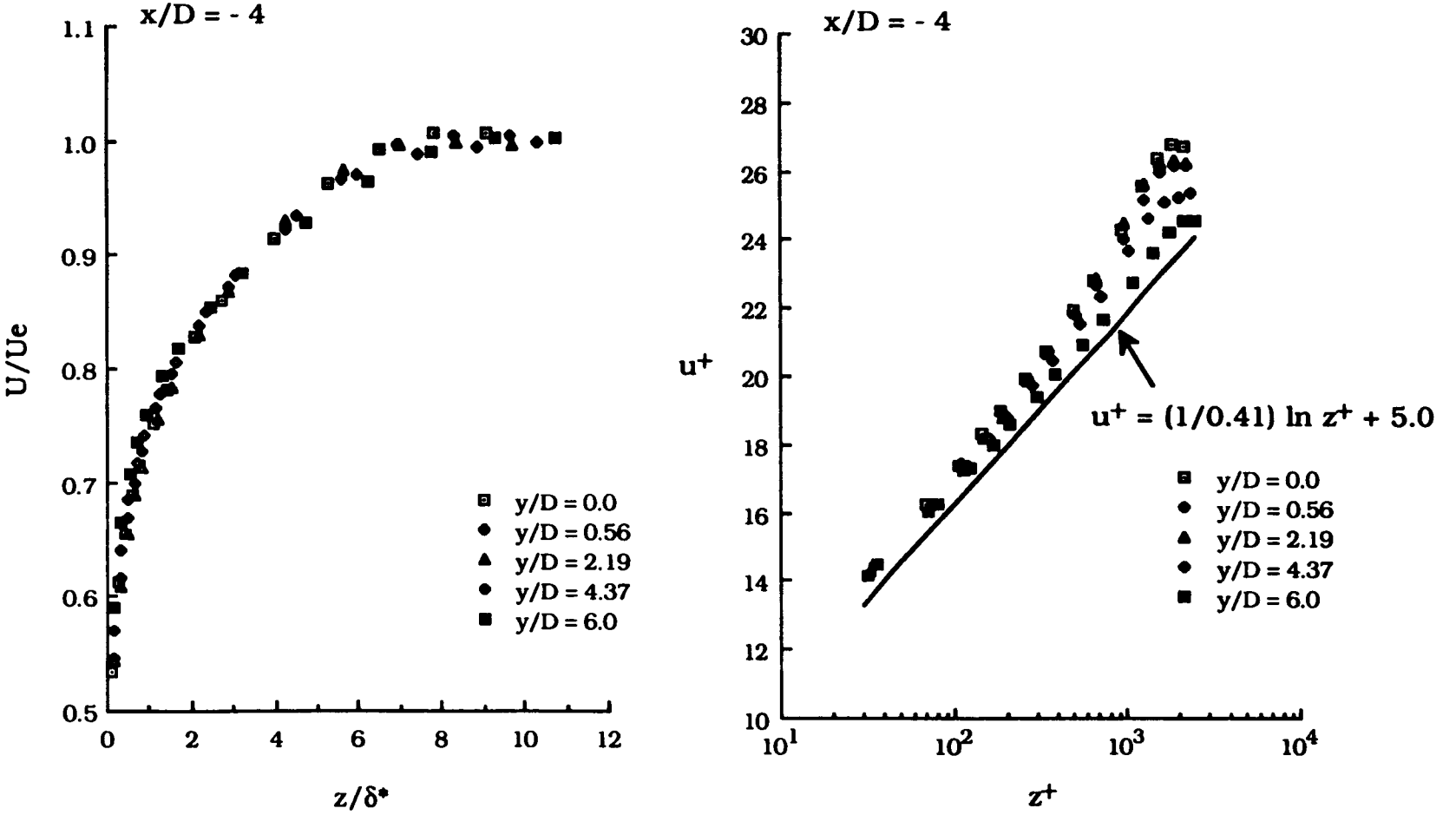

(a) In Outer-Layer Variables

(b) In Inner-Layer Variables

Fig. 5.17 Variation of Mean Velocity Profiles in Y-Direction at x/D = - 4

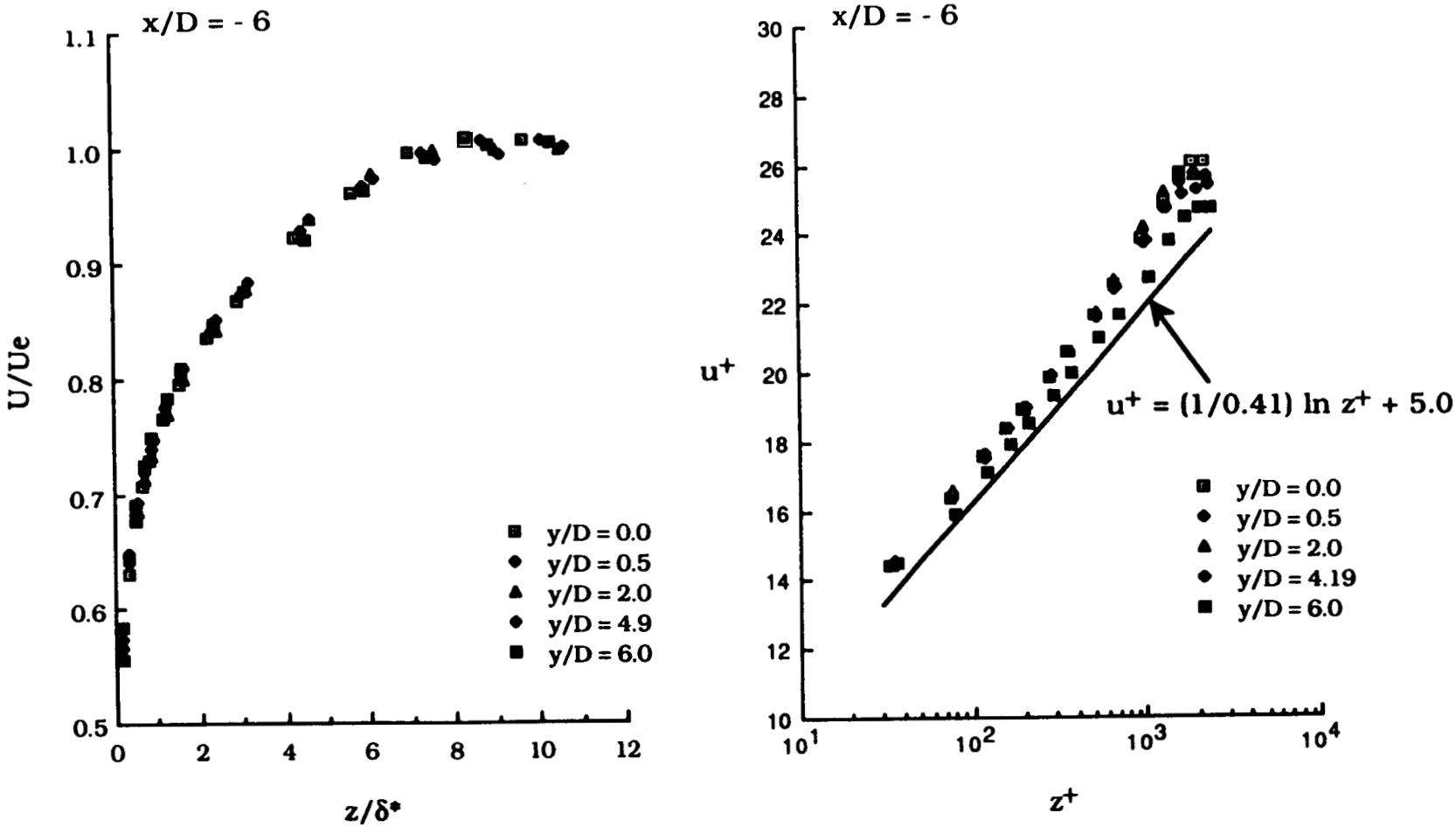

(a) In Outer-Layer Variables

(b) In Inner-Layer Variables

Fig. 5.18 Variation of Mean Velocity Profiles in Y-Direction at x/D = - 6

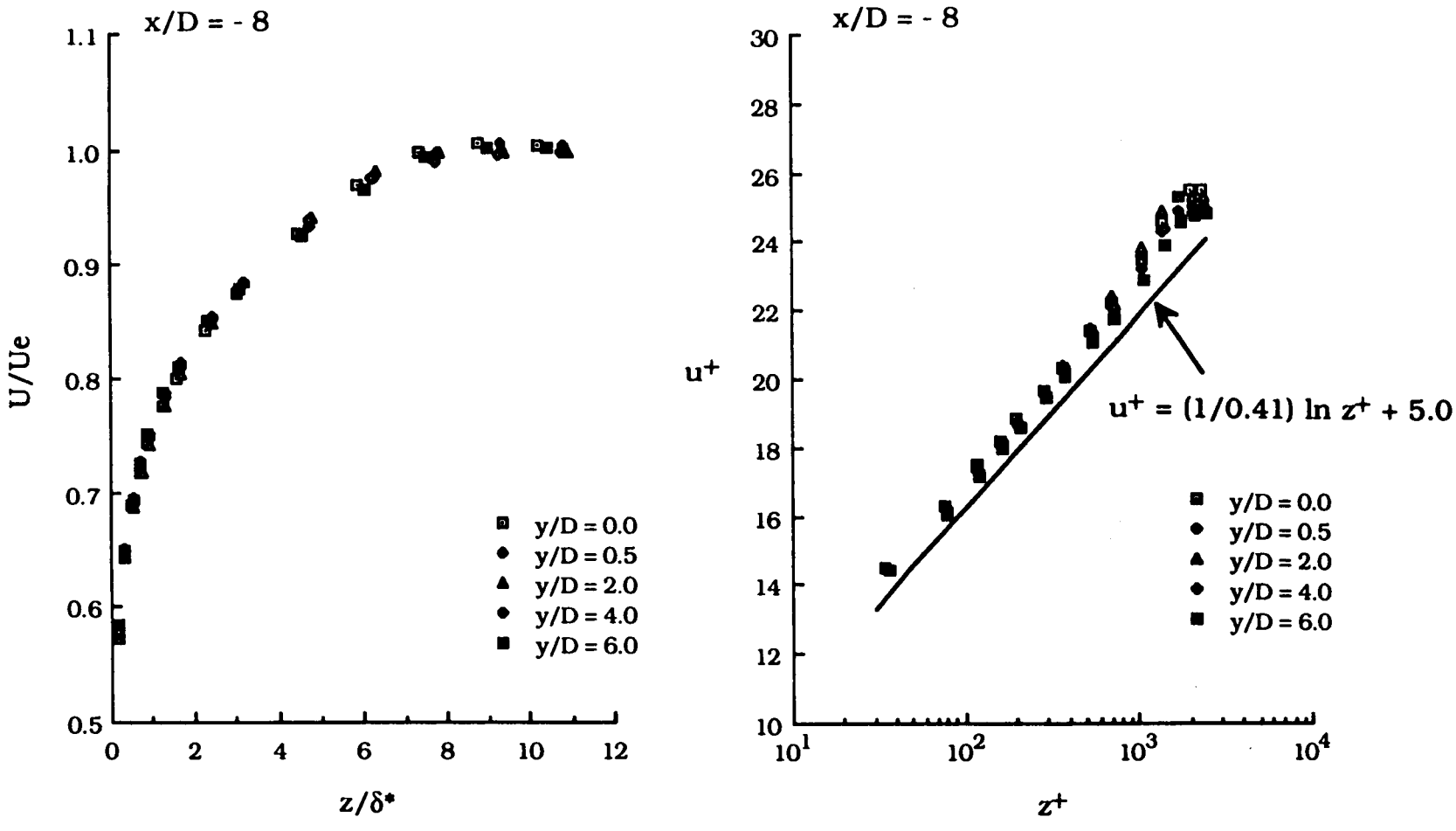

(a) In Outer-Layer Variables

(b) In Inner-Layer Variables

Fig. 5.19 Variation of Mean Velocity Profiles in Y-Direction at x/D = - 8

foregoing discussion that the observed differences in the variation of various boundary layer integral parameters in the X- and Y-directions can be attributed to the existence of varying adverse and favorable pressure gradients, respectively.

Based on the measured mean velocity profiles, surface static pressure, and the local wall shear stress in an upstream region of the blade end-wall corner, it can be stated that the extent of influence of the blade leading edge in the upstream region is ≈ 8D (where D is the blade leading edge diameter). However, in the lateral direction (Y-direction) the flow is influenced by the blade leading edge up to a distance of ≈ 6D.

5.2.5 Surface Static Pressure Variation in Blade End-Wall Corner Region

Fig. 5.20(a) shows the variation of C_p on the flat plate surface (end-wall) in the blade end-wall corner region. At each streamwise station up to x/D = 12, except at x/D = 2, the surface static pressure decreases as the cornerline (the locus of point of intersection of the blade surface and the flat plate) is approached relative to the value far away from the cornerline. This variation occurs because the streamlines are more curved near the cornerline compared to those far away from the blade surface. However, at x/D = 2, the value of C_p first decreases as the blade surface is approached and then increases by a small amount in the close vicinity of the cornerline. Moreover, the trend in the C_p variation reverses downstream of x/D = 12. Also, the rate at which surface static pressure decreases at any streamwise station (except at x/D = 16 and 19.75) as the cornerline is approached is

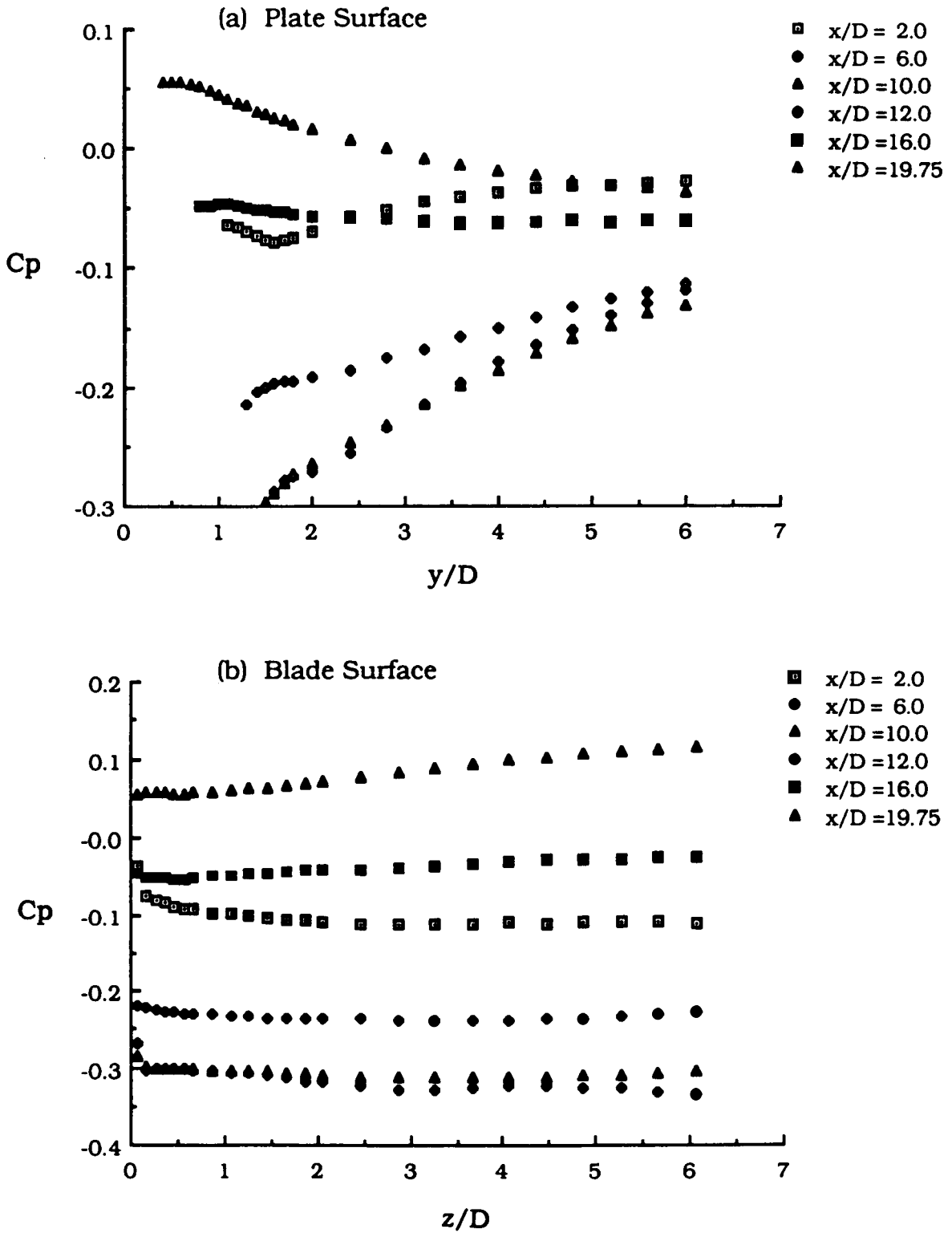

Fig. 5.20 Surface Static Pressure Distribution in Blade End-Wall Corner Region for Case A

larger upstream compared to that downstream of the maximum blade thickness location. In the streamwise direction, i.e., along the corner, the surface static pressure first decreases up to x/D = 10 and, thereafter, it increases as the flow approaches the blade trailing edge. This trend in the variation of C_p along the corner is mainly because of the presence of the streamwise curvature. The flow is expected to accelerate from the blade leading edge up to its maximum thickness location and then decelerate as the flow approaches towards the blade trailing edge.

On the blade surface, the static pressure variation at different streamwise stations is smaller in comparison to that observed on the end-wall surface (Fig. 5.20(b)). At each streamwise station up to x/D = 12, the surface static pressure increases relative to values far away from the cornerline as the cornerline (end-wall surface) is approached. However, at the last two streamwise stations (x/D = 16 and 19.75), the surface static pressure decreases as the end-wall surface is approached. In general, at any streamwise station, the observed increase or decrease in C_p towards the cornerline is within 5% of the free stream dynamic pressure. Also, in the streamwise direction the surface static pressure variation is as expected on the blade surface i.e., it first decreases up to the blade maximum thickness location and, thereafter, it increases. Shabaka[36] reported that his preliminary measurements of surface static pressure on the wing surface of a simplified wing-body junction, at a given streamwise station, showed very little change along the span. Sepri[42] also measured the surface static pressure on the blade surface (airfoil section), at different streamwise stations, in a blade end-wall corner region and found very small

changes in C_p values along its span. The spanwise surface static pressure variation at different streamwise stations on the blade surface in a blade end-wall corner region observed in the present investigation is in good agreement with the results reported by other investigators [36, 42].

Fig. 5.21 shows the comparison of measured surface static pressure on the blade surface, at different streamwise stations and spanwise positions, with the values obtained from potential flow calculations. The potential flow calculation is based on the vortex panel method described by Kuethe and Chow[144]. In this numerical technique, the blade surface is replaced by vortex panels on which the circulation density varies linearly. A computer program developed also by Kuethe and Chow was used. This program required information about the blade geometry as input data. Therefore, the available computer program was modified to incorporate the generation of the blade geometry. At each streamwise station the measured values of C_p at a distance of z = 6D, i.e., far away from the end-wall surface, are generally higher (within 10% of the free stream dynamic pressure) compared to the values obtained from the potential flow calculation. Moreover, the differences in the values of C_p by the two methods are observed to be larger before the maximum thickness section of the blade than at streamwise stations following it. These observed differences can possibly be because the potential flow calculation does not take into consideration the displacement thickness effect. However, the measured C_p distribution clearly shows that the trend in the variation of C_p is similar to that obtained by the potential flow calculation.

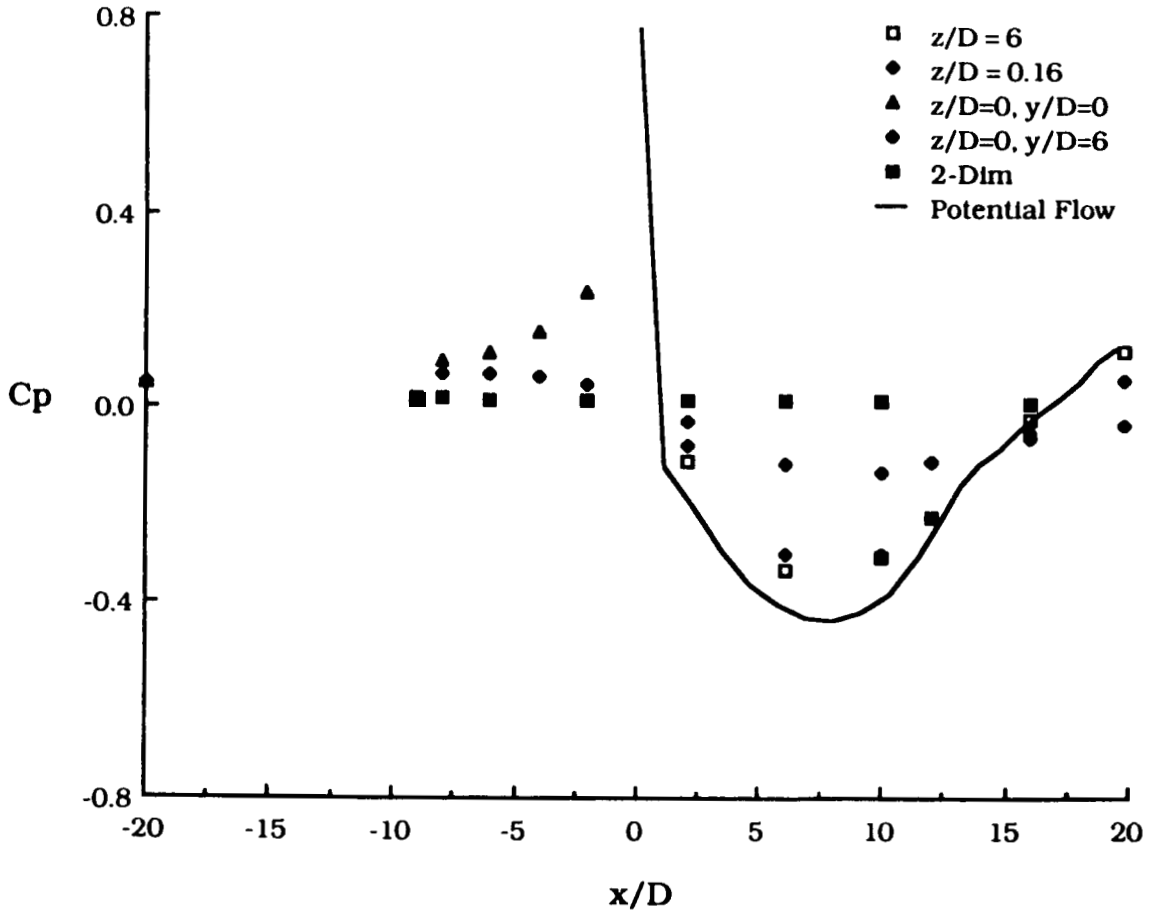

Fig. 5.21 Surface Static Pressure Distribution on Blade Surface- A Comparison Between Measured and Potential Flow Calculation (Case A)

The measured distribution of C_p, at various streamwise stations on the blade surface, in the close vicinity of the end-wall surface (at z/D = 0.16) is also shown in Fig. 5.21. This distribution of C_p compared to its value far away from the end-wall surface (at z/D = 6) suggests that the surface static pressure on the blade surface, in blade end-wall corner region, is not influenced by the corner effects. The variation of the measured C_p on the end-wall surface upstream, in the corner region at a distance of y = 6D, and on the flat plate centerline (two-dimensional case) is also included in Fig. 5.21. The comparison of the C_p distribution for the above mentioned cases shows that C_p values in the three-dimensional case, upstream of the blade leading edge, are higher than the values for the two-dimensional flow. However, in the corner region, C_p values at different streamwise stations are consistently smaller than the values for the two-dimensional flow. The larger differences in C_p in the corner region compared to the values for two-dimensional flow implies the existence of corner effects up to distances of y/D = 6.

As mentioned in chapter III, the distribution of surface static pressure, at three streamwise stations, in the blade end-wall corner region was also obtained by using the conventional technique (i.e., wall taps). Fig. 5.22 shows the comparison of C_p obtained by the surface static tube with the values of C_p measured with the wall taps. The three streamwise locations were chosen such that the accuracy of the surface static tube could be examined in strong to mild favorable and adverse pressure gradients and also in the presence of varying skewness of the turbulent boundary layer. At all streamwise locations, except at x/D = 2 where the boundary layer is strongly skewed, C_p values

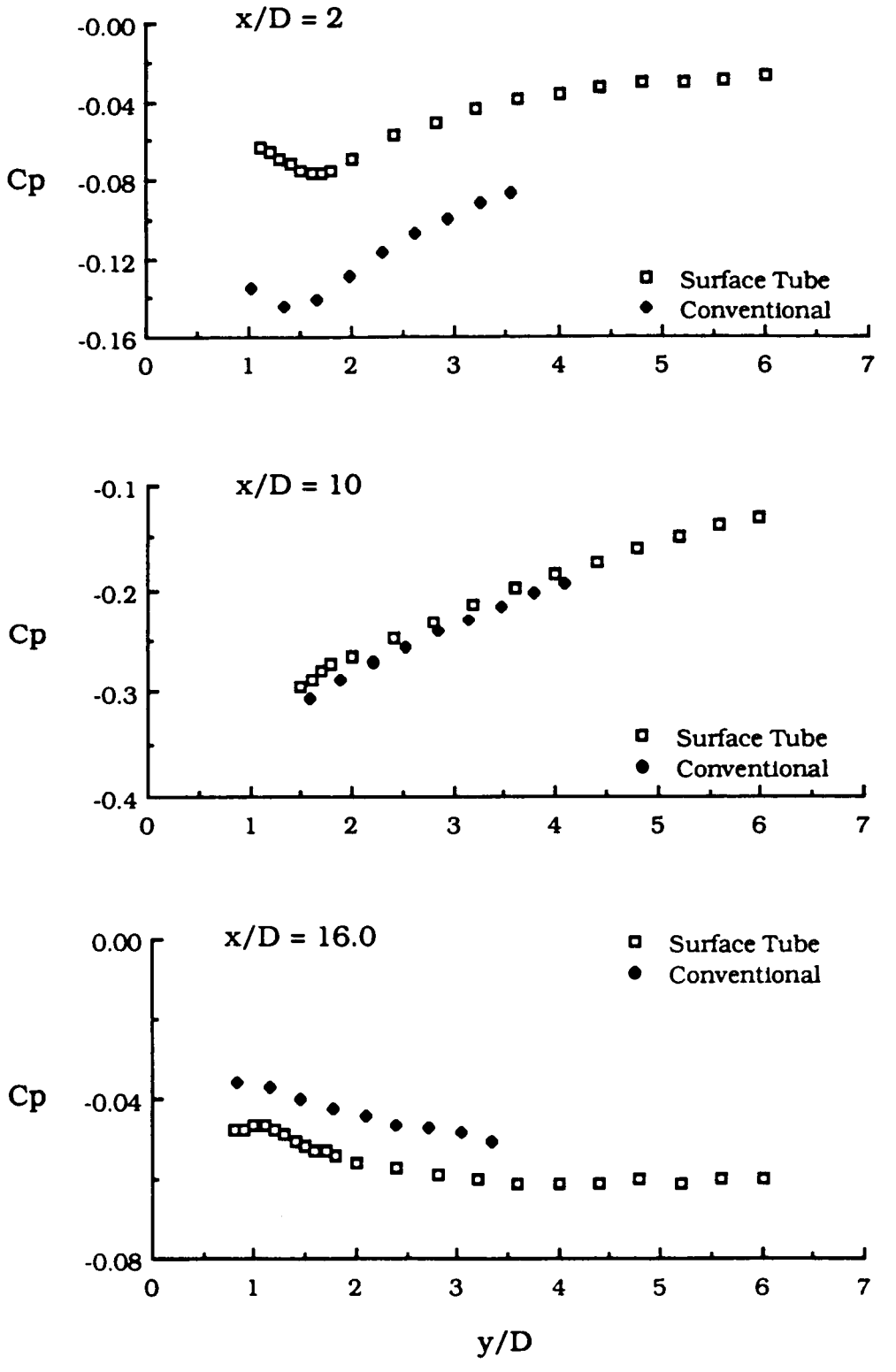

Fig. 5.22 Surface Static Pressure Variation in Blade End-Wall Corner Region- A Comparison Between Surface Static Tube and Conventional Methods (Case A)

obtained from the static tube are in agreement with the values obtained from the wall taps within ± 2% (maximum) of the free stream dynamic pressure. However, at x/D = 2, the differences in C_p obtained with the two techniques are observed to be higher i.e., a maximum of 7% of the free stream dynamic pressure. These large differences in C_p, at x/D = 2, resulting from the two different measurement techniques, probably can be attributed to the presence of large skewness and strong secondary flows.

It is also observed that the absolute magnitude of the surface static pressure measured by the two techniques differ as much as 50% if expressed as a fraction of one another. Generally, if the measured surface static pressure is used for the calculation of velocity, the error in surface static pressure expressed as a fraction of free stream dynamic pressure is commonly used. However, in calculating parameters such as the wall shear stress, the absolute magnitude of the surface static pressure is required. The calculations of the wall shear stress using the observed errors in surface static pressure were made. The results of the analysis showed that large errors (of the order of ≈ 50%) in the surface static pressure measurements would cause very small errors in the calculated value of the wall shear stress. The maximum error in the wall shear stress was observed to be within 7%.

5.2.6 Wall Shear Stress Variation in Blade End-Wall Corner Region

The variation of normalized local wall shear stress on the end-wall surface at different streamwise stations in the corner region is shown in Fig. 5.23(a). At different streamwise locations up to x/D = 12, the wall shear stress increases as the blade surface is approached and

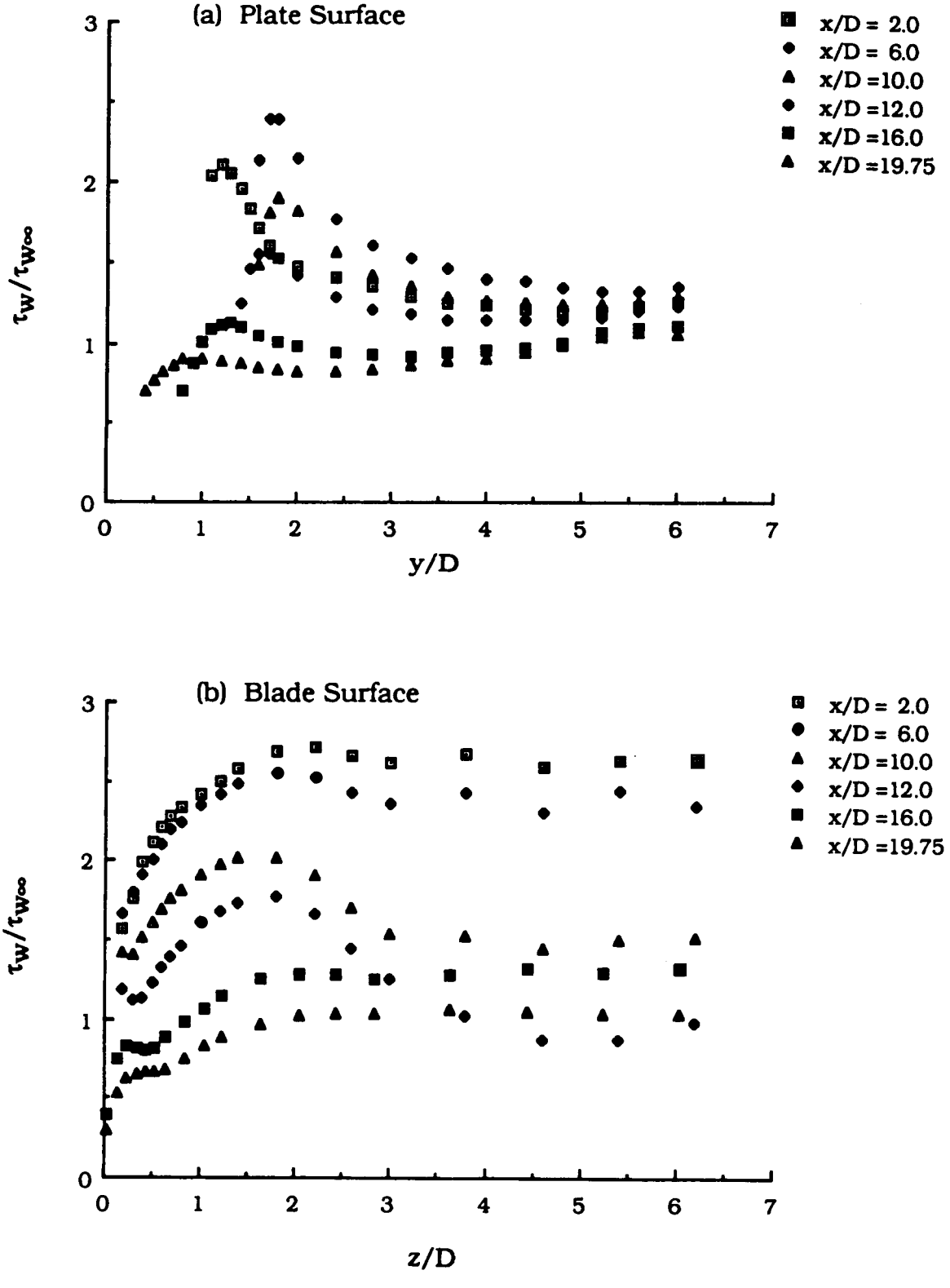

Fig. 5.23 Wall Shear Stress Variation in Blade End-Wall Corner Region for Case A

very close to the cornerline its value decreases. However, at the last two streamwise locations, the value of wall shear stress first decreases as the cornerline is approached and then increases. In the close vicinity of the blade surface it is found again to decrease. It is quite evident, that the maximum value of the normalized wall shear stress and its location from the cornerline changes at different streamwise stations (Figs. 5.24 and 5.25). The maximum value of $(\tau_w/\tau_{w_\infty})_{max}$ occurs at x/D = 6 and it is almost 2.4 times the value of wall shear stress far upstream (at x/D = - 20, y/D = 0) of the corner region as shown in Fig. 5.24.

At a given streamwise location, on the blade surface, the local wall shear stress also attains a maximum value in a region closer to the end-wall surface and then decreases at far distances acquiring an asymptotic value (the wall shear stress values at z/D = 6) as shown in Fig. 5.23(b). Also, at streamwise stations downstream of the maximum blade thickness location, the trend in the variation of the wall shear stress in the Z-direction is different relative to the trend upstream of the maximum blade thickness section (Fig. 5.23(b)). Moreover, at each streamwise station, the maximum value of the wall shear stress and its location from the end-wall surface changes (Figs. 5.24 and 5.25). However, the trend in the variation of the location of $(\tau_w/\tau_{w_\infty})_{max}$ on the blade surface differs from that observed on the end-wall surface (Fig. 5.25).

It is also interesting to note that, at different streamwise locations in the corner region the maximum values of the normalized wall shear stress are consistently higher on the blade surface than the values obtained on the end-wall surface of the test-model(Fig. 5.24).

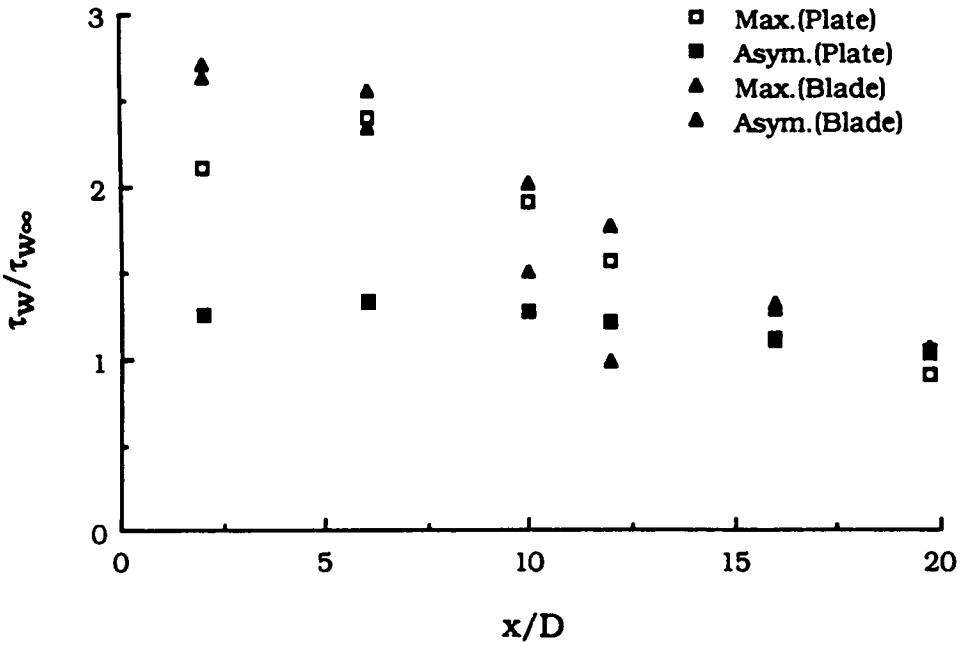

Fig. 5.24 Variation of Maximum and Asymptotic Values of Wall Shear Stress in Blade End-Wall Corner Region for Case A

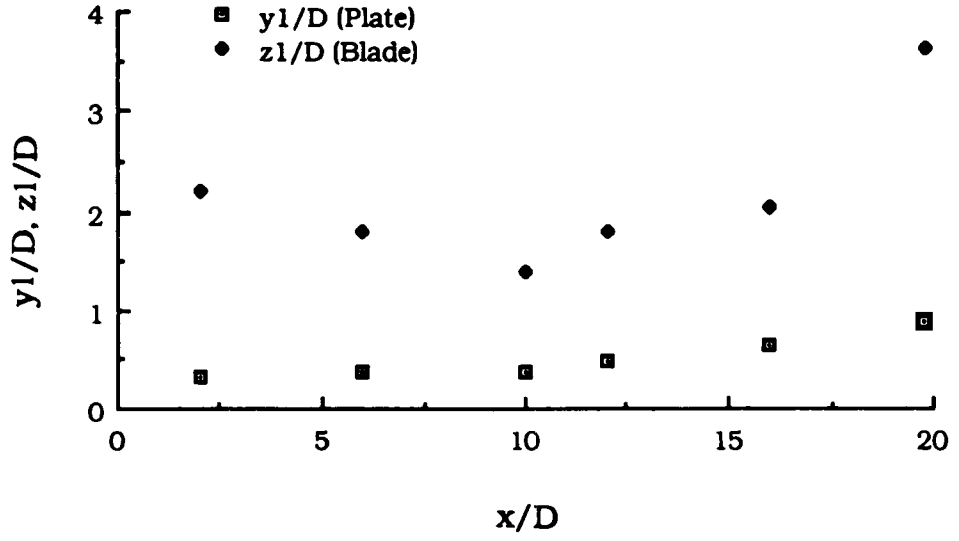

Fig. 5.25 Variation of the Location of Maximum Wall Shear Stress in Blade End-Wall Corner Region for Case A

These observed differences might possibly have been caused by the blade curvature. The asymptotic value (value of the wall shear stress at y/D = 6) of the wall shear stress at different streamwise locations on the end-wall surface in the corner region is approximately 35% higher than the value far upstream of the corner (Fig. 5.24). It is also important to mention that the local wall shear stress, at different streamwise stations and at a distance of y/D = 6 is found to be higher (maximum 30%) than the value at corresponding locations in an absence of the blade (two-dimensional case). Therefore, the corner effects are dominant even up to distance of y = 6 times the blade leading edge diameter.

On the blade surface preceding its maximum thickness section, especially at x/D = 2 and 6, the asymptotic values of the wall shear stress are of the same order as $(\tau_w/\tau_{w_\infty})_{max}$. However, beyond x/D = 6, asymptotic value of the wall shear stress decreases in the streamwise direction (Fig. 5.24).

The variation of the location of $(\tau_w/\tau_{w_\infty})_{max}$ along the corner on both the surfaces of the test-model is shown in Fig. 5.24. On the end-wall surface, the location of the maximum value of the normalized wall shear stress moves from a distance of 0.3D to 0.9D from the blade surface. However, on the blade surface, the location of $(\tau_w/\tau_{w_\infty})_{max}$ moves closer to the end-wall surface and then moves away from it at the last streamwise location, to a distance of ≈ 3.6 times the blade leading edge diameter.

The possible reasons for an increase in the wall shear stress values in the vicinity of the cornerline and changes in the maximum value and the location of the maximum value with respect to the cornerline

are discussed here. The plausible explanation is presented in combination with the flow visualization and three-dimensional mean velocity profile measurements, on the same test-model, by Hazarika, Raj, and Boldman[77]. A detailed discussion of the flow visualization and mean velocity profile measurements in the blade end-wall corner region is given in reference[47]. It is quite evident from the earlier investigations[36, 47, 77] in a blade end-wall corner region that a horseshoe shaped vortex is formed due to the deflection of a two-dimensional vortex sheet as it encounters the blade leading edge. The two legs of the horseshoe vortex wrap around the blade. As this horseshoe vortex moves along the corner it stretches or compresses depending on whether it encounters acceleration or deceleration in the flow. Moreover, at a given streamwise location in the corner region, the presence of the horseshoe vortex causes high momentum fluid to move from the outer region towards the cornerline on both the surfaces. As a result, the mean velocity gradient is expected to increase near the surface consequently giving rise to an increase in the value of wall shear stress. Considering the end-wall surface of the test-model, the maximum value of the wall shear stress at any streamwise location increases up to the blade maximum thickness section (Fig. 5.24). This increase in $(\tau_w/\tau_{w_\infty})_{max}$ can be associated with the stretching of the horseshoe vortex because of acceleration of the flow in the streamwise direction. However, downstream of the blade maximum thickness location the horseshoe vortex gets attenuated because of deceleration of the flow and, as a result, the value of $(\tau_w/\tau_{w_\infty})_{max}$ decreases. The variation in the location of the maximum value of the wall shear stress along the corner on both surfaces of the test-model suggests that the

horseshoe vortex gets distorted as it moves in the downstream direction.

5.2.7 Wall Shear Stress Vectors in Blade End-Wall Corner Region

The wall shear stress vectors obtained with the Preston tube at different streamwise locations on the end-wall surface are shown in Fig. 5.26(a). The dashed lines correspond to the limiting streamline directions obtained from the flow visualization study conducted by Hazarika[47] on the same test-model using an oil dot matrix method. The solid lines correspond to the wall shear stress directions obtained with the Preston tube. The magnitude of both solid and dashed line vectors is based on measurements with the Preston tube. A separation line, obtained from flow visualization, is also shown in Fig. 5.26(a). A variation in the wall shear stress direction, at a fixed streamwise station in the Y-direction, is clearly observed. The maximum value of the wall shear stress direction is observed at streamwise station 5 (x/D = 2) located near the blade leading edge. At streamwise stations 5 and 6, the magnitude of the wall shear stress direction increases as the blade surface is approached. The flow visualization studies revealed that, up to the point of maximum thickness of the blade, the flow turned away from the cornerline. Subsequently, in the region downstream, the flow was directed towards the cornerline. Also, the maximum magnitude and direction of the wall shear stress occurs between the blade surface and the separation line.

The wall shear stress vectors at different streamwise stations on the blade surface are shown in Fig. 5.26(b). At x/D= 2, the magnitude of the wall shear stress direction is larger (maximum value 11 de-

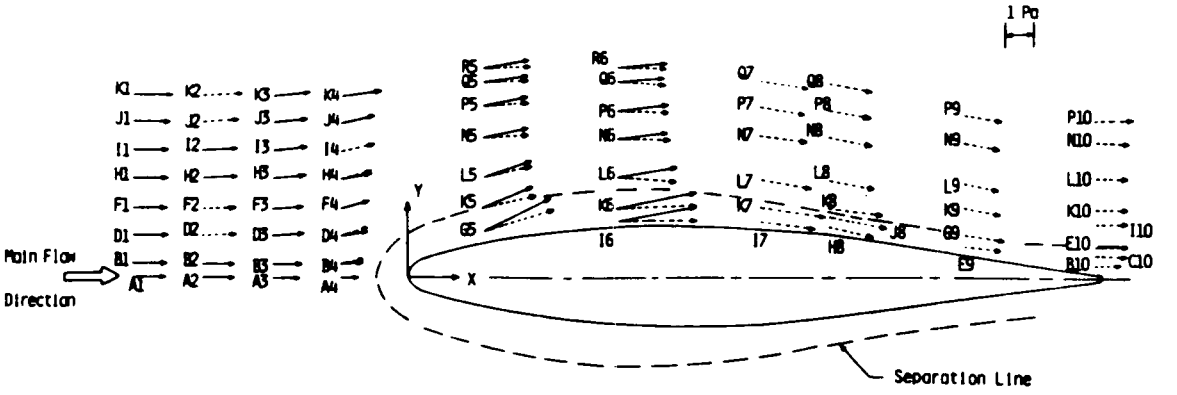

(a) Flat Plate Surface

Preston Tube

Flow Visualization

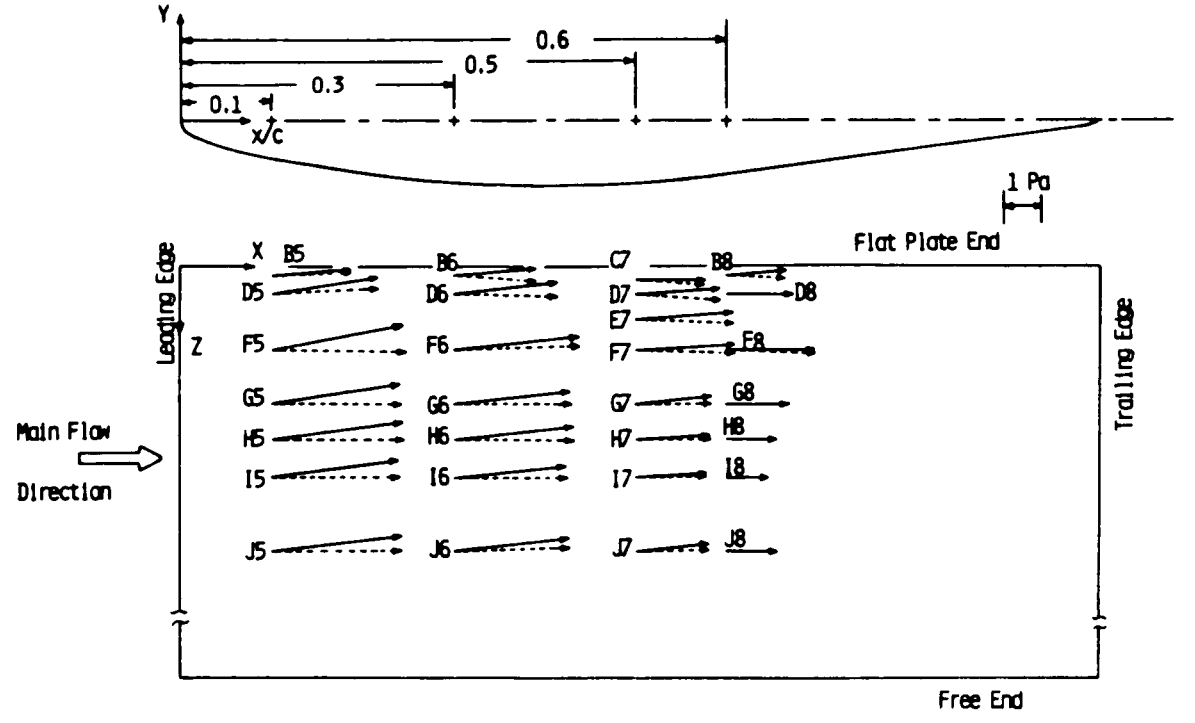

(b) Airfoil Surface

Fig. 5.26 Wall Shear Stress Vectors in Blade End-Wall Corner Region for Case A (for Measurement Locations See Figs. 3.14, 3.16 and 3.17)

grees) than the values at other streamwise locations. Also, a very small change in the wall shear stress direction in the Z-direction is observed. A similar trend in the variation of the limiting streamline direction is evident from the flow visualization study (see Tables 5.2 and 5.3).

The comparison of wall shear stress directions obtained by the two methods shows that the value of the angles obtained with the Preston tube generally differ by 6 to 8 degrees compared to those obtained from the flow visualization study. One of the reasons for this difference can be because the Preston tube measures the flow direction at a distance equal to the effective center of the Preston tube opening. In a three-dimensional flow, the local flow direction changes in a direction normal to the surface. McAllister, Pierce, and Tennant [93] have also reported the existence of differences in the wall shear stress direction obtained from the velocity probe resting on the surface and the limiting streamline directions obtained using the oil streak pattern. Another reason is the yaw sensitivity of the Preston tube. As discussed in section 5.2.1, the Preston tube used in the present study was found to be insensitive to the yaw angle of $\pm 5^0$. This is one reason why the wall shear stress directions obtained with the Preston tube beyond x/D = 6 on the end-wall surface were zero. The limiting streamline directions at streamwise stations beyond x/D = 6 show small angles within the range in which the Preston tube is insensitive.

Table 5.2 Measured Wall Shear Stress Directions With the Preston Tube on End-Wall Surface in Corner Region for Case A (Limiting Streamline Directions Obtained From Flow Visualization Also Included)

Station No.	5		6		7		8		9		10	
	α (degree)		α (degree)		α (degree)		α (degree)		α (degree)		α (degree)	
y (mm)	Preston Tube	Limiting Streamline	Preston Tube	Limiting Streamline	Preston Tube	Limiting Streamline	Preston Tube	Limiting Streamline	Preston Tube	Limiting Streamline	Preston Tube	Limiting Streamline
76.20	11.0	4.0	4.4	-1.50	0.0		0.0		0.0		0.0	
71.12	9.0	3.75	3.6	-2.41	0.0	-7.83	0.0	-10.25	0.0		0.0	
66.04	9.8	5.41	4.6	-2.0	0.0	-7.66	0.0	- 8.25	0.0		0.0	
60.96	12.0	5.50	6.2	-0.41	0.0	-8.25	0.0	- 9.41	0.0	-8.58	0.0	-1.08
55.88	12.2	4.75	6.8	-2.58	0.0	-8.50	0.0	- 7.83	0.0	-9.0	0.0	-3.66
50.80	12.0	4.50	5.8	-0.75	0.0	-7.75	0.0	-10.83	0.0	-9.41	0.0	-3.08
45.72	14.0	7.0	8.0	-3.08	0.0	-9.41	0.0	-13.75	0.0	-9.66	0.0	-2.08
40.64	14.6	10.83	8.4	-2.50	0.0	-10.25	0.0	-13.58	0.0	-9.08	0.0	0.58
35.56	18.8	14.50	8.8	-3.08	0.0	-9.75	0.0	-10.08	0.0	-10.41	0.0	-1.58
30.48	20.8	18.91	8.6	2.66	0.0	-8.50	0.0	- 9.66	0.0	- 9.83	0.0	-1.83
25.40	22.0	18.16	10.4	1.66	0.0	-8.41	0.0	- 8.0	0.0	- 9.91	0.0	-1.66
22.86	23.4	18.0	10.2	-1.83	0.0	-9.0	0.0	- 9.25	0.0	- 8.50	0.0	-0.58
21.59	25.0	17.5	10.8		0.0	-9.0	0.0	-10.25		- 7.08		-0.16
20.32	25.4		9.4	0.08	0.0	-6.75	0.0	-10.58	0.0		0.0	0.25
19.05	29.0	21.0								- 7.25		
17.78	27.0	19.58						-12.41	0.0	- 5.75	0.0	0.33
16.51	26.4	18.16							0.0	- 6.50		1.33
15.24	27.0								0.0		0.0	
13.97	25.8								0.0	- 7.41		0.16
12.70									0.0	- 5.83	0.0	1.16
11.43									-	- 8.25		
10.16									-		0.0	-1.83
8.89											0.0	-3.25
7.62											0.0	-1.83
6.35											0.0	
5.26											0.0	1.91

Table 5.3 Measured Wall Shear Stress Directions With the Preston Tube on Blade Surface in Corner Region for Case A (Limiting Streamline Directions Obtained From Flow Visualization Also Included)

Station No.	5		6		7		8	
z (mm)	α (degree)		α (degree)		α (degree)		α (degree)	
	Preston Tube	Limiting Streamline	Preston Tube	Limiting Streamline	Preston Tube	Limiting Streamline	Preston Tube	Limiting Streamline
2.40	-5.0	-1.91	-5.0	4.75	-5.0		-5.0	3.0
3.67	-5.0		-5.0		0	3.75	-5.0	
4.94	-9.0	-0.25	-6.0	0.50	0	3.16	0	3.91
6.21	-8.0		-5.0	1.25	-4.0		-3.0	4.0
7.48	-9.0	-2.66	-6.0	1.83	-4.0	4.25		0.83
8.75	-9.0		-5.0		-4.0			
10.02	-11.0		-6.0		-4.0	1.75		
12.56	-11.0	-1.16	-6.0	-0.08	-5.0			2.25
15.10	-11.0		-6.0		-4.0	2.75	-3.0	1.75
17.64	-11.0		-6.0		-4.0			
22.72	-11.0	1.0	-6.0	-1.33	-4.0	1.75		2.33
27.80	-10.0	0.41	-6.0	1.0	-4.0	-0.08		2.16
32.88	-8.8	0.41	-6.0	0.25	-4.0			
37.96	-9.0	0.0	-6.0	0.41	-6.0	-0.50		0.41
48.12	-8.0	-0.41	-6.0	0.33	-4.0	-0.33		-0.08
58.28	-8.0	-0.41	-6.0	0.41	-4.0	-1.50		-0.83
68.44	-9.0	-0.33	-6.0		-4.0	-0.41		-4.58
78.60	-7.0	-0.50	-6.0	-1.75	-6.0	-0.91		-1.66

SECTION B

5.3 Three-Dimensional Flow (Case B)

The measured mean velocity profiles at a streamwise location of x/D = - 20, the surface static pressures, and the wall shear stress vectors in the presence of the separation bubble in blade end-wall corner region are discussed in this section.

5.3.1 Mean Velocity Profile Upstream of the Blade Leading Edge (Case B)

The non-dimensional mean velocity profile in terms of outer-layer variables at a streamwise location of x/D = - 20 is shown in Fig. 5.27(a). The non-dimensional mean velocity profile at the same streamwise location in an absence of the blade (two-dimensional flow case) is also included in Fig. 5.27(a). The mean velocity profiles for the two flow conditions (two- and three-dimensional flows) are clearly observed to be self-similar.

Fig. 5.27(b) shows the mean velocity profiles in terms of inner law variables at x/D = - 20 for the two- and three-dimensional flows. The solid line in Fig. 5.27(b) corresponds to the logarithmic law of the wall with the universal constants mentioned earlier. For both the flow conditions the inner law of the wall exists but with different values of the universal constants in the logarithmic law of the wall.

5.3.2 Surface Static Pressure Distribution in Blade End-Wall Corner Region (Case B)

Fig. 5.28 shows the distribution of the surface static pressure at five streamwise locations on both surfaces in the blade end-wall corner region. On the end-wall surface at streamwise location up to x/D = 12

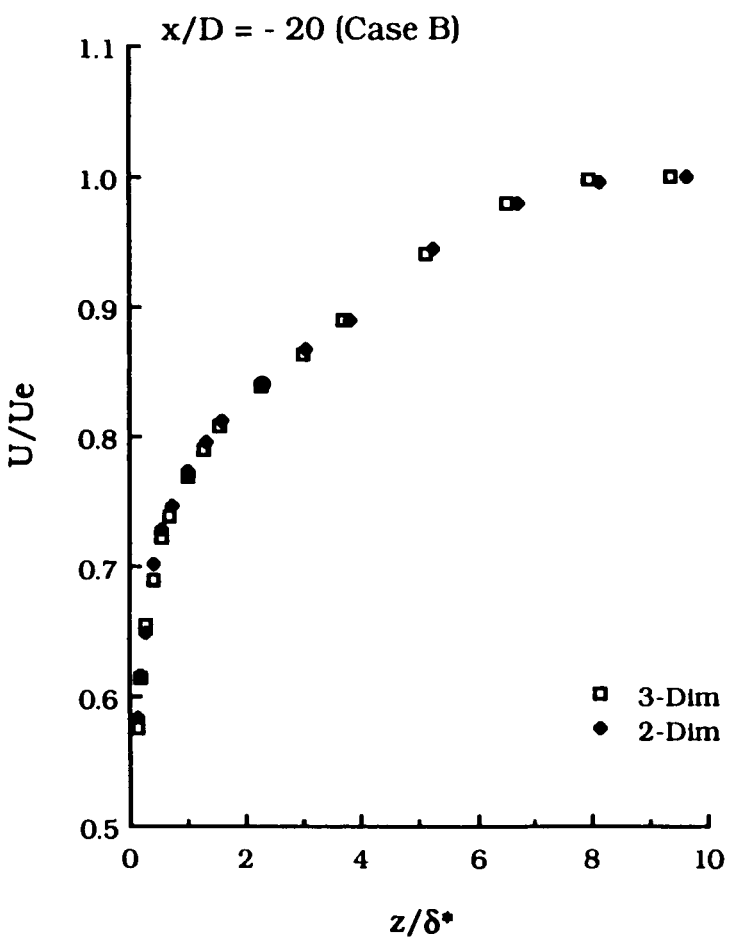

(a) In Outer-Layer Variables

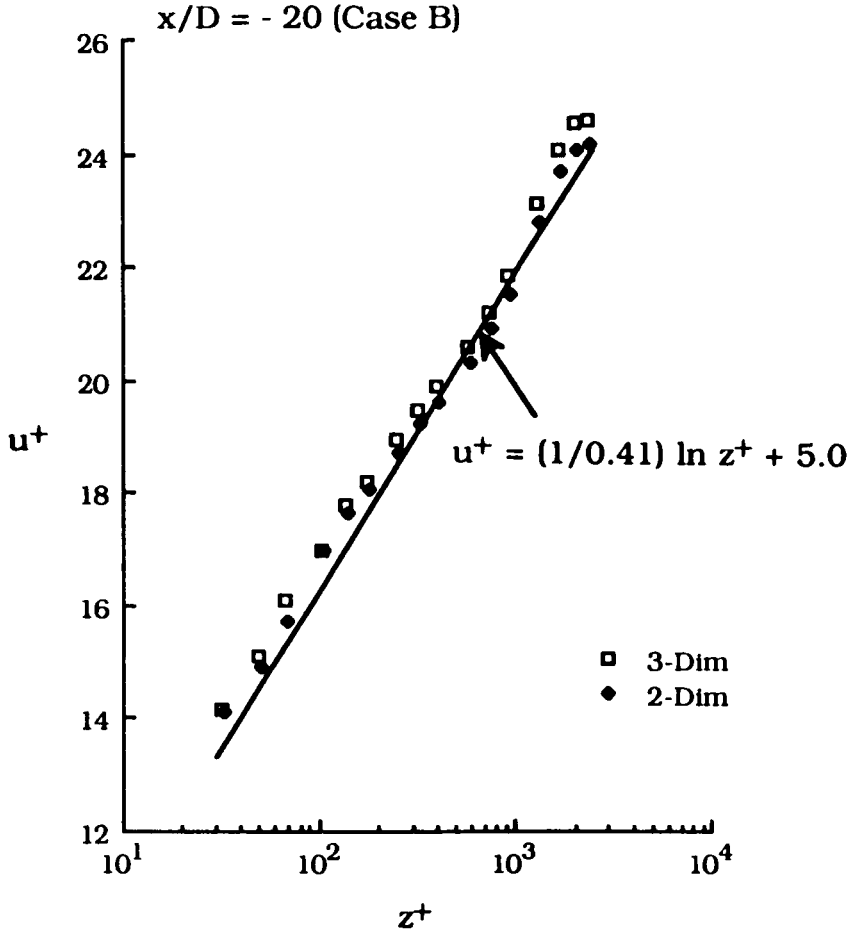

(b) In Inner-Layer Variables

Fig. 5.27 Mean Velocity Profiles Upstream of the Blade Leading Edge at x/D = - 20 for Case B

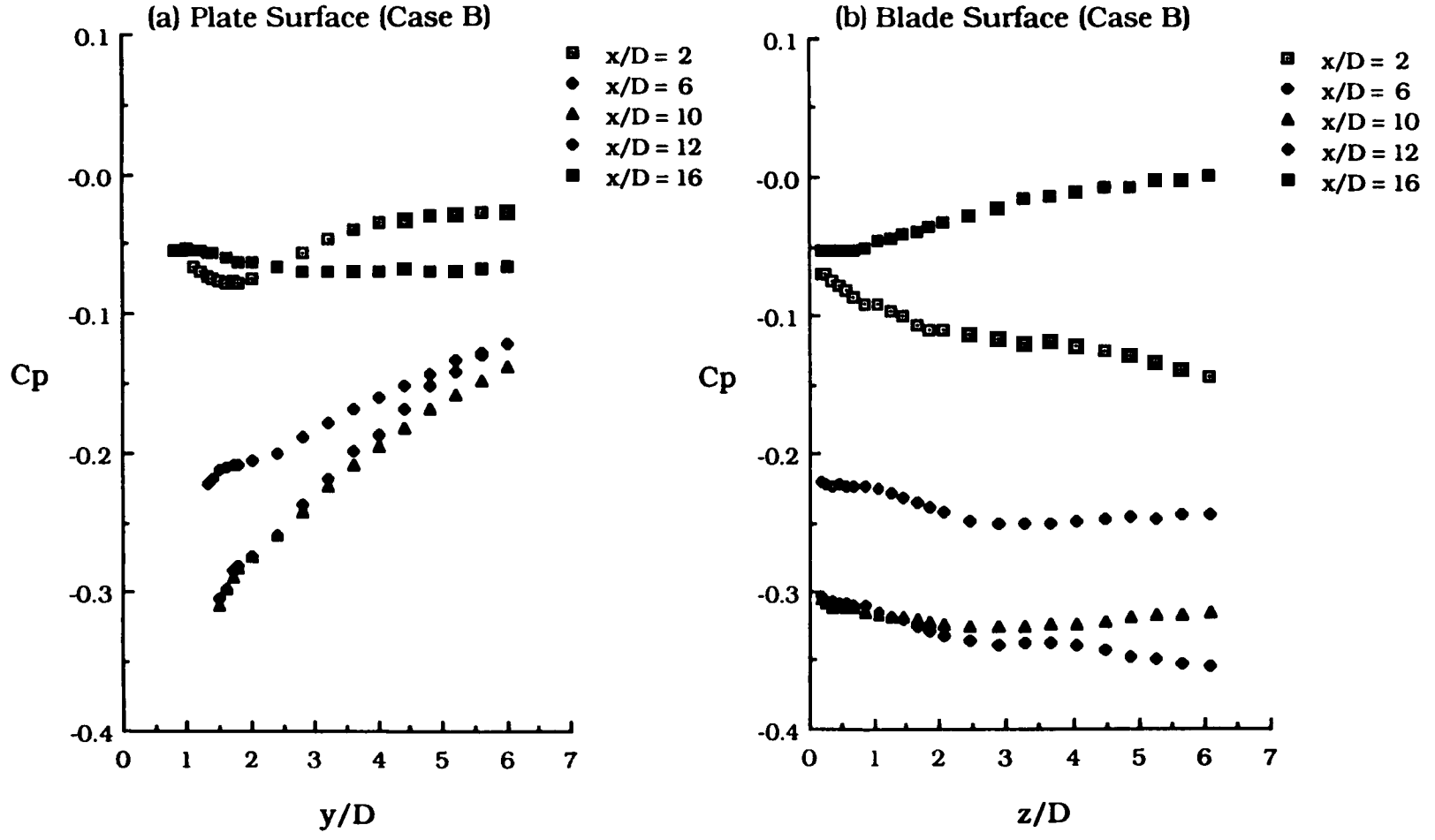

Fig. 5.28 Surface Static Pressure Variation in Blade End-Wall Corner Region for Case B

the surface static pressure decreases as the blade surface is approached (Fig. 5.28(a)). Also the rate in which the surface static pressure decreases changes at different streamwise locations up to x/D = 12. At the streamwise location nearer to the blade leading edge (x/D = 2) the values of C_p first decrease as the blade surface is approached. However, in the vicinity of the blade surface C_p increases. At a streamwise location of x/D = 16, the surface static pressure increases as the blade surface is approached.

On the blade surface, the surface static pressure variation at a fixed streamwise station is smaller than on the end-wall surface (Fig. 5.28(b)). A maximum change in C_p in the Z-direction of approximately 7% of the free stream dynamic pressure is observed at a streamwise location of x/D = 2.

The trend in the variation of the surface static pressure on both the surfaces of the test-model for Case B is similar to the trend for Case A. A detailed discussion of the comparison of different measured parameters for Case A and Case B is presented in section 5.4.

5.3.3 Wall Shear Stress Variation in Blade End-Wall Corner Region (Case B)

The variation of normalized wall shear stress at four streamwise stations on both surfaces of the test-model in the blade end-wall corner region is shown in Fig. 5.29. On the end-wall surface at each streamwise location the magnitude of the wall shear stress increases as the blade surface is approached. However, in the vicinity of the blade surface the wall shear stress decreases (Fig. 5.29(a)). The maximum value of τ_w/τ_{w_∞} and its location with respect to the cornerline

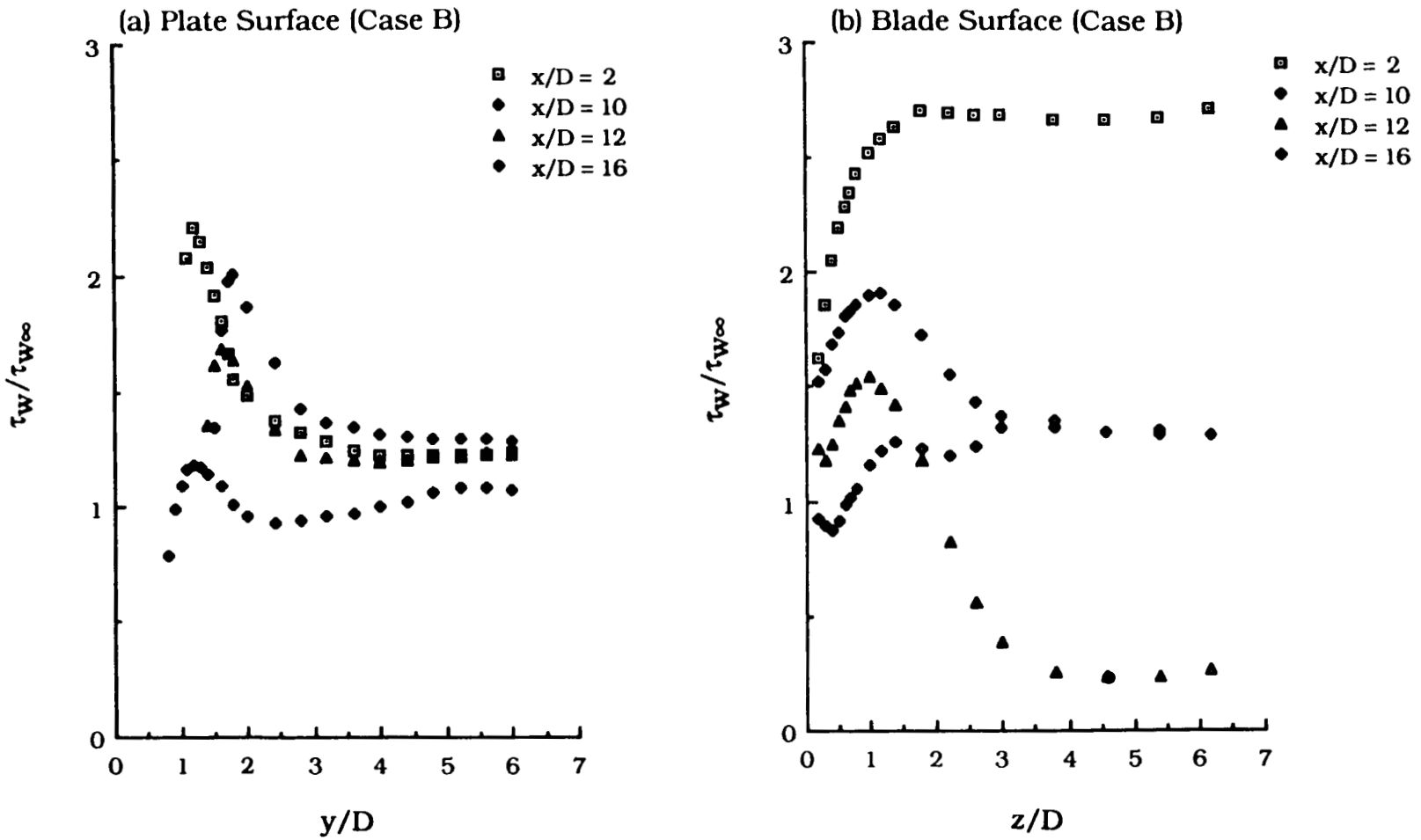

Fig. 5.29 Wall Shear Stress Variation in Blade End-Wall Corner Region for Case B

(i.e., the blade surface) at each streamwise station is different (Figs. 5.30 and 5.31). Among the four streamwise stations considered, the maximum value of $(\tau_w/\tau_{w_\infty})_{max}$ occurs at x/D = 2, and it is approximately 2.2 times the far upstream value (at x/D = -20, y/D = 0) of wall shear stress as shown in Fig. 5.30. The asymptotic values of τ_w/τ_{w_∞} at different streamwise locations are higher (by approximately 30%, maximum) compared to the wall shear stress at x/D = - 20 (Fig. 5.30). These higher asymptotic values of τ_w/τ_{w_∞}, at y/D = 6, relative to far upstream value of wall shear stress, imply the existence of corner effects on the wall shear stress up to distances of y = 6 times the blade leading edge diameter.

On the blade surface at x/D = 2, the normalized value of wall shear stress increases rapidly in the vicinity of the end-wall surface (Fig. 5.29(b)). Furthermore, once the local wall shear stress attains its maximum value at x/D = 2, it does not decrease as is observed at other streamwise stations. A similar variation of the wall shear stress is also observed at streamwise location of x/D = 6 (see Fig. 5.37). It should be mentioned that at x/D = 2 and 6, a similar trend in the variation of local wall shear stress was observed for Case A (see Figs. 5.23(b) and 5.37). There exists a distinctive maximum value of τ_w/τ_{w_∞} at each streamwise location. The location of the maximum value with respect to the end-wall surface varies in the downstream direction as shown in Fig. 5.31. Also, the maximum value of $(\tau_w/\tau_{w_\infty})_{max}$ occurs at x/D = 2 where its value is 2.68, indicating an increase of 168% relative to the far upstream value of the wall shear stress (Fig. 5.30).

At x/D = 12 on the blade surface, a significant decrease in the wall shear stress value is observed. The value of τ_w/τ_{w_∞} starts de-

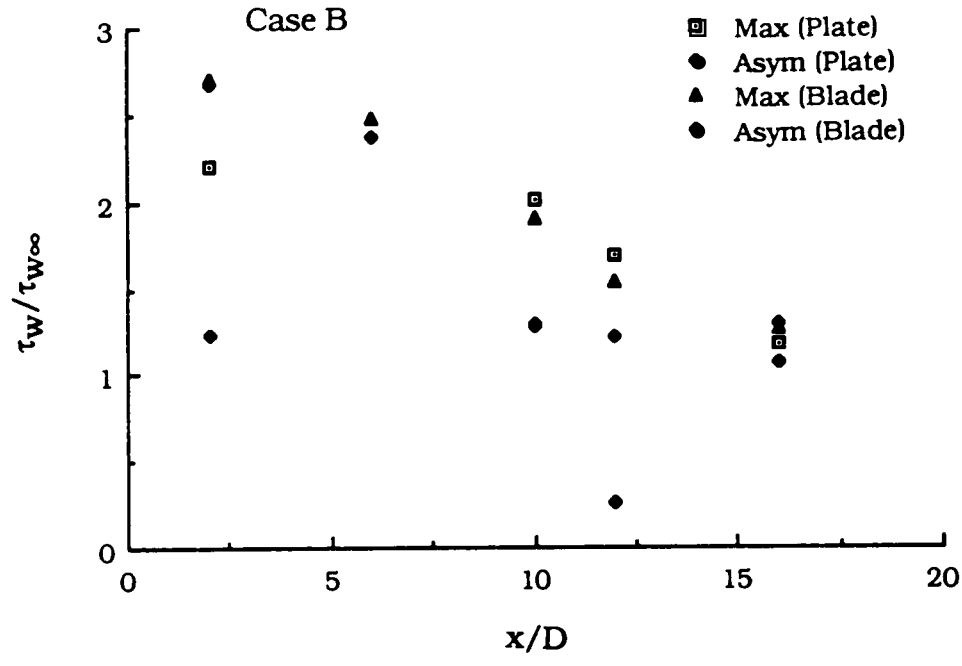

Fig. 5.30 Variation of Maximum and Asymptotic Values of Wall Shear Stress for Case B

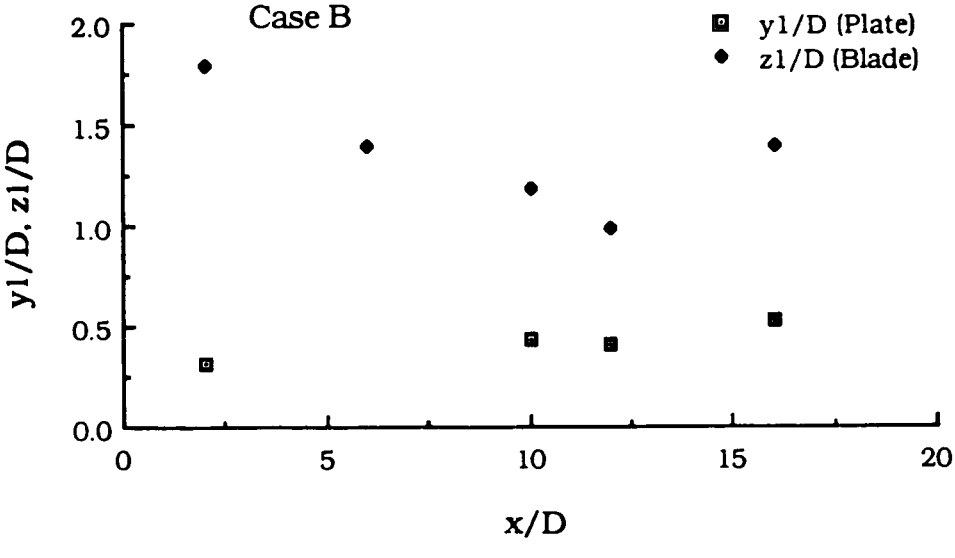

Fig. 5.31 Variation of the Location of Maximum Wall Shear Stress for Case B

creasing sharply at z/D ≈ 1.19 and continues to decrease up to z/D ≈ 3.8. In a distance of approximately 2.6D the value of τ_w/τ_{w_∞} decreased by ≈ 80% (Fig. 5.29(b)). This large decrease in the wall shear stress value is directly related to the presence of the separation bubble. It can also be stated that in the Z-direction the separation bubble extends from z/D ≈ 1.2 to 2.6. Also, at x/D = 16 on the blade surface, the variation of the wall shear stress shows the usual trend i.e., in the vicinity of the end-wall surface, the wall shear stress increases. Thereafter, it decreases and achieves an asymptotic value. This variation at x/D = 16 implies the flow has reattached to the blade surface again. The above mentioned discussion also suggests that the separation bubble formed somewhere after x/D = 10, and then the flow reattached before the streamwise location of the x/D = 16. These results are found to be in good agreement with the flow visualization studies (Fig. 5.32). Fig. 5.32 shows a photographic view of the limiting streamlines obtained with the oil dot matrix technique. The separation bubble can be clearly seen in Fig. 5.32. In the Z-direction the separation bubble extends from a distance of z = 2D to 5.6D, whereas in the streamwise direction it starts after x = 10D and ends between x = 14D to 16D (Fig. 5.32).

The variation of the maximum and asymptotic values of τ_w/τ_{w_∞} on both surfaces of the test-model in the blade end-wall corner region is shown in Fig. 5.30. On both the surfaces the variation of $(\tau_w/\tau_{w_\infty})_{max}$ is similar to that observed in Case A (see Fig. 5.24). Therefore, the reasons given earlier are applicable for this case. A sudden drop in the asymptotic value observed at x/D = 12 is mainly attributed to the presence of the separation bubble. The maximum val-

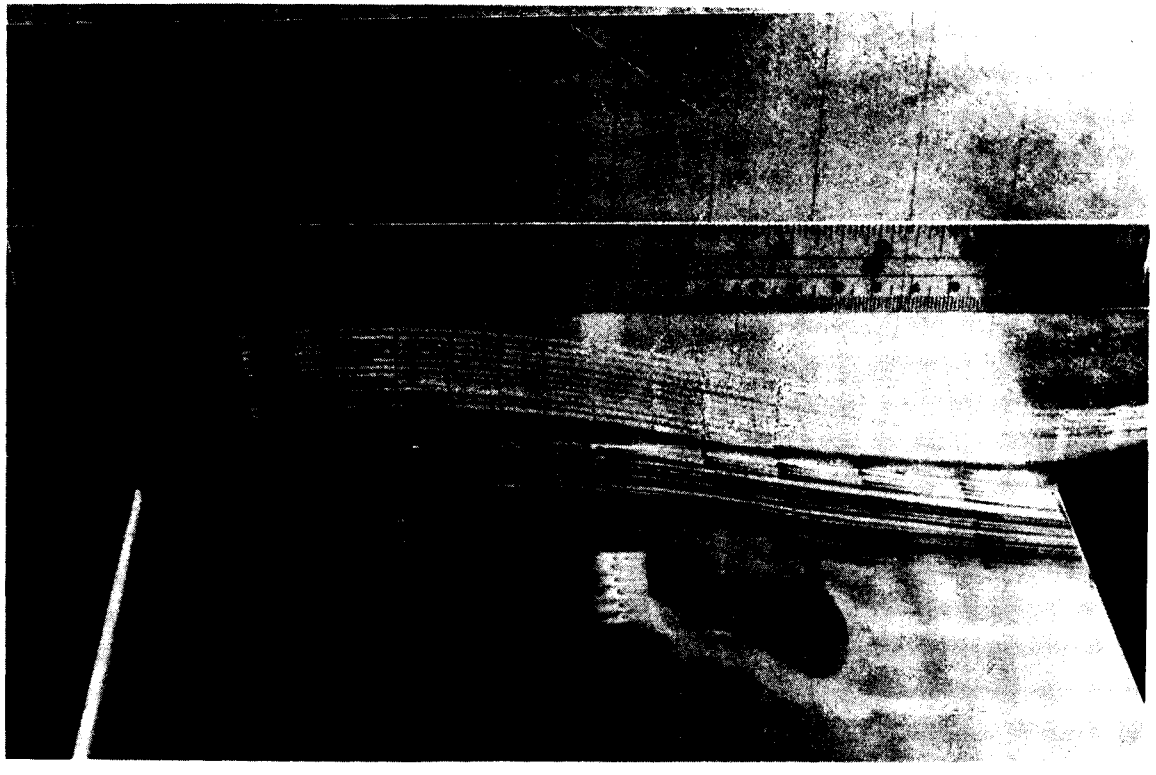

Fig. 5.32 Location and Shape of Separation Bubble on the Blade Surface of the Test-Model Obtained From Flow Visualization for Case B

ues of τ_w/τ_{w_∞} at x/D = 10 and 12 are smaller on the blade surface relative to the values on the end-wall surface. This is also possibly caused by the presence of the separation bubble on the blade surface.

Fig. 5.31 shows the variation of the location of the maximum values of τ_w/τ_{w_∞} on both the surfaces in the blade end-wall corner region. On the end-wall surface, the location of $(\tau_w/\tau_{w_\infty})_{max}$ is observed to change from a distance of y = 0.32D to 0.53D. On the blade surface, the location of the maximum value of the wall shear stress first moves closer to the cornerline (i.e., nearer to the end-wall surface) up to streamwise location of x/D = 12 and, thereafter, it moves away from the end-wall surface as the flow progresses closer to the blade trailing edge.

5.3.4 Wall Shear Stress Vectors in Blade End-Wall Corner Region (Case B)

5.33(a) shows wall shear stress vectors at different streamwise locations on the end-wall surface of the test-model. For comparison purposes, the wall shear stress vectors for case A are also included. The wall shear stress vectors represented by solid and dashed lines correspond to Case A and Case B, respectively. Also, only at streamwise location of x/D = 2, the wall shear stress direction was obtained by using the Preston tube. However, at other streamwise locations, the directional information was obtained from the flow visualization study because the wall shear stress directions were found too small for the Preston tube to sense. On the end-wall surface, the wall shear stress at various measurement locations is higher for Case A than for Case B, whereas the magnitude of the wall shear stress directions for the two

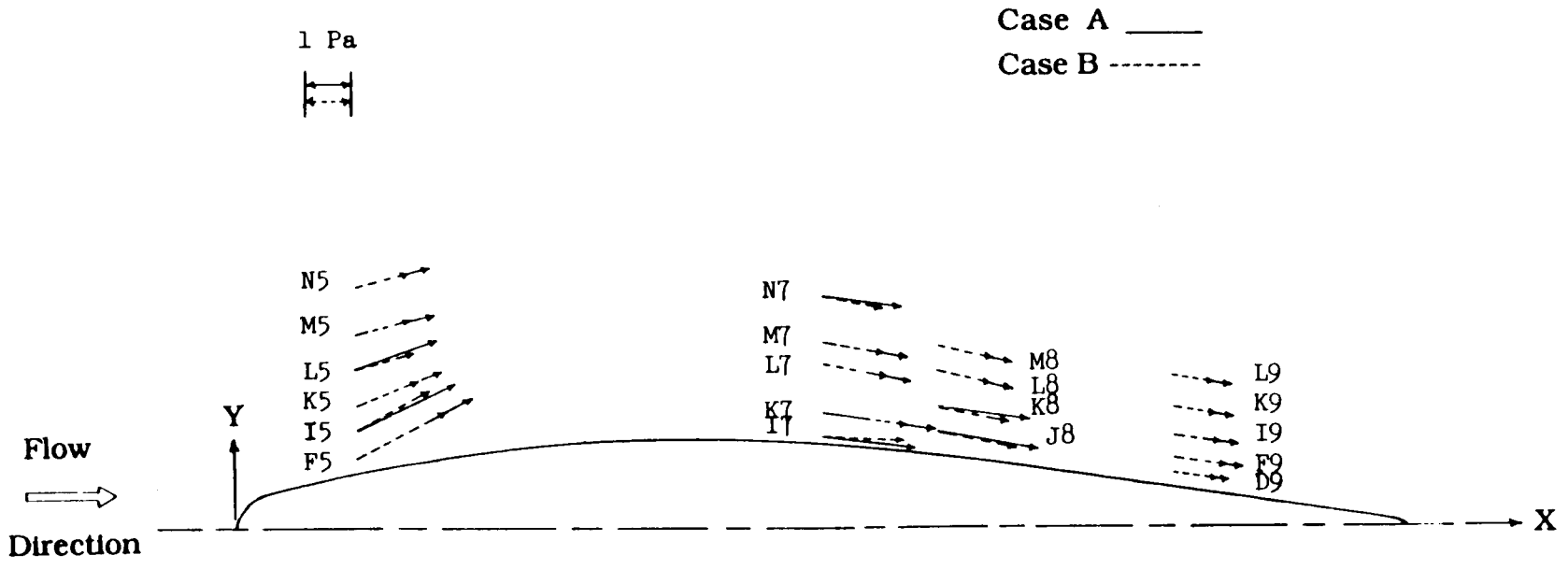

Fig. 5.33(a) Comparison of Wall Shear Stress Vectors on the Flat Plate Surface of the Test-Model For Case A and Case B

cases did not differ appreciably. One of the main reasons for the observed increase in the magnitude of the wall shear stress for Case A relative to Case B is the presence of an increased level of free stream turbulence in Case A. As mentioned in Chapter III, the turbulence generating grids were employed in Case A to avoid the formation of a separation bubble. Also, in Case B the free stream velocity was 23 m/s compared to 27.3 m/s for Case A.

A comparison of the wall shear stress directions on the end-wall surface obtained from the flow visualization for Case A and Case B (see Tables 5.2 and 5.4) indicates small differences in the magnitude of the wall shear stress directions at different streamwise locations, except at x/D = 2. At a streamwise location of x/D = 2, the maximum difference in angles for the two cases is approximately 5 to 6 degrees.

On the blade surface the wall shear stress vectors at different streamwise locations are shown in Fig. 5.33(b). In this figure the vectors represented by dashed lines correspond to the limiting streamline direction obtained from the flow visualization. The separation bubble is also traced by using the flow visualization picture. The wall shear stress directions obtained with the Preston tube, at different streamwise locations, vary only slightly in the Z-direction (see also Table 5.5). The variation of the wall shear stress direction obtained from the flow visualization technique is similar to the variation obtained with the Preston tube.

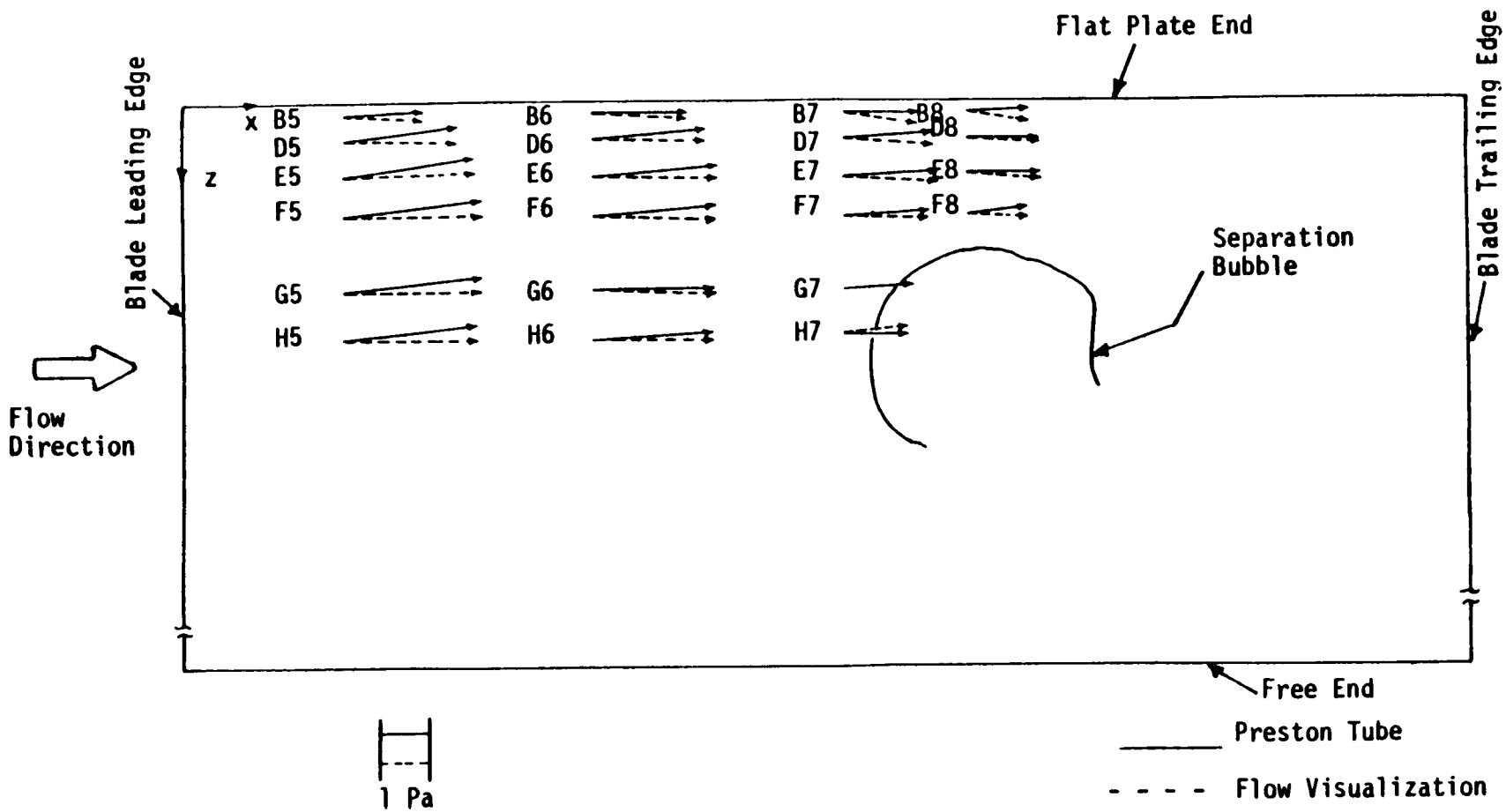

Fig. 5.33(b) Wall Shear Stress Vectors at Various Streamwise Stations on the Blade Surface of the Test-Model for Case B (for Measurement Locations See Figs. 3.16 and 3.17)

Table 5.4 Measured Wall Shear Stress Directions With the Preston Tube on End-Wall Surface in Corner Region for Case B (Limiting Streamline Directions Obtained From Flow Visualization Also Included)

Station No.	5		7		8		9	
	α (degree)		α (degree)		α (degree)		α (degree)	
y (mm)	Preston Tube	Limiting Streamline	Preston Tube	Limiting Streamline	Preston Tube	Limiting Streamline	Preston Tube	Limiting Streamline
76.2	9.0		0.0		0.0		0.0	
71.12	9.0		0.0		0.0		-4.6	
66.04	11.0		0.0		0.0		-3.8	
60.96	11.0		0.0		0.0		0.0	
55.88	12.8		0.0		0.0		0.0	
50.80	13.0	7.50	0.0	-9.16	0.0		0.0	
45.72	14.0	9.41	0.0	-10.83	0.0	-15.08	0.0	
40.64	14.0	11.0	0.0	-9.75	0.0	-12.41	0.0	
35.56	14.8	12.0	0.0	-10.75	0.0	-13.66	0.0	-9.41
30.48	17.0	12.08	0.0	-9.50	0.0	-12.25	-5.8	-8.25
25.40	21.4	11.91	0.0	-7.75	0.0	-11.66	0.0	-8.83
22.80	23.8	13.50	0.0	-8.91	0.0	-12.41	-3.8	-8.66
21.59	27.2	15.75	0.0	-8.16	0.0	-12.0		-8.91
20.32	28.0	16.41	0.0	-3.66	0.0	-10.41	0.0	-8.66
19.05	27.2		0.0					
17.78	28.8	15.91					0.0	-7.50
16.51	26.6					- 6.41	0.0	-7.83
15.24	26.4	18.58					0.0	-8.0
13.97	25.4						0.0	-4.0
12.70							0.0	
11.43								-4.91
10.16								-6.0

Table 5.5 Measured Wall Shear Stress Directions With the Preston Tube on Blade Surface in Corner Region for Case B (Limiting Streamline Directions Obtained From Flow Visualization Also Included)

Station No.	5		6		7		8	
Z (mm)	α (degree)		α (degree)		α (degree)		α (degree)	
	Preston	Limiting Streamline	Preston	Limiting Streamline	Preston	Limiting Streamline	Preston	Limiting Streamline
2.40	-3	2.83	0	3.16	0	8	-3	9
3.67	0	-	0	1.0	0	4.91	0	3.75
4.94	-4	-	-5	-	0	-	0	-
6.21	-6	-	-4	-	0	4	0	-
7.48	-7	0.83	-5	0.67	-4	3.5	0	3.17
8.75	-7	-	-4	0.83	0	-	0	-
10.02	-7	-	-4	0.83	0	2.67	0	3.75
12.56	-8	-2.30	-5	1.25	0	2.0	-3	4.08
15.10	-8	-1.58	-5	0.83	-3	2.75	0	4.42
17.64	-6	-	-5	1.25	-	-	-6	4.0
22.72	-6	0	-5	1.67	-4	1.75	-7	3.25
27.80	-7	-	-5	1.83	-4	1.67	-6	2.25
32.88	-6	0	-4	1.67	-4	1.25	-8	-
37.96	-6	-0.25	0	1.50	-4	-4.17	-10	-
48.12	-6	0	-4	0.54	0	-5.62	0	-
58.28	-6	-	-4	-	0	-	0	-
68.44	-4	-	-4	-	0	-	0	-
78.60	0	-	-4	-	0	-	0	-

5.4 Comparison of Surface Static Pressure and Wall Shear Stress for Case A and Case B

As mentioned in Chapter III, the free stream velocity for Case A and Case B was different. Therefore, a quantitative comparison of the results can not be made. However, the results for the two cases are compared qualitatively. Furthermore, the effects of the presence of separation bubble on the measured surface static pressure and the wall shear stress are qualitatively analyzed.

5.4.1 Comparison of Surface Static Pressure

Fig. 5.34 shows a comparison of the surface static pressure at five streamwise locations on the end-wall surface of the test-model for Case A and Case B. A similar trend in the variation of the surface static pressure at different streamwise locations is observed for the two cases. No significant influence of the separation bubble is seen in the measured surface static pressure.

The comparison of surface static pressure at five streamwise locations on the blade surface for the two cases is shown in Fig. 5.35. At each of the streamwise locations, the variation in surface static pressure in the Z-direction is small (maximum of 7% of the free stream dynamic pressure). There is no influence of the separation bubble, which existed on the blade surface, on the surface static pressure distribution.

5.4.2 Comparison of Wall Shear Stress

Fig. 5.36 shows the comparison of the normalized wall shear stress at four streamwise locations on the end-wall surface for case A and case B. The variation of normalized wall shear stress for the two cases at different streamwise locations clearly shows a similar trend.

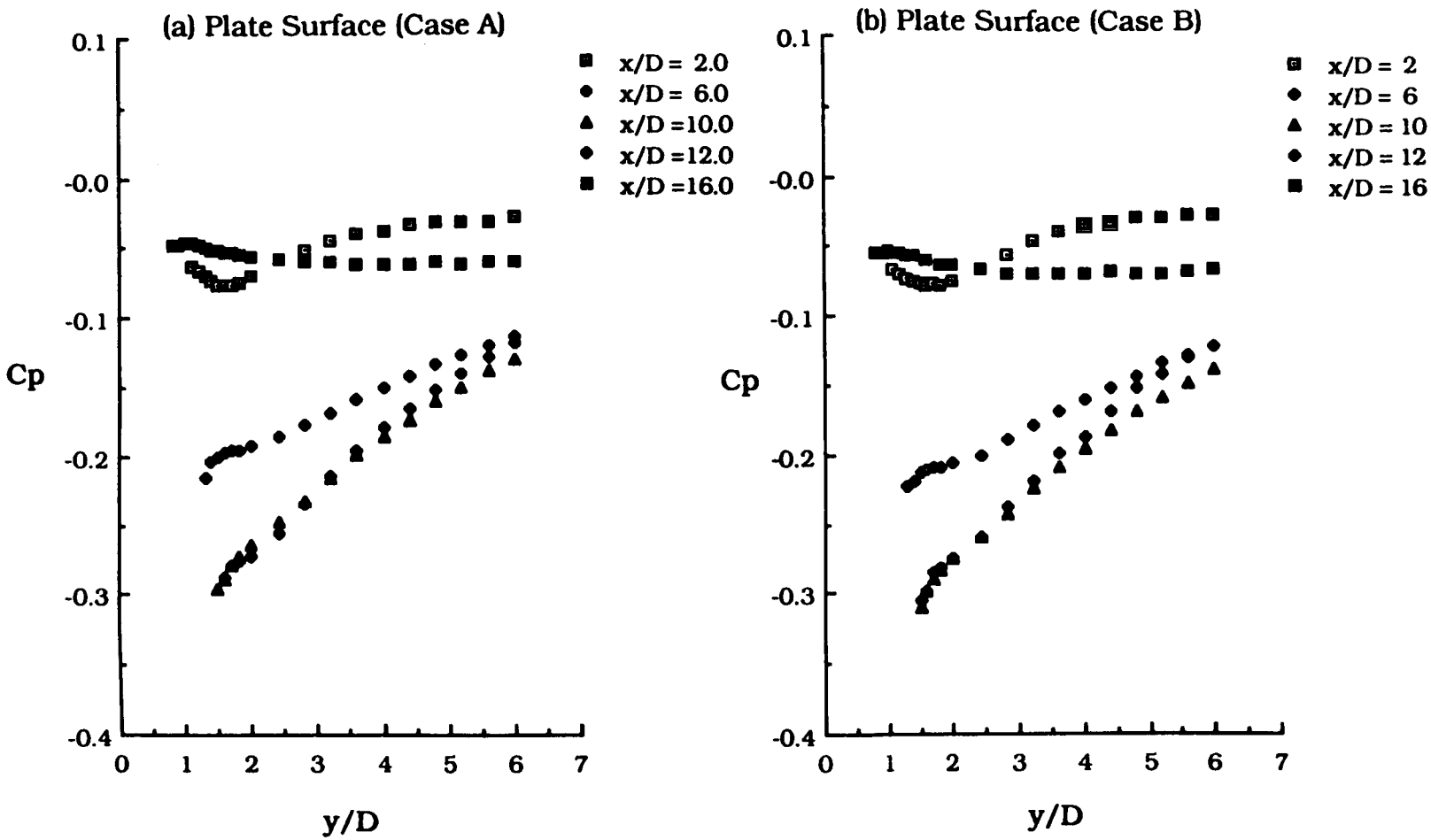

Fig. 5.34 Surface Static Pressure Variation on the Flat Plate Surface of the Test-Model- A Comparison Between Case A and Case B

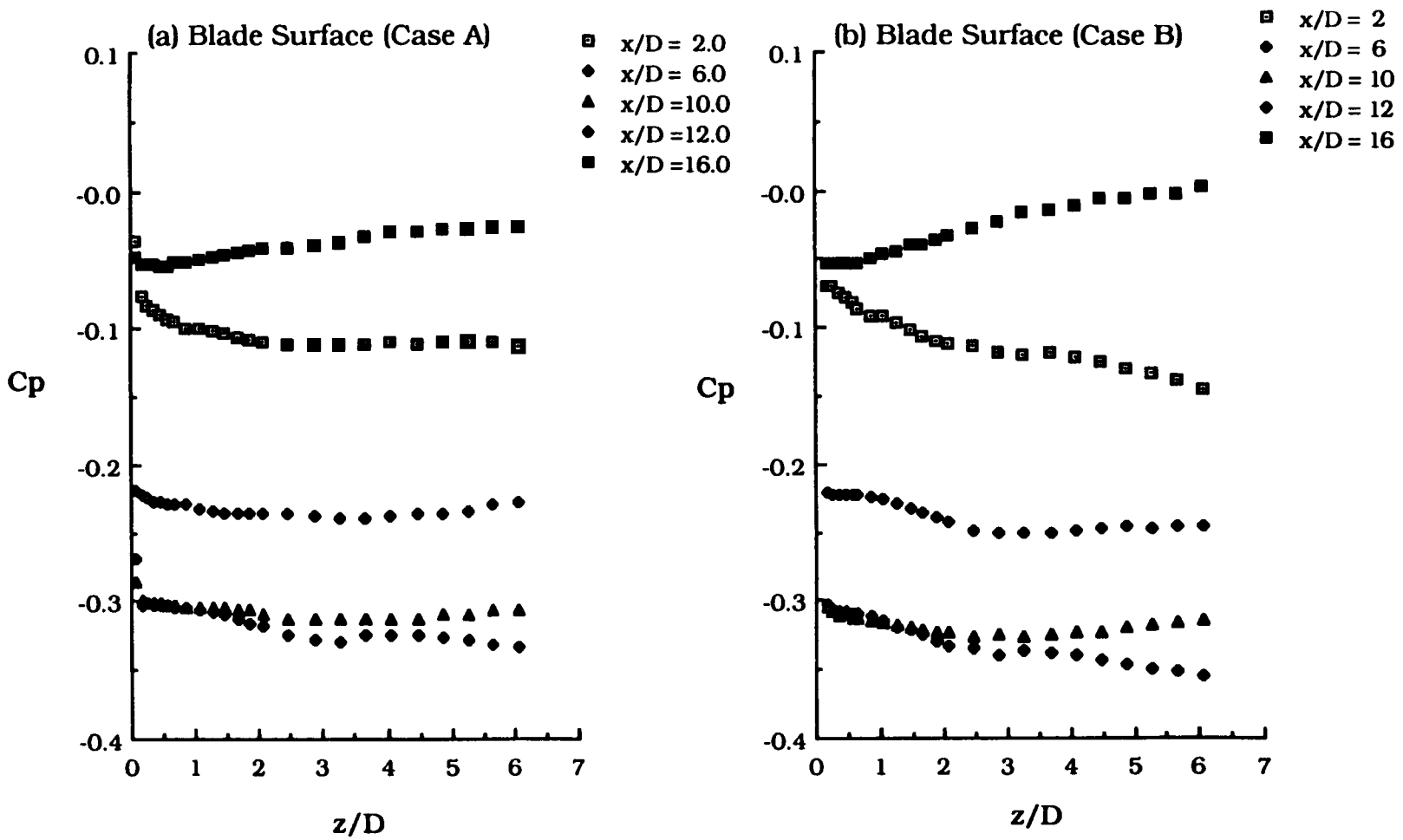

Fig. 5.35 Surface Static Pressure Variation on the Blade Surface of the Test-Model- A Comparison Between Case A and Case B

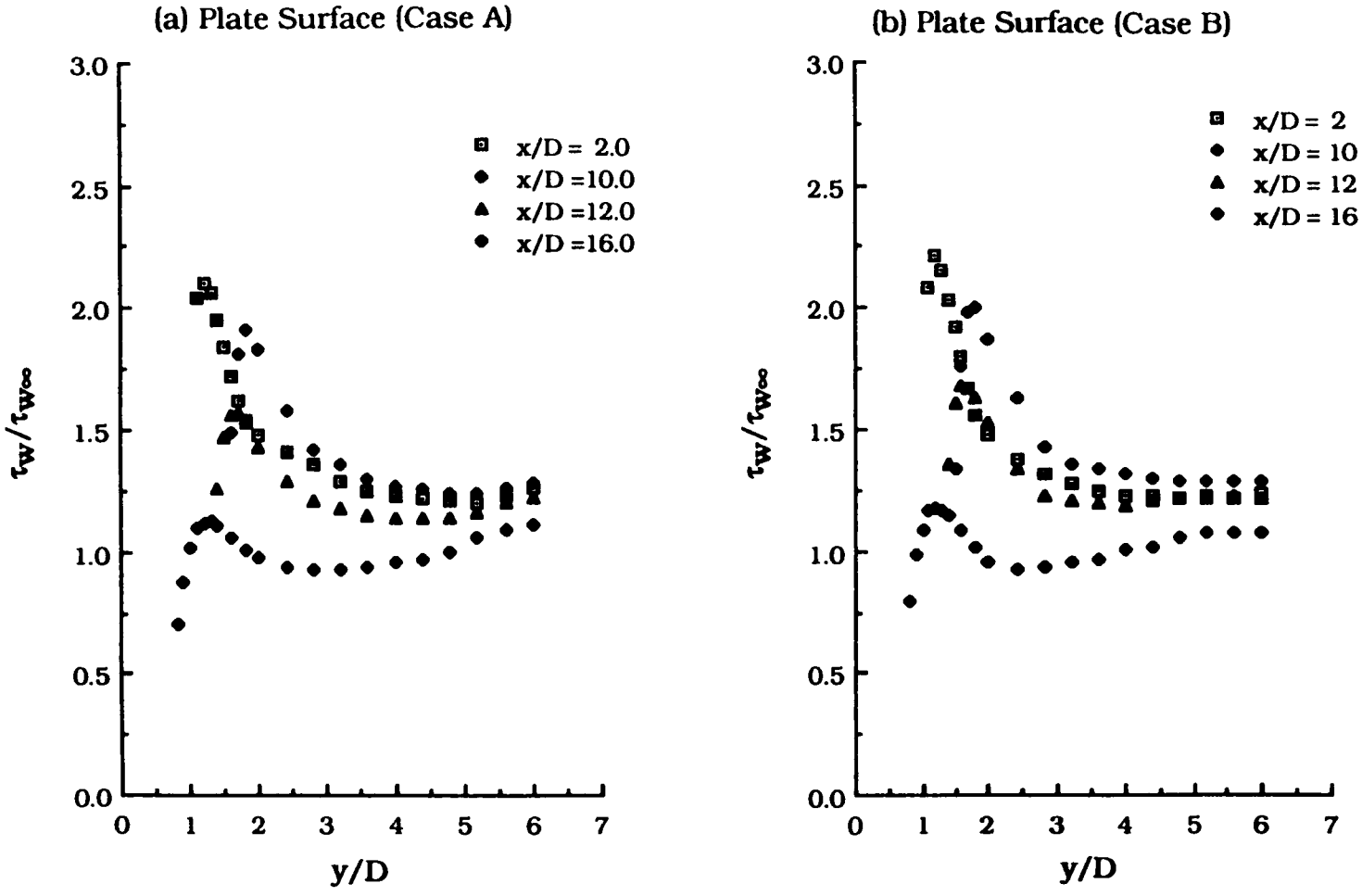

Fig. 5.36 Wall Shear Stress Variation on the Flat Plate Surface of the Test-Model- A Comparison Between Case A and Case B

The magnitude of τ_w/τ_{w_∞} at each streamwise locations is in general higher for Case A than for Case B. The higher value of the wall shear stress for Case A is caused by the increased level of free stream turbulence intensity and increased magnitude of the free stream velocity.

The comparison of normalized wall shear stress variation on the blade surface at five streamwise locations for the two cases is shown in Fig. 5.37. The variation of the wall shear stress at different streamwise stations (except at station 8 (x/D = 12)) is same for both the cases. At x/D = 12, the variation of the wall shear stress is different for two cases. For Case B the value of normalized wall shear stress starts decreasing rapidly at z = 1.2D and continues to decrease up to z = 3.8D. Thereafter, it changes only by a small amount (within 1%). This sharp decrease in the value of normalized wall shear stress is mainly due to the presence of the separation bubble in Case B.

Fig. 5.38(a) shows a comparison of the maximum and the asymptotic values of the normalized wall shear stress on the end-wall surface at different streamwise stations for the two cases. A similar trend in the variation of maximum and asymptotic values of τ_w/τ_{w_∞} for the two cases is observed.

A comparison of the maximum and the asymptotic values of τ_w/τ_{w_∞} on the blade surface for the two cases is shown in Fig. 5.38(b). A similar variation of the maximum and the asymptotic values of the normalized wall shear stress for the two cases is evident in the figure. Also, both the maximum and the asymptotic values of τ_w/τ_{w_∞} for Case A are higher relative to the values for case B. The decrease in the maximum and the asymptotic values of τ_w/τ_{w_∞} for Case B can be at-

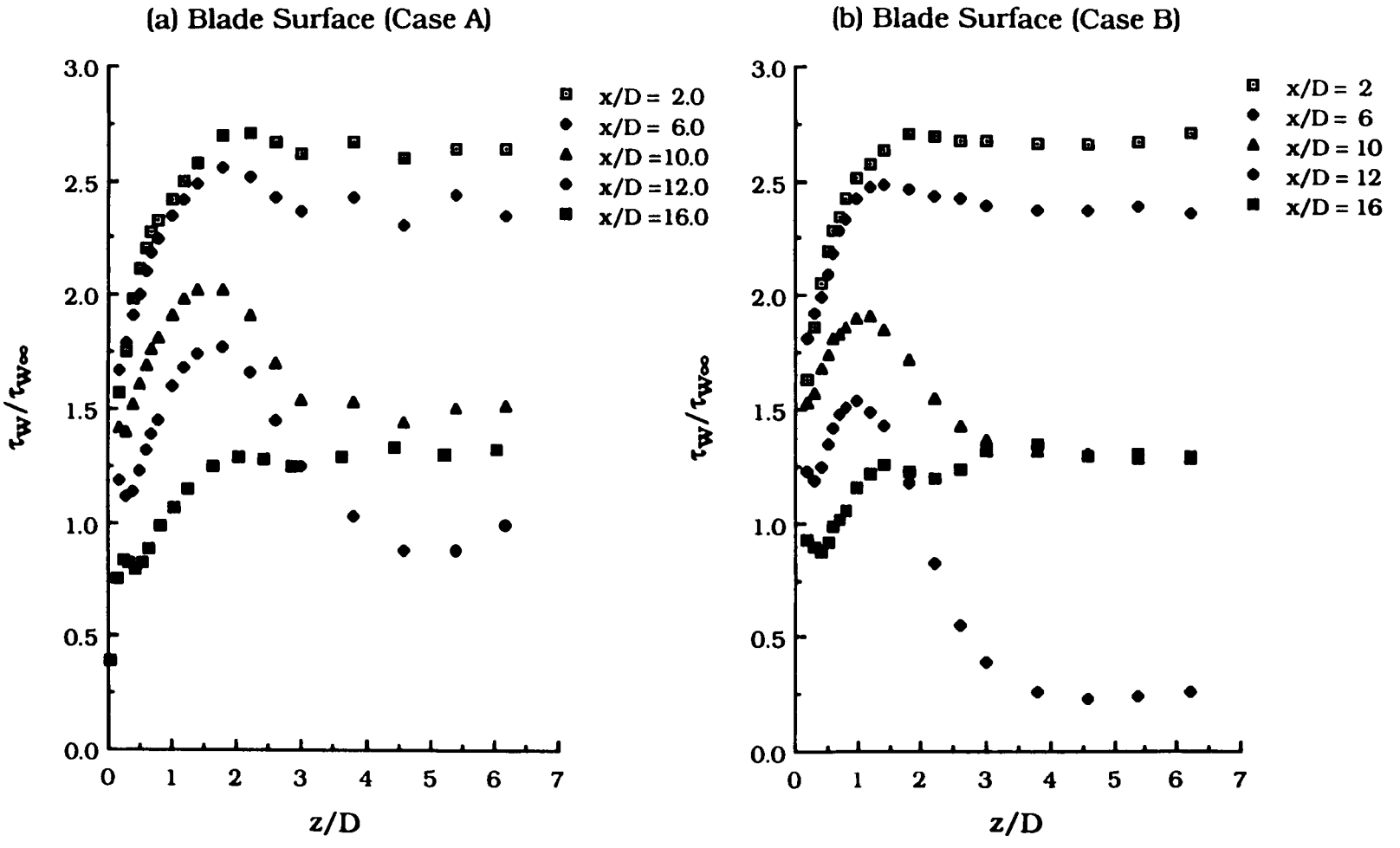

Fig. 5.37 Wall Shear Stress Variation on the Blade Surface of the Test-Model- A Comparison Between Case A and Case B

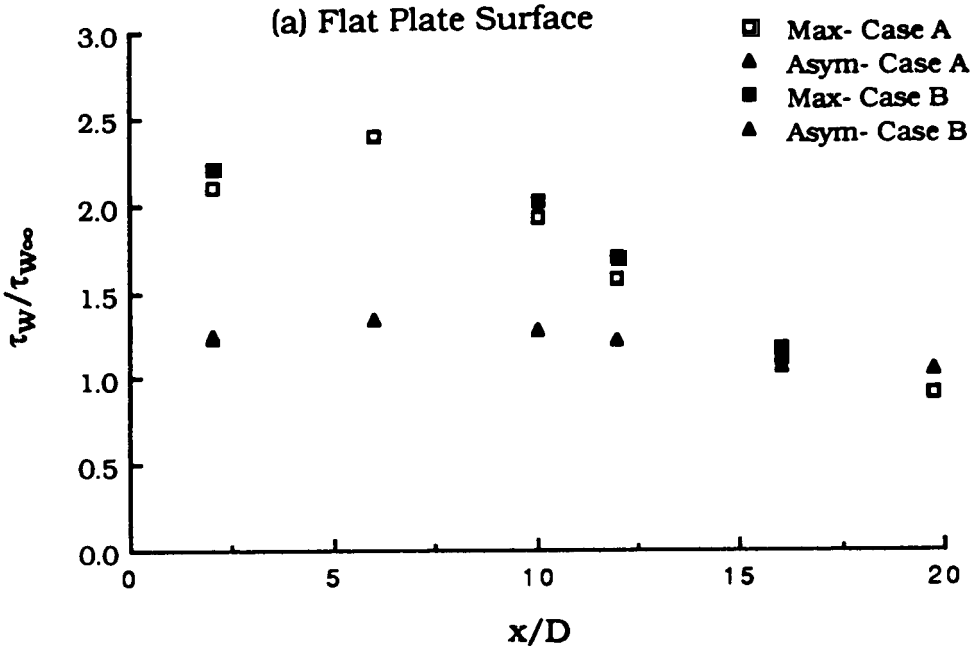

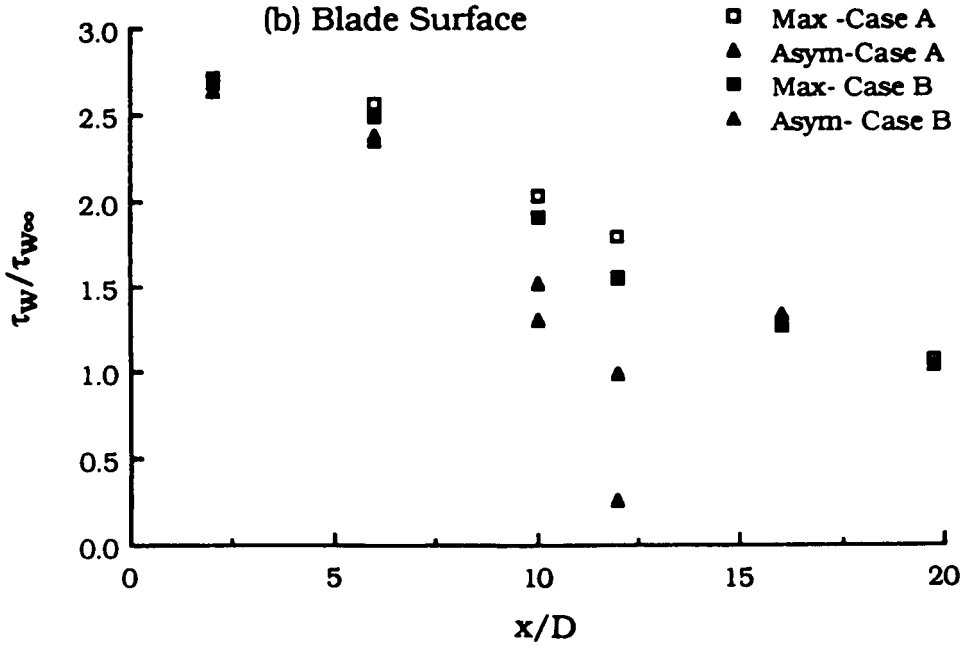

Fig. 5.38 Variation of Maximum and Asymptotic Values of Wall Shear Stress- A Comparison Between Case A and Case B

tributed to a lower level of free stream turbulence intensity and lower free stream velocity in case B.

Fig. 5.39(a) shows a comparison of the location of the maximum value of τ_w/τ_{w_∞} on the end-wall surface for the two cases. A similar variation of the location of $(\tau_w/\tau_{w_\infty})_{max}$ for two cases is evident in Fig. 5.39(a). Also, the location of the maximum value of the normalized wall shear stress at different streamwise stations is almost identical.

A comparison of the location of the maximum values of the normalized wall shear stress on the blade surface for the two cases is shown in Fig. 5.39(b). A similar variation of the location of the maximum value of τ_w/τ_{w_∞} is noticed for the two cases. However, in Case B the location of $(\tau_w/\tau_{w_\infty})_{max}$ moves closer to the end-wall surface.

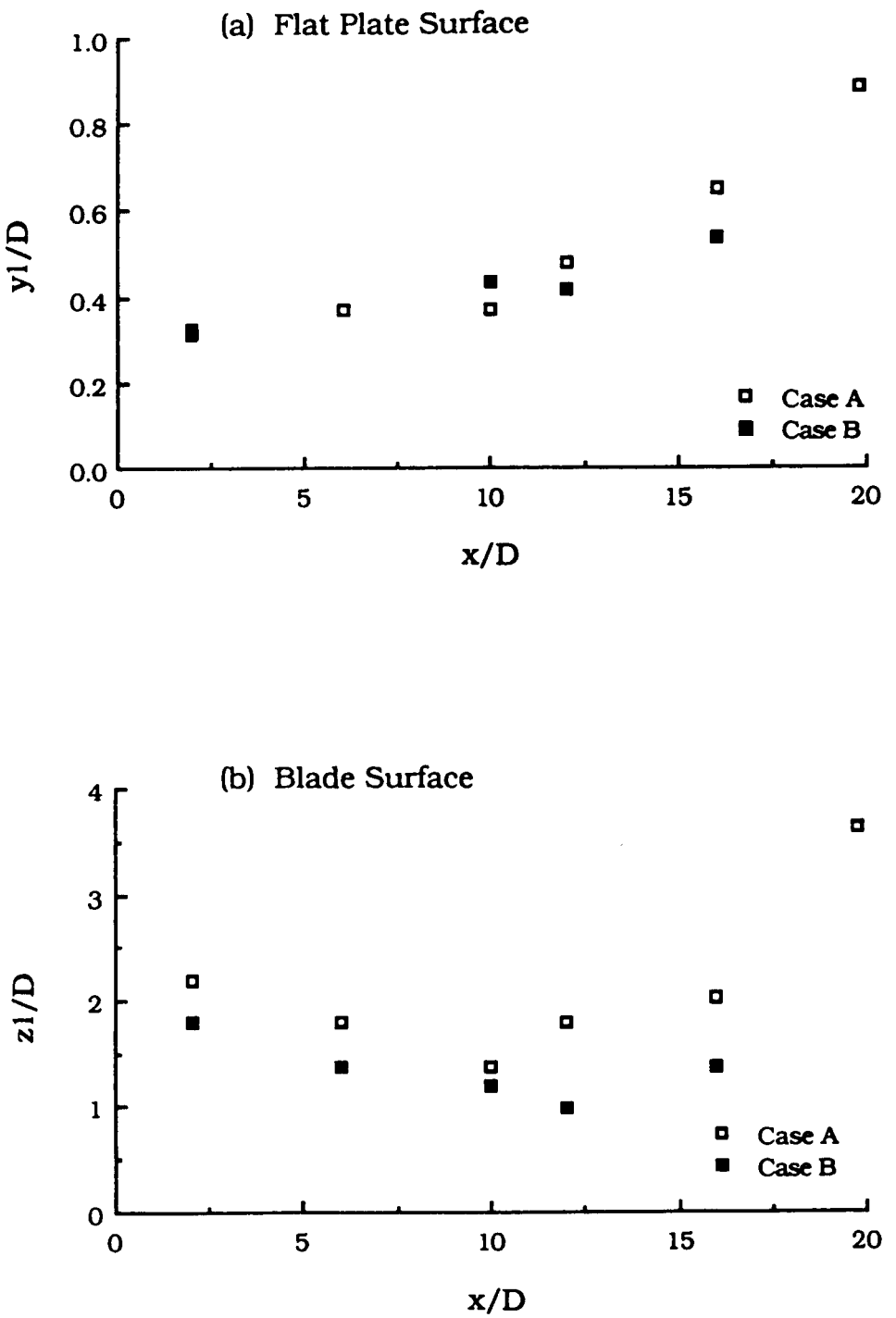

Fig. 5.39 Variation of the Location of Maximum Wall Shear Stress- A Comparison Between Case A and Case B

CHAPTER VI

RESULTS AND DISCUSSION ON THE WALL PRESSURE FLUCTUATION AND ITS CORRELATION WITH THE VELOCITY FLUCTUATION IN BLADE END-WALL CORNER REGION

Experimental results of the wall pressure fluctuation and its correlation with the velocity fluctuation in the blade end-wall corner region are presented in this chapter. Measurements of the wall pressure fluctuation and its correlation with the velocity fluctuation in the absence of the blade i.e., for two-dimensional flow, were also obtained and compared with the blade end-wall corner flow results.

6.1 Two-Dimensional Flow

6.1.1 Wall Pressure Fluctuation Intensity

The RMS value or the intensity of the wall pressure fluctuation, p'_w, normalized by the free stream dynamic pressure, q_∞ obtained in the present investigation is 2.79 $x10^{-2}$. The value of p'_w/q_∞ obtained in the present study is higher by a factor of approximately 3 compared to the values reported in the literature (see Table 2.4). The non-dimensional diameter, d_1^+ (= d_1u^*/ν), of the pressure transducer has been reported to influence the value of the wall pressure fluctuation intensity[52,127]. The value of p'_w/q_∞ increased with a decrease in the value of d_1^+ mainly because of the improved spatial resolution[52]. The value of $d_1^+ \approx 60$, in the present study, lies in the lower range of the values reported by other investigators (Table 2.4). The other possible reason for the observed high value of p'_w/q_∞ in the present study appears to be the presence of the initial roughness or the combined

effects of the initial roughness and the increased level of free stream turbulence. The results presented in Chapter IV indicated that the mean flow boundary layer parameters and the inner region of the boundary layer were influenced by the presence of the initial roughness. Therefore, the wall pressure fluctuation intensity is expected to be influenced by the presence of the initial roughness.

The value of p'_w was also measured without the turbulence generating grids at the same streamwise location to estimate the effect of increased free stream turbulence level on the value of p'_w. The value of p'_w increased by only approximately 1.4% with the increased level of free stream turbulence. This result suggests that the high value of p'_w/q_∞ obtained in the present investigation is probably caused by the initial roughness. As a consequence of high wall pressure fluctuation intensity, the value of p'_w/τ_w is also relatively larger than the usual value of ≈ 3[52]. In the present study, the value of p'_w/τ_w obtained is 8.4.

6.1.2 Frequency Spectra of the Wall Pressure Fluctuation

The frequency spectral distribution with and without the turbulence generating grids is shown in Fig. 6.1. No significant change is observed for the two cases at frequencies below 3500 Hz. However, the spectral content increases at frequencies above 3500 Hz. This implies that the increase in free stream turbulence level increases the spectral content of the wall pressure fluctuation. This is in agreement with the observed increase in the overall wall pressure fluctuation intensity because of the increased free stream turbulence level.

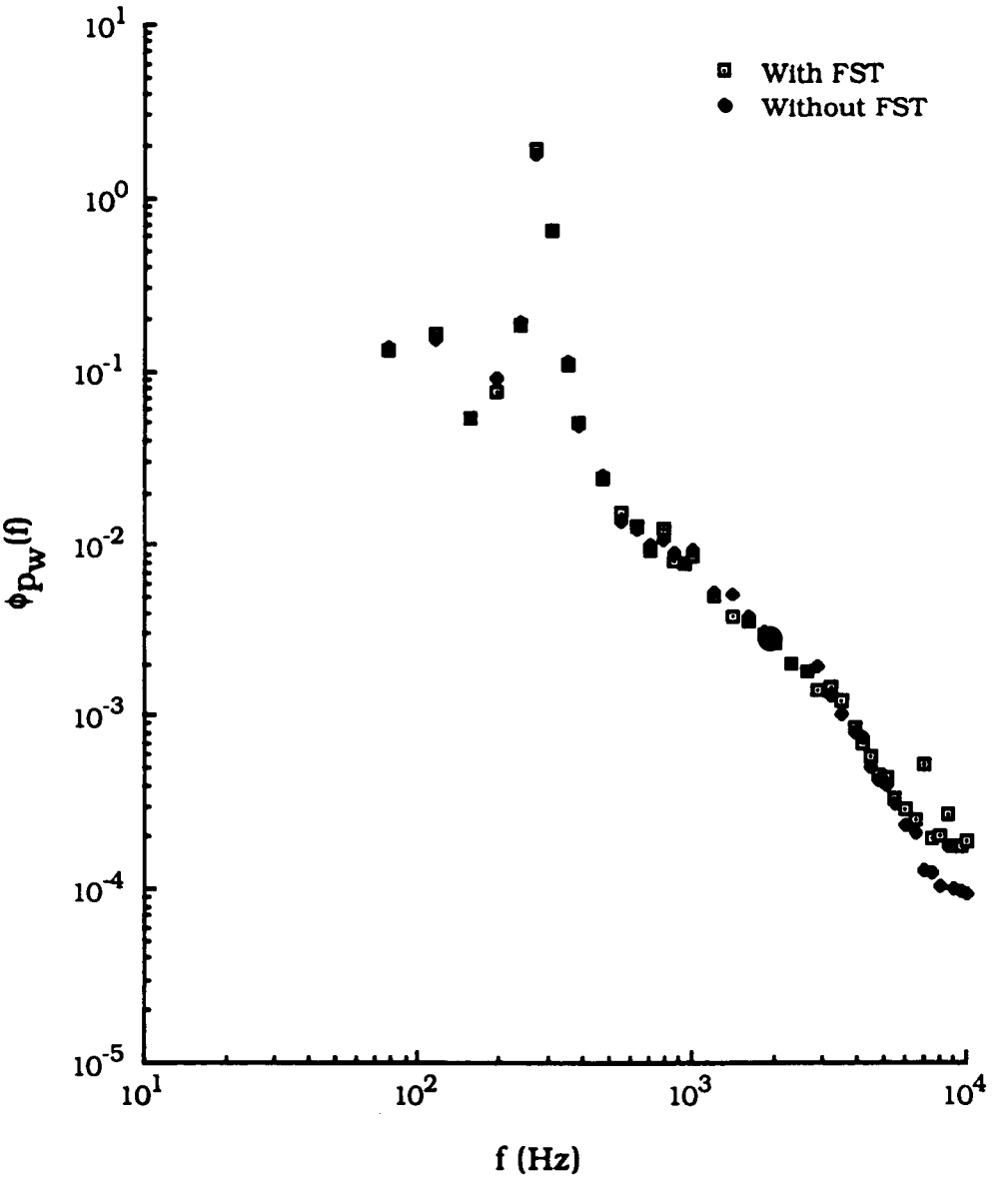

Fig. 6.1 Frequency Spectral Distribution of Wall Pressure Fluctuation (Two-Dimensional Flow)

6.1.3 Wall Pressure-Velocity Correlation

The correlation of the wall pressure fluctuation with the streamwise fluctuating velocity component across the boundary layer is shown in Fig. 6.2. The results for the case in which turbulence generating grids were not used are also included. The trend in the variation of R_{pu} for $z/\delta > 0.15$ is observed to be the same for both the cases. For $0.15 < z/\delta < 0.6$, the value of R_{pu} first increases up to a distance of $z/\delta \sim 0.4$ and, thereafter, slightly decreases. The maximum value of R_{pu} is approximately 0.05 for both of the cases. The turbulent boundary layer can be divided into two regions, namely, the inner and the outer regions. In the inner region, $0.15 < z/\delta < 0.4$, the value of R_{pu} increases and attains its maximum value. This implies that the fluctuating velocity field in this region contributes more to the wall pressure fluctuation field than the outer region. In the outer region, $z/\delta > 0.4$, the value of R_{pu} decreases compared to its value in the inner region which is the indication of a smaller contribution from the outer region. Also, close to the boundary layer edge the value of R_{pu} increases again. The increase in the value of R_{pu} in the inner region was also reported by Serafini[53]. Moreover, Serafini's study revealed that the intermittent region of the turbulent boundary layer contributed approximately half to the wall pressure fluctuation field than that of the inner region. However, in the present study, the values of R_{pu} close to the boundary layer edge are found to be of the same order as the maximum value of R_{pu} in the inner region.

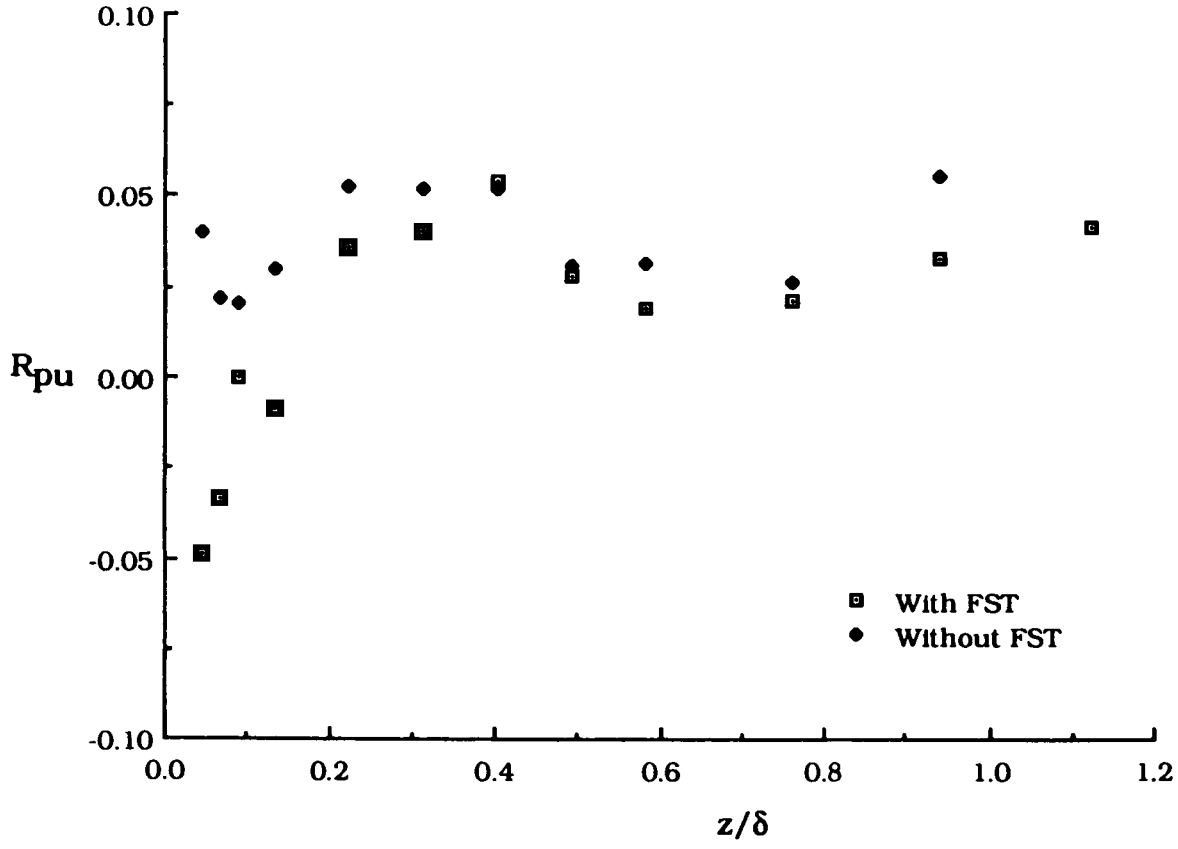

Fig. 6.2 Wall Pressure-Velocity Correlation Coefficient (Two-Dimensional Flow)

6.2 Three-Dimensional Flow- Upstream of the Blade Leading Edge

6.2.1 Wall Pressure Fluctuation Intensity

The intensity of the wall pressure fluctuation measured upstream of the blade leading edge at x/D = - 8 is the same as obtained for the current two-dimensional case. Therefore, from the point of view of the wall pressure fluctuation field, the flow in the upstream region is not influenced by the presence of the blade at an axial distance of 8D.

6.2.2 Frequency Spectra of the Wall Pressure Fluctuation

Fig. 6.3 shows the frequency spectral distribution at x/D = - 8. For comparison, the frequency spectral distribution at the same streamwise location in absence of the blade is also included in Fig. 6.3. It is evident that at streamwise location, x/D = - 8, the spectral content at different frequencies with and without the blade is the same. This again implies, as mentioned earlier, that in the upstream region the wall pressure fluctuation field is not influenced by the presence of the blade at x/D = - 8.

6.2.3 Wall Pressure-Velocity Correlation

The variation of correlation coefficient, R_{pu} in the Z-direction upstream of the blade leading edge at x/D = - 8 is shown in Fig. 6.4. At the same streamwise location, the results obtained in the absence of the blade i.e., for the two-dimensional case are also included in Fig. 6.4. A similar trend in the variation of R_{pu} for the two cases is evident.

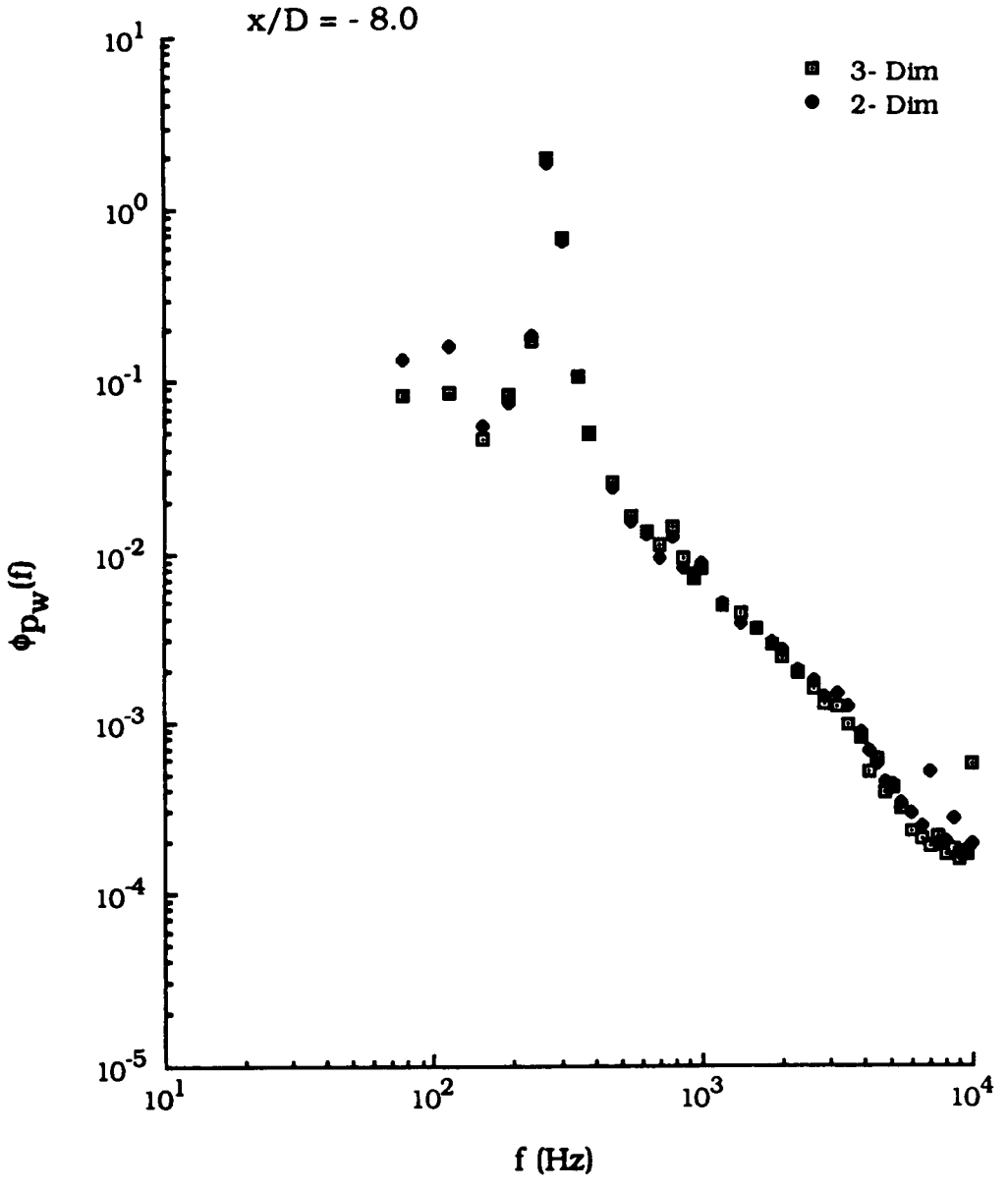

Fig. 6.3 Frequency Spectral Distribution of Wall Pressure Fluctuation Upstream of the Blade Leading Edge

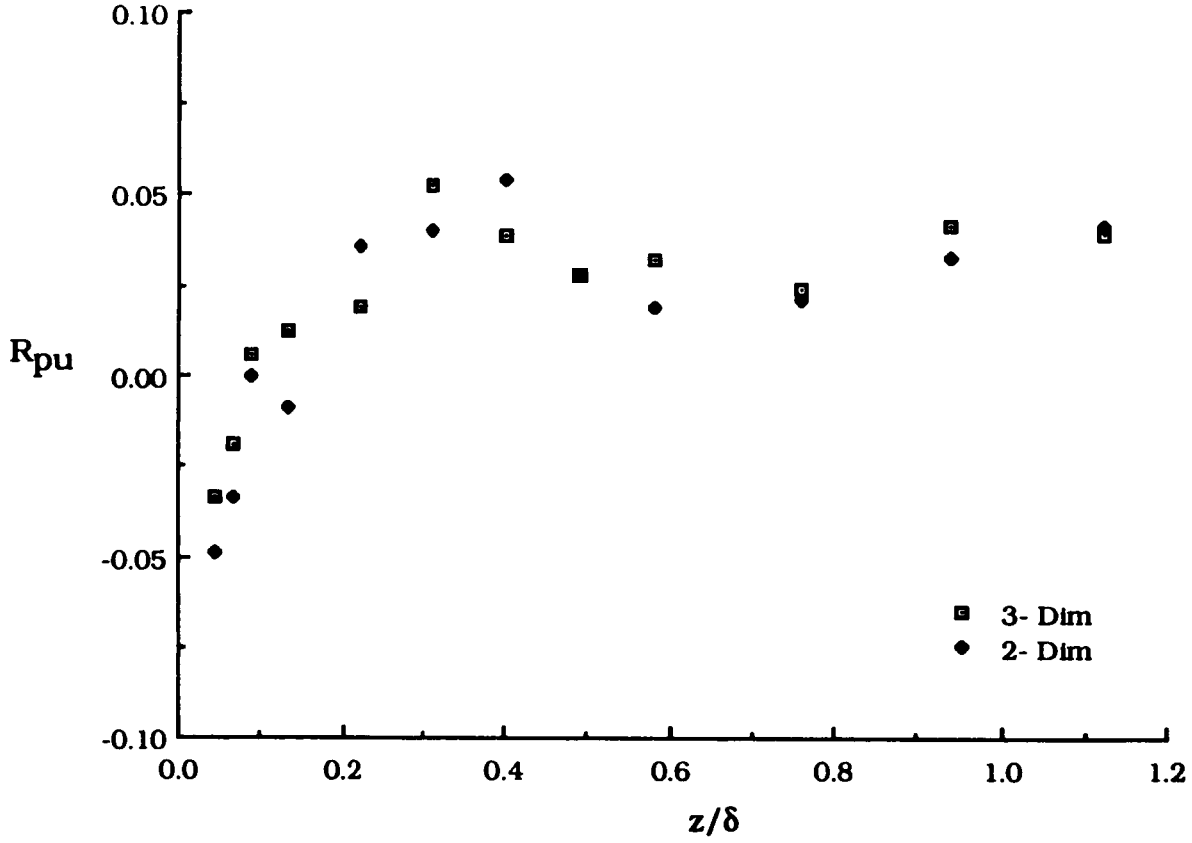

Fig. 6.4 Wall Pressure-Velocity Correlation Coefficient Upstream of the Blade Leading Edge

6.3 Three-Dimensional Flow- Blade End-Wall Corner Region

6.3.1 Wall Pressure Fluctuation Intensity

Fig. 6.5(a) shows variation of the wall pressure fluctuation intensity at three streamwise stations in the blade end-wall corner region normalized by the far upstream value (p'_{w0}) measured at a streamwise location of x/D = - 8. At all of the streamwise stations in the blade end-wall corner region the value of p'_w is less than the far upstream value. At x/D = 2, the normalized wall pressure fluctuation intensity is observed to increase in a small distance close to the blade surface and, thereafter, it decreases with some scatter. The maximum value of the normalized wall pressure fluctuation intensity is found to be 0.75. Also, the maximum value of the normalized wall pressure fluctuation intensity is located close to the separation line. The traces of the separation line obtained from the flow visualization study of Hazarika[47] are shown in Fig. 5.26. The variation of normalized wall pressure fluctuation intensity in the Y-direction at x/D = 2 also shows that p'_w/p'_{w0} increases with a decrease in the mean surface pressure, whereas, its value decreases as the mean surface pressure increases (see Fig. 5.20(a) for mean surface static pressure distributions).

At x/D = 10, the normalized wall pressure fluctuation intensity has a maximum value of 0.83 which occurs very close to the blade surface as shown in Fig. 6.5(a). The values of p'_w/p'_{w0} at x/D = 10 are consistently higher than the values at x/D = 2. In the streamwise direction the mean surface static pressure, as discussed in Chapter V (Fig. 5.20(a)), decreased from x/D = 2 to x/D = 10 and, thereafter, its value increased. In the Y-direction at x/D = 10, the mean surface static pressure increases, whereas, the wall pressure fluctuation intensity

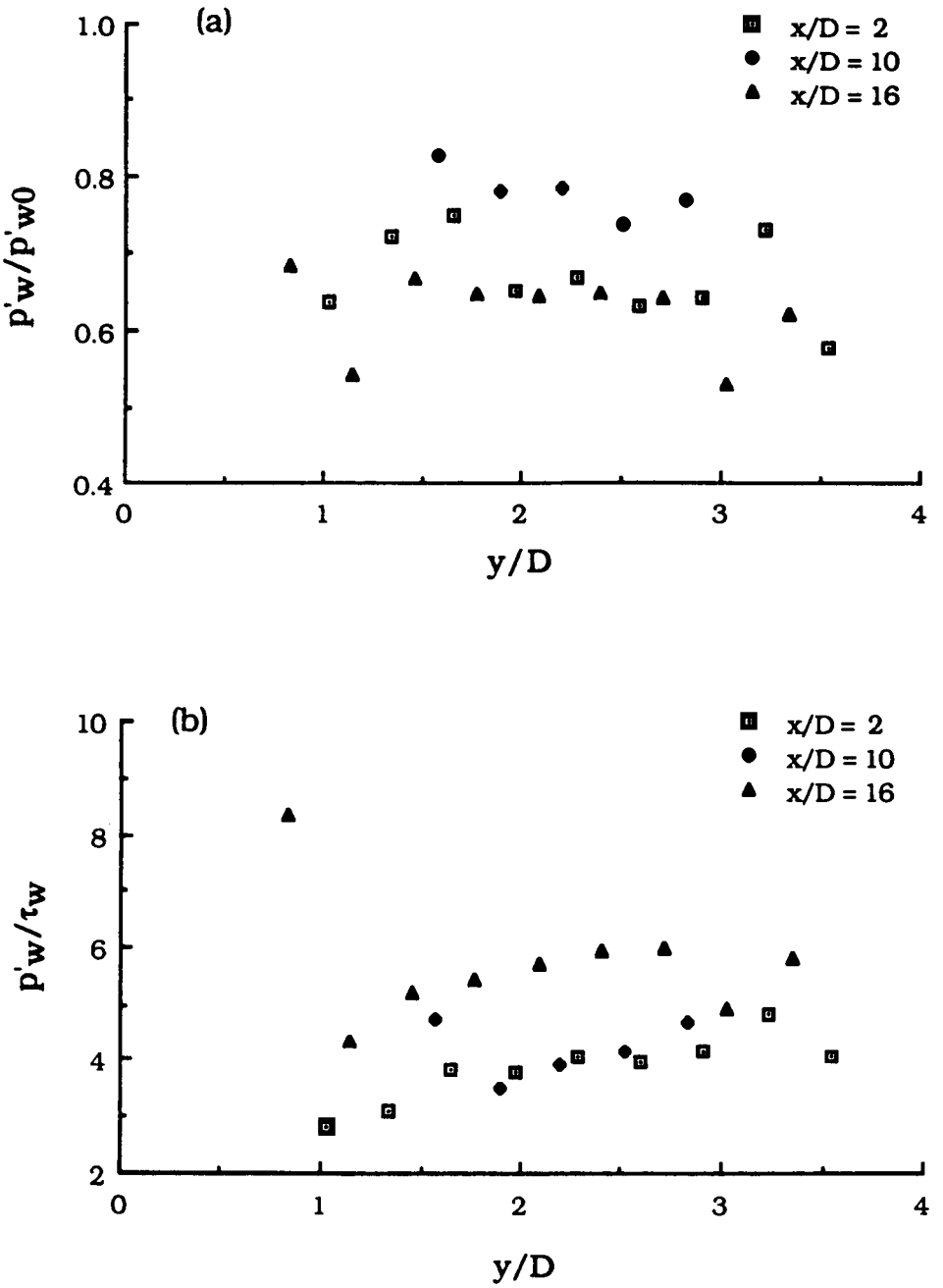

Fig. 6.5 Variation of Normalized Wall Pressure Fluctuation Intensity in Blade End-Wall Corner Region: (a) Normalized by the Value Far Upstream of the Blade Leading Edge; (b) Normalized by the Local Wall Shear Stress

decreases with some scatter (see Fig. 5.20(a) and 6.5(a)). In the streamwise direction, as in the Y-direction, the wall pressure fluctuation intensity increases with the decrease in surface static pressure.

At x/D = 16, very close to the blade surface the normalized wall pressure fluctuation intensity has a maximum value of 0.68 (Fig. 6.5(a)). In the Y-direction the normalized wall pressure fluctuation intensity first decreases and attains a second maximum value of approximately 0.67 and, thereafter, it slowly decreases with some scatter. The mean surface static pressure in the Y-direction at x/D = 16 slightly decreases up to y/D = 1.5, whereas, the value of wall pressure fluctuation intensity increases, except very close to the blade surface (see Figs. 5.20(a) and 6.5(a)). At distances of y/D > 1.5, the mean surface static pressure and the wall pressure fluctuation intensity values show small changes. In the streamwise direction the adverse pressure gradient exists beyond x/D = 10 (see Fig. 5.20(a)). However, the values of wall pressure fluctuation intensity at x/D = 16 are smaller than the values at x/D = 2 and x/D = 10 as shown in Fig. 6.5(a).

The above discussion on the variation of the wall pressure fluctuation intensity at different streamwise stations in the blade endwall corner region clearly indicates that the wall pressure fluctuation intensity increases in the presence of a favorable pressure gradient, whereas, its value decreases in the presence of adverse pressure gradient. The aforementioned observation has been observed both in the streamwise and lateral directions. However, the available measurements in a two-dimensional turbulent boundary layer showed a higher value of wall pressure fluctuation intensity in the presence of adverse pressure gradient and lower value in the presence of favorable pres-

sure gradient compared to the zero pressure gradient case[131]. At all the three streamwise stations examined in the blade end-wall corner region, the maximum normalized wall pressure fluctuation intensity occurred between the blade surface and the separation line.

The presence of the horseshoe vortex in the blade end-wall corner region and the changes in its strength appear to significantly influence the variation of the wall pressure fluctuation intensity. The observed increase in values of wall pressure fluctuation intensity at x/D = 10 compared to the values at x/D = 2 is probably associated with the stretching of the horseshoe vortex due to the existence of a favorable pressure gradient in this region. Moreover, beyond x/D = 10 the horseshoe vortex becomes attenuated because of the adverse pressure gradient. Therefore, the observed decrease in the values of the wall pressure fluctuation intensity at x/D = 16 can possibly be attributed to the attenuation of the horseshoe vortex.

The measurements of wall pressure fluctuation intensity, in the simplified wing-body junction, were recently also reported by Hasan, Casarella and Rood[130]. The wing used in their study had a semi-elliptic leading edge followed by a constant thickness section for some length and then a tapered tail section. The investigation of Hasan et al. revealed that the normalized values (normalized by the value far upstream of the wing leading edge) of wall pressure fluctuation intensity in the blade end-wall corner region were greater than unity. However, the normalized values of wall pressure fluctuation intensity are found to be less than unity in the present investigation. The value of p'_{w0}, used for normalizing the wall pressure fluctuation intensity values in the corner region in the present investigation, is relatively high com-

pared to the values for two-dimensional flows available in the literature. The high value of p'_{w0} obtained in the present study might have caused the observed difference with the study of Hasan et al.

Fig. 6.5(b) shows the variation in the Y-direction of the wall pressure fluctuation intensity normalized by the local time averaged wall shear stress. The value of p'_w/τ_w varies from approximately 3-6.

6.3.2 Frequency Spectra of the Wall Pressure Fluctuation

Fig. 6.6(a) shows the variation of the frequency spectral distribution in the Y-direction at x/D = 2. The spectral content at different frequencies increases, except at y/D = 1.65, as the blade surface is approached. However, at y/D = 1.65 the spectral content for f < 2500 Hz is higher and for f > 2500 Hz is smaller compared to the value at y/D = 1.02. The observed increase in spectral content at y/D = 1.65 is consistent with the maximum value of wall pressure fluctuation intensity obtained at this streamwise station (see Fig. 6.5(a)).

The variation of frequency spectral distribution in the Y-direction at x/D = 10 is shown in Fig.6.6(b). Although the change in spectral content for different y locations is small at this streamwise station the spectral content is observed to increase as the blade surface is approached.

The variation of frequency spectral distribution in the Y-direction at x/D = 16 is shown in Fig.6.6(c). At this streamwise station the variation of the spectral distribution with different y-locations is similar to that observed at x/D = 2. However, the changes in spectral content at the different y locations are not significant.

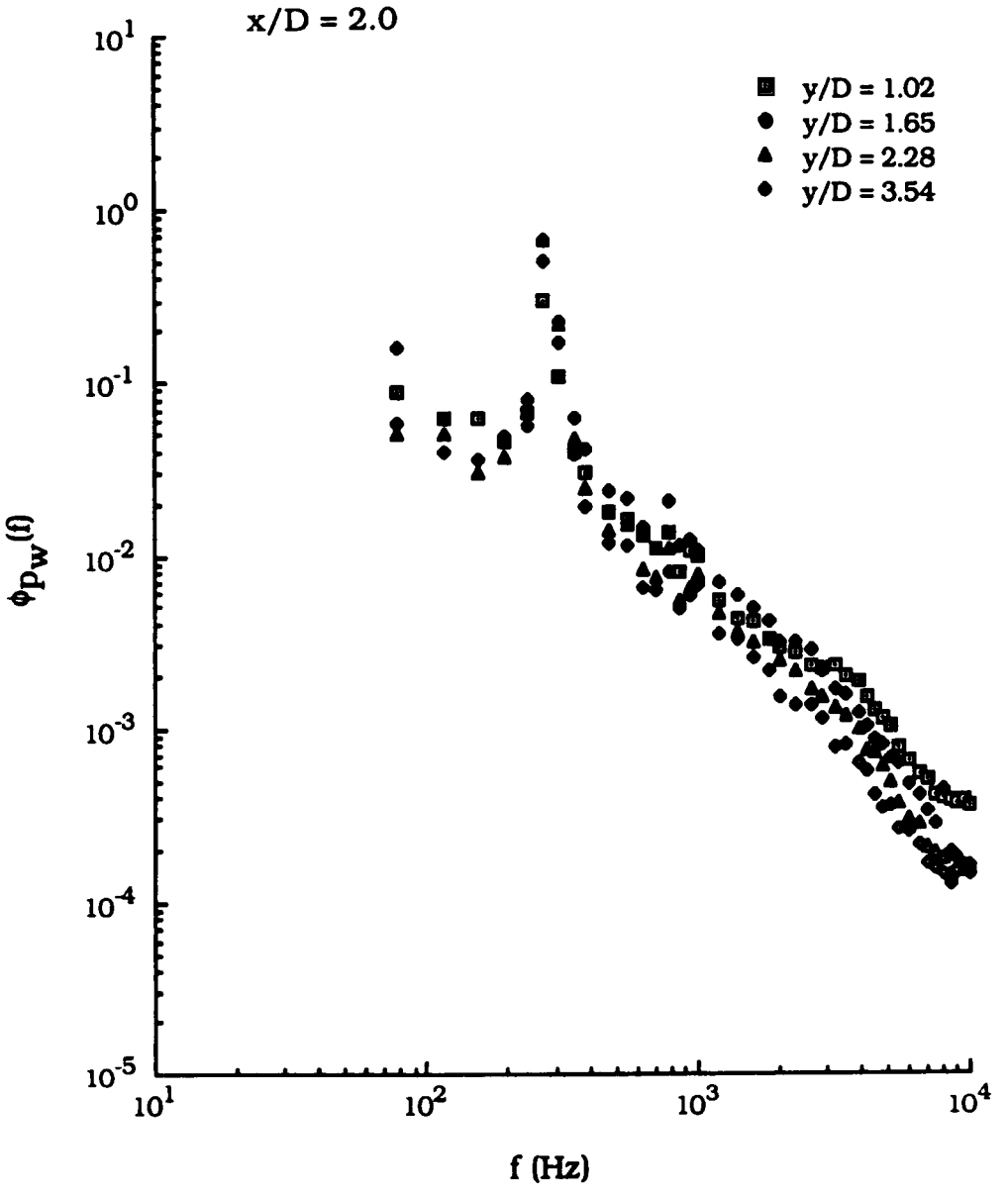

Fig. 6.6(a) Variation of Frequency Spectra of Wall Pressure Fluctuation in Y-Direction at x/D = 2 in Blade End-Wall Corner Region

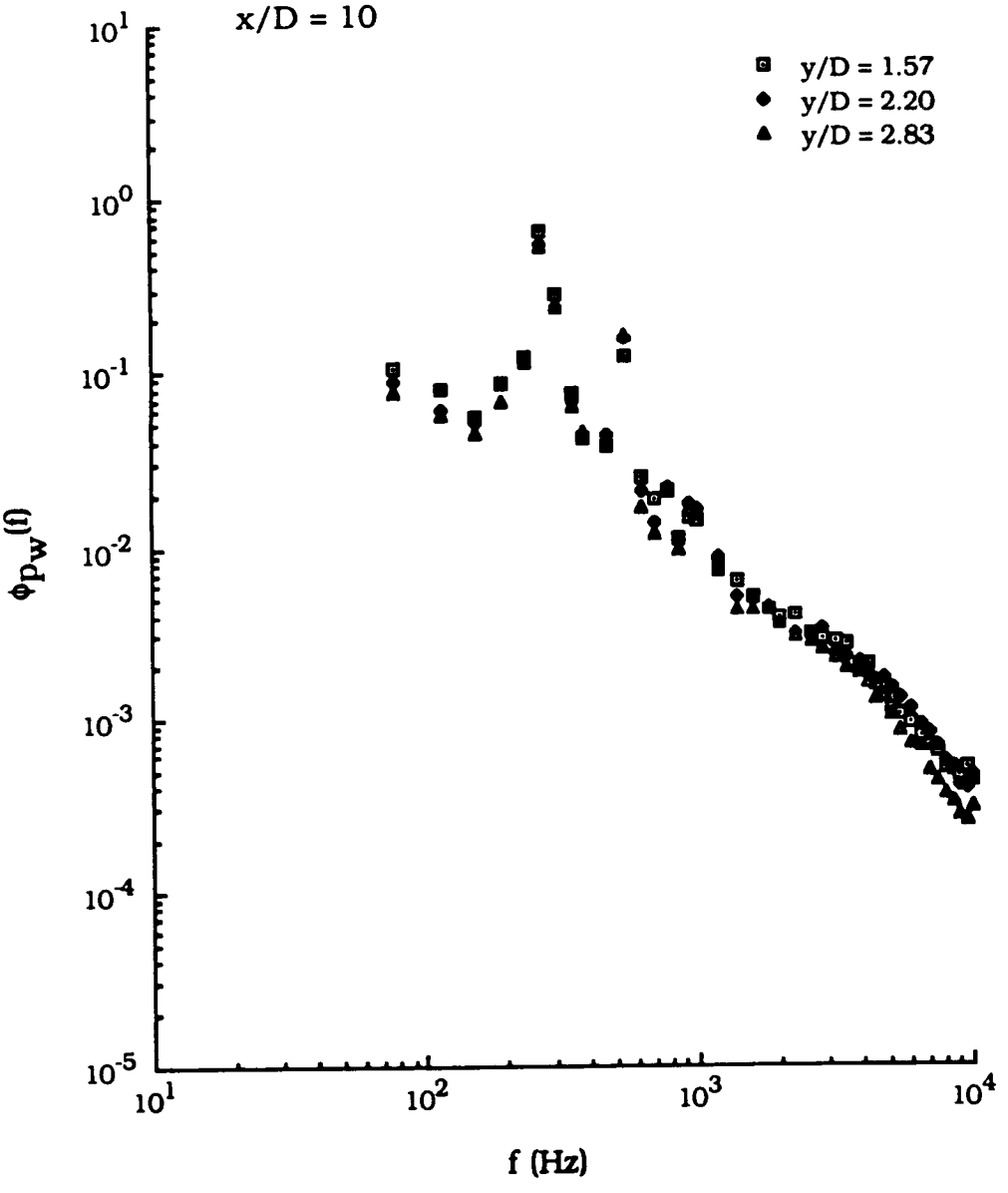

Fig. 6.6(b) Variation of Frequency Spectra of Wall Pressure Fluctuation in Y-Direction at x/D = 10 in Blade End-Wall Corner Region

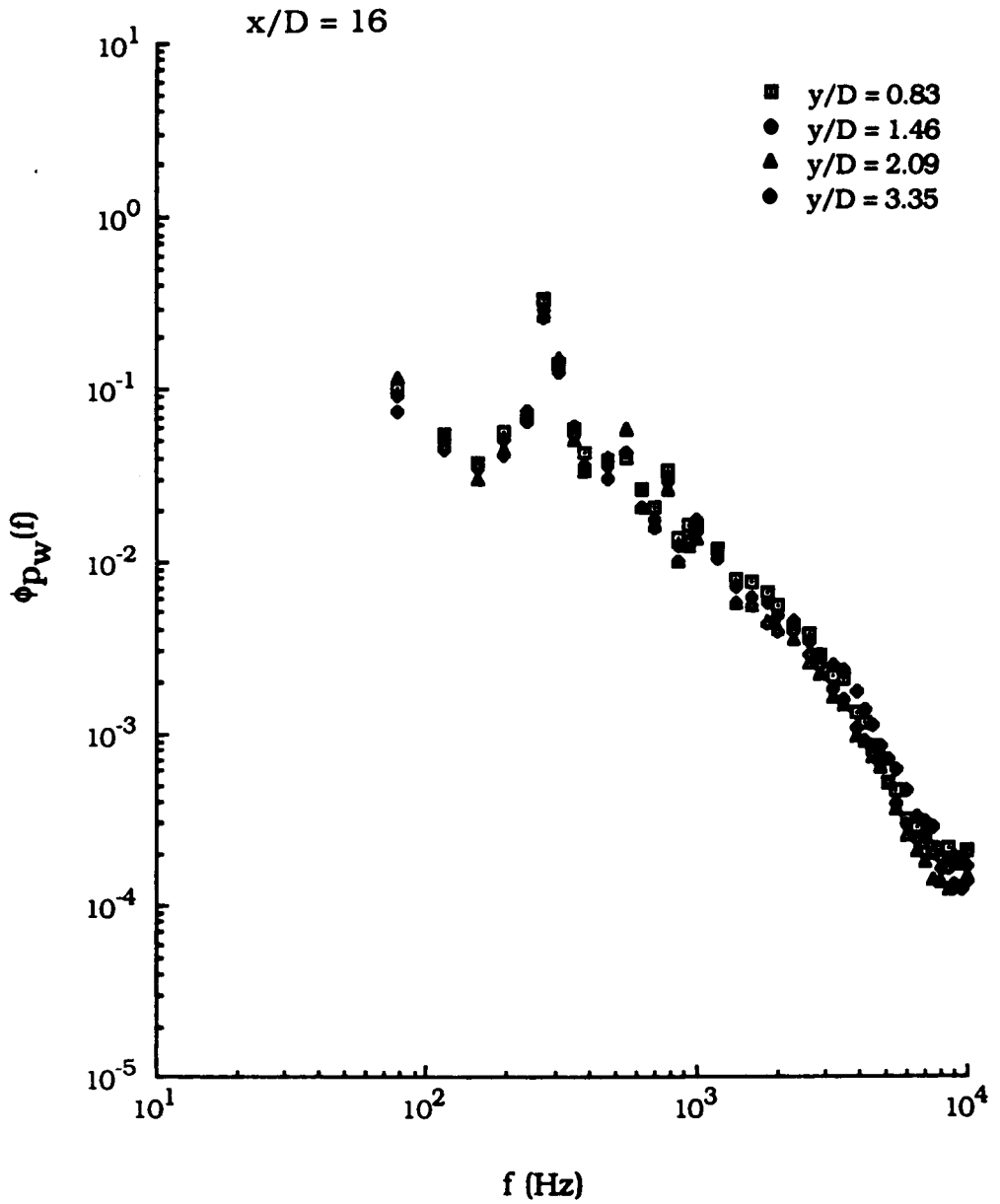

Fig. 6.6(c) Variation of Frequency Spectra of Wall Pressure Fluctuation in Y-Direction at x/D = 16 in Blade End-Wall Corner Region

6.3.3 Wall Pressure -Velocity Correlation

The variation of correlation coefficient normal to the end-wall at three streamwise stations in the blade end-wall corner region is shown in Fig.6.7. Firstly, it is observed that a large scatter in the values of correlation coefficient exists. Also, at each streamwise station the variation of R_{pu} at the two y-locations is similar within the experimental scatter. In general, it is noticed that for $z/\delta < 0.6$ the magnitude of correlation coefficient increases with the increase in distance in the Y-direction. However, this trend appears to reverse near the shear layer edge.

The values of R_{pu} beyond $z/\delta > 0.2$ at $x/D = 10$ are smaller than the values at $x/D = 2$. These lower values of R_{pu} are due to the existence of a favorable pressure gradient between these two streamwise stations. However, at $x/D = 16$, the values of R_{pu} beyond $z/\delta > 0.2$ are higher than the values at the other two streamwise stations with some scatter. The existence of a strong adverse pressure gradient(Fig. 5.20(a)) beyond the streamwise location of $x/D = 10$ appears to be the reason for the observed increase in the values of R_{pu} at $x/D = 16$. In the two-dimensional turbulent boundary layer flow, the increase in the value of R_{pu} in the presence of the adverse pressure gradient relative to the zero pressure gradient case was reported by Bradshaw[49].

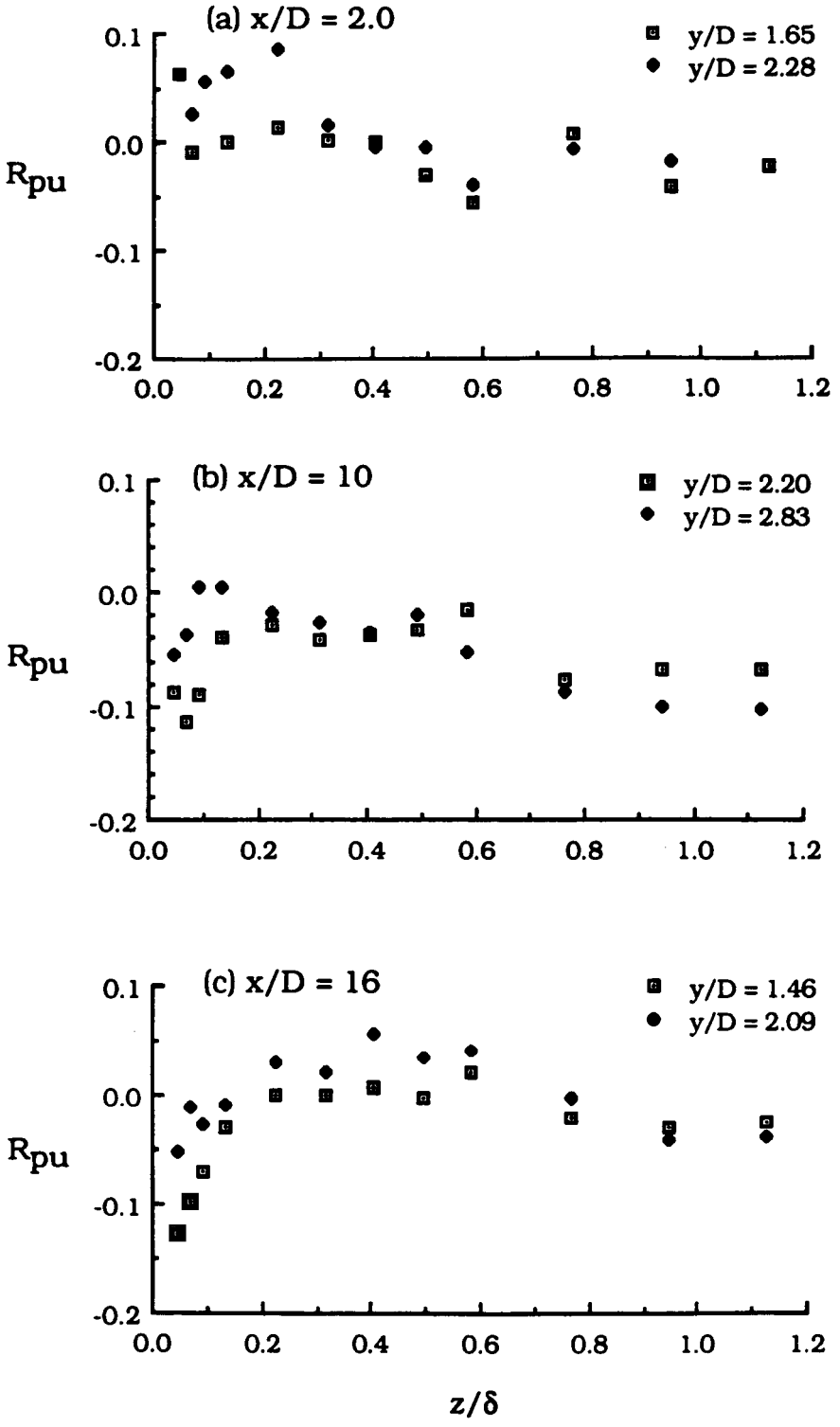

Fig. 6.7 Variation of Wall Pressure-Velocity Correlation Coefficient at Different Streamwise Locations in Blade End-Wall Corner Region

CHAPTER VII

SUMMARY OF RESULTS

The combined effects of initial roughness and the increased level of free stream turbulence on the development of a two-dimensional turbulent boundary layer were investigated. The wall shear stress and the mean surface static pressure measurements, upstream of the blade leading edge and in the blade end-wall corner region, were obtained with and without a separation bubble on the blade. Measurements of wall pressure fluctuation and its correlation with the velocity fluctuation were made upstream of the blade and in the blade end-wall corner region. The results of the above mentioned measurements are presented and discussed in Chapters 4-6. Based on the results of the various measurements, the following main conclusions were drawn:

(1) The surface static pressure on the end-wall varied significantly in the streamwise and lateral (Y) directions upstream of the blade leading edge (Fig. 5.3). An adverse pressure gradient existed in the streamwise direction because the flow decelerated as it approached the blade leading edge. However, the surface static pressure, at different streamwise stations, decreased in the Y-direction. The rate of decrease of the surface static pressure in Y-direction was observed to be a maximum at x = - 2D where the streamlines had large curvature due to the presence of the blade leading edge. The values of C_p, at different streamwise stations, were observed to approach the far upstream value (value at x/D = - 20) within 2% of the free stream dynamic pres-

sure at a distance of y = 6D. This result implied the influence of the blade on the surface static pressure diminished within a distance of approximately 6D in the Y-direction.

(2) The wall shear stress decreased in the upstream region as the blade leading edge is approached. The maximum decrease in the value of wall shear stress was approximately 40% relative to the value far upstream of the blade leading edge. This decrease in wall shear stress occurred on the stagnation streamline where the maximum adverse pressure gradient was observed (Fig. 5.5). The wall shear stress and surface static pressure in the upstream region at different streamwise stations approached the far upstream values within a distance of approximately 6D in the Y-direction.

(3) The mean velocity profiles obtained along different streamlines in the upstream region of the blade leading edge indicated variation in the values of the constants (K, B and Π) in Eqn. 5.2 (Fig. 5.13). The values of 1/K (the coefficient of the term ln z^+ in Eqn. 5.2) and Π increased, whereas, the value of B decreased in the streamwise direction. This trend prevailed along the streamlines nearest to the stagnation streamline. However, the trend in the variation of these constants reversed along the streamlines far away from the stagnation streamline. The observed variation in the values of these constants was attributed to the changes in adverse pressure gradient and curvature of the streamlines. The mean flow boundary layer parameters in the upstream region were influenced by the changes in pressure gradient (Figs. 5.14 and 5.15). The various boundary layer parameters showed an

opposite trend in the streamwise and lateral directions because of the presence of adverse and favorable pressure gradients, respectively.

(4) At different streamwise stations, in the blade end-wall corner region, the surface static pressure varied significantly on the end-wall surface. However, on the blade surface at any streamwise station a small variation (< 5% of the free stream dynamic pressure) in the surface static pressure existed along its span (Fig. 5.20).

(5) At different streamwise stations on the end-wall surface, except at first station in the corner region, the surface static pressure measurements obtained by the surface static tube and the wall taps were in good agreement (within ± 2% of the free stream dynamic pressure (Fig. 5.22)). However, at the first streamwise station (x/D = 2), the differences in C_p obtained by the two techniques were higher (maximum 7% of the free stream dynamic pressure). These observed large differences in C_p at x/D = 2 resulting from the two methods of measurements were attributed to the presence of large skewness in the flow.

(6) At different streamwise stations on the end-wall surface, except at the last two stations, the normalized wall shear stress values increased in the corner region as the blade surface was approached (Fig. 5.23(a)). The maximum value of the normalized wall shear stress and also its location from the blade surface were observed to change at different streamwise stations (Figs. 5.24 and 5.25).

(7) The variation of the wall shear stress on the blade surface was not the same as on the end-wall surface. However, on both the blade surface and the end-wall surface, the maximum value of the normalized wall shear stress and its location from the end-wall surface changed at different streamwise stations (Fig. 5.24 and 5.25). Moreover, the maximum values of the normalized wall shear stress at different streamwise stations in the corner region were found to be consistently higher on the blade surface compared to the values on the end-wall surface (Fig. 5.24).

(8) The trend in the variation of the wall shear stress directions obtained from the Preston tube measurements, on both the surfaces of the test-model, was in agreement with the values obtained from the flow visualization method. The differences in the wall shear stress directions obtained by the two methods were within the ranges of yaw angles in which the Preston tube was found to be insensitive.

(9) In the presence of a separation bubble (Case B), the wall shear stress variation at different streamwise stations on the end-wall surface was similar to that observed without the separation bubble, Case A (Fig. 5.36). On the blade surface, a similar trend in the variation of wall shear stress at different streamwise stations, except at $x/D = 12$, for the two cases was observed (Fig. 5.37). At $x/D = 12$ on the blade surface, for Case B, the wall shear stress decreased sharply at $z/D \approx 1.2$ and continued to decrease up to $z/D \approx 3.8$. This decrease in the wall shear stress was mainly caused by the presence of the separation bubble .

(10) The values of wall pressure fluctuation intensity on the end-wall surface, at different streamwise stations in the blade end-wall corner region, were significantly influenced by the changes in the strength of the horseshoe vortex as it moved along the corner (Fig. 6.5(a)). At any streamwise station in the blade end-wall corner region, the spectral contents at different frequencies were observed to increase as the blade surface was approached (Fig. 6.6).

(11) The values of correlation coefficient, in the streamwise direction, were observed to decrease and increase because of the presence of favorable and adverse pressure gradients, respectively, in the blade end-wall corner region. Also, at distances beyond $z/\delta \approx 0.2$, the values of R_{pu} were higher in the inner region compared to the outer region of the shear layer.

(12) The development of turbulent boundary layer in the presence of natural transition (Case 1) showed the existence of self-similarity at all streamwise stations, except at the first streamwise station (Fig. 4.1(a)). The lack of self-similarity at the first streamwise station suggested that the boundary layer had not attained its fully developed state. Similar results on the existence of self-similarity at different streamwise stations were evident either if initial roughness was introduced, Case 3 (Fig. 4.13(a)) or when the free stream turbulence level was increased with or without the presence of initial roughness, viz., Cases 4 and 2, respectively (see Figs. 4.15(a) and 4.7(a)).

(13) The velocity-defect was observed to decrease at a given streamwise station with an increase in the free stream turbulence in

the absence of initial roughness (Fig. 4.9). A fullness of the mean velocity profile indicates an increase in the value of wall shear stress. The measured wall shear stress values in Case 2 were found to be higher than the values in Case 1 and, therefore, support the above observation (Fig. 4.12). However, the velocity-defect increased and the mean velocity profiles became less full with an increased level of free stream turbulence in the presence of initial roughness (see Figs. 4.8 and 4.9).

(14) The comparison of C_f values at the same streamwise stations with and without initial roughness i.e., Case 3 with Case 1, indicated lower values of C_f closer to the roughness strip. Further downstream C_f increased relative to Case 1. It was noted that a distance of $\approx 40\ \delta_0$ (δ_0 being the boundary layer thickness at the first streamwise station in Case 1) from the roughness strip was required for C_f to reach the values obtained in Case 1 (Fig. 4.12(a)). However, the comparison of C_f results for Case 4 with Case 1 indicated that a larger distance $\approx 65\ \delta_0$ downstream of the roughness strip was needed to reach the C_f values of Case 1.

(15) A comparison of mean flow boundary layer parameters for four cases revealed that in the presence of initial roughness, the increased level of free stream turbulence had an effect opposite in nature compared to the case when initial roughness was absent (see Tables 4.2 and 4.3 and Figs. 4.3-4.6). The variation of wall shear stress appeared to be one of the possible reasons for this observed trend.

APPENDIX A

NORMAL SENSOR HOT-WIRE PROBE CALIBRATION

The normal sensor hot-wire probe was calibrated against the pitot-static tube. The anemometer output E_b and the velocity U are related by King's law written as,

$$E_b^2 = A_1 + B_1 U^n \qquad (A.1)$$

In the above equation A_1, B_1 and n are calibration constants which are obtained by calibrating the hot-wire probe. The hot-wire and the pitot-static probes were placed in the wind tunnel test-section where the uniform flow existed. Corresponding to the known velocity, which was measured with the pitot-static probe, anemometer output was recorded. The outputs from both the probes were simultaneously digitized using the MASSCOMP mini computer system. The number of data sets, containing hot-wire and pitot-static probes outputs, were obtained by varying the free stream velocity. For different values of exponent n, constants A_1 and B_1 in Eqn. A.1 were calculated in a least square sense. The optimum values of A_1, B_1 and n were obtained such that the normalized standard deviation for calculated velocity is minimized. The normalized standard deviation for velocity was calculated using the relation,

$$\varepsilon_u = [\ (1/N1)\ \Sigma(1- U_c/U)^2\ ]^{0.5} \qquad (A.2)$$

where U is the measured velocity, U_c is the value of velocity calculated by using Eqn. A.1 and N1 is the number of measured data sets. The above mentioned procedure for calculating the optimum values of A_1,

B_1 and n was proposed by Bruun and Tropea[145]. A typical calibration curve is shown in Fig. A.1. Fig. A.2 shows the variation of normalized standard deviation for the calculated velocity against the value of exponent n. It is quite evident that the optimum value of n exists at which the error in calculated velocity is minimum (Fig. A.2). A listing of the computer program used for calibrating the hot-wire probe using the digitized data is also included here.

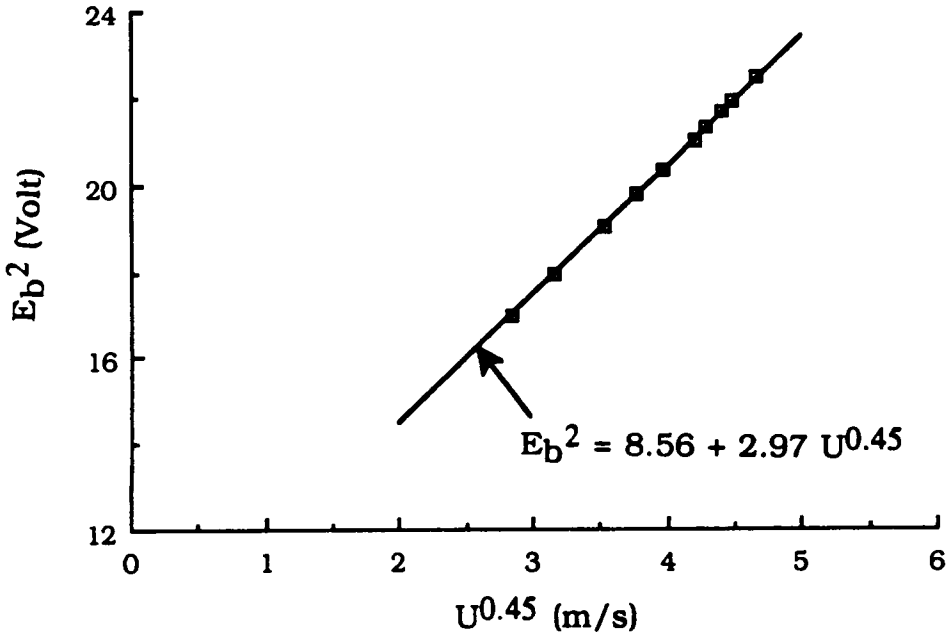

Fig. A.1 A Typical Calibration of Normal Single Sensor Hot-Wire Probe

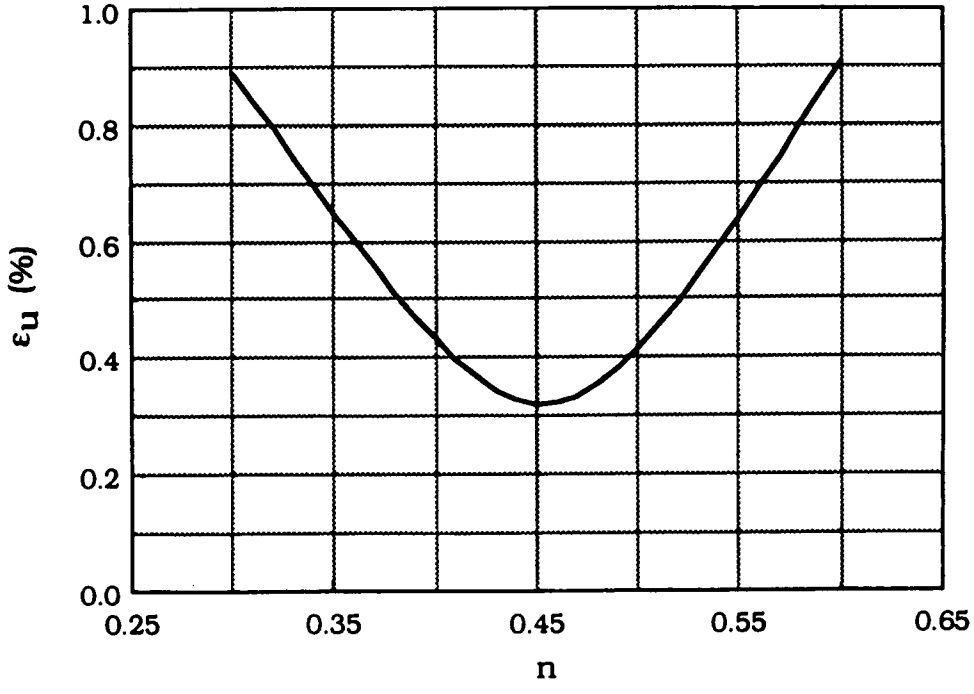

Fig. A.2 A Typical Variation of ε_u With n

```
      INCLUDE '/USR/INCLUDE/MR.F'
C
C     PROGRAM TO CALCULATE OPTIMUM VALUES OF CALIBRATION
C     CONSTANTS IN KING'S LAW IN LEAST SQUARE SENSE FOR
C     SINGLE NORMAL SENSOR HOT-WIRE PROBE
C     PROGRAM READS DIGITIZED DATA STORED ON DISC FILES
C     UNDER NAME 'DAT.IJK'
C     PROGRAM WRITTEN IN USER INTERACTIVE MODE
C     CALDATA - DIGITIZED SAMPLES
C     NCH - TOTAL NO. OF DIGITIZED CHANNELS
C     TNSAMPL - TOTAL NO. OF DIGITIZED SAMPLES COLLECTED
C     RFRQ - SAMPLING RATE
C     BRFRQ - THROUGHPUT RATE OF A/D UNIT = 1MHZ
C     M - NO. OF DATA SETS
C     CC = CALIBRATION CONST. FOR VARIABLE RELUCTANCE TYPE
C          DIFFERENTIAL PRESSURE TRANSDUCER IN IN./VOLT
C     CF1 = CONVERSION FACTOR FROM 1IN. OF HG TO N/M**2
C     CF2 = CONVERSION FACTOR FROM 1IN. OF WATER TO N/M**2
C     RAIR = GAS CONST. FOR AIR IN J/KG.K
C     AVMN1(I) AND AVMN2(I) ARE USED AS OUTPUTS OF CH.1
C     AND CH.2, RESPECTIVELY
C     AVMN1 IS USED TO CALCULATE MEASURED VELOCITY, UM(I)
C
      INTEGER*2 CALDATA(300000)
      DIMENSION AVMN1(30),AVMN2(30),UM(30)
      INTEGER NCH,TNSAMPL,M,NTCH
      REAL RFRQ,BRFRQ
      CHARACTER*20 FLNM
      CHARACTER*20 OUTFILE
      PRINT *,'ENTER FILE NAME WHERE DATA ARE STORED'
      READ 1001,FLNM
 1001 FORMAT(A)
      OPEN(9,FORM='UNFORMATTED',STATUS='OLD',FILE=FLNM)
      REWIND 9
      READ(9) NCH,TNSAMPL,RFRQ,BRFRQ,M
      PRINT *, NCH,TNSAMPL,RFRQ,BRFRQ,M
      NTCH = TNSAMPL
      NSAMPL = TNSAMPL/NCH
      CALL DISCREAD(CALDATA,NTCH,NCH,M,RFRQ,AVMN1,AVMN2)
      PRINT *, 'ENTER FILE NAME FOR OUTPUT AS CALOUT.IJ'
      READ 1001, OUTFILE
      PRINT 1001, OUTFILE
      OPEN(8,FORM='FORMATTED',FILE=OUTFILE)
      REWIND 8
      WRITE(8,101) TEXT
  101 FORMAT(2X,A)
      DO 10 I = 1, M
   10 PRINT *, 'DATASET #',I,AVMN1(I),AVMN2(I)
      PRINT *, ' ENTER TRANSDUCER SENSITIVITY IN IN./VOLT'
```

```
      READ *, CC
      PRINT *, ' ENTER ATM. PRESSURE IN IN. OF HG = PATM'
      READ *, PATM
      PRINT *, ' ENTER ROOM TEMP. IN DEG. F = TATM'
      READ *, TATM
      CF1 = 3386.6
      CF2 = 249.09
      RAIR = 287.1
      TABS = 5.0*(TATM - 32.0)/9.0 + 273.15
      RHO = PATM * CF1/(RAIR * TABS)
      WRITE(8,102) RFRQ,NSAMPL,PATM,TABS,CC,RHO
  102 FORMAT(/2X,'SAMPLING RATE =',F7.1,10X,'SAMPLES/CHANNEL =',
     1  I6//2X,'ATM. PRESS.(IN. HG) =',F7.3,5X,'ATM. TEMP(K) =',
     2  F8.3//2X,'TRANSDUCER SENSITIVITY =',F7.4//2X,
     3  'AIR DENSITY =',F7.4/)
      WRITE(8,103)
  103 FORMAT(/5X,'I',2X,'UREF(VOLTS)',2X,'BRIDGE OUTPUT(VOLTS)'/)
      DO 11 I = 1,M
   11 WRITE(8,104) I,AVMN1(I),AVMN2(I)
  104 FORMAT(3X,I2,2(4X,F8.5)/)
      DO 20 I = 1,M
      UM(I) = SQRT(2.0*AVMN1(I)*CC*CF2/RHO)
   20 PRINT *, UM(I),AVMN2(I)
      CALL CALBRT(UM,AVMN2,M,AOPT,BOPT,OPTN,ERMIN)
      WRITE(8,107) AOPT,BOPT,OPTN
  107 FORMAT(//5X,'OPTIMUM A = ',F8.5//5X,'OPTIMUM B =',F8.5//
     1  5X,'OPTIMUM N =',F8.5/)
      CLOSE (8)
      STOP
      END
C
C
C     SUBROUTINE DISCREAD
C     READS DIGITIZED DATA AND CALCULATES MEAN VALUES OF
C     DATA (IN VOLTS) FROM TWO CHANNELS
C
      SUBROUTINE DISCREAD(CALDATA,NTCH,NCH,M,RFRQ,VMN1,VMN2)
      INTEGER*2 CALDATA(M*NTCH)
      DIMENSION VMN1(M),VMN2(M)
      CHARACTER*80 TEXT
      READ(9) TEXT
      PRINT 1001, TEXT
 1001 FORMAT(A)
      READ(9) CALDATA
      REWIND 9
      PRINT *, 'DATA READING FINISHED'
      CLOSE(9)
      NSAMPL = NTCH/NCH
      J = 1
      K = NTCH
```

```
      DO 44 II = 1,M
      SUM1 = 0.0
      SUM2 = 0.0
      DO 33 I = J,K,NCH
      DATA1 = FLOAT(CALDATA(I))*5.0/2048.0
      DATA2 = FLOAT(CALDATA(I+1))*5.0/2048.0
      SUM1 = SUM1 + DATA1
      SUM2 = SUM2 + DATA2
   33 CONTINUE
      VMN1(II) = SUM1/FLOAT(NSAMPL)
      VMN2(II) = SUM2/FLOAT(NSAMPL)
      J = J + NTCH
   44 K = K + NTCH
      PRINT *, 'SAMPLES SEPARATED AND AVERAGING DONE'
      RETURN
      END
C
C
C     SUBROUTINE CALBRT
C
C     PROGRAM TO CALCULATE OPTIMUM VALUE OF CONSTANTS IN
C     CALIBRATION EQUATION OF HOT-WIRE
C     CAIBRATION EQUATION: E**2 = A + B U**N
C     INPUT:
C       X = U
C       FX = E
C       M = NO OF DATA SETS
C     OUTPUT:
C       OPTIMUM VALUES OF A, B, N
C       ERMIN = MINIMUM ERROR IN CALCULATED VALUE OF X
C
      SUBROUTINE CALBRT(X,FX,M,AOPT,BOPT,OPTN,ERMIN)
      DIMENSION X(M),FX(M)
      EXPNT = 0.3
      DEXP = 0.01
      J = 1
      WRITE(8,105)
   50 CALL LSTSQ(X,FX,EXPNT,M,A,B)
      SUM = 0.0
      DO 1 I = 1,M
      XC = ((FX(I)**2 - A)/B)**(1.0/EXPNT)
      FACT = (1.0 - XC/X(I))**2
    1 SUM = SUM + FACT
      ERX = SQRT(SUM/FLOAT(M))
      IF (J .EQ. 1) GO TO 10
      IF (ERX .LT. ERMIN) GO TO 10
      GO TO 30
   10 ERMIN = ERX
      AOPT = A
      BOPT = B
```

```
      OPTN = EXPNT
   30 IF (EXPNT .LE. 0.6) THEN
  105 FORMAT(8X,'A',10X,'B',10X,'N',7X,'ERR(U)'/)
      WRITE(8,106) A,B,EXPNT,ERX
  106 FORMAT(2X,3(3X,F8.5),2X,E12.5)
      EXPNT = EXPNT + DEXP
      J = J + 1
      GO TO 50
      ENDIF
      RETURN
      END
C
C
C     SUBROUTINE LSTSQ
C
C     SUBROUTINE TO CALCULATE CONSTANTS (A AND B) IN
C     EQUATION:  FX**2 = A + B X**EXPNT IN LEAST
C     SQUARE SENSE FOR A GIVEN VALUE OF EXPNT
C
      SUBROUTINE LSTSQ(X,FX,EXPNT,M,A,B)
      DIMENSION X(M),FX(M)
      SMX = 0.0
      SMFX = 0.0
      SMXFX = 0.0
      SMX2 = 0.0
      DO 1 I = 1,M
      X1 = X(I)**EXPNT
      FX1 = FX(I)**2
      SMX = SMX + X1
      SMFX = SMFX + FX1
      XFX = X1 * FX1
      SMXFX = SMXFX + XFX
      X2 = X1 * X1
    1 SMX2 = SMX2 + X2
      DET = SMX2*FLOAT(M) - SMX*SMX
      A = (SMFX*SMX2 - SMX*SMXFX)/DET
      B = (SMXFX*FLOAT(M) - SMFX*SMX)/DET
      RETURN
      END
```

APPENDIX B

COMPUTER PROGRAMS FOR CALCULATING WALL PRESSURE-VELOCITY CORRELATION AND POWER SPECTRA OF FLUCTUATING WALL PRESSURE

A brief description on the computer programs, written for the calculation of wall pressure-velocity correlation and the power spectra of the fluctuating wall pressure, and their FORTRAN listings are presented in this appendix.

B.1 Computer Program for the Calculation of Wall Pressure-Velocity Correlation

A computer program was written to calculate the wall pressure-velocity correlation incorporating the steps outlined in Chapter III (Section 3.3.4). The digitized data in the program was processed by dividing the complete record length of the signal in to number of blocks containing equal number of digitized samples. The various required parameters were calculated first for each block and then averaged over the number of blocks selected. The temperature correction for the hot-wire voltage output was included in the computer program. In an absence of the fluctuating velocity data, a provision was made in the program to analyze only the fluctuating wall pressure data for the calculation of mean and RMS values of the wall pressure fluctuation. A FORTRAN listing (PROGRAM 1) of the computer program is included here.

PROGRAM 1

```
      INCLUDE ' /USR/INCLUDE/MR.F'
C
C     PROGRAM TO CALCULATE CORRELATION OF WALL PRESSURE
C     FLUCTUATION WITH THE VELOCITY FLUCTUATIONS USING
C     DIGITIZED DATA
C     PROGRAM READS DIGITIZED DATA STORED ON DISK FILES UNDER
C     NAME 'DAT.IJK'
C     PROGRAM WRITTEN IN USER INTERACTIVE MODE
C     NCH- TOTAL NO. OF DIGITIZED CHANNELS
C     TNSAMPL- TOTAL NO. OF SAMPLES COLLECTED
C     RFRQ- SAMPLING RATE
C     BRFRQ- THROUGHPUT RATE OF A/C UNIT = 1MHZ
C     MDP- NO. OF DATA SETS
C     CALDATA- DIGITIZED SAMPLES
C
      INTEGER*2 CALDATA(1000000)
      INTEGER NCH, TNSAMPL,MDP
      REAL RFRQ,BRFRQ
      CHARACTER*20 FLNM
      PRINT *, 'ENTER FILE NAME WHERE DATA ARE STORED'
      READ 101, FLNM
  101 FORMAT(A)
      OPEN(9,FORM='UNFORMATTED',STATUS='OLD',FILE=FLNM)
      REWIND 9
      READ(9) NCH,TNSAMPL,RFRQ,BRFRQ,MDP
      PRINT *, NCH,TNSAMPL,RFRQ,BRFRQ,MDP
      NSAMPL = TNSAMPL/NCH
      CALL DISCREAD(CALDATA,NSAMPL,NCH,MDP,RFRQ)
      STOP
      END
C
C     SUBROUTINE DISCREAD
C
      SUBROUTINE DISCREAD(CALDATA,NSAMPL,NCH,MDP,RFRQ)
C
C     READS DIGITIZED DATA AND PROCESS IT TO OBTAIN
C     CORRELATION OF WALL PRESSURE FLUCTUATION WITH
C     THE VELOCITY FLUCTUATION
C     CALCULATIONS DONE IN BLOCKS EACH HAVING 4096
C     SAMPLES MAXIMUM
C     A, B, AN- CALIBRATION CONSTANTS IN KING'S LAW
C     DELT- TEMPERATURE DIFFERENCE IN DEG. F FOR
C     CORRECTING HOT-WIRE OUTPUT
C     CC = CALIBRATION CONST. FOR VARIABLE RELUCTANCE TYPE
C          DIFFERENTIAL PRESSURE TRANSDUCER IN IN./VOLT
C     CF1 = CONVERSION FACTOR FOR 1 IN. OF HG TO N/M**2
C     CF2 = CONVERSION FACTOR FOR 1 IN. OF WATER TO N/M**2
C     CF3 = CONVERSION FACTOR FOR 1 PSI TO N/M**2
C     RAIR = GAS CONSTANT FOR AIR IN J/KG.K
```

```
C      CH. 1 USED FOR REF. TOT. PRESSURE
C      CH. 2 USED FOR WALL PRESSURE FLUCTUATION
C      CH. 3 USED FOR VELOCITY FLUCTUATION
C
C
      INTEGER*2 CALDATA(NCH,NSAMPL)
      DIMENSION PI(4096),UI(4096)
      CHARACTER*80 TEXT
      CHARACTER*20 OUTFILE
      READ(9) TEXT
      PRINT 102, TEXT
  102 FORMAT(2X,A)
      READ(9) CALDATA
      REWIND 9
      PRINT *, 'DATA READING FINISHED'
      CLOSE (9)
      PRINT *, 'ENTER FILE NAME FOR OUTPUT DATA AS DATOUT.IJK'
      READ 101, OUTFILE
  101 FORMAT(A)
      PRINT 102, OUTFILE
      OPEN(8,FORM='FORMATTED',FILE=OUTFILE)
      REWIND 8
      WRITE(8,200) TEXT
      PRINT *, 'ENTER BLOCK SIZE OF SAMPLES- NBLKSZ'
      READ *, NBLKSZ
    1 PRINT *, 'ENTER NO. OF BLOCK- NBLK'
      READ *, NBLK
      MBLK = INT(NSAMPL/NBLKSZ)
      IF(NBLK .GT. MBLK) THEN
      PRINT *, 'REDUCE NO. OF BLOCKS < OR = TO', MBLK
      GO TO 1
      ENDIF
      PRINT *, 'ENTER ATM. PRESS. IN IN. OF HG = PATM'
      READ *, PATM
      PRINT *, 'ENTER ROOM TEMP. IN DEG. F = TATM'
      READ *, TATM
      PRINT *, 'ENTER CALIBRATION CONST. IN IN./VOLT'
      READ *, CC
      PRINT *, 'ENTER AMPLIFICATION GAIN FACTOR'
      READ *, GF
      PRINT *, 'ENTER TRANSDUCER SENSITIVITY IN MV/PSI'
      READ *, S
      CF1 = 3386.6
      CF2 = 249.09
      RAIR = 287.1
      CF3 = 6894.76
      TABS = 5.0*(TATM - 32.0)/9.0 + 273.15
      RHO = PATM*CF1/(RAIR*TABS)
      WRITE(8,201) RFRQ,NSAMPL
      WRITE(8,202) NBLKSZ,NBLK
```

```
      WRITE(8,203) PATM,TABS,GF,S,CC,RHO
C     BRANCHING
      PRINT *, 'ENTER 1 FOR RMS OR 2 FOR PU-CORRELATION'
      READ *, INUM
      IF (INUM .EQ. 1) GO TO 500
      PRINT *, 'ENTER A, B, N :'
      READ *, 'A, B, AN
      PRINT *, 'A, B, N:', A, B, AN
      WRITE(8,204) A, B, AN
      PRINT *, 'ENTER DELT'
      READ *, DELT
      DELC = DELT*5.0/9.0
      ALPHA = 0.0042
      R = 1.5
      FAC1 = ALPHA/(2.0*(R - 1.0))
      FAC2 = - FAC1*DELC
      UREF = 0.0
      UM = 0.0
      UI2M = 0.0
      PI2M = 0.0
      PM = 0.0
      PUIM = 0.0
      DO 11 II = 1,NBLK
      SUREF = 0.0
      SPI = 0.0
      SPI2 = 0.0
      SUI = 0.0
      SUI2 = 0.0
      SPUI = 0.0
      DO 12 I = 1,NBLKSZ
      K = I + (II - 1)*NBLKSZ
      VDAT = FLOAT(CALDATA(1,K))*5.0/2048.0
      PDAT = FLOAT(CALDATA(2,K))*5.0/2048.0
      UDAT = FLOAT(CALDATA(3,K))*5.0/2048.0
      UDAT = UDAT*(1 - FAC2)
      PI(I) = PDAT*1000.0*CF3/(GF*S)
      UI(I) = ((UDAT*UDAT - A)/B)**(1.0/AN)
      UI2 = UI(I)*UI(I)
      PI2 = PI(I)*PI(I)
      SPI = SPI + PI(I)
      SUI = SUI + UI(I)
      SUI2 = SUI2 + UI2
      SPUI = SPUI + PI(I)*UI(I)
      SPI2 = SPI2 + PI2
   12 SUREF = SUREF + VDAT
      SUREF = SUREF/FLOAT(NBLKSZ)
      UREF = SQRT(2.0*SUREF*CC*CF2/RHO) + UREF
      PM = SPI/FLOAT(NBLKSZ) + PM
      PI2M = SPI2/FLOAT(NBLKSZ) + PI2M
      UM = SUI/FLOAT(NBLKSZ) + UM
```

```
      UI2M = SUI2/FLOAT(NBLKSZ) + UI2M
      PUIM = SPUI/FLOAT(NBLKSZ) + PUIM
      PRINT *,'THE ',II, 'TH BLOCK CALCULATION OVER'
   11 CONTINUE
      UREF = UREF/FLOAT(NBLK)
      QINF = 0.5*RHO*UREF*UREF
      PM = PM/FLOAT(NBLK)
      PP2M = PI2M/FLOAT(NBLK) - PM*PM
      UM = UM/FLOAT(NBLK)
      UP2M = UI2M/FLOAT(NBLK) - UM*UM
      PUM = PUIM/FLOAT(NBLK) - PM*UM
      RMSP = SQRT(PP2M)
      RATIO = RMSP/QINF
      RMSU = SQRT(UP2M)
      TU = RMSU/UREF
      CORPU = PUM/(RMSP*RMSU)
      PRINT *, 'UREF(M/S)',UREF, ' QINF(PA)',QINF
      PRINT *, 'U-AVG(M/S)',UM,'  P-AVG(PA)',PM
      PRINT *, 'RMS-P(PA)',RMSP,'  RMS-U(M/S)',RMSU
      PRINT *, 'PU-AVG',PUM,'  CORCOF-PU',CORPU
      WRITE(8,205) UREF,QINF,PM,RMSP,RATIO,UM,
     1  RMSU,TU,PUM,CORPU
      CLOSE (8)
      RETURN
  500 PRINT *, 'RMS VALUE CALCULATION OF WALL PRESSURE'
      UREF = 0.0
      PI2M = 0.0
      PM = 0.0
      DO 21 II = 1,NBLK
      SUREF = 0.0
      SPI = 0.0
      SPI2 = 0.0
      DO 22 I = 1,NBLKSZ
      K = I + (II - 1)*NBLKSZ
      VDAT = FLOAT(CALDATA(1,K))*5.0/2048.0
      PDAT = FLOAT(CALDATA(2,K))*5.0/2048.0
      PI(I) = PDAT*1000.0*CF3/(GF*S)
      SUREF = SUREF + VDAT
      PI2 = PI(I)*PI(I)
      SPI = SPI + PI(I)
   22 SPI2 = SPI2 + PI2
      UREF = SUREF/FLOAT(NBLKSZ) + UREF
      PM = SPI/FLOAT(NBLKSZ) + PM
      PI2M = SPI2/FLOAT(NBLKSZ) + PI2M
   21 CONTINUE
      UREF = UREF/FLOAT(NBLK)
      IF (UREF .LE. 0.0) UREF = ABS(UREF)
      UREF = SQRT(2.0*UREF*CC*CF2/RHO)
      QINF = 0.5*RHO*UREF*UREF
      PM = PM/FLOAT(NBLK)
```

```
      PP2M = PI2M/FLOAT(NBLK) - PM*PM
      RMSP = SQRT(PP2M)
      RATIO = RMSP/QINF
      PRINT *, 'UREF(M/S): ',UREF,'  QINF(PA):',QINF
      PRINT *, P-AVG(PA): ',PM
      PRINT *, 'RMS-P(PA):',RMSP,'  RMS-P/QINF:',RATIO
      WRITE(8,207)UREF,QINF
      WRITE(8,206) PM,RMSP,RATIO
206   FORMAT(5X,'P-MEAN(PA)=',F10.4//5X,'P-RMS(PA)=',
     1  F10.4,5X,'P-RMS/QINF=',E15.7//)
201   FORMAT(//5X,'SAMPLING RATE=',F8.1,10X,
     1  'SAMPLES/CHANNEL=',I6//)
202   FORMAT(5X,'BLOCK SIZE=',I5,5X,'NO. OF BLOCKS=',I3//)
203   FORMAT(/2X,'ATM. PRESS.(IN. HG)=',F7.3,4X,
     1  'ABS. TEMP.(DEG.K)=',F10.3//2X,'GAIN FACTOR=',F8.1,
     2  10X,'TRANSDUCER SENSITIVITY(MV/PSI)=',F7.3//2X,
     3  'DIFF. TRANSDUCER SENSITIVITY(IN./VOLT)=',F7.4//
     4  2X,'AIR DENSITY(KG/M**3)=',F7.4/)
204   FORMAT(/5X,'A=',F10.4,5X,'B=',F10.4,5X,'N=',F10.4/)
205   FORMAT(/5X,'U-REF(M/S)=',F7.4,11X,'QINF(PA)=',F8.4//
     1  5X,'P-MEAN(PA)=',F10.4,8X,'P-RMS(PA)=',F8.4//5X,
     2  'P-RMS/QINF=',E15.7//5X,'U-MEAN(M/S)=',F10.4,7X,
     3  'U-RMS(M/S)=',F10.4//5X,'TU=',E12.5//5X,
     4  'PU-MEAN(N/M-S)=',E15.7,5X,
     5  'CORR. COEFF=',E15.7//)
200   FORMAT(5X,A)
207   FORMAT(/5X,'U-REF(M/S)=',F6.4,5X,'QINF(PA) =',F8.4/)
      CLOSE (8)
      RETURN
      END
```

B.2 Computer Program for the Calculation of Power Spectra of Fluctuating Wall Pressure

The procedure for calculating the power spectra of fluctuating wall pressure using Fast Fourier Transform (FFT) technique was presented in Chapter III (Section 3.3.2). A computer program was written to calculate the power spectral density function of fluctuating wall pressure, at discrete frequencies, from its Fourier components obtained by a standard FFT subroutine. The calculations of power spectral density functions at discrete frequencies were obtained in blocks containing equal number of digitized samples. The averaging carried out over the number of blocks selected, then gave the final power spectral density function at discrete frequencies. The frequency bandwidth could be varied, if required, by changing the size of the block. The steps to calculate the intensity of wall pressure fluctuation, from the power spectral density distribution obtained, were also included in the program. A FORTRAN listing (PROGRAM 2) of the computer program is included here.

PROGRAM 2

```
      INCLUDE ' /USR/INCLUDE/MR.F'
C
C     PROGRAM TO CALCULATE POWER SPECTRAL DENSITY FUNCTION
C     OF WALL PRESSURE FLUCTUATIONS USING FAST FOURIER
C     TRANSFORM TECHNIQUE
C     PROGRAM READS DIGITIZED DATA STORED ON DISC FILES
C     UNDER NAME 'DAT.IJK'
C     PROGRAM WRITTEN IN USER INTERACTIVE MODE
C     NCH- TOTAL NO OF SIMULTANEOUSLY DIGITIZED CHANNELS
C     TNSAMPL- TOTAL NO. OF SAMPLES COLLECTED
C     RFRQ- SAMPLING RATE
C     BRFRQ- THROUGHPUT RATE OF A/D UNIT = 1MHZ
C     MDP- NO. OF DATA SETS
C     RAWDATA- DIGITIZED SAMPLES
C     NCN- CH. NO. ON WHICH FFT ANALYSIS TO BE DONE
C
      INTEGER*2 RAWDATA(400000)
      INTEGER NCH,TNSAMPL,NCN,NU
      REAL RFRQ,BRFRQ
      CHARACTER*20 FLNM
      PRINT *,'ENTER FILE NAME WHERE DATA ARE STORED'
      READ 1001, FLNM
 1001 FORMAT(A)
      PRINT *,'ENTER CHANNEL NO. FOR FFT'
      READ *, NCN
      PRINT *,'ENTER EXPONENT FOR LENGTH OF DATA ARRAY'
      READ *, NU
      NL = 2**NU
      PRINT *,'CHANNEL=',NCN,'LENGTH OF DATA ARRAY = ',NL
      OPEN(8,FORM='UNFORMATTED',STATUS='OLD',FILE=FLNM)
      REWIND 8
      READ(8) NCH,TNSAMPL,RFRQ,BRFRQ,MDP
      PRINT *, NCH,TNSAMPL,RFRQ,BRFRQ,MDP
      NSAMPL = TNSAMPL/NCH
      NFFT = INT(NSAMPL/NL)
  111 PRINT *, 'ENTER NO. OF 2**NU BLOCKS TO AVG. FFT'
      READ *, NF1
      IF (NF1 .GT. NFFT) THEN
      PRINT *,'REDUCE NO. OF BLOCKS < OR = TO', NFFT
      GO TO 111
      ENDIF
      PRINT *,'ENTER GAIN FACTOR OF AMPLIFICATION'
      READ *, GF
      PRINT *,'ENTER TRANSDUCER SENSITIVITY IN MV/PSI'
      READ *, SF
      CALL DISCREAD(RAWDATA,NSAMPL,NCH,NCN,NU,RFRQ,NF1,GF,SF)
      STOP
      END
C
```

```
C       SUBROUTINE DISCREAD
C
        SUBROUTINE DISCREAD(RAWDATA,NSAMPL,NCH,NCN,NU,RFRQ,NF,GF,SF)
C
C       READS DIGITIZED DATA AND PROCESS IT TO OBTAIN
C       POWER SPECTRAL DENSITY FUNCTION DISTRIBUTION
C       N- LENGTH OF DATA ARRAY FOR FFT = 2**NU
C       NU- EXPONENT FOR FFT (SHOULD NOT BE > 12), ALSO
C           CONTROLS FREQUENCY BANDWIDTH AT A GIVEN
C           SAMPLING RATE
C
        INTEGER*2 RAWDATA(NCH,NSAMPL)
        DIMENSION DATARY(4096),XIMAG(4096),SPC(4096)
        DIMENSION SMDB(4096)
        CHARACTER*80 TEXT
        CHARACTER*20 OUTFILE
        READ (8) TEXT
        PRINT 1002, TEXT
 1002   FORMAT(2X,A)
        READ (8) RAWDATA
        REWIND 8
        PRINT *,'DATA READING FINISHED'
        CLOSE (8)
        PRINT *,'ENTER FILE NAME FOR OUTPUT AS DATOUT.IJK'
        READ 1001, OUTFILE
 1001   FORMAT(A)
        PRINT 1002, OUTFILE
        OPEN(8,FORM='FORMATTED',FILE=OUTFILE)
        REWIND 8
        WRITE(8,1) TEXT
      1 FORMAT(2X,A)
        N = 2**NU
        WRITE(8,2) NCN,RFRQ,NSAMPL,NU,N,NF,GF,SF
      2 FORMAT(2X,'CHANNEL NO. FOR FFT:'I2//2X,
       1  'SAMPLING RATE =',F10.1,5X,
       2  'SAMPLES/CHANNEL =',I6//2X,
       2  'EXPONENT FOR FFT =',I3//2X,
       3  'LENGTH OF DATA ARRAY FOR FFT =',I5//2X,
       4  'NO. OF BLOCKS TO AVERAGE FFT =',I4//2X,
       5  'AMPLIFICATION GAIN FACTOR =',F7.1//2X,
       6  'TRANSDUCER SENSITIVITY(MV/PSI) =',F7.3/)
C       CFI = CONVERSION FACTOR FOR 1 PSI TO PASCAL
        CFI = 6894.76
        DO 133 I = 1,N
        SPC(I) = 0.0
  133   SMDB(I) = 0.0
        NM1 = N/2 - 1
        DO 34 IT = 1,NF
        DO 33 I = 1,N
        I1 = I + (IT - 1)*N
```

```
      DATA = FLOAT(RAWDATA(NCN,II))*5.0/2048.0
      DATARY(I) = DATA*1000.0*CF1/(GF*SF)
      XIMAG(I) = 0.0
   33 CONTINUE
      SMSPC = 0.0
      PRINT *,'THE',IT,'TH FFT STARTS'
      CALL FFT(DATARY,XIMAG,N,NU)
      REFDB = 20.0*1.0E-06
      DO 99 J = 1,N
      SP = (DATARY(J)**2 + XIMAG(J)**2)*2/(RFRQ*FLOAT(N))
      DB = 20.0*ALOG10(SQRT(SP)/REFDB)
      SPC(J) = SP + SPC(J)
      SMDB(J) = DB + SMDB(J)
      FREQ = FLOAT(J)*RFRQ/FLOAT(N)
   99 CONTINUE
      DO 199 JJ = 2,NM1
      SMSPC = SMSPC + (SPC(JJ) + SPC(JJ + 1))/IT
  199 CONTINUE
      PSQ = 0.5*SMSPC*RFRQ/FLOAT(N)
      RP = SQRT(PSQ)
      PRINT *, 'P-RMS  ',RP
   34 CONTINUE
      WRITE(8,3)
    3 FORMAT(/5X,'I',4X,'F(HZ)',7X,'SPC(PA**2/HZ)',
     1  5X,'SPC(DB)'/)
      M = N/2
      DO 35 I = 1,M
      FREQ = FLOAT(I)*RFRQ/FLOAT(N)
      SPC(I) = SPC(I)/FLOAT(NF)
      SMDB(I) = SMDB(I)/FLOAT(NF)
   35 WRITE(8,4) I,FREQ,SPC(I),SMDB(I)
    4 FORMAT(2X,I4,2X,F10.3,3X,E13.5,5X,F7.2/)
      WRITE(8,5) RP
    5 FORMAT(5X,'P-RMS(PA) =',F10.4)
      RETURN
      END
C
C     SUBROUTINE FFT
C
      SUBROUTINE FFT(XREAL,XIMAG,N,NU)
C
C     XREAL- REAL PART OF THE INSTANTANEOUS SIGNAL
C     XIMAG- IMAGINARY PART OF THE INSTANTANEOUS SIGNAL
C
      DIMENSION XREAL(N),XIMAG(N)
      N2 = N/2
      NU1 = NU - 1
      K = 0
      DO 100 L = 1,NU
  102 DO 101 I = 1,N2
```

```
      P = IBITR(K/2**NU1,NU)
      ARG = 6.283185*P/FLOAT(N)
      C = COS(ARG)
      S = SIN(ARG)
      K1 = K + 1
      K1N2 = K1 + N2
      TREAL = XREAL(K1N2)*C + XIMAG(K1N2)*S
      TIMAG = XIMAG(K1N2)*C - XREAL(K1N2)*S
      XREAL(K1N2) = XREAL(K1) - TREAL
      XIMAG(K1N2) = XIMAG(K1) - TIMAG
      XREAL(K1) = XREAL(K1) + TREAL
      XIMAG(K1) = XIMAG(K1) + TIMAG
  101 K = K + 1
      K = K + N2
      IF(K .LT. N) GO TO 102
      K = 0
      NU1 = NU1 - 1
  100 N2 = N2/2
      DO 103 K = 1,N
      I = IBITR(K - 1,NU) + 1
      IF(I .LE. K) GO TO 103
      TREAL = XREAL(K)
      TIMAG = XIMAG(K)
      XREAL(K) = XREAL(I)
      XIMAG(K) = XIMAG(I)
      XREAL(I) = TREAL
      XIMAG(I) = TIMAG
  103 CONTINUE
      RETURN
      END
C
C     FUNCTION IBITR
C
      FUNCTION IBITR(J,NU)
      J1 = J
      IBITR = 0
      DO 200 I = 1,NU
      J2 = J1/2
      IBITR = IBITR*2 + (J1 - 2*J2)
  200 J1 = J2
      RETURN
      END
```

APPENDIX C

YAW SENSITIVITIES OF THE SURFACE STATIC AND THE PRESTON TUBE

The yaw characteristics of the static tube resting on the surface (termed as the surface static tube) and the Preston tube were experimentally investigated in two- and three-dimensional flows. The results obtained on the yaw characteristics for both the tubes are presented and discussed here.

C.1 Yaw Sensitivity of the Surface Static Tube

Fig. C.1 shows the variation of $[P_S(\alpha) - P_S(\alpha_0)]$, normalized by the free stream dynamic pressure, with the yaw angle for three different flow conditions, where $P_S(\alpha)$ is the static pressure read by the surface static tube at an arbitrary yaw angle α and $P_S(\alpha_0)$ is the static pressure recorded by the surface static tube when aligned in the local flow direction α_0. The value of the angle α_0 corresponds to the maximum output recorded by the surface static tube. It is quite evident, from the different flow conditions investigated, that the static pressure obtained with the surface static tube is less if it is not aligned in the local flow direction. Also, the static tube resting on the surface, similar to the static tube away from the solid wall, is insensitive to the yaw angle of $\pm 5^0$. However, the error in measured static pressure increases with the increase in the yaw angle. It is also noted that the surface static tube is comparatively less sensitive to the yaw angle in the presence of adverse pressure gradient.

C-4

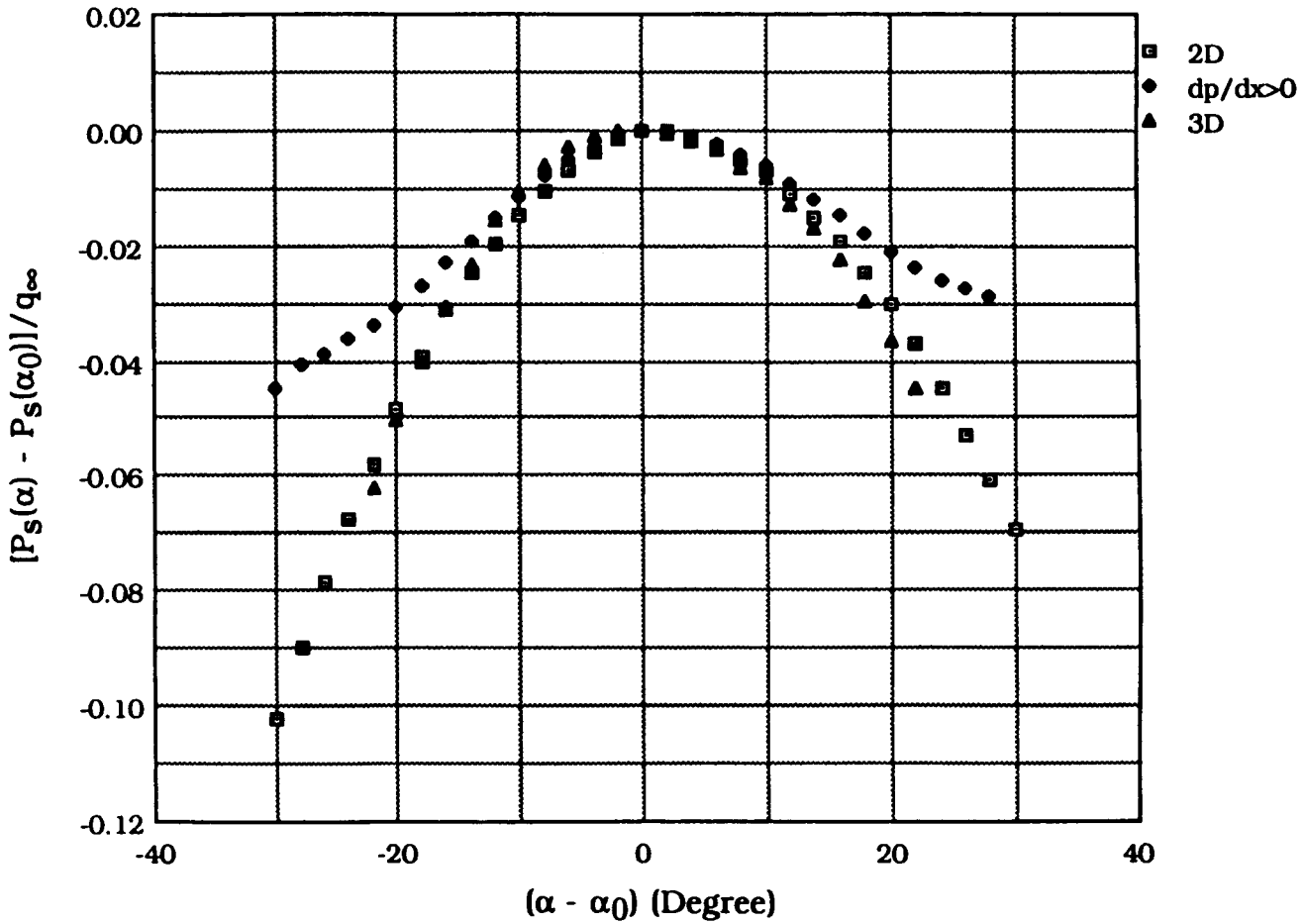

Fig. C.1 Yaw Sensitivity of Static Tube Resting on the Surface in Different Flow Conditions

In a three-dimensional flow with high degree of skewness, the error in measured static pressure using the surface static tube due to its misalignment with the local flow direction is shown in Fig. C.2. It is clearly observed that the smaller value of the static pressure will be obtained if the static tube is not aligned in the local flow direction. Moreover, the magnitude of the error in static pressure due to misalignment is small (<1%) if the error is expressed as a fraction of free stream dynamic head. It is important to mention here that, in general, the normalization of static pressure with the free stream dynamic pressure is used to evaluate error in the calculated velocity. In Fig. C.2(b) the error in measured static pressure due to misalignment is normalized with the static pressure recorded by the surface static tube when it is aligned in the local flow direction. It is quite evident, that if the static tube were not aligned in the local flow direction it would have recorded approximately 20% smaller static pressure.

C.2 Yaw Sensitivity of the Preston Tube

Fig. C.3(a) shows the variation of $[P_p(\alpha) - P_p(\alpha_0)]$, normalized by $P_p(\alpha_0)$, with the yaw angle for three different flow conditions, where $P_p(\alpha)$ is the total pressure read by the Preston tube at an angle α with the local flow direction and $P_p(\alpha_0)$ is the total pressure recorded by the Preston tube when it is aligned in the local flow direction. The Preston tube is observed to be insensitive, the error being less than 2%, to the yaw angle of $\pm 5^0$. However, the pressure recorded by the Preston tube reduces rapidly beyond the yaw angle of 5^0.

Fig. C.3(b) shows error in the total pressure recorded by the Preston tube, in a three-dimensional flow with the high degree of

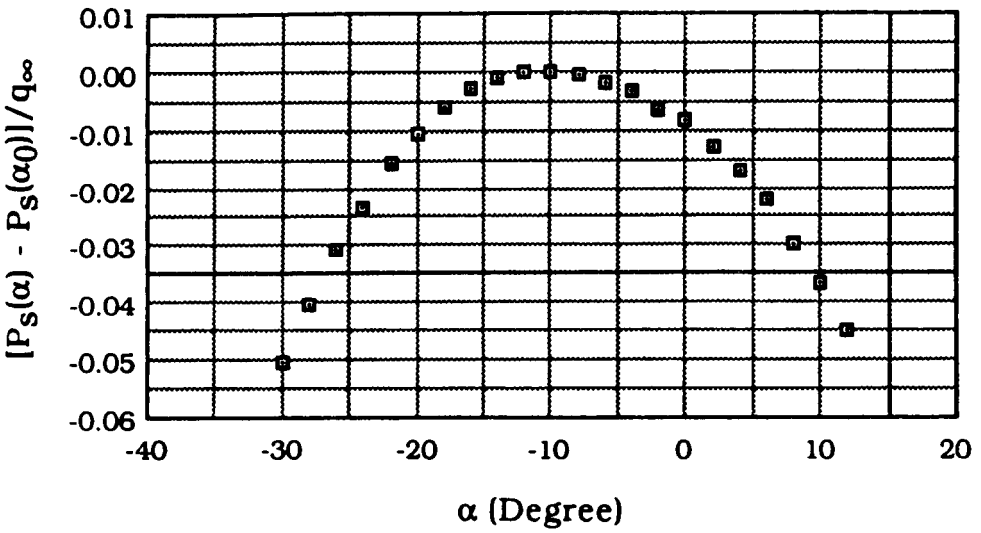

(a) Error in Surface Static Pressure as a Fraction of Free Stream Dynamic Pressure

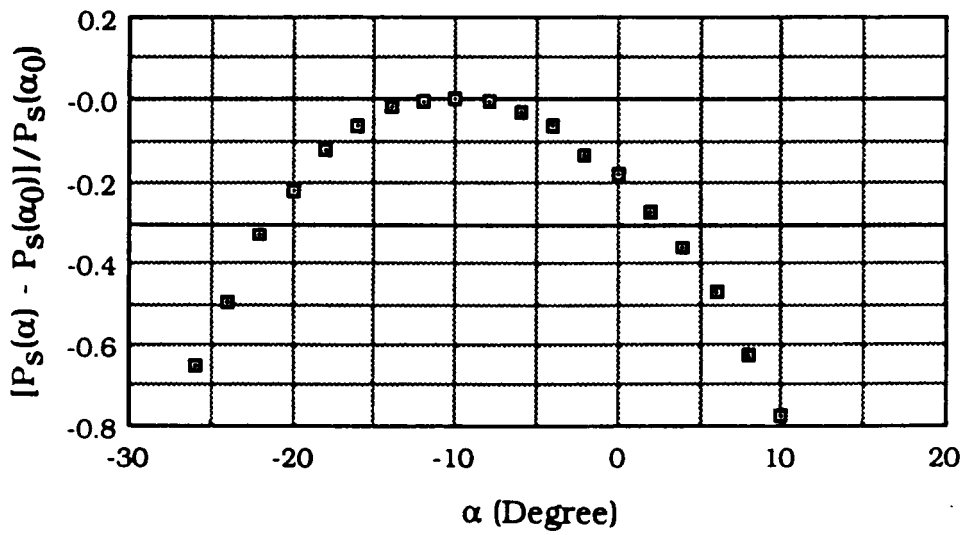

(b) Error as a Fraction of Surface Static Tube Pressure When Aligned in Local Flow Direction

Fig. C.2 Error in Surface Static Tube Pressure Due to its Misalignment (Note: $\alpha = 0$ Implies that the Centerlines of the Surface Static Tube and the Flat Plate are Parallel)

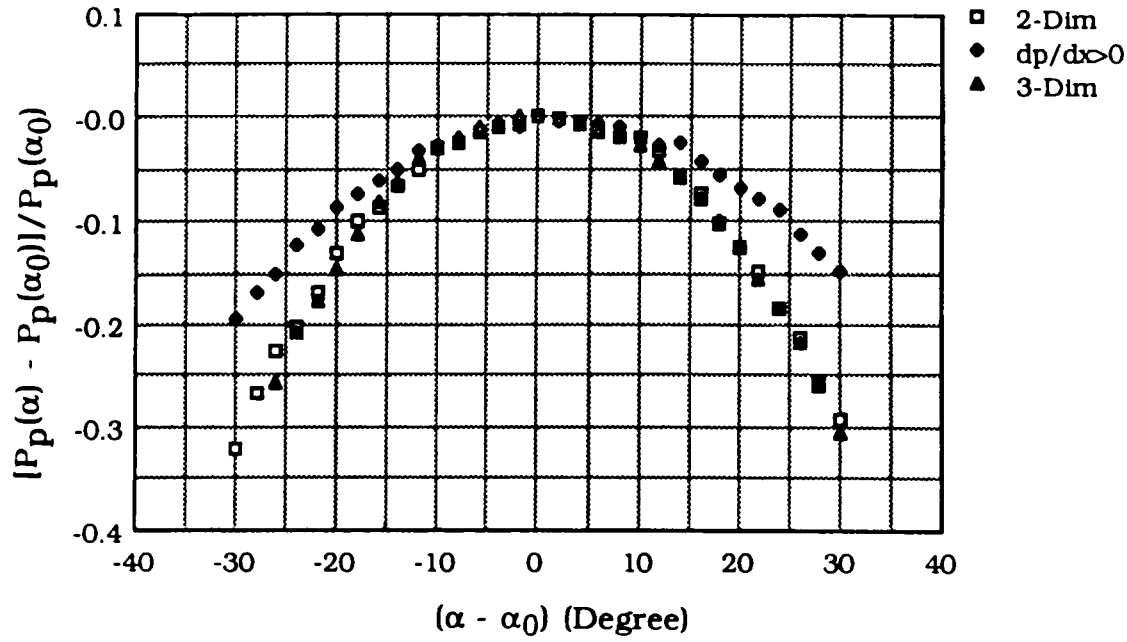

(a) Yaw Sensitivity of Preston Tube in Different Flow Conditions

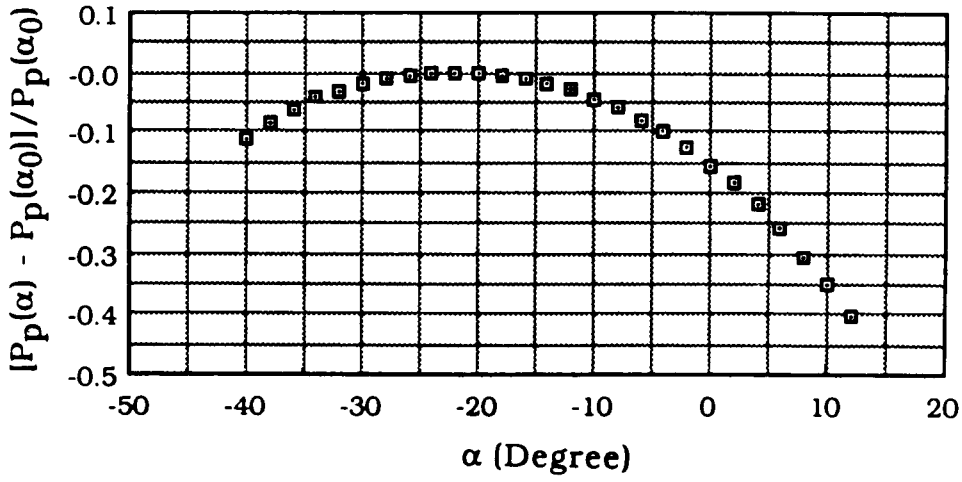

(b) Error in Preston Tube Pressure Due to its Misalignment With the Local Flow Direction- A Typical Error Distribution in Three-Dimensional Flow
(Note: $\alpha = 0$ Implies that the Centerlines of the Preston Tube and the Flat Plate are Parallel)

Fig. C.3 Yaw Sensitivity of the Preston Tube

skewness, due to its misalignment. The value of $\alpha = 0$ corresponds to the normal setting, i.e., parallel to the undisturbed flow direction, of the Preston tube. It is observed, that if the Preston tube were not aligned in the local flow direction, it would have recorded approximately 15% less total pressure. For the wall shear stress measurement, this observed error in the Preston tube output due to misalignment would cause approximately 10% error in the calculated value of the wall shear stress.

REFERENCES

1. Dring, R. P., "A Momentum Integral Analysis of the Three-Dimensional Turbine End-Wall Boundary Layer", Trans. ASME, Journal of Engineering for Power, Vol. 93, Oct. 1971, pp 386-396

2. Langston, L. S., Nice, M. L., and Hooper, R. M., "Three-Dimensional Flow Within a Turbine Cascade Passage", Trans. ASME, Journal of Engineering for Power, Vol. 99, Jan 1977, pp 21-28

3. Marchal, P., and Sieverding, C. H.,"Secondary Flows Within Turbomachinery Bladings", Secondary Flows in Turbomachines, AGARD CP-214, 1977

4. Belik, L., "Three-Dimensional and Relaminarization Effects in Turbine Blade Cascades- An Experimental Study", JSME-ASME Joint Gas Turbine Conference, Paper No. 37, 1977

5. Langston, L. S., "Crossflows in a Turbine Cascade Passage", Trans. ASME, Journal of Engineering for Power, Vol. 102, Oct. 1980, pp 866-874

6. Hunter, I. H., "Endwall Boundary Layer Flows and Losses in an Axial Turbine Stage", Trans. ASME, Journal of Engineering for Power, Vol. 104, Jan. 1982, pp 184-193

7. Binder, A., and Romey, R., "Secondary Flow Effects and Mixing of the Wake Behind a Turbine Stator", ASME Paper No. 82-GT-46, 1982

8. Sieverding, C. H., and Van Den Bosche, P., "The Use of Coloured Smoke to Visualize Secondary Flows in a Turbine-Blade Cascade", Journal of Fluid Mechanics, Vol. 134, 1983, pp 85-89

9. Gregory-Smith, D. G., and Graves, C. P., "Secondary Flows and Losses in a Turbine Cascade", Viscous Effects in Turbomachines, AGARD CP-351, 1983

10. Moore, J., and Ransmayr, A., "Flow in a Turbine Cascade: Part 1- Losses and Leading-Edge Effects", Trans. ASME, Journal of Engineering for Gas Turbines and Power, Vol. 106, April 1984, pp 400-408

11. Moore, J., and Adhye, R. Y., "Secondary Flows and Losses Downstream of a Turbine Cascade", ASME Paper No. 85-GT-64, 1985

12. Sonoda, T., "Experimental Investigation on Spatial Development of Streamwise Vortices in a Turbine Inlet Guide Vane Cascade", ASME Paper No. 85-GT-20, 1985

13. Moustapha, S. H., Paron, G. J., and Wade, J. H. T., "Secondary Flow in Cascades of Highly Loaded Turbine Blades", ASME Paper No. 85-GT-135, 1985

14. Govardhan, M., Venkatrayulu, N., and Prithvi Raj, D., "Secondary Losses in a Large Deflection Annular Turbine Cascade: Effect of the Entry Boundary Layer Thickness", ASME Paper No. 86-GT-171, 1986

15. Moore, J., Shaffer, D. M., and Moore, J. G., "Reynolds Stresses and Dissipation Mechanisms Downstream of a Turbine Cascade", ASME Paper No. 86-GT-92, 1986

16. Yamamoto, A., "Production and Development of Secondary Flows and Losses Within Two Types of Straight Turbine Cascades- Part 1: A Stator Case, ASME Paper No. 86-GT-184, Part 2: A Rotor Case, ASME Paper No. 86-GT-185, 1986

17. Sharma, O. P., and Butler, T. L., "Predictions of Endwall Losses and Secondary Flows in Axial Flow Turbine Cascades", ASME Paper No. 86-GT-228, 1986

18. Gregory-Smith, D. G., Graves, C. P., and Walsh, J. A., "Growth of Secondary Losses and Vorticity in an Axial Turbine Cascade", ASME Paper No. 87-GT-114, 1987

19. Zunino, P., Ubaldi, M., and Satta, A., "Measurements of Secondary Flows and Turbulence in a Turbine Cascade Passage", ASME Paper No. 87-GT-132, 1987

20. Lakshminarayana, B., and Ravindranath, A., "Interaction of Compressor Rotor Blade Wake With Wall Boundary Layer/Vortex in the End-Wall Region", ASME Paper No. 81-Gr/GT-1, 1981

21. Inoue, M., and Kuroumaru, M., "Three-Dimensional Structure and Decay of Vortices Behind an Axial Flow Rotating Blade Row", Trans. ASME, Journal of Engineering for Gas Turbines and Power, Vol.106, July 1984, pp 561-569

22. Cyrus, V., "Experimental Study of Three-Dimensional Flow in an Axial Compressor Stage", ASME Paper No. 86-GT-118, 1986

23. Gallus, H. E., and Hoenen, H., "Experimental Investigations of Airfoil- and Endwall Boundary Layers in a Subsonic Compressor Stage", ASME Paper No. 86-GT-143, 1986

24. Dong, Y., Gallimore, S. J., and Hodson, H. P., "Three-Dimensional Flows and Loss Reduction in Axial Compressors", ASME Paper No. 86-GT-193, 1986

25. Sieverding, C. H., "Recent Progress in the Understanding of Basic Aspects of Secondary Flows in Turbine Blade Passages", Trans. ASME, Journal of Engineering for Gas Turbines and Power, Vol. 107, April 1985, pp 248-257

26. Hawthorne, W. R., "The Secondary Flow About Struts and Airfoils", Journal of the Aeronautical Sciences, Sept. 1954, pp 588-608

27. Eichelbrenner, E. A., and Preston, J. H., "On the Role of Secondary Flow in Turbulent Boundary Layers in Corners (and Salients)", Journal de Me'canique, Vol. 10, Mar.1971, pp 91-112

28. Johnston, J. P., 'The Turbulent Boundary Layer at a Plane of Symmetry in a Three-Dimensional Flow", Trans. ASME, Journal of Basic Engineering, Sept. 1960, pp 622-628

29. Belik, L., "The Secondary Flow About Circular Cylinders Mounted Normal to a Flat Plate", Aeronautical Quarterly, Vol. 24, Feb. 1973, pp 47-54

30. Han, L. S., Ma, C., and Rapp, J. R., "The Endwall Influence on Heat Transfer From a Single Cylinder (The Horseshoe Vortex Effect)", 83-TOKYO-IGTC-3, 1983

31. Moore, J., and Forlini, T. J., "A Horseshoe Vortex in a Duct", ASME Paper No. 84-GT-202, 1984

32. Eckerle, W. A., and Langston, L. S., "Horseshoe Vortex Formation Around a Cylinder," ASME Paper No. 86-GT-246, 1986

33. Ishii, J., and Honami, S., "A Three-Dimensional Turbulent Detached Flow With a Horseshoe Vortex", ASME Paper No. 85-GT-70, 1985

34. East, L. F., and Hoxey, R. P., "Boundary Layer Effect in an Idealized Wing-Body Junction at Low speed", RAE Technical Report TR 68161, 1968

35. Hsing, T. D., and Teng, H. Y., "Experimental Study of the Behavior of 3D-Turbulent Boundary Layer in a Simplified Wing/ Body Junction", AIAA Paper No. 84-1529, 1984

36. Shabaka, I. M. M. A., "Turbulent Flow in an Idealized Wing-Body Junction", Ph.D. Thesis, Department of Aeronautics, Imperial College of Science and Technology, London, 1979

37. Oguz, E. A., "An Experimental Investigation of the Turbulent Flow in the Junction of a Flat Plate and a Body of Constant Thickness", Ph.D. Thesis, Georgia Institute of Technology, 1981

38. Kubendran, L. R., "Study of Turbulent Flow in a Wing-Fuselage Type Juncture", Ph.D. Thesis, Georgia Institute of Technology, 1983

39. Mehta, R. D., "Effect of Wing Nose Shape on the Flow in a Wing-Body Junction", Aeronautical Journal, Dec. 1984, pp 456-460

40. Chu, J. K., Rios-Chiquete, E., Sarohia, S., and Bernstein, L., "The 'Chu-Tube' : A Velocimeter for Use in Highly-Sheared, Three-Dimensional Steady Flows", Aeronautical Journal, March 1987, pp 142-149

41. Gorski, J. J., Govindan, T. R., and Lakshminarayana, B., "Computation of Three-Dimensional Turbulent Shear Flows in Corners", AIAA Journal, Vol. 23, May 1985, pp 685-692

42. Sepri, P., "An Investigation of the Flow in the Region of the Junction of a Wing and a Flat Surface Normal to the Wing Span", Queen Mary College, Department Engineering Report, QMC ER-1002, 1973

43. Barber, T. J., "An Investigation of Strut-Wall Intersection Losses", Journal of Aircraft, Vol. 15, Oct. 1978, pp 676-681

44. Rood, E. P., "The Separate Spatial Extents of the Trailing Horseshoe Root Vortex Legs From a Wing and Plate Junction", AIAA Paper No. 84-1526, 1984

45. Kubendran, L. R., and Harvey, W. D., "Juncture Flow Control Using Leading-Edge Fillets"., AIAA Paper No. 85-4097, 1985

46. Scheiman, J., and Kubendran, L. R., "Juncture Flow Measurement Using Laser Velocimetry", AIAA Paper No. 85-1612, 1985

47. Hazarika, B. K., "An Investigation of the Flow Characteristics in the Blade End-Wall Corner Region", Ph.D. Thesis, The City College of New York, CUNY, 1986

48. Townsend, A. A., "Equilibrium Layers and Wall Turbulence", Journal of Fluid Mechanics, Vol. 11, 1961, pp 97-120

49. Bradshaw, P., "Inactive Motion and Pressure Fluctuations in Turbulent Boundary Layers", Journal of Fluid Mechanics, Vol. 30, 1967, pp 241-258

50. Thomas, A. S. W., "Organized Structure in the Turbulent Boundary Layer", Advanced Flight Sciences Department, Lockheed-Georgia Company Report, LG77ER0210, 1977

51. Bradshaw, P., Cebeci, T., and Whitelaw, J. H., "Engineering Calculation Methods for Turbulent Flow (Text Book), Academic Press, 1981, Chapter 4

52. Willmarth, W. W., "Pressure Fluctuations Beneath Turbulent Boundary Layers", Annual Review of Fluid Mechanics, Vol. 7, 1975, pp 13-38

53. Serafini, J. S., "Wall-Pressure Fluctuations in a Turbulent Boundary Layer", Ph. D. Thesis, Case Institute of Technology, 1962

54. Willmarth, W. W., and Wooldridge, C. E., "Measurements of the Correlation Between the Fluctuating Velocities and the Fluctuating Wall Pressure in a Thick Turbulent Boundary Layer", AGARD Report No. 456, 1963

55. Willmarth, W. W., and Tu, B. J., "Structure of Turbulence in the Boundary Layer Near the Wall", The Physics of Fluids (Supplement), 1967, pp S134-S137

56. Klebanoff, P. S., and Diehl, Z. W., "Some Features of Artificially Thickened Fully Developed Turbulent Boundary Layers with Zero Pressure Gradient", NACA Report 1110, 1952, pp 1165-1191

57. Preston, J. H., "The Minimum Reynolds Number for a Turbulent Boundary Layer and the Selection of a Transition Device", Journal of Fluid Mechanics, Vol. 3, 1957, pp 373-384

58. Kline, S. J., Lisin, A. V., and Waitman, B. A., "Preliminary Experimental Investigation of Effect of Free-Stream Turbulence on Turbulent Boundary-Layer Growth", NASA-TND-368, 1960

59. Hall, D. J., and Gibbings, J. C., "Influence of Stream Turbulence and Pressure Gradient Upon Boundary Layer Transition", Journal of Mechanical Engineering Science, Vol. 14, 1972, pp 134-146

60. Evans, R. L., "Free-Stream Turbulence Effects on the Turbulent Boundary Layer", ARC CP-1282, 1974

61. Evans, R. L., "Freestream Turbulence Effects on Turbulent Boundary Layers in an Adverse Pressure Gradient", AIAA Journal, Technical Notes, Vol. 23, Nov. 1985, pp 1814-1816

62. Huffman, G. D., Zimmerman, D. R., and Bennet, W. A., "The Effect of Free-Stream Turbulence Level on Turbulent Boundary Layer Behaviour", AGARDOGRAPH No. 164, Paper No. I-5, 1972, pp 91-115

63. Robertson, J. M., and Holt, C. F., "Stream Turbulence Effects on Turbulent Boundary Layer", Proceedings of ASCE, Journal of Hydraulics Division, Vol. 98, No. HY6, June 1972, pp 1095-1099

64. Charnay, G., Comte-Bellot, G., and Mathieu, J., "Development of a Turbulent Boundary Layer on a Flat Plate in an External Turbulent Flow", AGARD CP-93, 1972, pp 27.1-27.10

65. Green, J. E., "On the Influence of Free Stream Turbulence on a Turbulent Boundary Layer, as it Relates to Wind Tunnel Testing at Subsonic Speeds", AGARD Report No. 602, 1973, pp 4.1-4.8

66. McDonald, H., and Kreskovsky, J. P., "Effect of Free Stream Turbulence on the Turbulent Boundary Layer", Int. Journal of Heat and Mass Transfer, Vol 17, 1974, pp 705-716

67. Meier, H. U., and Kreplin, H. P., "Influence of Freestream Turbulence on Boundary-Layer Development", AIAA Journal, Vol. 18, Jan. 1980, pp 11-15

68. Raghunathan, S., and McAdam, R. J. W., "Freestream Turbulence Effects on Attached Subsonic Turbulent Boundary Layers", AIAA Journal, Vol. 21, April 1983, pp 503-508

69. Hancock, P. E., and Bradshaw, P., "The Effect of Free-Stream Turbulence on Turbulent Boundary Layers", Trans. ASME, Journal of Fluids Engineering, Vol. 105, Sept. 1983, pp 284-289

70. Castro, I. P., "Effects of Free Stream Turbulence on Low Reynolds Number Boundary Layers", Trans. ASME, Journal of Fluids Engineering, Vol. 106, Sept. 1984, pp 298-306

71. Junkhan, G. H., and Serovy, G. K., "Effects of Free-Stream Turbulence and Pressure Gradient on Flat Plate Boundary-Layer Velocity Profiles and on Heat Transfer", Trans. ASME, Journal of Heat Transfer, May 1967, pp 169-176

72. Simonich, J. C., and Bradshaw, P., "Effect of Free-Stream Turbulence on Heat Transfer Through a Turbulent Boundary Layer", Trans. ASME, Journal of Heat Transfer, Vol. 100, Nov. 1978, pp 671-677

73. Blair, M. F., "Influence of Free-Stream Turbulence on Turbulent Boundary Layer Heat Transfer and Mean Profile Development, Part 1- Experimental Data, Part 2- Analysis of Results", Trans. ASME, Journal of Heat Transfer, Vol. 105, Feb. 1983, pp 33-47

74. Pal, S., "Wake Boundary Layer Interaction in Turbomachinery", Ph.D. Thesis, The City College of New York, CUNY, 1981

75. Lakshminarayana, B., and Horlock, J. H., "Review: Secondary Flows and Losses in Cascades and Axial-Flow Turbomachines", Int. Journal of Mechanical Science, Vol. 5, 1963, pp 287-307

76. Dunham, J., "A Review of Cascade Data on Secondary Losses in Turbines", Journal of Mechanical Engineering Science, Vol. 12, 1970, pp 48-59

77. Hazarika, B. K., Raj, R., and Boldman, D. R., "Three-Dimensional Fluid Flow Phenomena in the Blade End-Wall Corner Region", ASME Paper No. 86-GT-179, 1986

78. Bhargava, R. K., Raj, R., and Boldman, D. R., "Wall Shear Stress Measurement in Blade End-Wall Corner Region", ASME Paper No. 87-GT-181, 1987

79. Brown, K. C., and Joubert, P. N., "The Measurement of Skin Friction in Turbulent Boundary Layers With Adverse Pressure Gradients", Journal of Fluid Mechanics, Vol. 35, 1969, pp 737-757

80. Winter, K. G., "An Outline of the Techniques Available for the Measurement of Skin Friction in Turbulent Boundary Layers", Progress in Aerospace Sciences, Vol. 18, 1977, pp 1-57

81. Hanratty, T. J., and Campbell, J. A., "Measurement of Wall Shear Stress", Fluid Mechanics Measurements (Text Book), Edited by Richard J. Goldstein, Hemisphere Publishing Corporation,1983, Chapter 11

82. Monson, D. J., "A Nonintrusive Laser Interferometer Method for Measurement of Skin Friction", Experiments in Fluids, Vol. 1, 1983, pp 15-22

83. Tanner, L. H., "A Skin Friction Meter, Using the Viscosity Balance Principle, Suitable for Use With Flat or Curved Metal Surfaces", Journal of Physics E, Scientific Instruments, Vol. 10, 1977, pp 278-284

84. Monson, D. J., and Higuchi, H., "Skin Friction Measurements by a Dual-Laser-Beam Interferometer Technique", AIAA Journal, Vol. 19, June 1981, pp 739-744

85. Ferriss, D. H., "Preston Tube Measurements in Turbulent Boundary Layers and Fully Developed Pipe Flow", ARC 26 678, 1965

86. Head, M. R., and Rechenberg, I., "The Preston Tube as a Means of Measuring Skin Friction", Journal of Fluid Mechanics, Vol. 14, 1962, pp 1-17

87. Patel, V. C., "Calibration of the Preston Tube and Limitations on its Use in Pressure Gradients", Journal of Fluid Mechanics, Vol. 23, 1965, pp 185-208

88. Geremia, J. O., "Experiments on the Calibration of Flush Mounted Film Sensors", DISA Information No. 13, 1972

89. Schlichting, H., Boundary-Layer Theory (Text Book), 7th Edition, McGraw-Hill Book Co. Inc., 1979, pp 206

90. Kempf, G., "Neue Ergebnisse Der Widerstandsforschung", Werft, Reederei, Hafen 11, 1929, pp 234-239

91. Smith, D. W., and Walker, J. H., "Skin Friction Measurements in Incompressible Flow", NACA TN 4231, 1958

92. Tennant, M. H., Pierce, F. J., and McAllister, J. E. Jr., "An Omnidirectional Wall Shear Meter", Trans. ASME, Journal of Fluids Engineering, Vol. 102, Mar. 1980, pp 21-25

93. McAllister, J. E. Jr., Pierce, F. J., and Tennant, M. H., "Direct Force Wall Shear Measurements in Pressure-Driven Three-Dimensional Turbulent Boundary Layers", Trans. ASME, Journal of Fluids Engineering, Vol. 104, June 1982, pp 150-155

94. Acharya, M., Bornstein, J., Escudier, M. P., and Vokurka, V., "Development of a Floating Element for the Measurement of Surface Shear Stress", AIAA Journal, Vol. 23, Mar. 1985, pp 410-415

95. Pierce, F. J., and Krommenhoek, D. H., "Wall Shear Stress Diagnostics in Three-Dimensional Turbulent Boundary Layers", Interim Technical Report No. 2, ARO-D Project No. 6858E, Virginia Polytechnic Institute and State University, Sept. 1968

96. Clauser, F. H., "Turbulent Boundary Layers in Adverse Pressure Gradients", Journal of the Aeronautical Sciences, Vol. 21, Feb. 1954, pp 91-108

97. Bradshaw, P., "A Simple Method for Determining Turbulent Skin Friction From Velocity Profiles", Journal of the Aero/Space Sciences, Reader's Forum, Vol. 26, Dec. 1959, pp 841

98. Fage, A., and Falkner, V. M., "On the Relation Between Heat Transfer and Surface Friction for Laminar Flow", ARC R & M 1408, 1931

99. Ludwieg, H., "Instrument for Measuring the Wall Shearing Stress of Turbulent Boundary Layers", NACA TM 1284, 1950

100. Liepmann, H. W., and Skinner, G. T., "Shearing-Stress Measurements by Use of a Heated Element", NACA TN 3268, 1954

101. Bellhouse, B. J., and Schultz, D. L., "Determination of Mean and Dynamic Skin Friction, Separation and Transition in Low-Speed Flow With a Thin-Film Heated Element", Journal of Fluid Mechanics, Vol. 24, 1966, pp 379-400

102. McCroskey, W. J., and Durbin, E. J., "Flow Angle and Shear Stress Measurements Using Heated Films and Wires", Trans. ASME, Journal of Basic Engineering, Mar. 1972, pp 46-52

103. Higuchi, H., and Peake, D. J., "Bi-Directional, Burried-Wire Skin-Friction Gage", NASA TM 78531, Ames Research Center, 1978

104. Gessner, F. B., and Jones, J. B., "On Some Aspects of Fully-Developed Turbulent Flow in Rectangular Channels", Journal of Fluid Mechanics, Vol. 23, 1965, pp 689-713

105. Preston, J. H., 'The Determination of Turbulent Skin Friction by Means of Pitot Tubes", Journal of The Royal Aeronautical Society, Vol. 58, Feb. 1954, pp 109-121

106. McAllister, J. E. Jr., "Near-Wall Similarity in Two- and Three-Dimensional Turbulent Boundary Layers", Ph.D. Thesis, Virginia Polytechnic Institute and State University, 1979

107. Staff of the N. P. L., "On the Measurement of Local Surface Friction on a Flat Plate by Means of Preston Tubes", N. P. L. Report No. 3185, 1958

108. Bradshaw, P., and Unsworth, K., "Comment on Evaluation of Preston Tube Calibration Equations in Supersonic Flow", AIAA Journal, Technical Comments, Vol. 12, Sept. 1974, pp 1293-1296

109. Head, M. R., and Ram V. V., "Simplified Presentation of Preston Tube Calibration", Aeronautical Quarterly, Vol. 22, Aug. 1971, pp 295-300

110. Bertelrud, A., "Preston Tube Calibration Accuracy ", AIAA Journal, Technical Notes, Vol. 14, Jan. 1976, pp 98-100

111. Gupta, R. P., "New Device for Skin-Friction Measurement in Three-Dimensional Flows", AIAA Journal, Technical Notes, Vol. 13, Feb. 1975, pp 236-238

112. Bertelrud, A., "Total Head/Static Measurements of Skin Friction and Surface Pressure", AIAA Journal, Engineering Notes, Vol. 15, Mar. 1977, pp 436-438

113. Prahlad, T. S., "Wall Similarity in Three-Dimensional Turbulent Boundary Layers", AIAA Journal, Technical Notes, Vol. 6, Sept. 1968, pp 1772-1774

114. Prahlad, T. S., "Yaw Characteristics of Preston Tubes", AIAA Journal, Technical Notes, Vol.10, Mar. 1972, pp 357-359

115. Mojola, O. O., and Young, A. D., "An Experimental Investigation of the Turbulent Boundary Layer Along a Streamwise Corner", AGARD CP-93, 1971

116. Bragg, G. M., "The Turbulent Boundary Layer in a Corner", Journal of Fluid Mechanics, Vol. 36, 1969, pp 485-503

117. Anand, A. K., "An Experimental and Theoretical Investigation of Three Dimensional Turbulent Boundary Layers Inside the Passage of a Turbomachinery Rotor", Ph.D. Thesis, Department of Aerospace Engineering, The Pennsylvania State University, 1976

118. Willmarth, W. W., "Wall Pressure Fluctuations in a Turbulent Boundary Layer", The Journal of the Acoustical Society of America, Vol. 28, Nov. 1956, pp 1048-1053

119. Willmarth, W. W., and Wooldridge, C. E., "Measurements of the Fluctuating Pressure at the Wall Beneath a Thick Turbulent Boundary Layer", Journal of Fluid Mechanics, Vol. 14, 1962, pp 187 -210

120. Bull, M. K., "Wall-Pressure Fluctuations Associated with Subsonic Turbulent Boundary Layer Flow", Journal of Fluid Mechanics, Vol. 28, 1967, pp 719-754

121. Corcos, G. M., "Pressure Fluctuations in Shear Flows", University of California Institute of Engineering Research Report, Series 183, No. 2, 1962

122. Bakewell, H. P. Jr., Carey, G. F., Libuka, J. J., Schloemer, H, H., and Von Winkle, W. A., "Wall Pressure Correlations in Turbulent Pipe Flow", U. S. Navy Under-Water Sound Lab. Report No. 559, 1962

123. Corcos, G. M., "Resolution of Pressure in Turbulence", The Journal of the Acoustical Society of America, Vol. 35, Feb. 1963, pp 192-199

124. Willmarth, W. W., and Roos, F. W., "Resolution and Structure of the Wall Pressure Field Beneath a Turbulent Boundary Layer", Journal of Fluid Mechanics, Vol. 22, 1965, pp 81-94

125. Willmarth, W. W., and Yang, C. S., "Wall-Pressure Fluctuations Beneath Turbulent Boundary Layers on a Flat Plate and a Cylinder", Journal of Fluid Mechanics, Vol. 41, 1970, pp 47-80

126. Blake, W. K., "Turbulent Boundary-Layer Wall-Pressure Fluctuations on Smooth and Rough Walls", Journal of Fluid Mechanics, Vol. 44, 1970, pp 637-660

127. Schewe, G., "On the Structure and Resolution of Wall-Pressure Fluctuations Associated With Turbulent Boundary-Layer Flow", Journal of Fluid Mechanics, Vol. 134, 1983, pp 311-328

128. Beeler, G. B., "Turbulent Boundary-Layer Wall Pressure Fluctuations Downstream of a Tandem LEBU", AIAA Journal, Technical Notes, Vol. 24, April 1986, pp 689-691

129. Farabee, T. M., and Casarella, M. J., "Measurements of Fluctuating Wall Pressure for Separated/Reattached Boundary Layer Flows", Shear Flow-Structure Interaction Phenomena, The Noise Control and Acoustics Division of ASME, NCA Vol. 1, Nov. 1985, pp 17-25

130. Hasan, M. A. Z., Casarella, M. J., and Rood, E. P., "An Experimental Study of the Flow and Wall Pressure Field Around a Wing -Body Junction", Shear Flow-Structure Interaction Phenomena, The Noise Control and Acoustics Division of ASME, NCA Vol. 1, Nov. 1985, pp 89-95

131. Schloemer, H. H., "Effects of pressure Gradients on Turbulent-Boundary-Layer Wall-Pressure Fluctuations", The Journal of the Acoustical Society of America, Vol. 42, 1967, pp 93-113

132. Kobashi, Y., and Ichijo, M., "Wall Pressure and its Relation to Turbulent Structure of a Boundary Layer", Experiments in Fluids, Vol. 4, No. 1, 1986, pp 49-55

133. Coles, D., "The Law of the Wake in the Turbulent Boundary Layer", Journal of Fluid Mechanics, Vol. 1, 1956, pp 191-226

134. Coles, D., "The Young Person's Guide to the Data", Proceedings-Computation of Turbulent Boundary Layers, AFOSR-IFP-Stanford Conference, Vol. 2, 1968, pp 1-54

135. MacMillan, F. A., "Experiments on Pitot Tubes in Shear Flow", ARC R & M No. 3028, 1956

136. Sproston, J. L., and Goksel, O. T., "The Calibration of a Surface Static Tube", Aeronautical Journal, Technical Notes, Feb. 1972, pp 101-103

137. Bendat, J. S., and Piersol, A. G., Random Data: Analysis and Measurement Procedures (Text Book), Wiley Interscience, 1971, Chapter 9

138. Cooley, J. W., Lewis, P. A. W., and Welch, P. D., "The Finite Fourier Transform, Trans. IEEE, Audio and Electro-acoustics, AV-17, 1969, pp 77-85

139. Clauser, F. H., "The Turbulent Boundary Layer", Advances in Applied Mechanics, Vol. 4, 1956, pp 1-51

140. Ludwieg, H., and Tillmann, W., "Investigations of the Wall Shearing Stress in Turbulent Boundary Layers", NACA TM 1285, 1950

141. Coles, D., "The Turbulent Boundary Layer in a Compressible Fluid", USAF Project Report R-403-PR, The Rand Corporation, Santa Monica, 1962

142. Bradshaw, P., "Effects of Free Stream Turbulence on Turbulent Shear Layers", Imperial College Aero. Report 74-10, 1974

143. Purtell, L. P., Klebanoff, P. S., and Buckley, F. T., "Turbulent Boundary Layer at Low Reynolds Number", Physics of Fluids, Vol. 24, May 1981, pp 802-811

144. Kuethe, A. M., and Chow, C. Y., Foundations of Aerodynamics-Bases of Aerodynamics Design (Text Book), 4th Edition, John Wiley & Sons, 1986, pp 128

145. Bruun, H. H., and Tropea, C., "Calibration of Normal, Inclined and X- Array Hot-Wire Probes", Report No. SFB 80/M/170, Universitat Karlsruhe, Nov. 1980

☆U.S. GOVERNMENT PRINTING OFFICE:1989 -627 -064/ 86021

NASA
National Aeronautics and Space Administration

Report Documentation Page

1. Report No.	2. Government Accession No.	3. Recipient's Catalog No.
NASA CR-4211		

4. Title and Subtitle
An Experimental Study of Near Wall Flow Parameters in the Blade End-Wall Corner Region

5. Report Date
January 1989

6. Performing Organization Code

7. Author(s)
Rakesh K. Bhargava and Rishi S. Raj

8. Performing Organization Report No.
None (E-4506)

10. Work Unit No.
920-5-0

9. Performing Organization Name and Address
City College of New York
Mechanical Engineering Department
New York, New York 10031

11. Contract or Grant No.
NAG3-122

13. Type of Report and Period Covered
Contractor Report
Final

12. Sponsoring Agency Name and Address
National Aeronautics and Space Administration
Lewis Research Center
Cleveland, Ohio 44135-3191

14. Sponsoring Agency Code

15. Supplementary Notes
Project Manager, Donald R. Boldman, Propulsion Systems Division, NASA Lewis Research Center.

16. Abstract

The objective of the present study was to experimentally investigate the near wall flow parameters in the blade end-wall corner region. The blade end-wall corner region was simulated by mounting an airfoil section (NACA 65-015 base profile) symmetric blades on both sides of the flat plate with semi-circular leading edge. The initial 7 cm from the leading edge of the flat plate was roughened by gluing No. 4 floor sanding paper to artificially increase the boundary layer thickness on the flat plate. The initial flow conditions of the boundary layer upstream of the corner region are expected to dictate the behavior of flow inside the corner region. Therefore, an experimental investigation was extended to study the combined effect of initial roughness and increased level of free stream turbulence on the development of a two-dimensional turbulent boundary layer in the absence of the blade. The measurement techniques employed in the present investigation included, the conventional pitot and pitot-static probes, wall taps, the Preston tube, piezoresistive type pressure transducer and the normal sensor hot-wire probe. The pitot and pitot-static probes were used to obtain mean velocity profile measurements within the boundary layer. The measurements of mean surface static pressure were obtained with the surface static tube and the conventional wall tap method. The wall shear stress vector measurements were made with a specially constructed Preston tube. The flush mounted piezoresistive type pressure transducers were employed to measure the wall pressure fluctuation field. The velocity fluctuation measurements, used in obtaining the wall pressure-velocity correlation data, were made with the normal single sensor hot-wire probe. At different streamwise stations, in the blade end-wall corner region, the mean values of surface static pressure varied more on the end-wall surface than on the blade surface. The observed large changes in the values of mean surface static pressure on the end-wall surface in the corner region were mainly caused by the changes in the curvature of the streamlines. The magnitude of the wall shear stress in the blade end-wall corner region increased significantly in the close vicinity of the corner line. The maximum value of the wall shear stress and its location from the corner line, on both the surfaces forming the corner region, were observed to change along the corner. These observed changes in the maximum values of the wall shear stress and its location from the corner line could be associated with the stretching and attenuation of the horseshoe vortex. The wall shear stress vectors in the blade end-wall corner region were observed to be more skewed on the end-wall surface as compared to that on the blade surface. The differences in the wall shear stress directions obtained with the Preston tube and the flow visualization method were within the range in which the Preston tube was found to be insensitive to the yaw angle.

17. Key Words (Suggested by Author(s))	18. Distribution Statement
Corner flow; Blade end-wall flow; Wing-body junction; Horseshoe vortex; Wall shear stress; Wall pressure fluctuations; Pressure-velocity correlations; Boundary layer; Turbulence	Unclassified – Unlimited Subject Category 02

19. Security Classif. (of this report)	20. Security Classif. (of this page)	21. No of pages	22. Price*
Unclassified	Unclassified	314	A14

*For sale by the National Technical Information Service, Springfield, Virginia 22161